28th International Scientific Conference

MECHANIKA2024

31 MAY 2024
PROCEEDINGS

ktu
1922

ISSN 2783-5677 (online)

KAUNAS UNIVERSITY OF TECHNOLOGY
LITHUANIAN ACADEMY OF SCIENCE
IFTOMM NATIONAL COMMITTEE OF LITHUANIA
BALTIC ASSOCIATION OF MECHANICAL ENGINEERING

MECHANIKA 2024

PROCEEDINGS OF THE 28th INTERNATIONAL SCIENTIFIC CONFERENCE

31 May 2024
Kaunas University of Technology, Lithuania

KAUNAS – 2024

The proceedings of the 28th International Scientific Conference MECHANIKA 2024 contain selected papers covering the following topics:

- ✓ Advanced mechanical technologies;
- ✓ Biomechanics;
- ✓ Micro and nanosystem engineering;
- ✓ Composite materials;
- ✓ Robotics;
- ✓ Sensors, actuators and transducers;
- ✓ New manufacturing technologies and advanced material processing;
- ✓ Monitoring and optimization of manufacturing processes;
- ✓ Software for design;
- ✓ Assembly and manufacturing system maintenance;
- ✓ Machine tool and metrology;
- ✓ Surface tribology;
- ✓ Engineering materials and their application;
- ✓ Surface and coating engineering;
- ✓ Cloud manufacturing;
- ✓ Strength of materials and structural elements;
- ✓ Computational mechanics;
- ✓ Automation in production systems;
- ✓ Dynamics of mechanical systems;
- ✓ Technologies of graphics media;
- ✓ Advanced materials.

Only minor additional corrections of style and language have been carried out by the Publisher.

doi: 10.5755/e01.2783-5677.2024

SCIENTIFIC EDITORIAL COMMITTEE

Conference Chairman – *Prof. V. Ostaševičius,* member of the Lithuanian Academy of Sciences and Swedish Royal academy of Engineering Sciences, chairman of IFToMM National Committee, director of Mechatronics institute, Kaunas University of Technology.

Scientific Committee

Prof. Roberts Joffe (Lulea University of Technology, Sweden), *Dr. Antanas Daugėla* (Nanometronix LLC, United States), *Prof. Dimitrios Pavlou* (University of Stavanger, Norway), *Dr. Andrey Aniskevich* (University of Latvia, Latvia), *Prof. Jean Michel Nunzi* (Queen's University, Canada), *Prof. Sergio Cicero* (University of Cantabria, Spain), *Prof. Sergei Kruchinin* (Bogolyubov Institute for Theoretical Physics, National Ukrainian Academy of Science, Ukraine), *Prof. Daiva Zeleniakienė* (Kaunas University of Technology, Lithuania), *Prof. Antoni John* (Silesian University of Technology, Poland), *Prof. Rimantas Kačianauskas* (Vilnius Gediminas Technical University, Lithuania), *Prof. Petr Štemberk* (Czech Technical University, Czech Republic), *Dr. Dariusz Szpica* (Bialystok University of Technology, Poland), *Dr. Andrzej Borawski* (Bialystok University of Technology, Poland), *Dr. Eric Courteille* (Institut National des Sciences Appliquées de Rennes, France), *Prof. Gintautas Dundulis* (Kaunas University of Technology, Lithuania), *Dr. Grzegorz Mieczkowski* (Bialystok University of Technology, Poland), *Prof. Regita Bendikienė* (Kaunas University of Technology, Lithuania), *Prof. Arvydas Palevičius* (Kaunas University of Technology, Lithuania).

Organizing Committee

Chairperson: *Dr. Sigita Urbaitė* (Kaunas University of Technology, *Lithuania)*

Members: *Prof. Paulius Griškevičius* (Kaunas University of Technology, *Lithuania), Prof. Giedrius Janušas* (Kaunas University of Technology, *Lithuania), Dr. Vitalis Leišis* (Kaunas University of Technology, *Lithuania), Dr. Robertas Mikalauskas* (Kaunas University of Technology, *Lithuania), Dr. Marius Rimašauskas* (Kaunas University of Technology, *Lithuania), Dr. Ginas Čižauskas* (Kaunas University of Technology, *Lithuania)*

Contact us:

Conference Organizing Committee

Kaunas University of Technology
Faculty of Mechanical Engineering and Design
Department of Mechanical Engineering
Studentų str. 56-337

LT-51424 Kaunas, LITHUANIA

Phone: +370 (37) 323 498

E-mail: mechanic@ktu.lt

http://mechanic.ktu.edu/

Foreword

28th International Scientific Conference “Mechanika 2024” was made online via video conferencing, on May 31, 2024.

The on-going objective is to bring together scientists in the field of mechanics from the Baltic Region and other countries to continue debates about new challenges in this area. The conference covers a wide range of topics from advanced mechanical technologies to cloud manufacturing.

All Conference participants prepared manuscripts according the requirements, what makes our proceedings to be valuable resource of new information, which allows evaluating investigations of the scientists from different regions. Since the primary goal of the 28th International Scientific Conference “Mechanika 2024” is to present the highest quality research results, the Conference Program Advisory Committee selected the best materials and invited the authors to publish these materials in the journal “Mechanika” (https://mechanika.ktu.lt).

Editorial Committee from the best presentations formed the Conference Program. Appearing before the entire Program Committee, the Editorial Committee summarized the reviews and justified their selections and session proposals. The Program Chair resolved differences, finalized the program. The Conference Editorial Committee then notifies the authors of both accepted and rejected submissions and informs the Authors about the decision. This year the Conference Committee selected 37 topics for presentations and 33 manuscripts for conference proceedings to be published.

We hope that the proceedings of the 28th International Scientific Conference “Mechanika 2024” will be interesting for researches and engineers.

Prof. V. Ostaševičius

Content

Linear Inertial Piezoelectric Actuator Operating in Longitudinal – Bending Mode

Andrius ČEPONIS[1]*, Dalius MAŽEIKA[2], Piotr VASILJEV[3], Regimantas BAREIKIS[3], Arūnas STRUCKAS[3] and Sergejus BORODINAS[3]

1 Department of Engineering Graphics, Faculty of Fundamental Sciences, Vilnius Gediminas technical university, Vilnius, Lithuania

2 Department of Information Systems, Faculty of Fundamental Sciences, Vilnius Gediminas technical university, Vilnius, Lithuania

3 Education Academy, Vytautas Magnus University, K. Donelaičio str. 58, Kaunas, Lithuania

** andrius.ceponis@vilniustech.lt*

Abstract

The study conducts numerical and experimental investigations on a novel inertial piezoelectric linear actuator comprising a rectangular piezoelectric bimorph beam with a centrally positioned trapezoidal tooth. Actuator was developed for high-power applications such as gyroscope systems used in nano or microsatellites. The proposed piezoelectric actuator applies the principle of superimposing the rectangular beam's second longitudinal vibration mode and the trapezoidal tooth's first bending mode. The actuator's design and operational principle ensure the possibility of achieving high thrust forces. Furthermore, the utilization of a trapezoidal tooth mitigates buckling at the contact zone, especially under high preload forces, thereby enhancing the vibration energy transfer from the stator to the slider. A numerical investigation of the piezoelectric actuator was conducted. Modal analysis revealed that the natural frequency of the second longitudinal vibration mode and the first bending mode of the trapezoidal tooth is 68.22 kHz. Harmonic response analysis was used to identify the resonant frequency of the actuator, compute impedance-frequency characteristics, and find dependencies between vibration amplitudes and excitation voltage amplitudes. The outcomes revealed that the resonant frequency of the actuator is 68.2 kHz while the highest displacement amplitude of 214.5 µm was obtained when the excitation voltage of 200 V_{p-p} was used. A prototype of the actuator was made followed by an experimental investigation. The resonance frequency of 68.1 kHz was indicated experimentally. The experimental measurements showed that the actuator achieved a maximum linear speed of 81.1 mm/s and stall force of 6.1 N at a voltage of 200 V_{p-p}.

Keywords: inertial piezoelectric actuator, linear motion, longitudinal vibration mode, bending vibration mode.

1. Introduction

Nowadays nano and microsatellites become a key platform for space exploration, research activities in the space environment, communications, and Earth surveillance. Moreover, the usage of nano and microsatellites provides cost-effective payload possibilities and expands possibilities to perform small-scale research and technological development activities in space. However, the payload volume and mass are limited for these types of satellites and limit the scale and size of devices and systems that can be used for space missions. Therefore, optimization of systems mass and volume become key point challenge for these devices [1, 2]. Usually, the main mass and volume of orientation and pointing systems take electromagnetic actuators and motors that are used to drive different loads such as antennas and optical devices. In some cases, the orientation of the whole microsatellite is performed using these motors [3]. However, electromagnetic actuators and motors have some disadvantages such as relativity high mass and volume, low scaling options, limited motion resolution, required transmission system, and induced electromagnetic field [4]. Therefore, usage of electromagnetic motion devices for small scale satellites limits possible effective payload and raises the demand of another type of motion sources that can propose more efficient payload usage. One of the possible options is piezoelectric actuators and motors [5]. The main advantages of piezoelectric actuators and motors are the direct drive of load without additional transmission systems, energy free self-locking ability, low mass, and volume compared to electromagnetic motion sources, high scaling level, magnetic field-free operation, possibility to drive load in several degrees of freedom and finally motion resolution up to nanoscale [6, 7]. Therefore, considering to these advantages it can be found that the replacement of electromagnetic motion sources by piezoelectric ones could reduce the mass and volume demand of systems which are loaded to nano or micro satellites. State of art shows several examples of piezoelectric angular [8, 9] and linear actuators [10, 11] that are able to provide these advantages. On the other hand, in most cases, the output torques and forces of these piezoelectric actuators and motors are limited by the maximum possible preload forces between the stator and active part. It means that an increment of preload force inducts buckling of the stator and leads to parasitic sliding in the contact zone or negatively affects the transferring of the vibrations to the active part of the piezoelectric motion source. In addition, it increases wear of the contact zone and as a result reduces the reliability of whole system [12].

This paper represents numerical and experimental investigations of a novel piezoelectric linear motion actuator that provides stable operation under high preload forces and allows for increased output forces. The design of actuator is based on rectangular piezoelectric bimorph plate with a trapezoidal tooth that is placed at the center of piezoelectric bimorph plate

and matches with central antinode of the second longitudinal vibration mode of bimorph plate. The longitudinal vibrations of piezoelectric bimorph plate are inducted via sawtooth waveform electric signal so actuator operation is based on inertial stick-slip principle. Usage of trapezoidal tooth increases the buckling force compare to the rectangular shaped tooth and higher preload forces can be used that higher output motions forces can be obtained, respectively.

2. Design and operation principle of actuator

The design of actuator is based on rectangular plate with four piezoceramic plates placed on both top and bottom surfaces of the plate (Fig. 1). The piezoelectric plates are used to excite the second longitudinal vibration mode of bimorph plate. Trapezoidal-shaped tooth is placed at central antinode of the vibration mode. Alumina oxide contact cylinder is glued at the end of the tooth and is used to transfer vibrations of the actuator to slider. In addition, the actuator contains four clamping beams used to clamp it in the housing system. Clamping beam are placed in a such way that their longitudinal axis of symmetry matches with vibration nodes of the second longitudinal vibration mode of the bimorph plate. Finally, a cut-off is made at the center of the piezoelectric bimorph plate. It is used to reduce the structural stiffness of whole structure and to increase displacement amplitudes of trapezoidal tooth vibration.

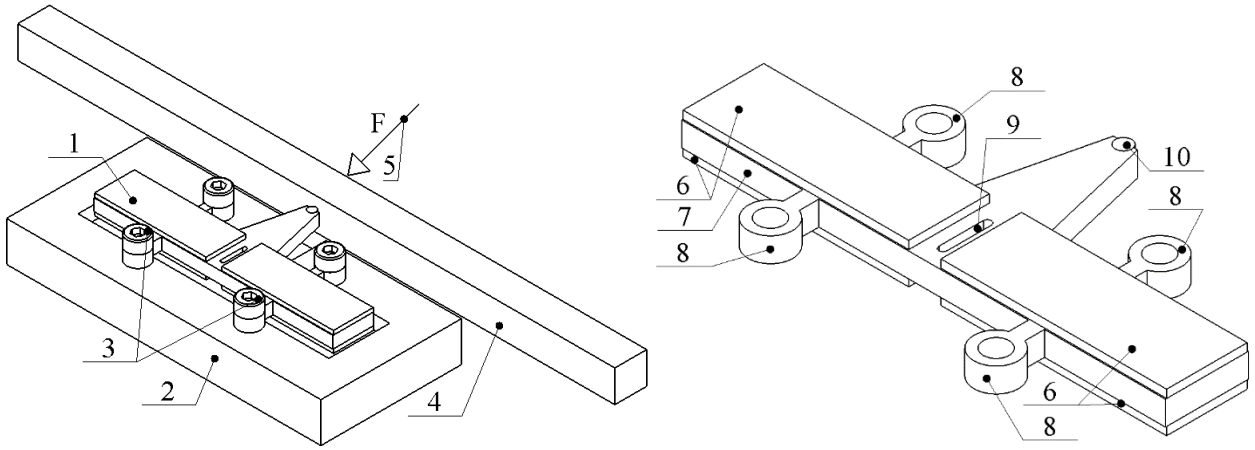

(a) (b)

Fig. 1 Structural design of the actuator; (a) – composition of actuator with slider; (b) – detailed composition of actuator; 1 – actuator; 2 – clamping frame of actuator; 3 – clamping bolt; 4 – slider; 5 – preload force; 6 – piezoelectric plates; 7 – elastic rectangular plate; 8 – clamping beams; 9 – a cut-oof; 10 – alumina oxide contact

The passive part of the actuator is made from high grade aluminum while PZT-8 type hard piezoceramic was chosen for active plates. The dimensions of the actuator are as follows: total length of the actuator is 60 mm while width without clamping beams is 10 mm (Fig. 1, a). The height of trapezoidal tooth is 14.75 mm while length of the bottom and top bases of the tooth is 10 mm and 3 mm, respectively. The total volume of the actuator is 3.49 cm^3 and the mass is 15.9 g.

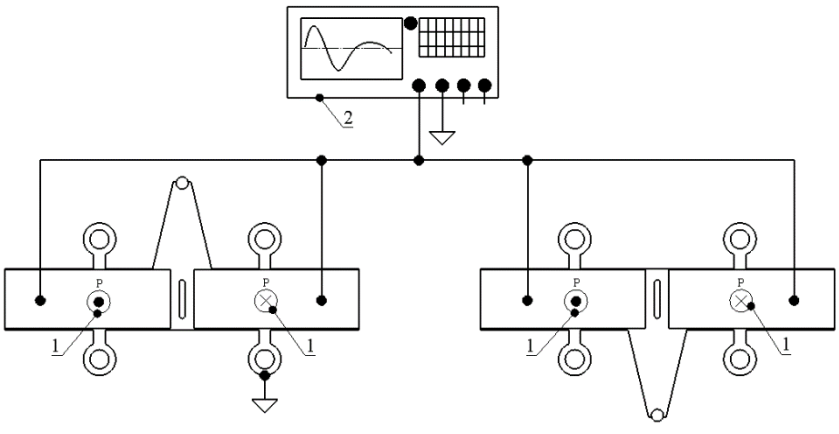

(a) (b)

Fig. 2 Excitation schematics of the actuator; (a) – top view; (b) – bottom view; 1 – polarization direction of piezoceramic plates; 2 – signal generator

Operation principle of the actuator is based on inertial stick-slip principle. Second longitudinal vibration mode of the piezoelectric bimorph plate is excited by applying sawtooth waveform excitation signal. In addition, the first bending

vibration mode of the tooth is induced, when the bimorph plate is excited. Such vibrations allow to increase displacement amplitude at the tip of the tooth. The central antinode of the second longitudinal vibration slowly moves the tooth in a forward direction during the stick stage of the actuator operation. Therefore, the slider inducts linear motion because of the friction force between the alumina oxide contact and the slider. Then the excitation signal changes its state to the opposite during a short time period and the slip stage of operation is obtained. The inertial force inducted by the second longitudinal vibration mode is higher than the friction force between alumina oxide contact and slider and as a result, slippage between contacting surfaces occurs and backward linear motion of the slider is not obtained. Continuous linear motion of the slider is obtained when a cyclic loop of these steps is used. The introduced actuator can be driven by a single electric signal when the polarization of all piezoceramic plates has opposite directions. Excitation schematics of the actuator are given in Fig. 2.

3. Numerical investigation of the actuator

A series of numerical investigations were performed with the goal of investigating the mechanical and electromechanical characteristics of the actuator. For this purpose, a numerical model was built using COMSOL Multiphysics software. Firstly, modal analysis of the actuator was performed with the aim to indicate natural frequency and vibration mode that is suitable for linear motion generation of the slider. The results are given in Figure 3.

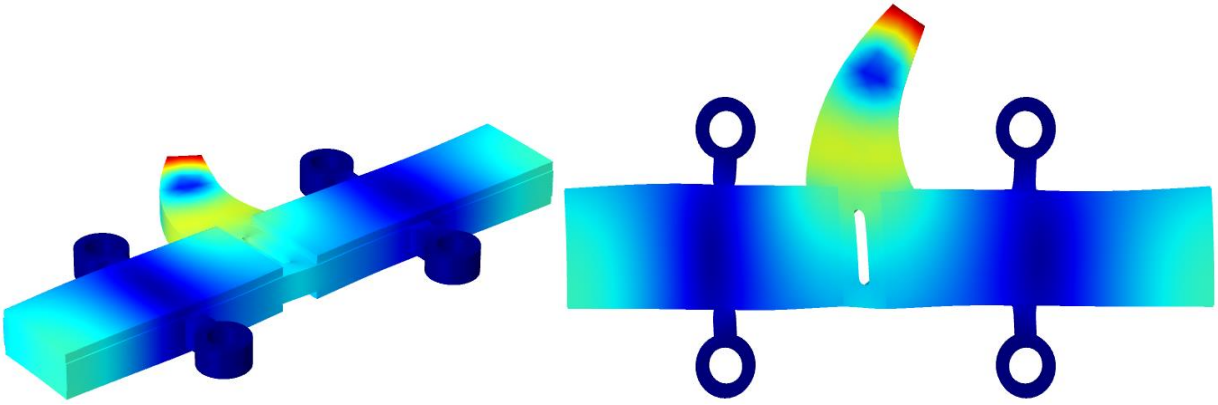

(a) (b)

Fig. 3 Vibration mode of the actuator at 68.22 kHz; (a) – side view of vibration mode; (b) – top view of vibration mode

It can be seen that the natural frequency of the second longitudinal vibration mode of the piezoelectric bimorph plate and the first bending vibration mode of the trapezoidal tooth coincides at the natural frequency of 68.22 kHz. Considering the vibration mode, it can be seen that the linear motion of the slider will be obtained when a sawtooth waveform electric signal is applied. Moreover, it can be noticed that amplification of displacements of longitudinal vibrations will be implemented because of bending vibrations of the trapezoidal tooth. The next step of the numerical investigation was to analyze impedance and phase characteristics in the frequency domain. For this purpose, frequency domain study was used while the amplitude of the excitation signal was set to 100 $V_{p\text{-}p}$. The excitation scheme of the actuator was set as it is shown in Figure 2. The results of the calculations are given in Figure 4.

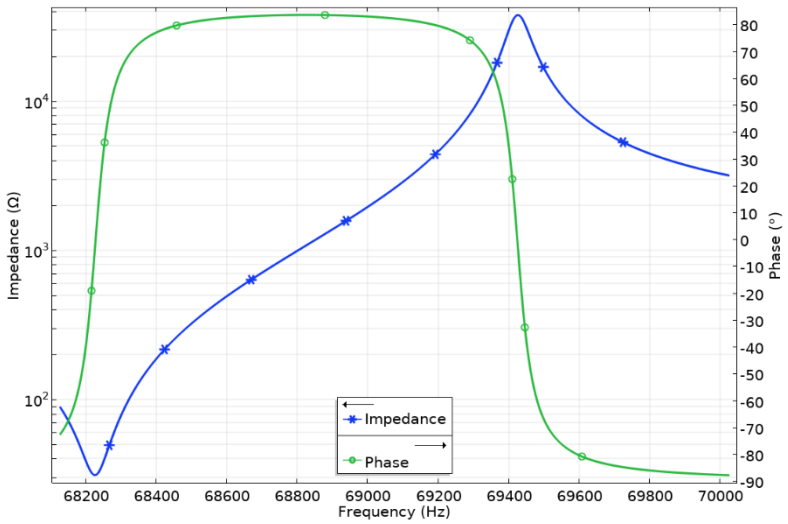

Fig. 4 Impedance and phase frequency characteristics of the actuator

It can be found that the resonance frequency of the actuator is 68.2 kHz while the impedance value at this frequency is 31.5 Ω. The slight difference between natural and resonance frequencies equal to 0.02 kHz was obtained due to the discreet calculation step used in the frequency domain study. On the other hand, it can be stated that these results confirm the results of modal analysis and indicate the operation frequency of the actuator. In addition, effective coupling coefficients (k_{eff}) were calculated and are equal to 0.18. It shows the high effectiveness of the proposed actuator.

The next stage of numerical calculations was focused on the indication of displacement amplitudes at the tip of a trapezoidal tooth while different excitation signal amplitudes were applied (Fig. 5). The analyses were made in the frequency domain while a range of excitation signal amplitudes was from 50 V_{p-p} to 200 V_{p-p} with incremental step of 50 V_{p-p}.

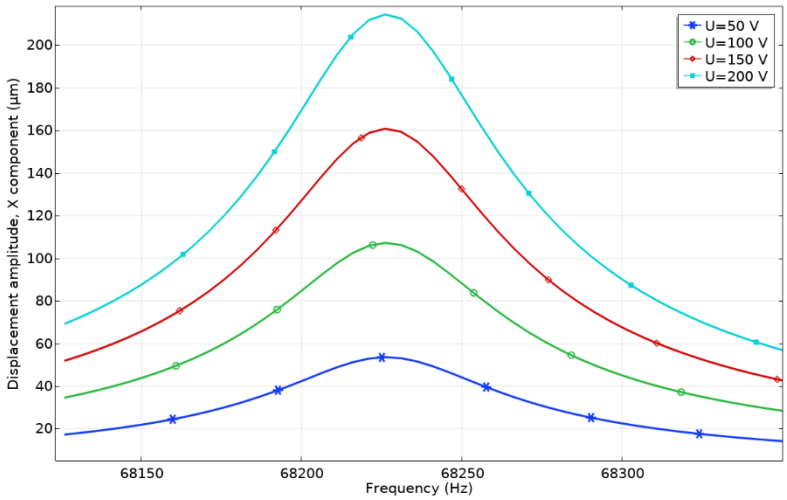

Fig. 5 Displacement – frequency characteristics of the actuator

Analysis of the results shown in Figure 5 indicates that peaks of displacement amplitudes were obtained at the frequency of 68.22 kHz. It confirms previous calculations of natural and resonant frequencies. The highest displacement amplitude was obtained while the excitation signal amplitude was set to 200 V_{p-p} and reached 214.5 µm or 1.07 µm/ V_{p-p}. The lowest displacement amplitude was obtained while 50 V_{p-p} excitation signal amplitude was used and reached 53.3 µm or 1.07 µm/V_{p-p}. It was found that the amplitude of the vibrations is almost linear depending on the excitation voltage and the actuator can provide stable and well-predictable displacement amplitudes at a wide range of excitation signal amplitudes.

4. Experimental investigation of the actuator

An experimental study was performed with the aim to verify the results of numerical investigations as well as to indicate the dynamic characteristics of the actuator. For this purpose, a prototype of the actuator was made with strict respect to the physical and mechanical characteristics given in Section 2. The view of the actuator prototype is given in Figure 6.

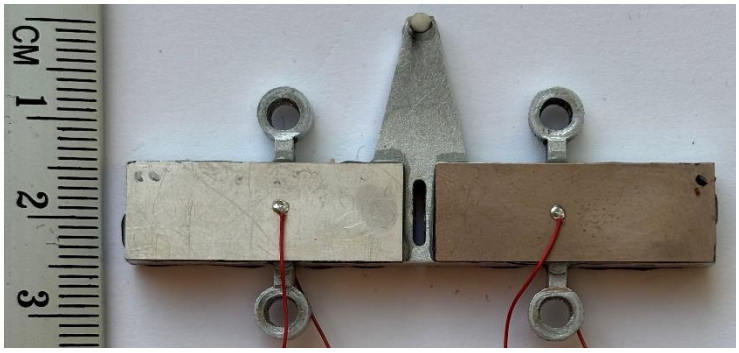

Fig. 6 Prototype of the actuator

Impedance and phase frequency of the actuator were measured using Hewlett Packard 4192 A LF impedance analyzer. The results of the measurements are given in Figure 7. It can be found that the resonance frequency of the actuator is 68.1 kHz. The difference between computed and measured is less than 1%. The measured impedance value at resonance frequency is 167.5 Ω, while the effective coupling coefficient (k_{eff}) reached a value of 0.169. The difference between computed and measured values mainly occurred because of the glue layer between elastic and piezoelectric plates that was neglected in the numerical model and minor errors in manufacturing and assembly. However, the results are in good agreement, and further experimental investigations were performed.

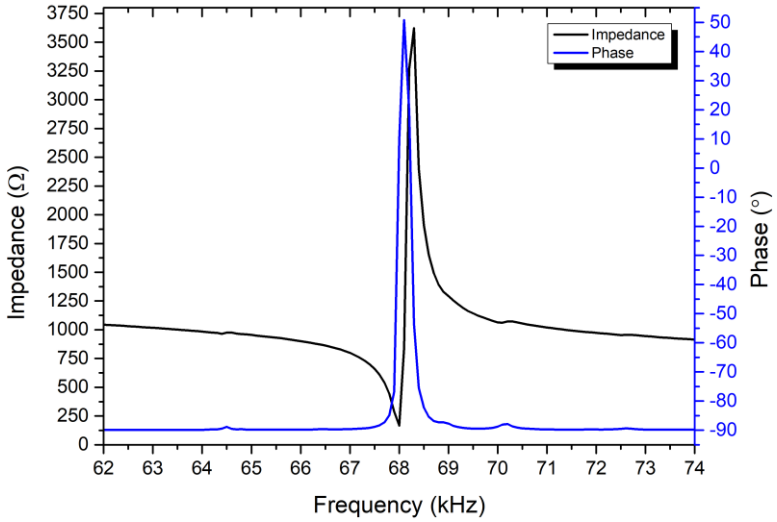

Fig. 7 Impedance and phase frequency characteristics of the actuator

The next stage of experimental investigations was dedicated to the measurement of linear motion speed and output force of the actuator. The results of the measurements are given in Figure 8.

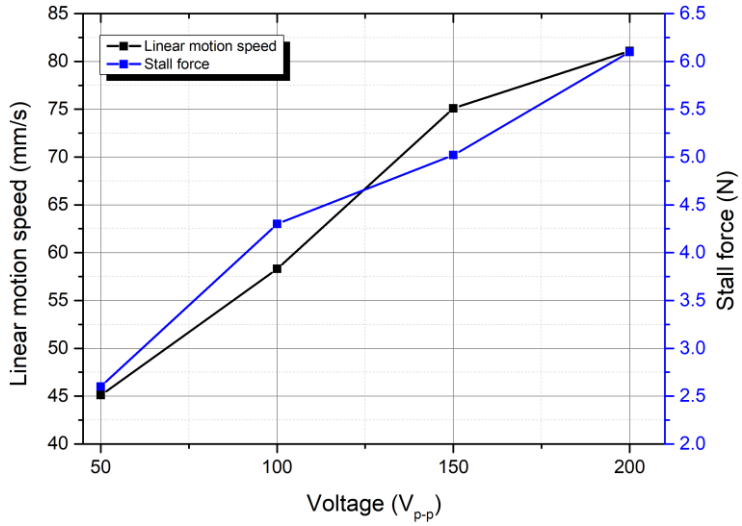

Fig. 8 Linear motion speed and stall force characteristics of the actuator

As can be found the highest linear motion speed was obtained when the excitation signal amplitude was 200 V_{p-p} and reached 81.1 mm/s or 0.4 (mm/s)/V_{p-p}. The lowest linear motion speed was obtained while excitation signal amplitude was set to 50 V_{p-p} and reached 45.1 mm/s or 0.9 (mm/s) V_{p-p}. The highest and lowest stall force of the actuator were obtained when the voltage of 200 V_{p-p} and 50 V_{p-p} were applied, respectively, and reached the values of 6.1 N or 30 mN/V_{p-p} and 2.6 N or 52 mN/V_{p-p}. Also, it was found that speed and stall force almost linearly depend of the excitation voltage.

5. Conclusions

A novel design of inertial linear motion actuator was introduced and investigated. The design of the actuator is based on a piezoelectric bimorph plate with a trapezoidal tooth placed in the middle of the plate. Employment of a trapezoidal tooth allows for increased bucking force and as a result increased preload force of the actuator which leads to higher output forces. On basis of results of modal analysis was found that superimposing the rectangular beam's second longitudinal vibration mode and the trapezoidal tooth's first bending mode is at 68.22 kHz while calculated impedance and phase frequency characteristics have shown that resonance frequency of the actuator is at 68.2 kHz. These results confirmed operation frequency of the actuator. Moreover, frequency response analysis has shown that the highest displacement amplitude of trapezoidal tooth tip reached 214.5 µm or 1.07 µm/ V_{p-p} at 200 V_{p-p}. Results of experimental investigations have verified operation principle and showed that resonance frequency of the actuator is 68.1 kHz while maximum linear motion and stall force characteristics reached 81.1 mm/s and 6.1 N at 200 V_{p-p}, respectively.

Funding: This work has received funding from Research Council of Lithuania under agreement No. S-MIP-22-61

References

1. Alandihallaj, M. A.; Emami, M. R. Multiple-Payload Fractionated Spacecraft for Earth Observation. *Acta Astronautica* **2022**, 191, 451–471. https://doi.org/10.1016/j.actaastro.2021.11.026.
2. Kopacz, J. R.; Herschitz, R.; Roney, J. "Small Satellites: An Overview and Assessment. *Acta Astronautica* 2**020**, 170, 93–105. https://doi.org/10.1016/j.actaastro.2020.01.034.
3. Gaude, A.; Lappas, V. Design and Structural Analysis of a Control Moment Gyroscope (CMG) Actuator for Cubesats. *Aerospace* **2020**, 7(5). https://doi.org/10.3390/AEROSPACE7050055.
4. Zhang, B.; Song, Z.; Liu, S.; Huang, R.; Liu, C. Overview of Integrated Electric Motor Drives: Opportunities and Challenges." *Energies* **2022**, 15(21). https://doi.org/10.3390/en15218299.
5. Jin, H.; Gao, X.; Ren, K.; Liu, J.; Qiao, L.; Liu, M.; Chen, W.; He, Y.; Dong, S.; Xu, Z.; Li, F. Review on Piezoelectric Actuators Based on High-Performance Piezoelectric Materials. *IEEE Transactions on Ultrasonics, Ferroelectrics, and Frequency Control* **2022**, 69 (11), 3057–3069. https://doi.org/10.1109/TUFFC.2022.3175853.
6. Ryndzionek, R. Improving Output Performance of the Ultrasonic Multicell Piezoelectric Motor by Development of the Multi-Rotor Structure. *IEEE Access* **2024**, 12 (February), 32080–32088. https://doi.org/10.1109/ACCESS.2024.3370560.
7. DongMei, X.; BingJie, Z.; SiMiao, Y.; XuHui, Z. Review on Single-Phase Driven Ultrasonic Motors. *Journal of Intelligent Material Systems and Structures* **2023**, 34(5), 525–535. https://doi.org/10.1177/1045389X221121911.
8. Yang, L.; Hu, X.; Yang, M.; Huan, Y.; Ren, W.; Xiong, Y.; Li, H. A Novel Traveling Wave Rotary Ultrasonic Motor with Piezoelectric Backup Function. *Journal of Intelligent Material Systems and Structures* **2023**, 34(20), 2414–2427. https://doi.org/10.1177/1045389X231187484.
9. Zhou, Y.; Chang, J.; Liao, X.; Feng, Z. Ring-Shaped Traveling Wave Ultrasonic Motor for High-Output Power Density with Suspension Stator. *Ultrasonics* **2020**, 102(February 2019), 106040. https://doi.org/10.1016/j.ultras.2019.106040.
10. Ting, Y.; Yu, C. H.; Lin, J. H.; Johar, T.; Wang, C. W. Design of a Short-Beam Linear Traveling-Wave Piezoelectric Motor. *IEEE Transactions on Ultrasonics, Ferroelectrics, and Frequency Control* **2021**, 68(8), 2815–2823. https://doi.org/10.1109/TUFFC.2021.3075449.
11. Wu, J.; Wang, L.; Du, F.; Zhang, G.; Niu, J.; Rong, X.; Song, R.; Dong, H.; Zhao, J.; Li, Y. A Two-DOF Linear Ultrasonic Motor Utilizing the Actuating Approach of Longitudinal-Traveling-Wave/Bending-Standing-Wave Hybrid Excitation. *International Journal of Mechanical Sciences* **2023**, 248(December 2022), 108223. https://doi.org/10.1016/j.ijmecsci.2023.108223.
12. Chen, Y.; Yang, J.; Niu, Y.; Xiao, S.; Li, L. Design and Experiment of a Double-Sided Staggered Conical Teeth Traveling Wave Ultrasonic Motor. *Ferroelectrics* **2023**, 615(1), 143–156. https://doi.org/10.1080/00150193.2023.2243557.

Seismic Performance Assessment of a Strengthened RC Building: A Case Study

Baris GUNES[1], Kamran SAMADI[2], Baris SAYIN[1*]

1 Department of Civil Engineering, Istanbul University-Cerrahpasa, 34320, Istanbul, Türkiye
2 Institute of Graduate Sciences, Istanbul University-Cerrahpasa, Istanbul, Türkiye
** barsayin@iuc.edu.tr*

Abstract

As seismic performance requirements outlined in earthquake codes become increasingly stringent and the lifespan of reinforced concrete (RC) structures extends, seismic performance analysis of previously rehabilitated RC buildings has become an important topic of interest again. A RC building with a continuous foundation underwent retrofitting, involving the addition of a slab foundation, columns, and shear walls. Additionally, the columns were jacketed with RC, and certain beams were strengthened using Carbon Fiber Reinforced Polymer (CFRP) fabric and plates. Following the strengthening process, the building underwent seismic evaluation. First, soil and earthquake parameters were determined based on the soil investigation report. The strengths of the concrete and steel materials were obtained through laboratory tests. The strengthened state of the building was modeled using the Midas Gen finite element software and then subjected to nonlinear push-over analysis. According to the analysis results, the building was found to satisfy the Controlled Damage performance target for the DD-2 Earthquake Ground Motion Level envisaged in the local seismic code, TBEC 2018. Furthermore, the strengthened foundation exhibited adequate strength and met the safety limit for soil pressures.

Keywords: Seismic Analysis, Push-Over Analysis, Rehabilitated Structure, Foundation Performance, Existing RC Buildings.

1. Introduction

Throughout history, human beings have struggled with numerous natural disasters in their efforts to safeguard and sustain their lives and the civilizations they've built. Among these disasters, earthquakes stand out as one of the most significant disasters faced by humanity. Because this disaster has the power to halt life by causing loss of life, as well as damage to property and infrastructure. From this point of view, the retrofitting of existing buildings, especially those constructed with reinforced concrete (RC), has become an essential requirement and a priority on the agenda. Moreover, it has become an inevitable procedure to inspect and analyze even previously retrofitted structures in accordance with new regulations and codes. Consequently, numerous studies have been conducted to gain a deeper understanding of the nonlinear behavior of materials and to evaluate various strengthening techniques using novel analysis methods. Some case studies on the evaluation of existing RC structures are discussed below.

Mahdavipour et al. [1] examined the collapse capacity and ductility of an FRP-strengthened RC building. The authors utilized the results of nonlinear pushover analysis to assess the effectiveness of the rehabilitation method, which involved various Fiber Reinforced Polymer (FRP) strengthening applications in beams and columns, as well as the rate of increase in ductility. Shafaei and Naderpour [2] examined the collapse resistance of FRP-strengthened RC frames over mainshock-aftershock sequences. Their findings indicated that the strengthening project is effective for improving collapse resistance structures; however, the capacity reduction caused by mainshock damages was found to be independent of the strength and ductility capacities of the structures. Cruz et al. [3] proposed a multi-criteria decision making-based seismic retrofit procedure weighted according to various criteria for RC buildings. They reported that structure-ground interaction can increase the seismic damage of a 4-story RC building by 17%. Among the three different structural retrofitting methods they investigated, adding fiber reinforcement polymers and steel bracing was found to be the best retrofitting technique due to minimal architectural impact and outstanding structural improvement, respectively. Lima et al. [4] proposed an optimization-based procedure for strengthening existing RC buildings. They concluded that while an optimal combination of element- and whole building-level techniques may not necessarily be environmentally ideal, it could offer a more cost-effective solution. Talledo et al. [5] examined the effectiveness of skin technology for strengthening existing RC buildings. Their findings revealed that the proposed retrofitting technology improved the seismic performance of the existing RC building and the exterior plaster was effective in limiting damage during low-magnitude repeated earthquakes.

This paper presents seismic assessment of a strengthened RC building. In the retrofitting project, new slab foundations, columns, and shear walls were added to the examined building. Additionally, existing columns and certain beams were strengthened using RC jacketing and Carbon Fiber Reinforced Polymer (CFRP) fabric/plates, respectively. Given that the dimensions of the structural elements remain consistent across all floors in the original building, the construction area of the 1st and 2nd typical floors is 20% larger than the ground construction area. Moreover, the construction area of the penthouse floor is 28% smaller than that of the 2nd typical floor. As a result, the centers of mass and stiffness of the 2nd and 1st basement floors, as well as the ground floor, differ from those of the 1st and 2nd typical floors above. Even the center of mass and rigidity of the penthouse floor differ from those of all other floors. However, despite these specific conditions, the retrofitting project was found to meet the Controlled Damage performance target for DD-2 earthquake ground motion level.

2. Materials and Methods

2.1. The Examined Building

The examined strengthened RC building comprised 2 basement floors, 1 ground floor, 2 typical floors, and a penthouse floor. The floor heights were 2.7 m on the 2nd and 1st basement floors, 3 m on the ground floor, 1st and 2nd typical floors, and 2.5 m on the penthouse floor. The existing foundation system of the building comprises continuous foundations in both the x and y directions. Properties of the structural members are given in Table 1. The properties of the members added for strengthening and the details of strengthening are given in Tables 2 and 3, respectively.

Table 1. Properties of the structural members

Structural Member	Floor	Dimensions (cm)
Column	2 & 1 Basement Ground 1 & 2 Typical	25×40; 25×50; 25×65; 30×55;
	Penthouse	25×65; 30×30; 30×55;
Beam	2 & 1 Basement, Ground, 1 & 2 Typical, Penthouse	25×50;
Slab	2 & 1 Basement, Ground, 1 & 2 Typical, Penthouse	12; (thickness)
Basement Shear	2 & 1 Basement	25; (thickness)

Table 2. Properties of the structural members added for strengthening

Member	Floor	Dimensions (cm)	Longitudinal Rebar (mm)	Transverse Rebar (mm)
Column	2 & 1 Basement Ground 1 & 2 Typical	30×40	Φ16	Φ10 @ 9cm
Shear Wall	2 &1 Basement	20, 25, 30 (thickness)	Φ12, Φ14, Φ16	Φ14, Φ12 @10cm
	Ground	25, 30 (thickness)		
	1 & 2 Typical Penthouse			Φ12, Φ10@10cm
Foundation	Slab Foundation	60 (thickness)	Ø16 lower and upper rebars @ 12 cm Additional rebars Ø12, Ø16 @ 25~33 cm	

Table 3. Details of strengthening

Member	Floor	Method	Longitudinal Rebar (mm)	Transverse Rebar (mm)
Column	2 & 1 Basement Ground 1 & 2 Typical Penthouse	15 cm thick jacketing is applied to the columns on two, three, or four sides.	Φ16	Φ10 @ 8 ~ 9cm
Beam	Ground Penthouse	CFRP (600 gr/m^2) for one beam; Against shear force	-	-
	1 & 2 Typical	CFRP (600 gr/m^2) for some beams; Against shear force	-	-
	2 Typical	CFRP (600 gr/m2) for some beams + 1.2 mm thick CFRP plate under beam; Against shear and bending force		

2.2. Material Examinations

As a result of the laboratory tests performed in accordance with the local code, TBEC-2018 [6], the average compressive strength of unconfined concrete was found to be 15.7 MPa. The detection studies for the undamaged and damaged reinforcing bars (rebars) revealed that the longitudinal rebars and stirrups were un-ribbed steel (S220). Class C35 concrete and B420C rebar were used in the strengthened elements. The mechanical properties of CFRP fabrics and plates used in the beams are listed in Table 4.

Table 4. Mechanical properties of the CFRP fabric

CFRP	CFRP fabric	CFRP plate
Material	Carbon	Carbon
Modulus of elasticity (N/mm^2)	245000	160000
Tensile strength (N/mm^2)	4900	2400
Elongation at break (%)	2.0	1.50
Thickness (mm)	0.337	1.2
Weight (gr/m^2)	600	100

2.3. Soil and Earthquake Parameters

The soil and earthquake parameters, obtained from the soil and foundation survey report and the data received from AFAD concerning the building's location, are briefly presented in Table 5. [7]. According to the ground study, the site is not at risk of liquefaction. The measured settlement amount was 1.56 cm, indicating that it falls within the permissible range.

Table 5. Soil and earthquake parameters

Parameters	Value / Class
Ultimate Design Strength; q_t (kN/m^2)	180.27
Vertical Bedding Coefficient; K_s (kN/m^3)	10095.60
Average shear wave velocity; $V_{S(30)}$ (m/sn)	338
Local soil class	ZD
Earthquake Map Spectral Acceleration Coefficients (g)	DD-3; S_S = 0.383, S_1 = 0.105
	DD-2; S_S = 0.973, S_1 = 0.269
	DD-1; S_S = 1.705, S_1 = 0.447
Peak ground acceleration (g)	DD-3; PGA = 0.167
	DD-2; PGA = 0.399
	DD-1; PGA = 0.679
Local soil impact coefficients	DD-3; F_S = 1.494, F_1 = 2.390
	DD-2; F_S = 1.111, F_1 = 2.062
	DD-1; F_S = 1.000, F_1 = 1.823
Spectral acceleration coefficients	DD-3; S_{DS} = 0.572, S_{D1} = 0.251
	DD-2; S_{DS} = 1.081, S_{D1} = 0.555
	DD-1; S_{DS} = 1.705, S_{D1} = 0.870

2.4. Performance Analysis

The examined building was modeled using Midas Gen [8] finite element software to represent its strengthened state. In the numeric model, the slabs were solely defined to represent in-plane rigidity and slab loads were separately applied on the beams. Performance Analysis Parameters defined according to TBEC-2018 [6] are given in Table 6.

Table 6. Performance Analysis Parameters

Parameter	Value/Class
Earthquake Ground Motion Level / Target Performance	DD-2 / Controlled Damage
Performance Assessment Method	Nonlinear push-over
Building Information Level and Coefficient	Existing Members (Limited) 0.75
	Strengthening Members (Comprehensive) 1.00
Earthquake Load Reduction, R	DD-2: R=1; D=1

3. Results

3.1. Performance Assessment Results

The numerical model of the building was subjected to nonlinear push-over analysis and forces acting on sections and strains were obtained. A post-assessment software developed by the authors in C# programming language [9] was used to perform evaluations in accordance with the principles outlined in TBEC-2018 [6]. The analysis and performance assessment results are given in Tables 7 and 8 for vertical and lateral structural elements, respectively.

Table 7. Performance Analysis Results for Vertical Structural Members

Floor	Vertical Load-Bearing Members (Columns and Shear walls)			Target Performance (CD)
	Strain Check for Article 15.8.4 (b)	Strain Check for Article 15.8.4 (c)	Stiffness Check for Article 15.8.4	
	RC	RC	RC	
2nd Basement	√	√	√	√
1st Basement	√	√	√	√
Ground	√	√	√	√
1st Typical	√	√	√	√
2nd Typical	√	√	√	√
Penthouse	√	√	√	√

Table 8. Performance Analysis Results for Lateral Structural Members

Floor	Lateral Load-Bearing Members (Beams)		Target Performance (CD)
	Strain Check for Article 15.8.4 (b)	Strain Check for Article 15.8.4 (c)	
	RC	RC	
2nd Basement	√	√	√
1st Basement	√	√	√
Ground	√	√	√
1st Typical	√	√	√
2nd Typical	√	√	√
Penthouse	√	√	√

Base shear-top displacement and capacity-demand spectrum curves obtained from nonlinear push-over analyses for the DD-2 earthquake ground motion level are shown in Figure 1. Lateral displacements of the performance points under earthquake effects are illustrated in Figure 2.

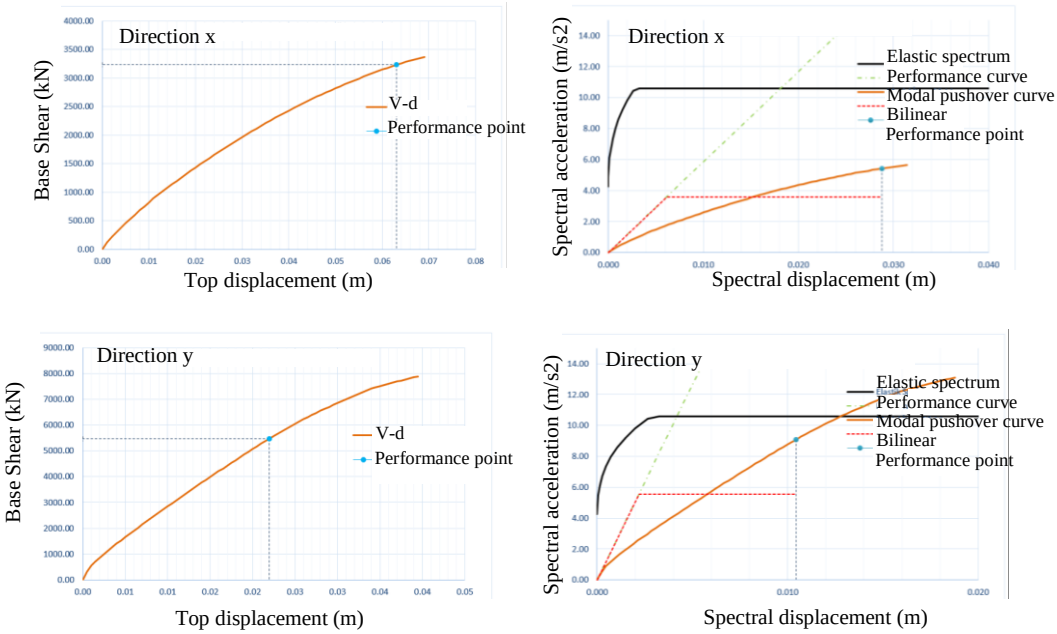

Fig. 1 Base shear-top displacement and capacity-demand spectrum curves

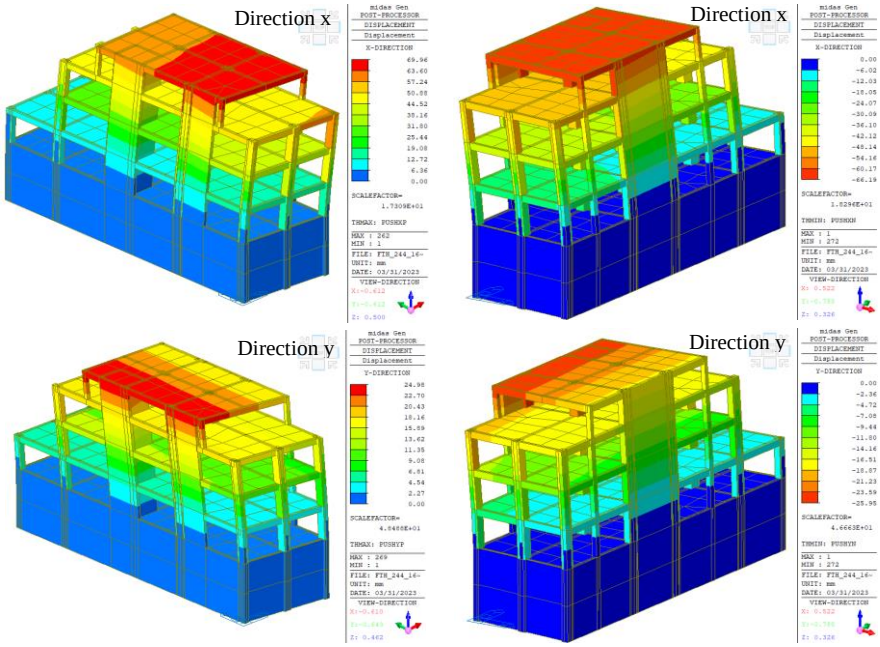

Fig. 2 Lateral displacements under earthquake effects

3.2. Performance Assessment of the Foundation

3.2.1. Bending Analysis of the Foundation

Examinations based on the moment distribution in the foundation of the building indicated that the foundation rebars were adequate. Moment envelopes obtained by the bending analysis of the foundation are shown in Figure 3.

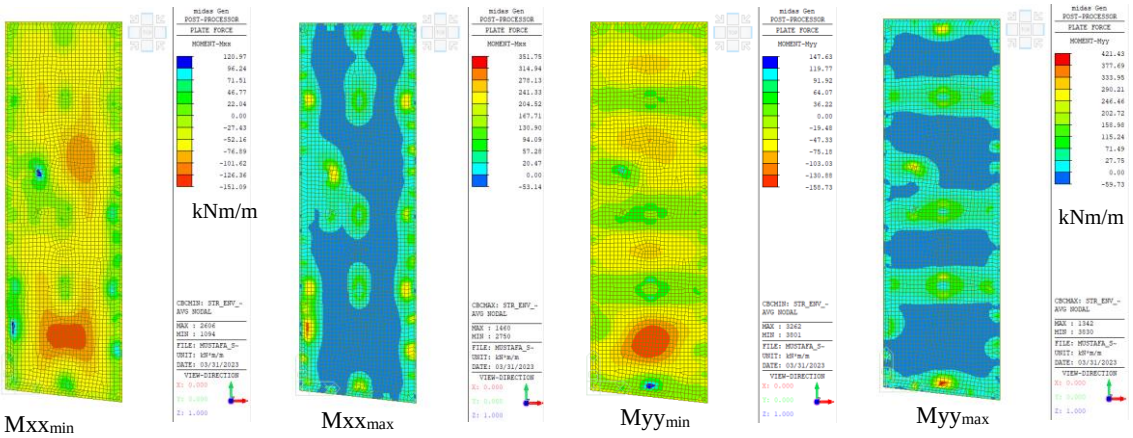

Fig. 3 Moment diagrams for the foundation

3.2.2. Soil Bearing Capacity Evaluations

The envelopes showing the soil pressures under the foundation are illustrated in Figure 4. The maximum soil pressure obtained from the analyses was q_0 = 178 kPa, which is less than the allowable limit q_t. Consequently, the soil pressure value satisfies the safety limit.

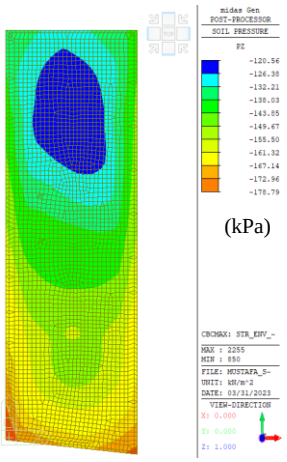

Fig. 4 Maximum soil pressures under the foundation

4. Conclusions

The seismic performance of the strengthened state of the building was determined according to the criteria outlined in TBEC-2018 using the numeric building model prepared based on the static strengthening project as well as concrete and rebar investigations. The key findings obtained from the performance assessment are as follows:

- The strengthened state of the building satisfies the criterion outlined in the TBEC-2018 Article 15.8.4 (a) for the “Controlled Damage” performance level. All primary RC beams of the structure fall within the "Limited Damage" or "Significant Damage" zones, with the exception of the secondary beams, which are not part of the horizontal load-bearing system. Additionally, no primary RC beam is classified within the "Advanced Damage" or "Collapse" state.
- The strengthened state of the building meets the criterion envisaged in the TBEC-2018 Article 15.8.4 (b) for the “Controlled Damage” performance level. All vertical RC structural members of the structure fall within the "Limited Damage" zone. No vertical RC structural member is in the “Significant Damage”, “Advanced Damage” or "Collapse" state.
- The strengthened state of the building satisfies the criterion outlined in the TBEC-2018 Article 15.8.4 (c) for "Controlled Damage". No RC vertical structural elements exceeded the “Significant Damage” limit in both upper and lower sections.
- The strengthened state of the building meets the stiffness criterion specified in the TBEC-2018 Article 15.8.4 for the “Controlled Damage” performance level. No RC elements exhibited “brittle” damage.

References

1. Mahdavipour, M.A.; Eslami, A.; Jehel, P. Seismic evaluation of ordinary RC buildings retrofitted with externally bonded FRPs using a reliability-based approach. Composite Structures, 2020; 232:1-11.
2. Shafaei, H.; Naderpour, H. Seismic fragility evaluation of FRP-retrofitted RC frames subjected to mainshock-aftershock records. Structures, 2020; 27:950-961.
3. Requena-Garcia-Cruz, M.V.; Morales-Esteban, A.; Durand-Neyra, P. Assessment of specific structural and ground-improvement seismic retrofitting techniques for a case study RC building by means of a multi-criteria evaluation. Structures, 2022; 38:265-278.
4. Lima, C.; Nigro, F.; Martinelli, E. Conceptual design formulation and comparative assessment of a seismic retrofit procedure for existing RC structures based on combining member and structure-level techniques. Structures, 2023; 55:1096-1108.
5. Talledo, D.A.; Federico, R.; Rocca, I.; Pozza, L.; Savoia, M.; Saetta, A. Seismic risk assessment of a new RC-framed skin technology for integrated retrofitting interventions on existing buildings, Procedia Structural Integrity, 2023; 44:918-925.
6. TBEC-2018, Turkey Building Seismic Code: Rules for design of buildings under earthquake effect, Official Gazette, 18.03. 2018, 30364 (in Turkish).
7. AFAD. (2019). Türkiye Deprem Tehlike Haritaları İnteraktif Web Uygulaması. https://tdth.afad.gov.tr/TDTH/main.xhtml adresinden alındı
8. Midas Gen (2021), Integrated Solution System for Building and General Structures, MIDAS Information Technology Co.
9. C# Programming language, Microsoft that runs on the NET Framework.

Evaluation of the Sensitivity of the Szpica-Warakomski Method to a Change in the Diameter of the Outlet Nozzle of a Gas Injector

Łukasz PAPROCKI[1]*, Dariusz SZPICA[1]

1 Bialystok University of Technology, Faculty of Mechanical Engineering, 45C Wiejska Str., 15-351 Bialystok, Poland
** lukasz.paprocki105346@student.pb.edu.pl, d.szpica@pb.edu.pl*

Abstract

This paper presents the results of flow testing using an innovative test method. The method serves to quickly assess the operating condition of gas injectors. On the basis of the test results and a new inference in relation to those already in use, decisions are ultimately made regarding possible repairs or adjustments. This is necessary in the course of diagnostics. This action is in line with current trends in the automotive industry to ensure precision in fuel dosing. The research objective was to assess the sensitivity of the adopted method to the diameter of the outlet nozzle, which fundamentally changes the flow parameters. An original test rig and associated inference procedures were used to achieve the objective. Testing of a selected injector type under conditions of varying supply pressure and injection time allowed, at a further stage, the determination of parameters necessary in the evaluation of the adopted test method. The test results and their analysis allowed the evaluation of the inference in the Szpica-Warakomski method.

Keywords: LPG injectors, injection testing, automotive, rapid diagnostics

1. Introduction

Human activity brings with it a continuous increase in solid waste and an increase in atmospheric gas concentrations, resulting in air pollution and the widespread type of environmental pollution found in most industrial cities and metropolitan areas [1]. Air pollutants entering from power plant chimneys, fuel combustion and exhaust systems include dust, smoke sulphur and carbon dioxides, nitrogen and carbon oxides and silicon. Human activity is constantly increasing the concentration of CO2 in the atmosphere, significantly intensifying this process leading to many negative effects. The increase in carbon dioxide on a global scale increases gas insulation, resulting in global warming. The 'Fit for 55' package reveals a very large role for the automotive industry [2]. Its aim is to implement the European Union's Green Deal and reduce greenhouse gas emissions by 55% by 2030 compared to 1990 levels. The main areas in which the package aims to take action include the European Climate Act, vehicle emissions, emissions trading, energy, transport and waste management [3]. Actions include reforming existing EU climate and energy legislation and making it more effective. With regard to the automotive sector, putting transport on a pathway to reduce air pollution is necessary because it accounts for almost a quarter of greenhouse gas emissions, which are also a major cause of urban air [4]. Despite the production of low-emission and electrically-powered cars, the vast majority of cars in use in Europe are internal combustion engine cars. The use of alternative fuels in vehicles is a common phenomenon these days. The most popular alternative fuels used in transport are: LPG, CNG and LNG. LPG for use in spark-ignition engines has a higher octane rating than petrol and generates fewer harmful substances during combustion and greenhouse gas emissions, thus having a positive impact on the environment [5]. LPG can be an effective tool in reducing air pollutant emissions in the transport sector and thereby accelerate the transformation of the transport sector in line with the objectives of the Fit to 55 package. LPG systems used in cars allow cars to be adapted to replace petrol with an alternative fuel and in the form of liquefied petroleum gas. Its advantages also include its availability and lower price. LPG injectors mounted in the engine intake manifold inject the liquefied gas into the combustion chamber in liquid form to form a fuel mixture with air. Matching the amount of gas injected to the driving conditions of the car ensures adequate performance with economical fuel consumption and exhaust gas reduction. The correct operation of the injector is crucial to the efficiency of the internal combustion engine. A number of different methods can be used to test injectors, depending on the adopted test objective [6]. Injector testing methods fall into two main groups, the first being analytical and numerical methods and the second being direct and indirect experimental methods. The constant search for new test methods to diagnose gas injectors is a response to the ever-growing interest in alternative fuels. One of the quick diagnostic methods allowing the determination of the current state of the injector and its parameters is the Szpica-Warakomski method, carried out on a test table using appropriate software [7]. On the basis of the data obtained during this test, a decision is made on the correctness of the injector's operation, changes to its operating settings, or possibly a decision on the need to replace the injector. This article will discuss the effect of changing the outlet nozzle on the indications obtained during testing.

2. Material and methods

The LPG injector undergoes rapid diagnostics using the Spitz-Warakomski method. below shows the construction of an example injector, on the left you can see a model *a* made in CAD [8]. The plunger *1* is pressed by spring *2* against the body *3* with a stop *4*. The plunger starts to move when the coil *5* is energised and the solenoid circuit *6* is closed towards channel *7*. This allows gas to flow from the inlet nozzle *8* to the outlet nozzle *9* with different outlet channel diameters. Shown to the right are images of the actual *b* Valtek Rail Type 30 injector.

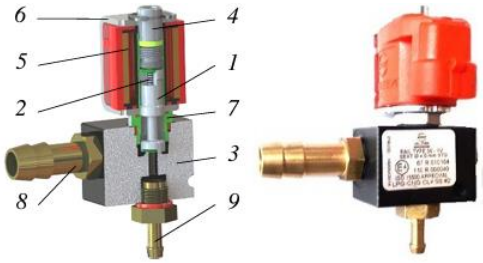

(a) (b)

Fig. 1 Structure of the Valtek gas injector [8]: a - model injector, b - actual injector, 1 - piston, 2 - spring, 3 - body, 4 - restrictor, 5 - coil, 6 - solenoid circuit, 7 - channel, 8 - inlet nozzle, 9 - outlet nozzle

The Szpica-Warakomski method allows injectors to be tested on a GIT (Gas Injector Tester) test bench using dedicated software [9]. During testing, test conditions such as pressure are specified and the injector opening time is determined. During the measurements, the dosage of the injector is assessed, on the basis of which the parameters of the trend line are determined, allowing the technical condition of the injector to be assessed. A schematic diagram of the stand's construction is presented below Fig. 2. A supply source *1* is responsible for supplying air to the buffer tank *3* after it passes through the pressure control system *2*. From the tank, the air flows through a flow meter *4* to the tested injector *5*. A temperature sensor *6* and a pressure sensor *7* are also connected to the tank to read out parameters of the working medium. All information is collected in a recording device *8* that is also responsible for opening the injector under test. The task of the central unit *9* equipped with a computer product is to control the pressure and opening time of the injector.

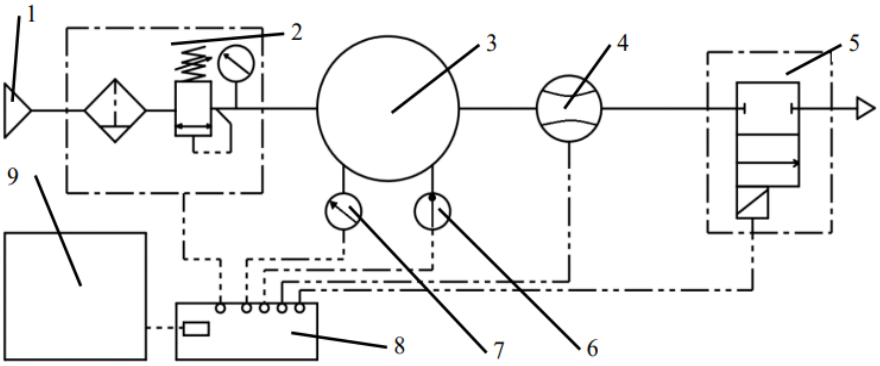

Fig. 2 Schematic of test stand based on [9]: 1 - power source, 2 - pressure control system, 3 - pressure buffer tank, 4 - flow meter, 5 - injector, 6 - temperature sensor, 7 - pressure sensor, 8 - recording device, 9 - central unit

The trend line is constructed on the basis of the expenditure values over time at different supply pressures and injector opening times, which involves determining the points read in the appropriate coordinate system. Fig. 3 shows an example of a graphical interpolation based on the averaged measurement results. The obtained trend lines were determined on the basis of points, respectively, *1* for line *2* determined for the reference injector, *3* for line *4* for the injector with a higher flow rate and *7* for line *8* determined for the injector with a faulty electric drive. The parameters of the trend line are the angle of inclination of the straight line, the coefficient of intersection with one of the characteristic axes and the coefficient of determination determining the spread of the results.

The tests were carried out on a GIT (Gas Injector Tester) test stand built within the "INNOSPIN" Politechniczna Sieć VIA Carpatia competition by researchers from the Białystok University of Technology, Lublin University of Technology and Rzeszów University of Technology. The view of the test stand is shown in Fig. 4. The base is formed by a housing *1* to which is fixed a bracket *3* to which the injector *5* is attached. Air is supplied through duct *4* as the working medium and electrical power to injector *2*. A drain *6* conveys the air flow to the measuring apparatus located inside the stand. A FSM3 CKD flow meter with an accuracy of ±3% was used. The pneumatic gauges *7*, the bench power supply *9* and the control panel with display, on which the results are shown, are visible on the previous part of the enclosure. Test settings can also be changed on it. Example settings *1* are shown in Fig. 5, where time parameters, pressures and simulated motor speeds are set. The relevant sensor and actuator parameters *2* with their settings and corresponding values. The injection flow range *3* is set for the new injector. On the monitor after the test, the results *4* are maintained in the form of a bar chart and an indication above them as to whether the measurement was within the range. All the results obtained during the tests remain stored and processed in a spreadsheet.

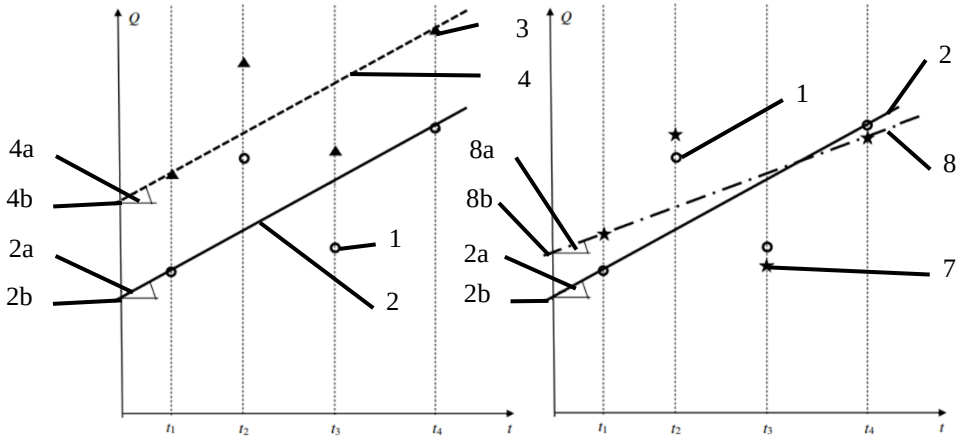

Fig. 3 Graphical interpretation for four measurement points [9]: 1 - averaged value of dosage, 2 - determined trend line, 2a - value of directional coefficient, 2b - point of intersection of the axis of the disbursement, 3 - value of dosage of the second injector, 4a - determined trend line of the second injector, 4b - point of intersection of the axis of the disbursement of the second injector

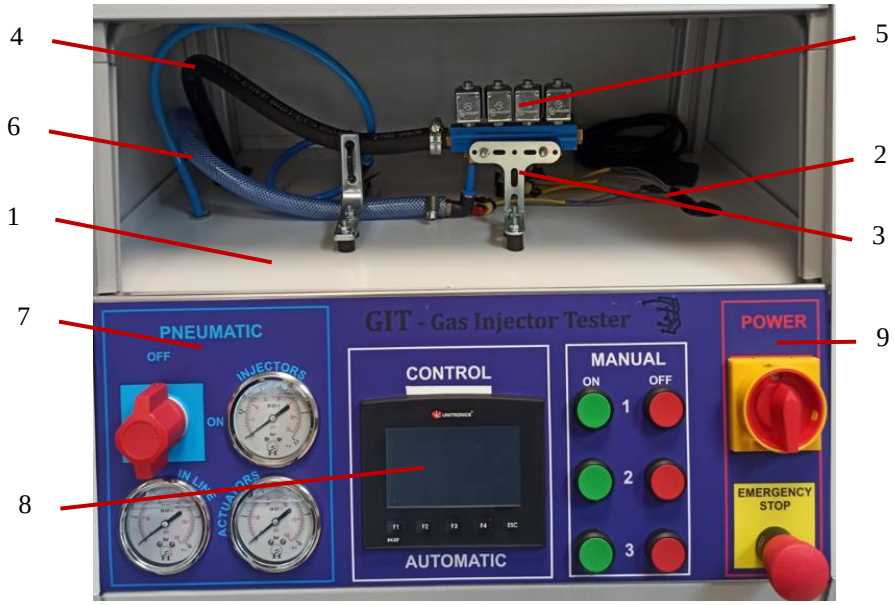

Fig. 4 View of the GIT Gas Injector Tester bench: 1 - housing, 2 - injector electrical supply, 3 - mounting, 4 - air line, 5- LPG injector, 6 - drain, 7 - pneumatic indicators, 8 - control panel with display, 9 - bench power supply

Fig. 5 View of the monitor panel: 1 - test settings, 2 - calibration of sensors and actuators, 3 - operating range values, 4 - visualization of results

The tests were carried out on an AC injector rail with the designation W01-4 shown in Fig. 6 z with outlet nozzles ranging from 1.5mm to 3.1mm in diameter with a 0.2mm stroke. The injector specifications are shown in Table 1 obtained from the vendor's website [10].

Fig. 6 AC W01-4 injection bar

Table 1. Technical data of the AC injector W01-4 [10]

Maximum capacity	38HP/cyl
Coil resistance	20Ohm
Voltage	12 V DC
Opening time	2.1ms
Closing time	1.5ms
Maximum operating pressure	4.5bar
Outside diameter of inlet spigots	12mm
Outside diameter of spigots	6mm
Plug	Superseal/Valtek
Operating temperature	(-20°C ÷ 120°C)

3. Results and discussion

On the basis of the data obtained during the tests, graphs were created, showing the dependence of the average flow rate at the measurement points on the injection times for the injector tested, shown in Fig. . Five measurements were taken for each nozzle, and trend lines were determined for the given nozzle diameter, taking into account its parameters: the directional coefficient, the coefficient of intersection with one of the characteristic axes, and the coefficient of determination determining the scatter of the results. Summaries of all parameters in the trend line for each tested nozzle diameter are shown in Table2. Error bars are also included. The lowest coefficient of determination, with a value of 0.8995, was seen when testing an injector with an outlet nozzle diameter of 1.5mm, while the highest coefficient of determination, with a value of 0.9795, was seen when testing an injector with an outlet nozzle diameter of 2.7 mm.

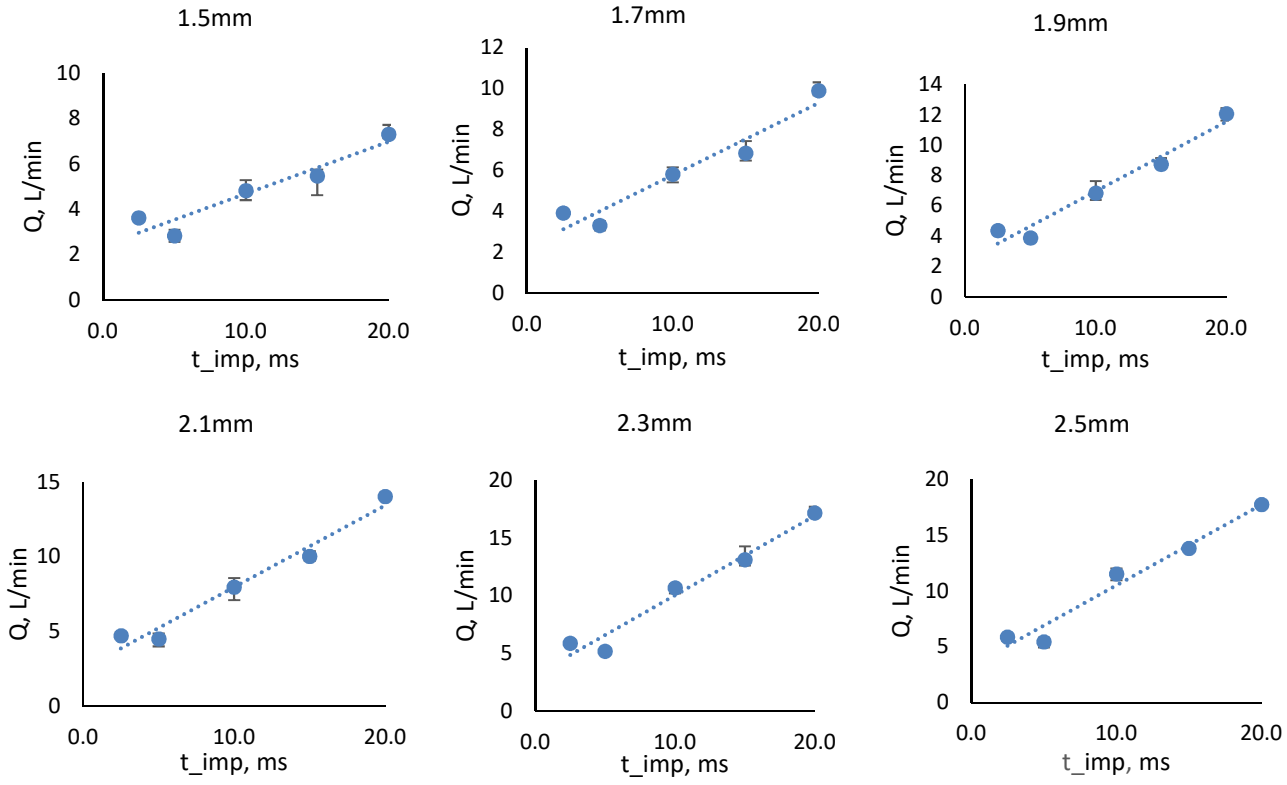

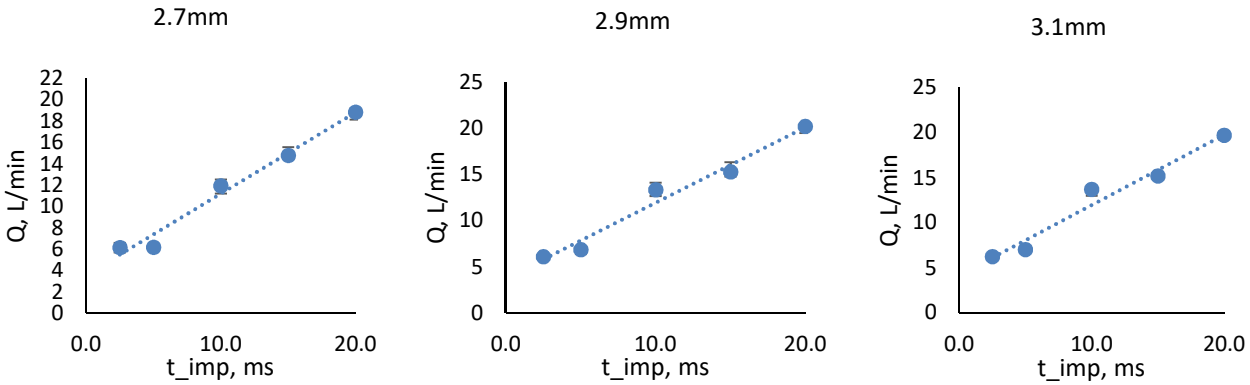

Fig. 7 Graphs showing the dependence of the average discharge on injection times for the AC injector W01-4

Table 2. Summary of trendline parameters depending on the outlet nozzle diameter used

Nozzle diameter *d*, mm	Directional coefficient *a*	Intersection coefficient *b*	Coefficient of determination R^2
1.5	0.2289	2.3974	0.8995
1.7	0.3530	2.2432	0.9289
1.9	0.4583	2.3819	0.9583
2.1	0.5464	2.5083	0.9671
2.3	0.6917	3.1228	0.9639
2.5	0.7212	3.2871	0.9653
2.7	0.7616	3.5824	0.9795
2.9	0.8181	3.7675	0.9749
3.1	0.7818	4.1631	0.9651

Fig. 8 shows a graph showing the obtained values of the individual parameters from the injector tests carried out. The influence between the injector nozzle used and the trendline parameters can be seen. As the installed nozzle diameter increases, the axis intersection point increases. In most cases, the directional coefficient of the trend line also increases. The coefficient of determination differs for the first two fitted diameters significantly from the others. The test method allows a quick diagnosis of the injector and a decision on its further use, a change of setting or the need for a new replacement.

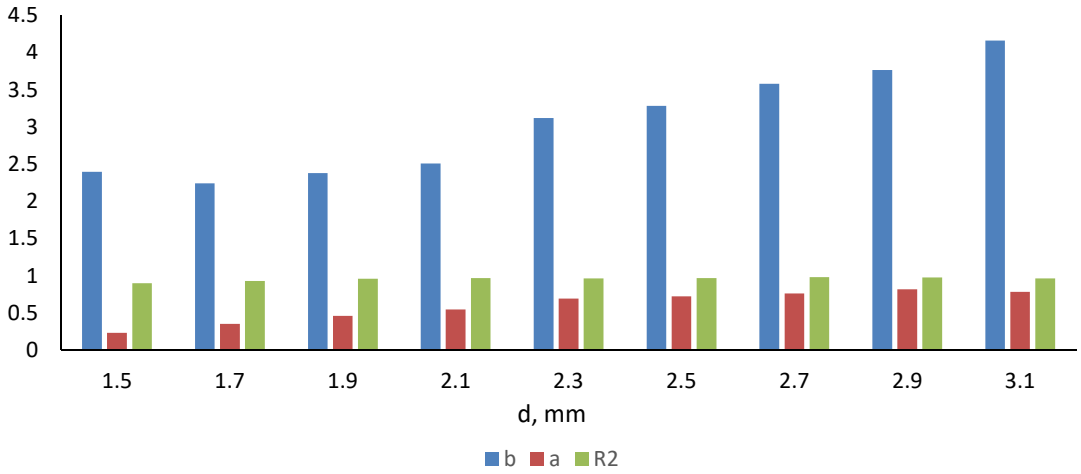

Fig. 8 Diagrams showing the dependence of the parameters on the nozzle fitted for the W01-4 AC injector

4. Conclusions

On the basis of the research carried out, it was found:

- significant effect of the injector nozzle used on the trend line parameters,
- the coefficient of determination differs for the tested nozzles, which influences changes in the injector efficiency,
- the Szpica-Warakomski research method allows for a quick diagnostics of the injector, the results obtained during its testing can positively influence the decision-making concerning further use of the injector, the necessity to change the settings or even the necessity to replace it with a new one.

References

1. PCC Grup, „www.products.pcc.eu," 31 01 **2022**. [Online]. [Data uzyskania dostępu: 04 05 2024].
2. K. KUTAWA. M. MAJ, „Wpływ pakietu Fit to 55 na przemysł motoryzacyjny w Grupie Wyszehradzkiej," w *ISBN 978-83-66698-88-8*, Warszawa, **2022**.
3. E.M. THIERJUNG. M. KOSTER. S. SCHLACKE. H. WENTZIEN, „Implementing the EU Climate Law via the 'Fit for 55' package," *Oxford Open Energy,* 10 01 **2022**.
4. Komisja Europejska, „commission.europa.eu," 14 07 **2021**. [Online]. [Data uzyskania dostępu: 04 05 2024].
5. R. KRAKOWSKI, „Paliwa i napędy alternatywne w kontekscie zasotrzania przepisów dotyczących emisji spalin," *Efektywnosć transportu,* pp. 1225-1230, 6 **2017**.
6. B. TOCZKO. A. BORAWSKI. G. MIECZKOWSKI. Dariusz SZPICA, „Experimental Evaluation of the Influence of the Diameter of the Outlet Nozzle Bore of a Gas Injector on Its Flow Characteristic," w *Advances in Homogeneous Charge Compression Ignition Engines and Alternative Fuels*, Białystok, **2023**.
7. J. WARAKOMSKI. Dariusz SZPICA, „Sposób testowania wtryskiwaczy paliw na stole probierczym, produkt komputerowy do realizacji sposobu testowania wtryskiwaczy na stole probierczym i stół probierczy do testowania wtryskiwaczy paliw, Wynalazek, Zgłoszenie potwierdzone, Numer zgłoszenia (Pol," Politechnika Białostocka, Białystok, **2023**.
8. D. SZPICA, „Determination of low pressure gas injector valve flow factor," w *Engineering for rual development*, Białystok, **2020**.
9. WARAKOMSKI. J. SZPICA D, „Sposób testowania wtryskiwaczy paliw na stole probierczym, produkt komputerowy do realizacji sposobu testowania wtryskiwaczy na stole probierczym i stół probierczy do testowania wtryskiwaczy paliw, Wynalazek, Zgłoszenie potwierdzone.," Politechnika Białostocka, Białystok, **2023**.
10. Jacus, „jacus.pl," Jacus. [Online] [Data uzyskania dostępu: 07 05 2024].

Development of Technical Maintenance Procedures Aimed to Improve Effectiveness of Maintenance

Azad ISMAYILOV[1]*, Kazimieras JUZĖNAS[1]

1 Faculty of Mechanical Engineering and Design, Kaunas University of Technology, Kaunas, Lithuania
** azad.ismayilov@ktu.edu, en.ktu.edu*

Abstract

Industrial companies aim to improve their performance indicators, increase efficiency and reduce the impact of their activities on the environment. One of the areas to be improved is the technical maintenance of their technological equipment. Improvement of reliability of technological equipment, reduction of cost of exploitation and improvement of effectiveness of maintenance processes may be achieved by better, more reliable planning of maintenance. This paper presents procedure proposed for improvement of maintenance at small or medium production company using mechanical processing equipment. One of the important elements of the procedure is the identification of equipment failures, which allows to improve the planning and execution of maintenance.

Keywords: technical maintenance, maintenance planning, vibration diagnostics.

1. Introduction

Industrial companies aim to enhance their performance and increase their efficiency but also reduced the cost of production processes and impact to environment. Several factors can stand on the way of this process as lack of skills of employees and training capabilities, not optimised processes, waste, lack of data tracking, adaptability to new methods and technologies, failing machines due to neglected maintenance and internal or external communication gaps [1]. In order to accomplish these objectives, Key Performance Indicators (KPIs) are essential for identifying areas of low performance and opportunities for development. Industrial companies always look for new solutions where the efficiency of processes can be reached by increasing the reliability of the production line and equipment. Technical maintenance and correct methods of chosen maintenance processes can improve the effectiveness of processes, as well as to reduce downtime of equipment and increase the productivity as well as decrease cost of whole production process. Preventive maintenance can be one of the examples that could minimise the unplanned downtime of production and emergency repairs. As well as proper planning of maintenance is crucial in order to reach improvements. Vibration diagnostics plays a significant role in predictive machine maintenance programmes. Vibration diagnostics has consistently demonstrated its effectiveness as the primary method for assessing the condition of machinery over time. Vibration diagnostic tools are utilised to forecast machine malfunctions. For analysis of data and comparison with calculated data, vibration diagnostics were performed. Gained results expected to be used as example for small or medium production company using mechanical processing equipment in order to early detect failures and plan the upcoming maintenance.

2. Maintenance procedures, maintenance planning and computerised detection of faults

Modern demands of industry rely on high productivity and efficiency of processes and lowered expenses on operations. However, equipment tends to fail and degrade over some period of time due to aging and wear and it can impact the production process by increasing downtime and expenses of processes. Over years, the perception of maintenance and its management has changed and currently enterprises implement various maintenance strategies in order to optimise their operations, reduce downtime and improve the reliability of assets and sustainability [2]. In most literature, maintenance is divided into corrective and preventive maintenance. According to Syamsundar et al., corrective maintenance, also can be known as repair, is performed to restore a malfunctioning system to its normal operational condition. In terms of reliability, maintenance effectiveness is classified into three distinct categories: optimal, imperfect, and minimal. Optimal maintenance results in the system being restored to a state that is equivalent to its original condition. Minimal maintenance puts the system back to the state it was in just before it failed, or a state that is as deteriorated as it was previously. Imperfect maintenance returns the system to a state that is somewhere between its original condition and its previous deteriorated one [3]. Corrective maintenance could lead to more expenses as it has no planning of maintenance and expenses can be higher than expected, increase the safety concerns and lead to unexpected and more failures. On the other hand, preventive maintenance can be the type of maintenance where proactive approach is used by performing maintenance before the equipment failures. Preventive maintenance is also classified into time and condition-based maintenance. Time based maintenance can be described as scheduled maintenance, while condition-based maintenance is done in accordance with the state of the object being studied. From real world examples, preventive maintenance widely used in fields as aviation, marine, construction and others. Example of preventive maintenance processes can include inspection, cleaning, lubrication and repair or replacements before failure. Preventive maintenance is necessary to minimise the likelihood of breakdowns, hence optimising overall expenditures. If preventive maintenance is not performed and only corrective maintenance is implemented in response to failures, the resulting costs will encompass maintenance expenses as well as other costs associated with failures, such as lost output due to unforeseen disruptions and extended delivery delays, which can result in a damaged

reputation. This might result in unfeasible operations due to the significant expense involved, and it can be enhanced through the implementation of well thought, planned and executed preventive maintenance [3]. Maintenance planning is important process for maintenance activities and plays big role in ensuring that maintenance is done according to plan and smooth operations for industries. Typical maintenance planning includes creating a structured plan for equipment maintenance, maintenance schedule and allocating necessary tools, skills and resources for maintenance efficiently. Maintenance planning has been proven to be significant in general once industries have grasped the primary risks and consequences associated with following the corrective maintenance strategy, often known as breakdown prevention. The primary hazards include production line interruption, additional expenses, and the duration of necessary urgent maintenance. A centralised or decentralised maintenance management structure, industry-related resources (such maintenance operators and equipment), and an appropriate maintenance planning technique are necessary for the implementation of a suitable maintenance planning system. The shop floor reality should be as closely resembled by the maintenance planning process as feasible. Industries have been able to lower their failure risks through the use of preventive maintenance strategies and regular or irregular maintenance activities planning [4]. By implementing effective maintenance planning, industrial companies can reach cost reduction, optimise the allocation of resources, enhance reliability of equipment and can enhance the safety of staff and preserve equipment. Enterprises can drastically cut their operating expenses by using efficient maintenance scheduling and planning. Industrial companies can prevent expensive downtime, emergency repairs, and lost production by proactively detecting and resolving equipment problems before they become serious failures.

In the present era, the practice of maintenance can gain advantages from the technological advancements that are advancing the Industry 4.0 revolution. The concept was initially introduced in Germany in 2011 as a component of the country's high-tech strategy [5]. It gained rapid global adoption as a means to drive the advancement and enhancement of 21st century industry. In the context of Industry 4.0, production systems are designed as intelligent systems known as Cyber Physical Systems (CPS). These systems facilitate real-time communication and collaboration between humans and machines, resulting in improved production efficiency and flexibility to meet increasingly demanding performance and safety requirements. Industry 4.0 relies on collecting big quantities of data from various systems and utilising advancements in sensors, robotics, and emerging technologies like Artificial Intelligence (AI), Machine Learning (ML), augmented reality, big data analytics, and Internet of Things (IoT) [2]. In context of maintenance and its influence from Industry 4.0, maintenance can benefit of analysis of big data and analytics as gathering, keeping, and evaluating massive datasets can gain insights, spot trends, forecast failures, and enhance decision-making. Afterwards, gathered big data and analytics can be very useful information to analyse and predict when maintenance is needed, allowing industrial companies to have more efficient maintenance processes and reach downtime reduction, reaching predictive maintenance. There can be several methods that can be useful to gather data as logging the data and having historical data of maintenance, utilisation of IoT devices equipped with sensors which collect real time data of equipment health and performance, utilisation of range of instruments, such as sensors, metres, checklists, work orders, reports, surveys, and audits, to gather diverse forms of data concerning the state, performance, maintenance history, costs, and feedback of the equipment and others. One of the methods to gather information about the health of equipment is considered vibration diagnostics. Vibration diagnostics plays a significant role in predictive machine maintenance programmes. Vibration diagnostics has consistently demonstrated its effectiveness as the primary method for assessing the condition of machinery over time. Vibration diagnostic tools are utilised to forecast machine malfunctions [6]. Implementing predictive maintenance and conducting regular machine inspections enables early detection of machine faults, allowing for prompt and appropriate intervention. By taking this action, companies can prevent unforeseen machine shutdowns and unnecessary replacement of parts that are still in good condition. Vibration analysis is a process of measuring and analysing the vibrations that occur in machines and mechanical systems. The goal of vibration analysis is to identify the source of the vibration and determine its cause, so that appropriate corrective actions can be taken to prevent machine failure or downtime. Vibration analysis typically involves the use of specialized instruments, such as accelerometers, to measure the vibrations of a machine or system. The data collected by these instruments is then analysed to identify any patterns or trends in the vibration levels. Through vibration analysis, it is possible to detect a wide range of machine faults, including unbalance, misalignment, bearing wear, and gear damage. By identifying these faults early, corrective action can be taken to prevent further damage and extend the lifespan of the machine or system. Vibration analysis can also be used to monitor the effectiveness of maintenance activities, such as balancing or alignment, to ensure that they are providing the desired results. In order to give example of vibration analysis and obtain results, vibration analysis was performed which can be used to diagnose faults of technological equipment.

3. Process of obtaining results of vibration analysis

Conventional not computerised machine has been selected ir order to analyse potential of automation of periodic equipment condition evaluation. Thus, vibration analysis and a conventional screw-cutter lathe (fig.1) was chosen aiming to develop proposals for improvement of maintenance suitable for some small or medium production company using mechanical processing equipment. Such machine tools are applied in conditions of individual and small-scale manufacturing in small companies lacking deeper competencies in technical diagnostic and aiming to reduce cost of maintenance s well as down-time of equipment.

The first step was experimental measurements of vibrations of the selected machine, analysis of features that could be used for automounted or semi-automated detections of faults and evaluation of condition equipment.

Fig. 1 Screw-cutter lathe 1K62 and "Schenk" Vibrotest 60 used to carry analysis

In order to determine vibration of the equipment, "Schenck" Vibrotest 60 was used, and it was employed to detect vibrations emitted by the 1K62 lathe and analyse them. Elements that were tested were shaft, belt drive system, gear mesh system, rolling element bearing, fundamental cage train assembly and ball pass. The experiment was done in 2 rotation speeds which were 500 and 800 r/min and were repeated twice with centred and off-centred rotation.

4. Results

Figures 2-3 show the results obtained by "Schenk" Vibrotest 60

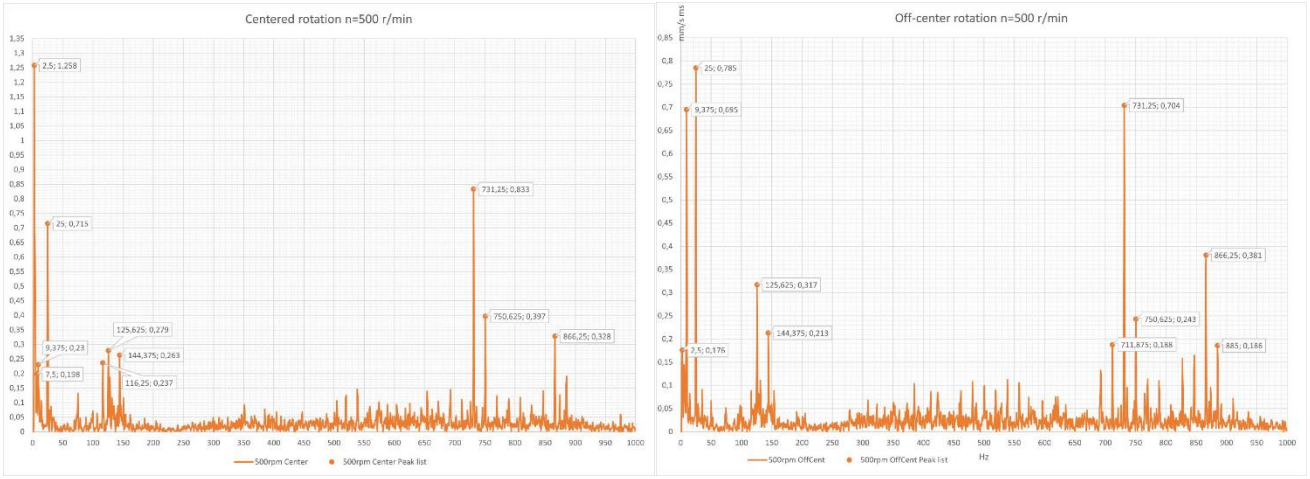

Fig. 2 Rotation n=500 r/min (a) centred and (b) off-centred rotation

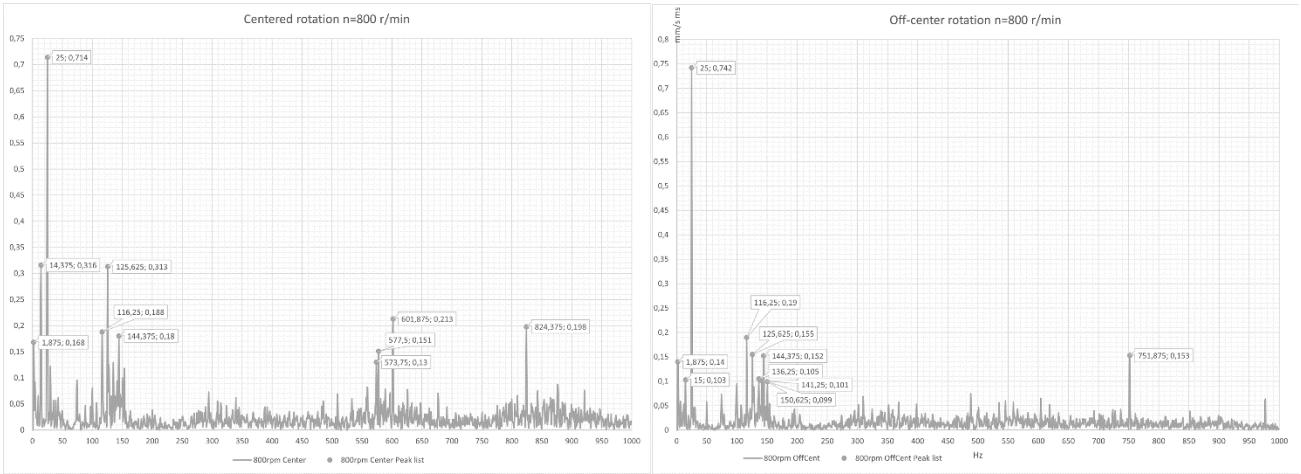

Fig. 3 Rotation n=800 r/min (a) centred and (b) off-centred rotation

Frequency of rotation of some component of the lathe is shown on table 1.

Table 1. Machine elements speed and frequency

Machine elements	N, *rpm*	Fz, *Hz*
Electric motor	1450	24.17
Input shaft	810	13.5
	500	8.33
	800	13.33

Rotational speed of the head stock gearbox input shaft is calculated using electric motor speed and dividing by transmission coefficient, which is calculated taking input and output shaft dimensions ratio which were in the scheme of machine elements, and it is 810 rpm. Gears on input (1, 2, 3) and output (24, 25, 26) shafts frequency calculation results are shown on table 2.

Table 2. Gears on input (1, 2, 3) and output (24, 25, 26) shafts frequency calculation results

Gear	Speed, *rpm*	Number of teeth, *unit*	F, *Hz*
G1	810	56	756
G2		51	688.5
G3		50	675
G24	500	52	433.33
G25		43	358.33
G26		60	500
G24	800	52	693.33
G25		43	573.33
G26		60	800

Table 3. Data of bearings on input (1, 2, 73, 74, 3, 4, 8) and output (20,21, 22) shafts

Element No. in scheme	Bearing No.	No. of rolling elements	Outer diameter, *mm*	Inner diameter, *mm*	Pitch diameter, *mm*	Rolling element diameter, *mm*	Angle of contact, °
1, 2, 73, 74	209	9	85	45	65	12.7	0
3, 4	7000108	16	68	40	54	6.35	0
8	208	9	80	40	60	12.70	0
20	3182120Y	15	150	100	125	14.30	0
21, 22	46215	17	130	75	102.5	17.46	26

Rolling element frequency using formula for bearing frequency calculations are presented in table 4.

Table 4. Rolling element frequency calculation results

Element No. in scheme	No. of rolling elements	810 rpm	500 rpm	800 rpm
1, 2, 73, 74	9	325.8	201	324
3, 4	16	357.6	220.8	353.4
8	9	319.2	196.8	315
20	15	-	221.4	354
21, 22	17	-	211.8	339

The last step was to compare answers obtained during the vibration diagnostics with the calculated results. In this way, it will be good to find out which gears have potential problems and to determine if those components need to be maintained or no.

Table 5. In centred rotation received results

Speed, rpm	Top peaks (Hz)									
500	2.50	7.50	9.38	25.00	116.25	125.63	144.38	751.25	750.63	866.25
800	1.88	14.38	25.00	116.25	125.63	144.38	573.75	577.50	601.88	824.38

From the table 5, it can be seen that when the revolutions are 500 rpm, the G1 gear is very close to the input gear, which shows that the issue may be in this and G1 gear indicated a possible problem. From this it can concluded that it is worth checking out the G1. On the second test, speed was increased to 800 rpm and G25 gear is close to the peak of 800 rpm calculated gear, which tells that there is a possible problem with this gear as well.

Table 6. Off centred rotation received results

Speed, rpm	Top peaks (Hz)									
500	2.50	9.38	25.00	125.63	144.38	711.88	731.25	750.63	866.25	885.00
800	1.88	3.13	5.63	13.75	25.00	29.38	125.63	135.00	577.50	601.88

Table 6 displays test results by off centring the machine's pivot point and the data that was gathered. It is possible to infer from the results that some of the responses match the machine's prioritised responses. When the loads are unevenly distributed, this is a good indicator because it shows that the device is functioning properly. As previously mentioned, it is evident that the same gears in the G1 at 500 rpm, and G25 at 800 rpm are problematic and there might be a gear problem.

4. Using vibration analysis results in order to improve maintenance processes

Vibration analysis can be good tool for improving maintenance planning by detecting equipment issues early and preventing costly breakdowns. Through the analysis of vibration data, a maintenance technician can detect trends and patterns that serve as indicators of potential failures. Algorithmic optimisation can be beneficial tool to show the needed steps that needs to be done in order to use vibration analysis results in order to improve maintenance processes. The first step starts with the selection of asset, which is mechanical processing equipment. Next, it is important to select parameters and input the results of measurement by data collection. Conducting data collection by means of sensors affixed to the machinery or equipment is crucial. Next, it is necessary to calculate the natural frequency. Following step consists of comparison of experimental results with nominal values which were calculated earlier. Afterwards, it is important to identify the range of results, if it is acceptable then work can be continued. However, if obtained results are not in the range, it is important to indicate defects and find the cause of them by diagnosing those asset defects. In both cases, it is important to store results obtained by analysis and it is important to plan the maintenance processes.

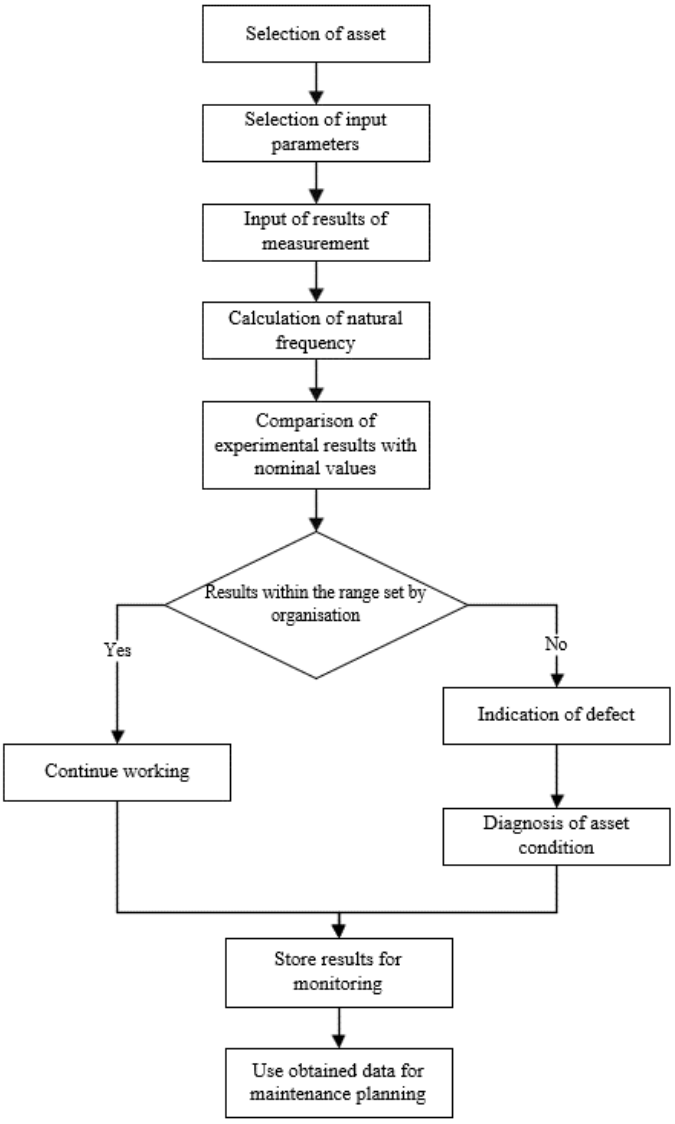

Fig. 4 Algorithm of planning maintenance by using vibration analysis

Unified data analysis is a useful technique for identifying and diagnosing various types of machinery faults, including unbalance, misalignment, bearing wear, and gear damage, etc. For example, through the analysis of vibration signals, it is feasible to determine the frequency and severity of faults, as well as pinpoint the underlying cause. Vibration analysis can additionally be used to assess the general state of machinery and forecast its remaining useful lifespan. Through the continuous monitoring of vibration patterns, it is feasible to identify any deviations or irregularities, and to approximate the remaining lifespan of the machine parts. This information can then be utilised to strategize scheduled maintenance measures.

5. Conclusions

Implementation of relatively simple automatic or computerised tools of diagnostics into maintenance system may result in significant improvement of effectiveness of fault detection, decision making and overall maintenance effectiveness. By applying diagnostics into maintenance system, small and medium sized industrial companies can achieve enhanced fault detection as well as to make informed decisions based on information provided by data analysis. By automating the analysis of equipment condition data and producing timely alerts for maintenance measures, the integration of automatic diagnostic tools optimises maintenance processes. Companies can switch from reactive to predictive maintenance strategies by utilising automated diagnostics which can help enterprises to plan maintenance tasks in advance and prevent breakdowns which can also save expenses on unplanned maintenance.

References

1. Cording data. How to Improve Productivity & Efficiency in Manufacturing. [online]. [Accessed 12 May 2024]. Available from: https://corningdata.com/improve-productivity-efficiency-in-manufacturing/
2. Pinciroli, Luca, Baraldi, Piero and Zio, Enrico. Maintenance optimization in industry 4.0. Reliability Engineering & System Safety. June **2023**. Vol. 234, p. 109204. DOI 10.1016/j.ress.2023.109204.
3. Syamsundar, A., Naikan, V.N.A. and WU, Shaomin. Estimating maintenance effectiveness of a repairable system under time-based preventive maintenance. *Computers & Industrial Engineering*. June **2021**. Vol. 156, p. 107278. DOI 10.1016/j.cie.2021.107278.
4. Einabadi, Behnam, Mahmoodjanloo, Mehdi, Baboli, Armand and Rother, Eva. Dynamic predictive and preventive maintenance planning with failure risk and opportunistic grouping considerations: A case study in the automotive industry. *Journal of Manufacturing Systems*. August **2023**. Vol. 69, p. 292–310. DOI 10.1016/j.jmsy.2023.06.012.
5. Vogel-Heuser, Birgit and Hess, Dieter. Guest Editorial Industry 4.0–Prerequisites and Visions. *IEEE Transactions on Automation Science and Engineering*. April **2016**. Vol. 13, no. 2, p. 411–413. DOI 10.1109/TASE.2016.2523639.
6. Adash. *Vibration analysis*. [online]. **2024**. [Accessed 10 May 2023]. Available from: https://adash.com/vibration-analysis/vibration-diagnostics/

A Fractional-Order Nonlinear Backstepping Controller Design for Current-Controlled Maglev System

Dorukhan ASTEKİN[1]*, Fatih ADIGÜZEL[1]

1 Yıldız Technical University, Electric-Electronic Faculty, Department of Control and Automation Engineering, İstanbul, Turkey

** dorukhan.astekin@std.yildiz.edu.tr*

Abstract

The magnetic levitation system (Maglev) is a nonlinear system by which an object is suspended with no support other than magnetic fields. The main control perspective of the Maglev system is to levitate a steel ball in air by the electromagnetic force. However, the Maglev system has highly nonlinear dynamics which is inconvenient in the sense of sensitive control/regulation of its nonlinear dynamics. In this paper, the nonlinear backstepping controller based on the fractional-order derivative is proposed for the control of the nonlinear current-controlled Maglev system. After, the system dynamics and fractional-order backstepping controller design are given, the asymptotic stability of the closed-loop system is proved by employing the Lyapunov theory. Some computer-based numerical experiments are carried out to show the effectiveness of the proposed controller for the control of Maglev system.

Keywords: nonlinear backstepping control, Caputo fractional-order derivative, current-controlled magnetic levitation system

1. Introduction

Fractional (non-integer) calculus is one of the oldest branches of mathematics, and its application to many dynamic systems around us has become a phenomenon. Such systems are expressed by differential equations and applications in control theory, where the fractional calculus concept is widely used, include observer design, system identification and discrete-time systems [1-4]. Studies in nonlinear control systems, which is one of the areas where this concept is extensively used, are increasing rapidly day by day. In nonlinear control systems, as the order of the system increases, the structure and solution of the system becomes more complex. If these systems are combined with fractional-order or complex-order systems, they can become real life applications. By doing so, the error difference between the theoretical and practical application is further eliminated. The application of fractional-order derivative is often based on rationalizing the selected optimal method and the aim is to use fractional-order control (FOC) to improve the performance and efficiency of the system.

Magnetic levitation systems, the most common type of levitation, are the process of counteracting gravity with a magnetic field. In these systems, especially in control theory, many controllers have been designed to make the system asymptotic stable. Some of the studies related to this subject can be listed as follows. In [5], a backstepping controller is designed based on a nonlinear system model in the presence of parameter uncertainties. In [6], a fractional-order controller is designed for an integer-order dynamic system with an adaptive backstepping control approach by considering model uncertainties and external disturbances. Related to this issue at [7], an adaptive fractional backstepping controller is designed for integer-order nonlinear uncertain systems of arbitrary order with prescribed performance subject to unknown time-varying disturbances. In [8], an adaptive non-singular terminal sliding mode controller based on disturbance compensation technique is proposed to control the position of the magnetic levitation system. In [9], a new PI-PD controller design procedure for magnetic levitation system using weighted geometrical center method is presented. In [10], a combination of a robust backstepping controller and an integral action for a magnetic levitation system is presented. In [11], the design and application procedure of an adaptive backstepping controller for magnetic levitation systems is presented. In [12], an implementation of a fractional-order PI controller in a magnetic levitation system is investigated. In [13], a digital fractional-order PID controller is designed to control the position of the levitated object in a magnetic levitation system and compared with an integer-order PID controller. In [14], a design method for tuning fractional-order controllers for second-order unstable processes using stability analysis for the magnetic levitation system is presented. In [15], a solution consisting of a special type of fractional-order controller for the stabilization of second-order unstable plants in a magnetic levitation system is given.

In this paper, a nonlinear fractional backstepping controller is addressed for the current-controlled magnetic levitation system. As different from the classical backstepping controller, the controller utilized in this paper is constructed with the help of the fractional-order derivative instead of the classic derivative operator. In this way, a fractional nonlinear controller is designed, and the asymptotic stability analysis of the closed-loop system is proved in the sense of Lyapunov. Some numerical simulation tests are performed to show the viability of the designed controller for the control of the Maglev system.

The rest of this article is organized as follows. In the next section, the nonlinear model of magnetic levitation is given. After this section, the proposed design controller is presented with the stability analysis in the sense of Lyapunov theory. In Section 4, the effectiveness of the designed controller for the current-controlled Maglev is tested via numerical simulations. The paper ends with some conclusions in Section 5.

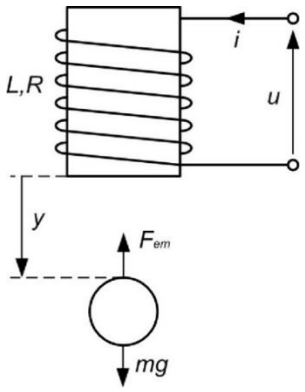

Fig. 1 The diagram of Maglev system

2. Model of Maglev System

In magnetic levitation system, a changeable electromagnetic field occurs through a coil, and a metal ball can be suspended with the help of the produced electromagnetic field. In order to control of the position of the metal ball in advanced, a well-structured controller is need. The diagram of Maglev system is presented in Fig. 1, where y, v and i denote the distance between the ball and the coil, the velocity of the ball on the vertical axis, and the coil current, respectively. The parameter R stands for the coil resistance. The parameter L is the coil inductance, m and g present the mass of the ball and the gravitational acceleration, respectively. F_{em} is the electromagnetic force generated by the coil. In the Maglev system, the coil current is adjusted by a current feedback power amplifier as in the many literature studies [5], [9], [16], and in this way the dynamics of the Maglev system is formulated as follows:

$$\frac{dy(t)}{dt} = v(t) \tag{1}$$

$$\frac{dv(t)}{dt} = g - \frac{F_{em}(t)}{m}u(t) \tag{2}$$

where: the following dynamic equation expresses the electromagnetic force F_{em} generated by the coil.

$$F_{em}(t) = \frac{Q}{2m\left(Y_{\infty} + y(t)\right)^2} \tag{3}$$

where: Q and Y_{∞} are positive system constants and their values are changed by the process of manufacture of the coil, magnetic core, and the metal ball. On the other hand, there are definitions such as Riemann-Liouville, Grünwald-Letnikov, Hölder, Caputo for the definition of fractional-order derivative in the literature. In this study, an application is performed based on the Caputo definition for the fractional-order derivative operator. For a differentiable function f, the definition of Caputo fractional-order derivative is defined as in (4) [17].

$${}_0D_t^{-\alpha} f(t) = \frac{1}{\Gamma(\alpha - n)} \int_0^t \frac{f^{(n)}(\tau)}{(t-\tau)^{\alpha+1-n}} d\tau, \quad \alpha \in (n-1, n) \tag{4}$$

where: $\Gamma(n)$ is the gamma function, and is described by the following integral:

$$\Gamma(n) = \int_0^{\infty} t^{n-1} e^{-t} dt \ . \tag{5}$$

Furthermore, the Gamma function satisfies the following functional equation:

$$\Gamma(n+1) = n!. \tag{6}$$

3. Controller Structure

This section presents the design procedure of a fractional-order backstepping controller. In the model described above, let us define $x_1 = y$, $x_2 = v$, $u(t) = i^2(t)$ and $\phi(x_1) = F_{em} / m$. Thus, the Maglev system can be transformed as equation (7) and

(8).

$$\dot{x}_1 = x_2 \tag{7}$$

$$\dot{x}_2 = g - \phi(x_1)u. \tag{8}$$

Hence, considering the system dynamics (1)-(2), the error dynamics can be given as follows:

$$e_1 = x_1 - x_{1d} \Rightarrow \dot{e}_1 = \dot{x}_1 - \dot{x}_{1d} = x_2 - x_{2d} \tag{9}$$

$$e_2 = x_2 - x_{2d} \Rightarrow \dot{e}_2 = \dot{x}_2 - \dot{x}_{2d} = g - \phi(x_1)u - \dot{x}_{2d} \tag{10}$$

where: x_{1d} denotes the reference trajectory, and $x_{2d} = \dot{x}_{1d}$. Utilizing the equations (9) and (10), the following relationship can be obtained:

$$\dot{e}_1 = e_2 \tag{11}$$

To provide the stability of the dynamic given in (11), the candidate Lyapunov function can be defined as:

$$V_1 = |e_1| \Rightarrow \dot{V}_1 = |\dot{e}_1| = \dot{e}_1 \mathrm{sgn}(e_1) = e_2 \mathrm{sgn}(e_1). \tag{12}$$

For the backstepping procedure, the following the dynamics of z_2 can be defined:

$$z_2 = e_2 - \phi_2. \tag{13}$$

Afterwards,

$$\dot{V}_1 = (z_2 + \phi_2)\mathrm{sgn}(e_1) \tag{14}$$

is obtained, and the virtual controller signal can be designed as

$$\phi_2 = -k_1 e_1. \tag{15}$$

Moreover, we consider ${}_0D_t^{-\alpha}|e_1(t)|$ as a fractional-order operator as different from the classical backstepping control method. Then, the dynamics of z_2 is analyzed as follows:

$$z_2 = -k_2 \mathrm{sgn}(e_1) - k_3 \mathrm{sgn}(e_1)\, {}_0D_t^{-\alpha}|e_1(t)|. \tag{16}$$

Utilizing (16), (14) becomes

$$\dot{V}_1 = \left(-k_1 e_1 - k_2 \mathrm{sgn}(e_1) - k_3 \mathrm{sgn}(e_1)\, {}_0D_t^{-\alpha}|e_1(t)|\right)\mathrm{sgn}(e_1) \tag{17}$$

$$\begin{aligned} \dot{V}_1 &= -k_1|e_1| - k_2 - k_3\, {}_0D_t^{-\alpha}|e_1(t)| \\ &\le -k_1|e_1| - k_2 - k_3 L_1 = -k_1|e_1(t)| - \gamma_1 \le -\kappa_1 \|Y\| \end{aligned} \tag{18}$$

where: ${}_0D_t^{-\alpha}|e_1(t)| \ge L_1$, $\gamma_1 = k_2 + k_3 L_1$ and $\kappa_1 = \min(k_1, \gamma_1)$. Another candidate Lyapunov function to guarantee the stability of the system can be defined as:

$$V_2 = |e_1| + |z_2|. \tag{19}$$

According to the above candidate Lyapunov function, the dynamics of z_2 is formed as follows:

$$\dot{z}_2 = \dot{e}_2 - \dot{\phi}_2 = g - \phi(x_1)u - \dot{x}_{2d} - \dot{\phi}_2. \tag{20}$$

Taking the derivative of the Lyapunov function,

$$\begin{aligned}\dot{V}_2 &= |\dot{e}_1| + |\dot{z}_2| = \dot{e}_1 \operatorname{sgn}(e_1) + \dot{z}_2 \operatorname{sgn}(z_2) \\ &= e_2 \operatorname{sgn}(e_1) + \left(g - \phi(x_1)u - \dot{x}_{2d} - \dot{\phi}_2\right)\operatorname{sgn}(z_2) \\ &= \left(z_2 + \phi_2\right)\operatorname{sgn}(e_1) + \left(g - \phi(x_1)u - \dot{x}_{2d} - \dot{\phi}_2\right)\operatorname{sgn}(z_2)\end{aligned} \tag{21}$$

$$\dot{V}_2 = -k_1 e_1 \operatorname{sgn}(e_1) + z_2 \operatorname{sgn}(e_1) + \left(g - \phi(x_1)u - \dot{x}_{2d}\right)\operatorname{sgn}(z_2) - \dot{\phi}_2 \operatorname{sgn}(z_2) \tag{22}$$

is obtained. Eventually, the control signal is defined for the asymptotic stability as follows:

$$u = \frac{1}{\phi(x_1)}\left(g - \dot{x}_{2d} + |z_2|\operatorname{sgn}(e_1) + k_2 z_2 + k_3 \operatorname{sgn}(z_2) + k_4 \operatorname{sgn}(z_2)\, {}_0D_t^{-\alpha}\left|e_1(t)\right| - \dot{\phi}_2\right). \tag{23}$$

Plugging the designed controller given in (23) into (22) gives

$$\begin{aligned}\dot{V}_2 &= -k_1|e_1| - k_2|z_2| - k_3 - k_4\, {}_0D_t^{-\alpha}\left|e_1(t)\right| \\ &\le -k_1|e_1| - k_2|z_2| - k_3 - k_4 L_1 \le -k_1|e_1| - k_2|z_2| - \gamma_2 \le -\kappa_2 \|Y\|\end{aligned} \tag{24}$$

where: ${}_0D_t^{-\alpha}\left|e_1(t)\right| \ge L_1$, $\gamma_2 = k_3 + k_4 L_1$ and $\kappa_2 = \min(k_1, k_2, \gamma_2)$.

4. Simulation Results

To show the effectiveness and viability of the fractional-order backstepping controller design for the control of current controlled magnetic levitation system, several numerical simulations are carried out using MATLAB. In these simulations, the solver step time for the Maglev system was set to 0.1 ms, while the controller sampling period was chosen as 1 ms. The nominal parameters of Maglev system are $m = 0.005\text{kg}$, $R = 22\Omega$, $L = 0.5H$, $g = 9.81 m/s^2$, $Q = 0.003$ and $Y_\infty = 0.041$.

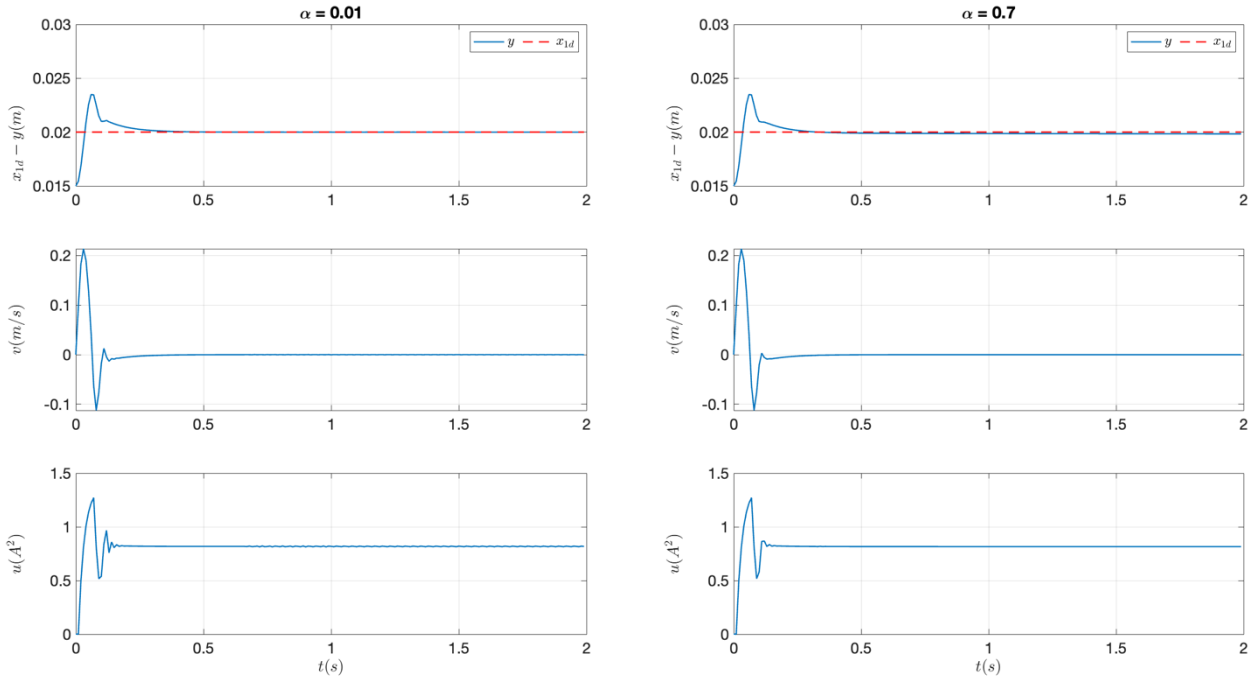

(a) (b)

Fig. 2 Changes in the vertical position, velocity of the ball, the controller signal of the coil for ball set-point regulation with $x_{1d} = 0.02$, (a) $\alpha = 0.01$ is selected, (b) $\alpha = 0.7$ is selected

Simulation results are performed for two different purposes, set point regulation, and time-varying trajectory tracking of ball position in Maglev system. The ball references in the set point regulation and time-varying trajectory tracking are considered as $x_{1d} = 0.02$ and $x_{1d} = 0.02 + 0.01\sin(2\pi t)$, respectively. In addition to that, the simulation results are presented for the analysis of the Caputo derivative selection with $\alpha = 0.01$ and $\alpha = 0.7$. The controller design parameters in the simulation cases for $\alpha = 0.01$ and $\alpha = 0.7$ are assigned as $k_1 = 50$, $k_2 = 100$, $k_3 = 0.01$ and $k_4 = 1$.

In the numerical simulation results, the changes in the vertical position, velocity of the ball, the controller signal of the coil for the ball set-point regulation in Fig. 2 and time-varying trajectory tracking in Fig. 3 are presented. It is observed from Fig. 2a that the ball converges successfully to set point value in 0.5 s. However, in Fig. 2b, there is a steady-state error in the ball position at a negligible level. Moreover, Fig. 3 shows the performance of the time-varying trajectory tracking of the magnetic ball. It can be seen that the results of steady state performance are close to each other in both simulations, but it is noticed that the oscillations are different in the transient response. Additionally, it is observed that the fluctuations in both the speed and the produced control signal are more numerous for $\alpha = 0.7$ due to this oscillation.

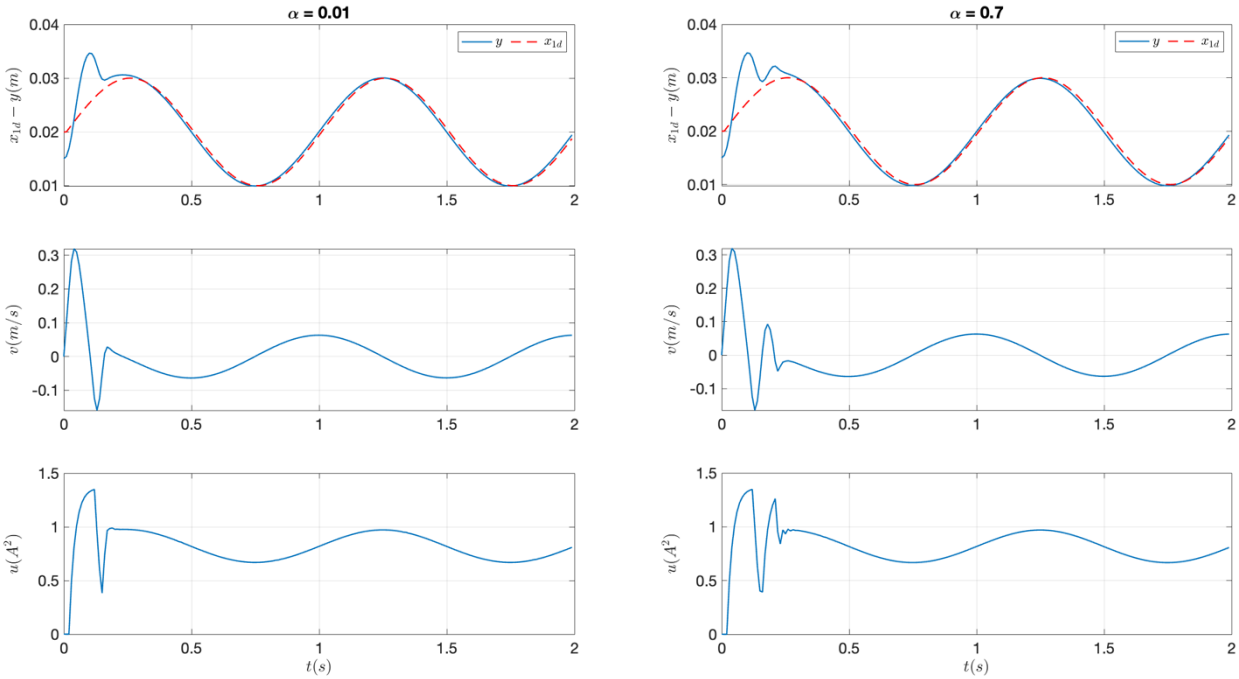

(a) (b)

Fig. 3 Changes in the vertical position, velocity of the ball, the controller signal of the coil for ball time-varying trajectory tracking with $x_{1d} = 0.02 + 0.01\sin(2\pi t)$, (a) $\alpha = 0.01$ is selected, (b) $\alpha = 0.7$ is selected

5. Conclusions

In this paper, a nonlinear backstepping controller with fractional-order calculation is proposed to control the ball position of the current-controlled magnetic levitation system. The mathematical formulation of the Maglev system is presented, and the structure of the proposed fractional-order controller is devised by operating the Caputo derivative in the steps of backstepping. The asymptotic stability in the sense of Lyapunov is shown in the system dynamics under the nonlinear backstepping controller including the fractional-order calculations. The computer-based numerical simulation results validate the effectiveness and validity of the fractional-order backstepping for the Maglev system.

References

1. Peng, C.; Yang, H.; Yang, A.; Ren, L. A new observer design for the joint estimation of states and unknown inputs for a class of nonlinear fractional-order systems. Mathematics 2024, 12(8), 1139.
2. Guo, R.; Xu, Y.; Hu, C.; Shen, W. Self-adaptive neural network-based fractional-order nonlinear observer design for state of charge estimation of lithium-ion batteries. IEEE/ASME Transactions on Mechatronics 2023, 1–12.
3. Bi, Y.; Ji, Y. Parameter estimation of fractional-order Hammerstein state space system based on the extended Kalman filter. International Journal of Adaptive Control and Signal Processing 2023, 37(7), 1827–1846.
4. Yang, D.; Yu, Y.; Hu, W.; Yuan, X.; Ren, G. Mean square asymptotic stability of discrete-time fractional order stochastic neural networks with multiple time-varying delays. Neural Processing Letters 2023, 55(7), 9247–9268.
5. Yang, Z.-J.; Tateishi, M. Adaptive robust nonlinear control of a magnetic levitation system. Automatica 2001, 37(7), 1125–1131.
6. Nikdel, N.; Badamchizadeh, M.; Azimirad, V.; Nazari, M. A. Fractional-order adaptive backstepping control of robotic manipulators in the presence of model uncertainties and external disturbances. IEEE Transactions on Industrial Electronics 2016, 63(10), 6249–6256.

7. Li, X.; Wen, C.; Deng, C. Prescribed performance-based adaptive fractional backstepping control of integer-order nonlinear systems. IEEE Transactions on Systems, Man, and Cybernetics: Systems 2024, 1–12.
8. Wang, J.; Zhao, L.; Yu, L. Adaptive terminal sliding mode control for magnetic levitation systems with enhanced disturbance compensation. IEEE Transactions on Industrial Electronics 2021, 68(1), 756–766.
9. Onat, C.; Daşkın, M.; Turan, A.; Özgüven, Ö. Manyetik levitasyon sistemleri için ağırlıklı geometrik merkez yöntemi ile PI-PD kontrolcü tasarımı. Mühendis ve Makina 2021, 62(704), 556–579.
10. Adıgüzel, F.; Türker, T. Robust position control of a levitating ball via a backstepping controller. Electrica 2022, 22(1), 61–69.
11. Adıgüzel, F.; Dokumacılar, E.; Akbatı, O.; Türker, T. Design and implementation of an adaptive backstepping controller for a magnetic levitation system. Transactions of the Institute of Measurement and Control 2018, 40(8), 2466–2475.
12. Yumuk, E.; Güzelkaya, M.; Eksin, İ. Application of fractional order PI controllers on a magnetic levitation system. Turkish Journal of Electrical Engineering and Computer Sciences 2021, 29(1), 98–109.
13. Chopade, A. S.; Khubalkar, S. W.; Junghare, A. S.; Aware, M. V.; Das, S. Design and implementation of digital fractional order PID controller using optimal pole-zero approximation method for magnetic levitation system. IEEE/CAA Journal of Automatica Sinica 2018, 5(5), 977–989.
14. Muresan, C. I.; Ionescu, C.; Folea, S.; De Keyser, R. Fractional order control of unstable processes: the magnetic levitation study case. Nonlinear Dynamics 2015, 80(4), 1761–1772.
15. Folea, S.; Muresan, C. I.; De Keyser, R.; Ionescu, C. M. Theoretical analysis and experimental validation of a simplified fractional order controller for a magnetic levitation system. IEEE Transactions on Control Systems Technology 2016, 24(2), 756–763.
16. Pandey, A.; Adhyaru, D. M. Robust-optimal control design for current-controlled electromagnetic levitation system with unmatched input uncertainty. International Journal of Dynamics and Control 2024, 1–11.
17. Podlubny, I. Fractional differential equations: an introduction to fractional derivatives, fractional differential equations, to methods of their solution and some of their applications, Publisher: Elsevier, 1998, 340 p.

Preliminary Study of a Mechanism Enabling the Crutch to Stand on it's Own

Małgorzata JOHN-BANACH[1]*, Jakub JANISIO[1], Antoni JOHN[1]

1 Silesian University of Technology, Faculty of Mechanical Engineering, Konarskiego 18A, Gliwice 44-100, Poland
** malgorzata.john-banach@polsl.pl*

Abstract

The paper presents the process of creating a self-supporting orthopaedic crutch. During the research, existing solutions were reviewed and analysed. The need to improve the comfort of disabled people was noticed. Based on existing solutions and knowledge, a solution was proposed that meets the adopted assumptions. The detailed model was analysed using the finite element method. Three cases were subjected to calculations: the case of kicking one of the tripod legs, the mechanism loaded evenly and the mechanism loaded on one of the bases. The results turned out to be satisfactory.

Keywords: Orthopaedic crutch, self-standing, FEM.

1. Motivation

Any physical disability, regardless of whether it results from surgery, disease, overload of the lower limbs or as a result of an unexpected accident, ends in balance disorders. Then it is important to eliminate motor coordination defects. Manufacturers are meeting this challenge, including: crutch, which greatly improve and facilitate the inability or abnormality of gait. The type of rehabilitation device is determined by the type of disease as well as medical recommendations. With the development of medicine, the level of quality and innovation of medical equipment also increases. As a result, more and more modern solutions appear on the market that enable disabled people to function almost efficiently in everyday life.

The concept of the crutch maintaining its own balance when it is not in use at a given moment has been proposed. The proposed solution is to install an external mechanism ensuring proper balance. The concept being developed is intended to be a response to the situation when an adolescent disabled person goes to a hospital for a doctor's visit. The chair he sits on is some distance away from the wall. It is assumed that there is no way to lean her against the wall as this would prevent her from reaching the seat. A situation in which the patient would have to hold an orthopaedic crutch in his hand, assuming that he must have his hands free at that moment, is also excluded. The essence then is to place the crutch within the user's reach.

Analysing the medical equipment market, it can be concluded that there is no clear solution to the problem posed in this work. The main manufacturers of orthopaedic crutches do not have a concept that could be widely used among the products they offer. The ideas that have been introduced to general sale so far can be divided into two types. The first one concerns the redesign of the lower part of the crutch, creating a removable set of supports in the form of a tripod. The second one refers to changing the geometry of the rubber element of the crutch, increasing the contact surface with the ground [1,2,5, 9, 10].

The issue of maintaining balance with a crutch is certainly one of the most desirable features among active owners of such biomedical equipment. It is this that determines the improvement of ergonomics during its use, and thus the increase in the owner's comfort. The lack of a clear solution and the small number of them certainly leaves a lot of scope for designers to explore. However, it should be remembered that any idea or concept has a number of advantages and disadvantages that, to a greater or lesser extent, determine whether a given product is functional or not. The medical industry is a sector where very high precision is crucial, so the functionality of a given product may be determined by the smallest details [6,7,8].

2. Concept and model

By selecting the appropriate concept for maintaining the orthopedic crutch using multi-criteria optimization, a solution was obtained that best meets the given criteria. Fig. 1 shows the finished assembled model of the tripod. To improve the contrast and visibility of individual elements, red and black colors were used, but the selection of the right color is an optional aspect.

This work presents the process of creating a self-supporting orthopedic crutch solution. During the research, a review of existing solutions was performed. Based on existing solutions and knowledge, a solution was proposed that meets the adopted assumptions. The detailed model was subjected to finite element analysis. Three cases were subjected to calculations: the case of kicking one of the tripod legs, the mechanism loaded evenly and the mechanism loaded on one of the bases. The results turned out to be satisfactory.

Another system of the detailed concept are the tripod leg assemblies, which, combined with the rest of the elements discussed earlier, create a fully operational mechanism responsible for maintaining the balance of the crutch. Each of the three units contains a base in the form of a cylinder, finished with a rubber, non-slip foot, connected together using a friction connection. Cylindrical columns have two lugs: in the upper part and halfway up. Tendons (rectangular elements rounded towards the end) were installed to them, one on each side for each hole, which connect the system feet with the fixed rings, creating an elbow connection. Pins with retaining rings are responsible for connecting the individual parts. In order to stiffen the

mechanism and to make it possible to adjust the angle of the tripod base, tie rods with turnbuckles with M5 right-hand and left-hand threads were used. They were mounted to rectangular tendons with pins with retaining rings. The lower end was finished with a sleeve, while the upper one with a fork, to which the cable was directly connected with a pin to the turnbuckle of the movable ring described above. The angle of the tripod's cylindrical columns can be adjusted using the turnbuckles of the vertical tie rods. For this purpose, it is necessary to use an open-end wrench, thanks to which it is possible to change the length of a particular cable, as a result of which it is possible to obtain different positions of the column opening. However, it should be remembered that each time the rod spacing is modified, the height of the lower ring must be changed to prevent the entire mechanism from blocking.

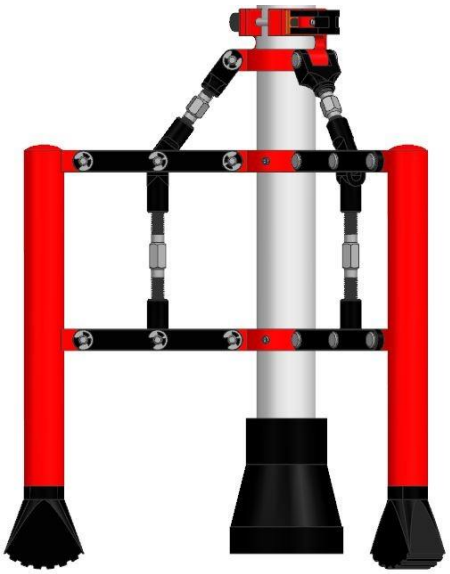

Fig. 1 Assembly model of the tripod

3. FEM analysis

In order to check whether the proposed solution for self-balancing of the orthopedic crutch has been constructed correctly, a strength analysis of the model should be carried out. The calculation program NX Nastran was used for calculations, which, using the finite element method, is able to graphically depict, among others, stresses and displacements of individual model members. Some elements of the tripod mechanism are not responsible for transmitting forces, so they were omitted during the finite element analysis. The process of simplifying the model enables a more efficient calculation process and also allows for obtaining calculation results that are more readable to the recipient. As a result, only elements that can be subjected to stress or displacement under the assumption of appropriate forces and boundary conditions are tested.

In the case of the discussed system, individual elements have been simplified:

- system locking rings on the lower seatpost - M3 set screws removed;
- pins with a retaining ring – the retaining rings were not taken into account for the FEM analysis;
- upper and lower links with a turnbuckle - individual links have been unified, the right- and left-hand threads have been replaced with a straight pin of the same diameter.

The obtained result allowed for a significant acceleration of the calculation process and also eliminated some errors during FEM analysis. The prepared mechanism contained 52 elements - before simplification 88.

The selection of materials is necessary to perform FEM analysis. Table 1 presents a list of individual elements and the materials assigned to them.

The main criterion for selecting the material of individual elements resulted from the process of manufacturing the tripod mechanism using the additive method using 3D FDM printing. Then the building material of most elements is ABS. This material is characterized by very high strength and high resistance to deformation - in the sense that when deformed, it is possible to spontaneously restore the original condition of the element [3]. The use of synthetic rubber in the case of rubber feet results from the very good properties of the material, i.e. abrasion resistance and a very low coefficient of friction, which characterizes anti-slip materials [4, 11].

For FEM analysis, it is necessary to create a finite element mesh of individual parts of the mechanism. The mesh of the discussed tripod was generated automatically by the NX Nastran program, dividing the model into tetrahedra with 10 nodes (CTETRA10) with a size individually selected for each part.

The following three cases were taken into account during the finite element computational analysis:

- unintentional, free kicking of one of the tripod bases by the user of the crutch,
- open mechanism under the user's load distributed over all tripod feet,
- open mechanism under the user's load, spread over one of the tripod's feet.

Table 1. Mechanical characteristics of pipes main steel, weld and heat affected zone metal

The type of element	Material
Fixed locking rings	ABS
Clamp ring	ABS
Clamping clamp	St3
Clamping clamp sleeve	St3
Clamping clamp screw	St3
Clamping clamp washer	St3
Pins	St3
Ties connecting the bases with the rings	ABS
Rubber feet	Synthetic rubber
Tripod bases	ABS
Ties connecting the upper ring with the base mechanism	St3
Vertical ties	St3

The assumption of the first case of the analysis was to check how the tripod mechanism would behave in the event of an inadvertent kick by the user of the crutch. The impact would result from the free movement of one of the legs accidentally catching the base of the open system. The crutch and tripod stand freely on the floor, unsupported.

During the analysis, displacements and reduced stresses were examined for the assumed force and boundary conditions. Fig. 2 show the FEM calculation result of the displacements, while Fig. 3 show, in the form of a color gradient, how the stresses in the mechanism change.

Based on the analysis carried out, it can be concluded that as a result of kicking or hooking one's foot on one of the tripod bases, significant displacements and stresses occur. The largest noticeable displacement is located near the upper eye of the kicked tripod foot, while the stresses were transferred to the individual tendons of the system. However, the obtained values should not be treated as critical, because thanks to the use of ABS in most elements, the displacements will not cause irreversible deformations.

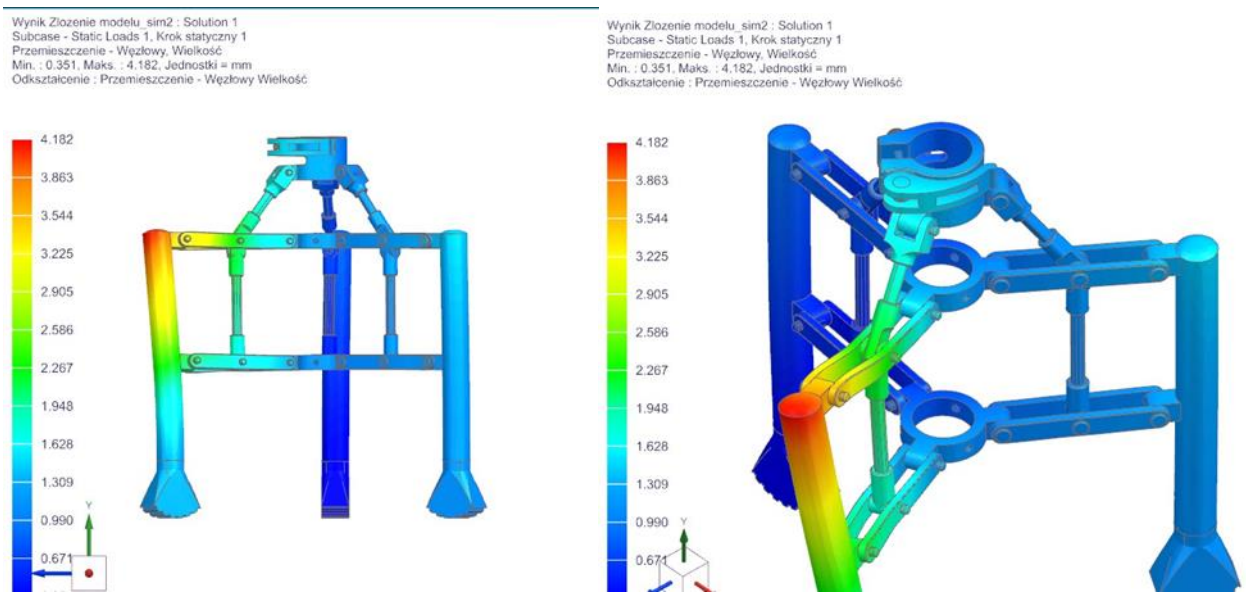

Fig. 2 FEM analysis result - displacements when the system is kicked

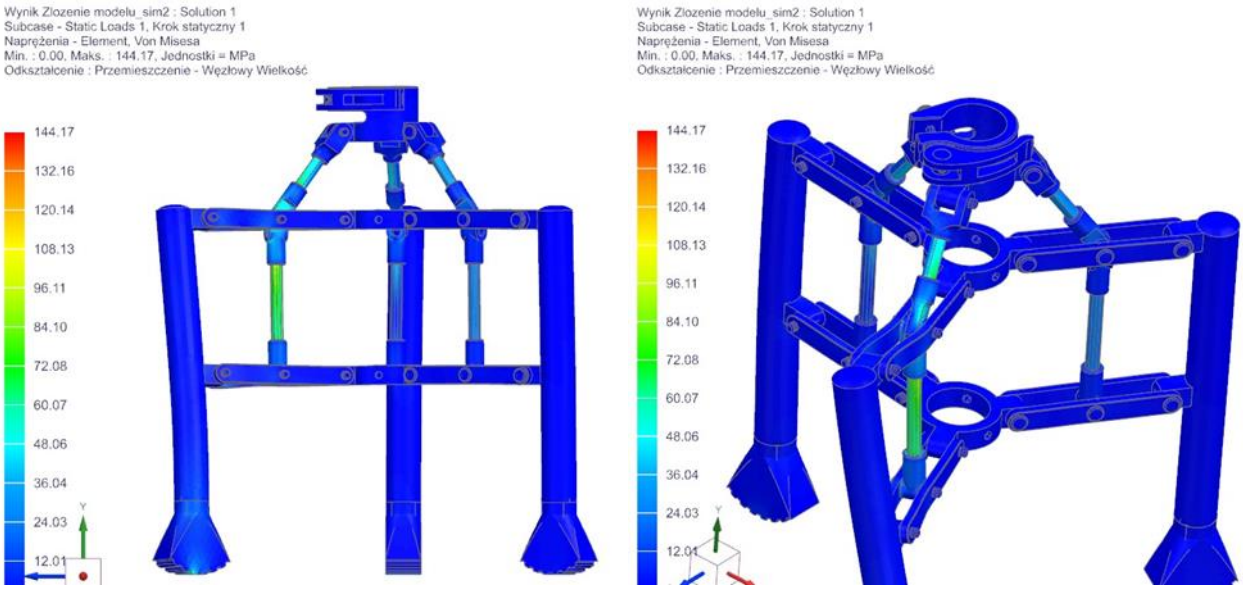

Fig. 3 FEM analysis result - stresses in the case of kicking the system

In the second analysis, the system was examined in a situation when the user of the crutch forgets to close the tripod while walking. The worst-case scenario is assumed, i.e. the tripod will be below the main foot of the crutch, as a result of which only the rubber supports of the tripod legs will provide support. It was assumed that the user weighed 75 [kg], i.e. he acted on the crutch with a force of 750 [N] in the case of static load. This load was distributed over three cables, so a force of 250 [N] acted on each cable. Supports with one degree of freedom were also installed, operating on each of the rubber feet of the tripod bases. The results of the analysis are displacements and reduced stresses, which were obtained assuming appropriate boundary conditions. Figures 4 show the color gradient of displacements. In Fig. 5 you can see the stresses reduced in the model.

Based on the obtained results of displacements and reduced stresses, it can be concluded that the mechanism does not allow maintaining the user's balance while walking. Therefore, during movement, it is necessary to close (lift the mechanism up) the tripod to prevent undesirable faults.

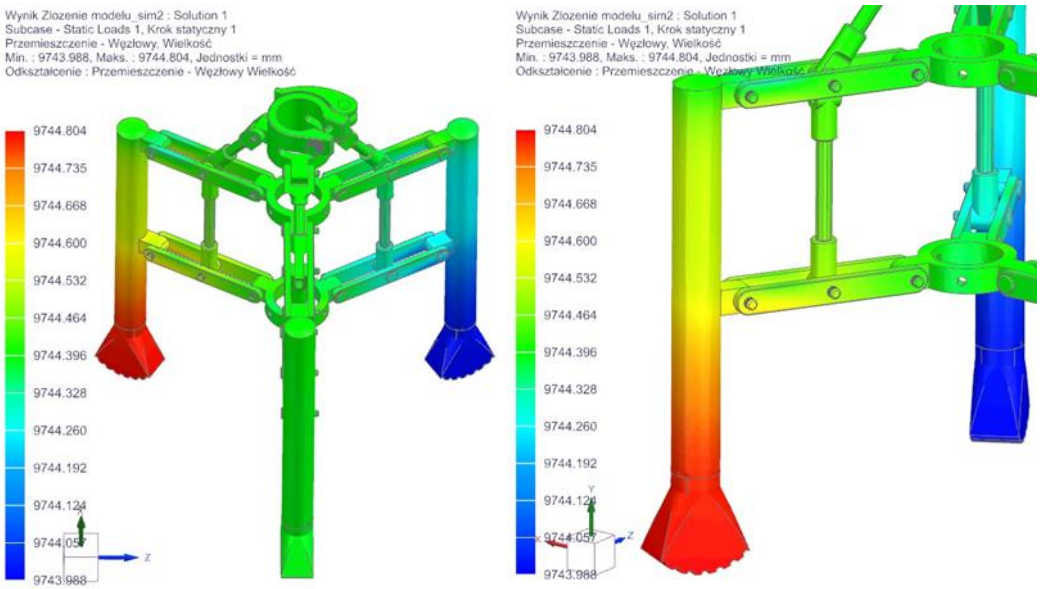

Fig. 4 Displacements in the case of uniform load on the system

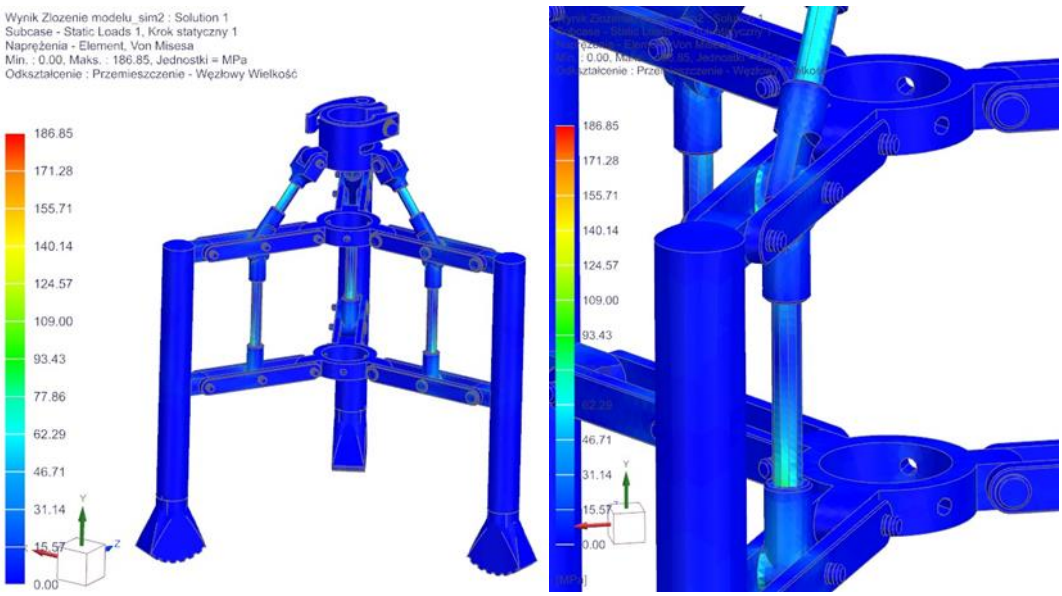

Fig. 5 Stresses in the case of uniform load on the system

The last FEM analysis concerned the examination of the tripod after applying a load to one of the legs of the open mechanism in the case of uneven positioning of the orthopedic crutch and the tripod in relation to the floor. The assumed weight of the user was 75 [kg], who exerted a force of 750 [N] on one of the tendons under the influence of a static load. Based on the analysis, displacements and stresses reduced under the influence of force on one leg of the orthopedic crutch were obtained, presented in the form of a color gradient. Fig. 6 show the displacements in the system, while Fig. 7 shows the reduced stresses.

In relation to the obtained results of the FEM analysis, one can notice a very large displacement and reduced stresses resulting from the large force applied in one place. It can then be concluded that the mechanism cannot be opened while running, because individual elements will be irreversibly damaged.

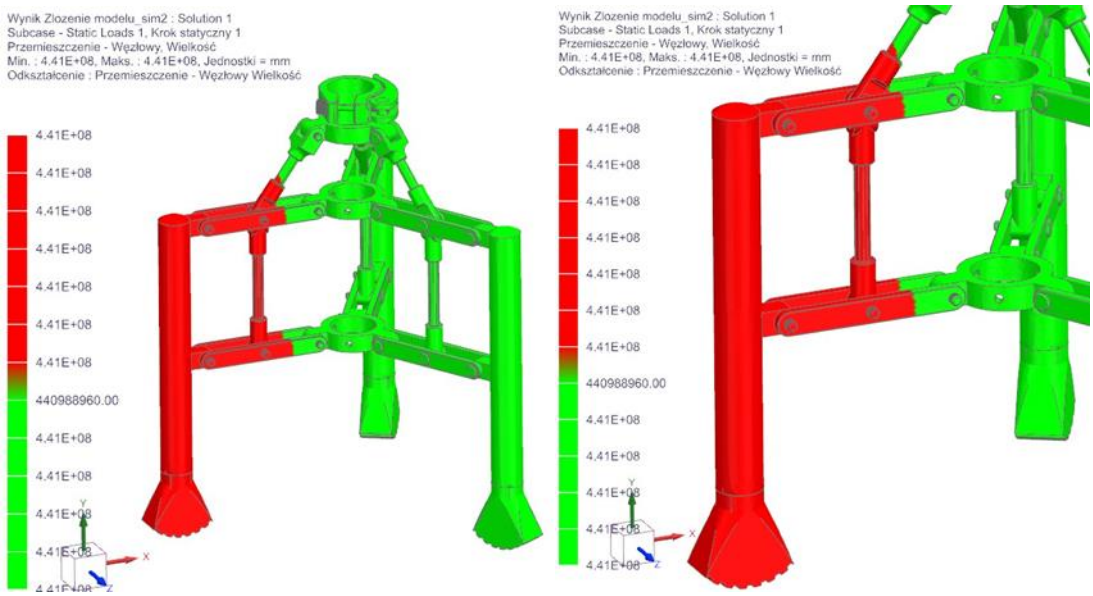

Fig. 6 Displacements in the case of one-sided load on the system.

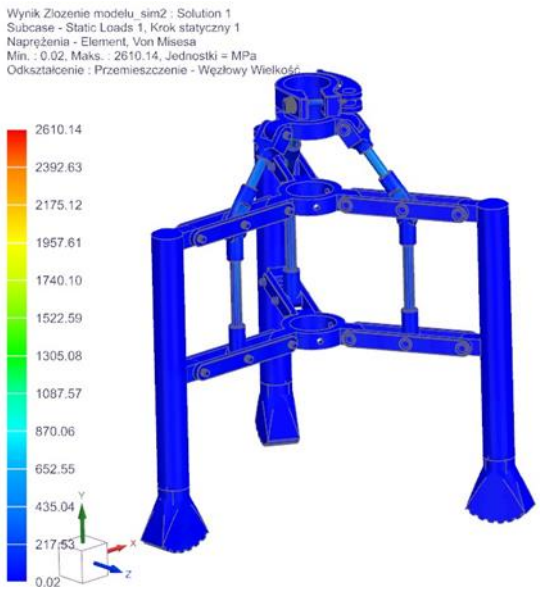

Fig. 7 Stresses reduced in the case of one-sided loading of the system.

4. Conclusions

The essence of the work was to investigate and understand the issue of maintaining the balance of a crutch. The research was focused on presenting certain solutions that would allow the discussed orthopedic equipment to be placed without fear of its falling. As a result, a removable and foldable mechanism in the form of a tripod was presented, which is able to cope with the tasks assigned to it.

The proposed mechanism is intended only for the orthopedic elbow crutch. In the case of a groin crutch, the solution will not meet its assumptions due to a different center of gravity. The movable mechanism of the tripod allows it to be folded when not in use, so it will not cause an unexpected kick or trip when using the crutch. The simplicity of the mechanism and the availability of standardized components used in the tripod in question allow you to make it yourself without the need for extensive manual skills. This solution is intended for people with a low degree of disability who will be able to activate the mechanism on their own. When deciding to use 3D printing in the production of this tripod, as well as ABS as the building material for individual elements, please remember that it will not be possible to use an open mechanism during walking due to the low durability of the structure.

References

1. Medical store esklepmedyczny.com.pl [accessed 10 December 2022].
2. Rehabilitation equipment store rehshop.pl [accessed 10 December 2022].
3. Bernasconi,R.; 3D Printing Technologies, MDPI AG 2022.
4. Shiva, M.; Effects of silicon carbide as a heat conductive filler in buty rubber for bladder tire curing applications, Birjand University of Technology 2021.
5. Popko, I.; Mobility crutches - history of invention, part 2 , Bezpieczna Podróż 2021.
6. Jurewicz, A.; Orthopedic crutches – types, strength, weight. How to choose orthopedic crutches, Warszawa 2018.
7. Krawaczyńska, J.; Orthopedic crutches – types and applications. Correct walking on crutches , https://www.ortopedio.pl/dobre-produkty/Kule-ortopedyczne-rodzaje-i-zastosowanie-Prawidlowy-chod-o-kulach/ [accessed 13 December 2022].
8. Hafner B. J., Sanders J. E., Czerniecki J. M., Transtibial energy-storage-and-return prosthetic devices: A review of energy concepts and a proposed nomenclature, Journal of Rehabilitation Research and Development, vol. 39, no 1, 2002, pp. 1-11.
9. Bober, T., Zawadzki, J.; Biomechanics of the human movement system , Department of Biomechanics, University of Physical Education in Wrocław , Wrocław 2003.
10. World Health Organization. Draft WHO Global Action Plan on Disability 2014–2021: Better health for all people with disabilities. Disability – issues, problems, solutions . IV/2014(13), pp. 42-72, https://kn.pfron.org.pl/kn/poprzednie-numery/296,Projekt-Globalnego-Planu-Dzialania#WHO-na-rzecz-niepelnosprawnosci-na-lata-20142.html [accessed 13 December 2022].
11. Liaw, Ch-Y., Guvendiren, M.; Current and emerging applications of 3D printing in medicine, Biofabrication, Vol. 9, No 2, 2017.

Finite Element Analysis of Forearm Bones

Simon ISASKAR[1], Knowledge MUSESE[1], Surendra Kumar SAINI[1,*], Thomas ALWEENDO[1]

1 Department of Mechanical and Metallurgical Engineering, School of Engineering and the Built Environment, University of Namibia, Namibia
** surendra1feb@gmail.com*

Abstract

Forearm fracture problem could be in any age group peoples. However, forearm fracture is a major problem in the adult population and players. This paper presents an insight on finite element analysis of ulna and radius of forearm bones. A three-dimensional geometry of ulna and radius of forearm bones are designed using solid works software. Then forearm bones geometrical models are meshed using mesh optimization method. Mechanical properties of poly lactic acid polymer are used for the analysis. Later, boundary and load conditions are applied to investigate the stress and displacement distribution into forearm bones models. Maximum stress and displacement are experienced in radius at the midspan of the bone under bending load condition in compared to tensile load. Furthermore, Ulna bone bends less than the radius bone under same load condition. The findings of present study may be used in the design optimization and three-dimensional printing of forearm bones.

Keywords: forearm bones model, finite element analysis, stress, and displacement.

1. Introduction

The upper limb is made up of the forearm bones which provide essential function in humans. The forearm bones are made up of the radius and ulna with complex structures compared to other bones [1]. These bones allow normal physiologic dynamic movements of muscles [2]. The radius and ulna allow a wide range of rotational motion because of their unique osteology. When subjected to external loading, these bones may deform and fracture when the load applied to them exceeds the specific yield stress. This type of deformation is unique and mostly missed injury in adults that may reduce forearm rotation.

Finite Element Analysis (FEA) is a computational analysis technique used to obtain approximated solutions to many engineering challenges. The method of FEA is composed of a finite element model which provides a piecewise approximated solution [3]. In this study, the FEA method is used to obtain results of the forearm bones subjected to external loading under tensile and bending loadings. Poly Lactic Acid (PLA) material is mostly used in three-dimensional printing of bone structures because it is a bio polymer and enables low temperature printing. Thus, the properties of PLA are applied to the forearm bone three dimensional models for analysis [4-5].

2. Materials and Methods

2.1 Forearm bone data collection

Several studies provide clinical data of the forearm bone structure. Although forearm bone dimensions vary from sex and age group, only elderly group male bones dimensions are used in this study. In Table 1 forearm bone dimensions of adult age group is shown.

Table 1. Forearm bone dimensions values in women and men of adult age group [1]

	Gender	Mean
Radius length (cm)	Women (W)	21.6357
	Men (M)	24.3298
Radius width (mm)	W	2.7193
	M	3.1606
AD width (mm)	W	2.2832
	M	2.7468
Caput Ulna width (mm)	W	1.5046
	M	1.7117
Ulna length (cm)	W	23.5854
	M	23.5854
Caput Radii width (mm)	W	1.6932
	M	2.0270

2.2 Forearm bone geometrical modelling

The forearm bones dimensions of the male group were used to prepare the three dimensional (3D) geometrical model. This model includes, 24.3298 cm ulna length, 3.1606 cm radius width, 2.7468 cm AD width, 1.7117 cm caput ulna width, 23.5854 cm ulna length, and 2.0270 cm caput radii width. The geometrical models of the forearm bones (right radius and ulna) were drawn using SolidWorks software as shown in Fig. 1. Surface modelling techniques were considered in this study to obtain a well smoothened surface that resembles the real forearm bone structure.

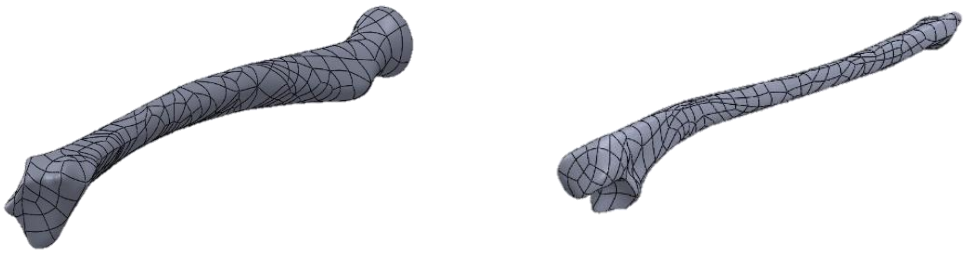

(a) (b)

Fig. 1 3D model of the (a) right radius and (b) right ulna

2.3 Finite element analysis of forearm bone

Three dimensional models of radius and ulna were separately analysed. The von Mises stress theory was used as default failure criterion. Properties of PLA were used to create a custom material that resembles the properties of PLA in SolidWorks. The Table 2 shows the properties of PLA as applied to both the ulna and radius bones.

Table 2. Mechanical properties of PLA [6]

Properties	Values
Yield strength	$2.6 \times 10^7 \frac{N}{m^2}$
Tensile strength	$3.0 \times 10^7 \frac{N}{m^2}$
Compressive strength	$6.2 \times 10^7 \frac{N}{m^2}$
Elastic modulus	$2.0 \times 10^9 \frac{N}{m^2}$
Poisson's ratio	0.394
Mass density	$1\,020\ \frac{kg}{m^3}$
Shear modulus	$3.189 \times 10^8\ \frac{N}{m^2}$

2.3.1 Mesh information of right radius and ulna

Blended curvature based mesh provides a quality mesh by reducing the aspect ratio [7]. Thus, for accurate results, a blended curvature-based mesher and solid mesh were used in present FEM analysis. The Table 3 shows the mesh properties of the right radius and ulna.

Table 3. Mesh details of the right radius and ulna

Mesh details	Radius	Ulna
Jacobian points for high quality mesh	16 Points	16 Points
Maximum element size	5,58197 mm	5.52337 mm
Minimum element size	0.279098 mm	0.276168 mm
Mesh quality	High	High
Total nodes	543 399	556 554
Total elements	355 818	365 355
Maximum aspect ratio	5.5315	8.0485
% of elements with aspect ratio less than three	99.4	99.4

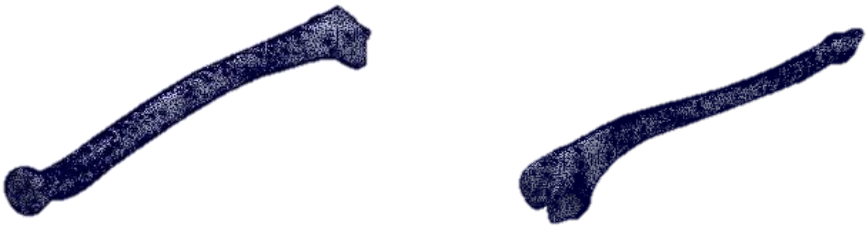

(a) (b)

Fig. 2 Meshed model of the (a) right radius and (b) right ulna

2.3.2 Load and fixtures of radius

The loading of the radius and ulna bones were restricted to tensile and bending load. For tensile analysis, an external force of 1000 N was applied normal to the articular facet plane and a fixture was applied at the styloid process covering 2 edges and 48 outer faces. The same force was applied at the mid-span of the radius while two fixtures were applied one at the articulate facet covering 2 edges, 38 faces and the other at the styloid process covering 18 faces to perform bending.

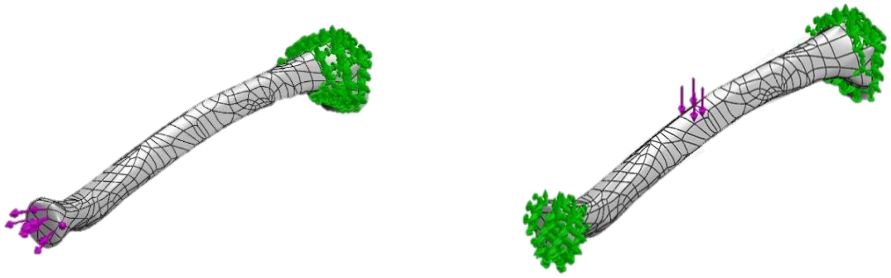

(a) (b)

Fig. 3 Load and fixture of (a) right radius under tensile (b) bending.

2.3.3 Reaction forces under tensile

For a loading of $F = 1000N$, the individual reaction forces are $F_x = 2.86\ N$, $F_y = 9.10\ N$, $F_z = 38.36\ N$ in the negative x, y, z directions respectively. This adds up a resultant force of $F_R = 39.5\ N$

2.3.4 Reaction forces under bending

Under bending, the individual reaction forces are $F_x = -0.042\ N$, $F_y = 999{,}99\ N$, $F_z = -0{,}056\ N$.This adds up to a resultant force of $F_R = 999.99\ N$.

2.3.5.1 Load and fixtures of Ulna

A similar approach was conducted to perform the FEA analysis of the ulna bone. For tensile analysis, an external force of $F = 1000\ N$ covering 3 faces was applied normal to the styloid process plane and a fixture was applied at the olecranon covering 1 edge and 32 outer faces. The same force was applied at the mid-span of the ulna while two fixtures were applied one at the olecranon covering 1 vertex, 20 faces and the other at the styloid process covering 18 faces to perform bending.

(a) (b)

Fig. 4 Load and fixture of right ulna under (a) tensile and (b) bending

2.3.5.2 Reaction forces under tensile

For a loading of $F = 1000N$, the individual reaction forces are $F_x = 2.61\ N$, $F_y = 7.22\ kN$, $F_z = 28.66\ N$ in the negative x, y, z directions respectively. This adds up a resultant force of $F_R = 29.67\ N$

2.3.5.3 Reaction forces under bending

Under bending, the individual reaction forces are $F_x = 334.1\ N$, $F_y = 354.5\ N$, $F_z = -404.6\ N$. This adds up to a resultant force of $F_R = 633.2\ N$ at the styloid process. At the articulate facet, the individual reaction forces are $F_x = 251.6\ N$, $F_y = 301.3\ N$, $F_z = 168.5\ N$. This adds up to a resultant force of $F_R = 427.2\ N$

3. Results and Discussions

Three study results are obtained from the von mises stress, resultant displacement, and equivalent strain for tensile and bending loads. The radius bone experienced a maximum von mises stress of $1.232 \times 10^8\ N/m^2$, a maximum displacement of $1.899\ mm$, and a maximum elongation of $1.314 \times 10^{-1}\ mm/mm$ under tensile load. Under bending load, a maximum von mises stress of $2.853 \times 10^8\ N/m^2$ is experienced at the midspan of the bone. The bone displaced by $2.472\ mm$, and reached a maximum strain of $2.328 \times 10^{-1}\ mm/mm$. The ulna bone reached $4.802\ N/m^2$ von mises stress, while it displaced $1.175\ mm$ and reached a maximum strain is $2.306 \times 10^{-1}\ mm/mm$ under tensile load. Under bending load, the maximum von mises stress is $1.688\ N/m^2$, an overall displacement of $2.046\ mm$ and a maximum strain of $2.316 \times 10^{-1}\ mm/mm$.

The radius bone is subjected to the stress that exceeds the yield strength of the polylactic acid. Thus, the bone deforms plastically under a load of $F = 1000N$. It is also observable that the ulna bone deforms within the elastic region, thus it does not exceed the yield strength of PLA. Furthermore, the ulna bone bends less than the radius bone under the same loading conditions.

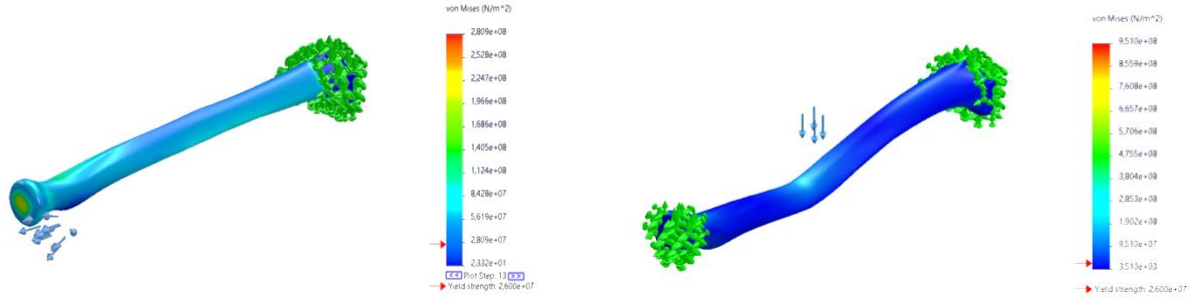

(a) (b)

Fig. 5 Right Radius (a) tensile stress and (b) bending stress

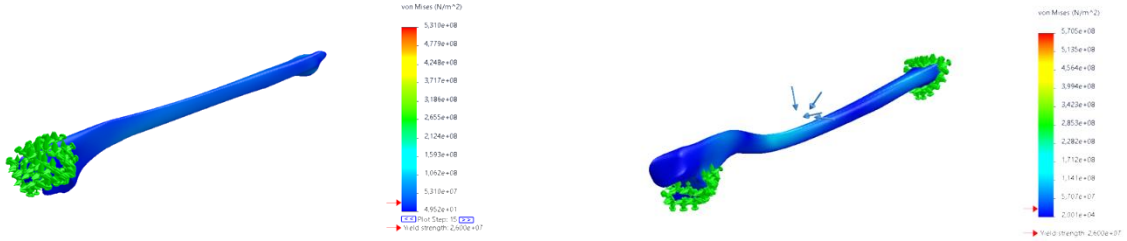

(a) (b)

Fig. 6 Right Ulna (a) tensile stress and (b) bending stress

4. Conclusions

In this study design and finite element analysis of forearm bone of adult age group have been performed. The poly lactic acid material properties have used for the analysis. Three study results are obtained from the von mises stress, resultant displacement, and equivalent strain for tensile and bending loads. Maximum stress and displacement are experienced in radius at the midspan of the bone under bending load condition. Furthermore, Ulna bone bends less than the radius bone under same load condition. This analytical study can be useful to understand the forearm bone fracture behaviour in response to external load. This research can be useful for forearm bone design that can benefit a wide range of patients, especially adults and athletes who are more prone to such injuries.

References

1. A. Nalbant, "Radiological Evaluation of Forearm Bones in Anatolian Population," *Eurasian J. Med. Investig.*, vol. 7, no. 4, pp. 384–393, 2023, doi: 10.14744/ejmi.**2023**.30880.
2. M. Patel and M. Varacallo, "Anatomy, Shoulder and Upper Limb, Forearm Bones," *StatPearls*, no. August, **2020**, [Online]. Available: http://www.ncbi.nlm.nih.gov/pubmed/31424844
3. V. Jagota, A. P. S. Sethi, and K. Kumar, "Finite element method: An overview," *Walailak J. Sci. Technol.*, vol. 10, no. 1, pp. 1–8, **2013**.
4. T. Hirashima, Y. Matsuura, T. Suzuki, T. Akasaka, A. Kanazuka, and S. Ohtori, "Long-term Evaluation Using Finite Element Analysis of Bone Atrophy Changes after Locking Plate Fixation of Forearm Diaphyseal Fracture," *J. Hand Surg. Glob. Online*, vol. 3, no. 5, pp. 240–244, 2021, doi: 10.1016/j.jhsg.**2021**.05.013.
5. T. M. Joseph *et al.*, "3D printing of polylactic acid: recent advances and opportunities," *Int. J. Adv. Manuf. Technol.*, vol. 125, no. 3–4, pp. 1015–1035, **2023**, doi: 10.1007/s00170-022-10795-y.
6. S. Farah, D. G. Anderson, and R. Langer, "Physical and mechanical properties of PLA , and their functions Physical and mechanical properties of PLA , and their functions in," *Adv. Drug Deliv. Rev.*, vol. 107, no. Dec., pp. 367–92, **2016**.
7. A. Gouaillard, A. Gelas, S. Valette, E. Boix, and R. Prost, "Curvature-based adaptive remeshing for wavelet-based multiresolution 3D meshes," *Proc. - Int. Conf. Image Process. ICIP*, vol. 1, no. May, pp. 1033–1036, **2005**, doi: 10.1109/ICIP.2005.1529930.

The Influence of the Frequency of Operation of the Low-pressure Gas-phase Injector on Its Dosage

Mateusz SKARZYŃSKI[1]*, Dariusz SZPICA[1]

1 Bialystok University of Technology, Faculty of Mechanical Engineering, 45C Wiejska Str., 15-351 Bialystok, Poland
** mateusz.skarzynski.108093@student.pb.edu.pl*

Abstract

The article presents the results of testing the volumetric flow rate of a low-pressure gas-phase injector. The measurements were intended to determine the relationship between the injector's dosage, in this case, for safety reasons, for air, depending on the frequency of its operation. In order to achieve the assumed research goal, the original station enabling the determination the volumetric flow rate during cyclic injector's operation was used. The results and their analysis will be helpful in configuring the gas supply system. As the engine speed increases, the degree of filling of its cylinder changes. Therefore, it is important to determine the characteristics of the gas-phase injector, which provides the flammable mixture and influences its composition (fuel-air proportions). The research goal is consistent with the current trend in research on power supply systems, which mainly includes functional assessment as well as operating characteristics to ensure power supply precision.

Keywords: combustion engine, supply system, gas injector, research.

1. Introduction

Liquefied petroleum gas (LPG) is a source of cars supply of great importance in Europe, especially in Poland, which from years has been among the top of countries with the highest consumption of this fuel in the world. According to data from annual report of Polish Liquefied Gas Organization, in 2022 Poland was on the fourth place, behind Russia, Turkey and South Korea, in terms of world LPG consumption for transport purpose, with a score of 7.4% [1]. The main reason of its great popularity is relatively low price, but also the belief in the reliability of automotive gas installation technology[2]. Due to the constantly growing number of cars equipped with the LPG supply system, the need to conduct research and improve the technology also grows.

In order to implement gas injectors to given gasoline powered engine it is necessary to compare its operating characteristics with characteristics of the new injectors. The characteristics of the original, gasoline injectors is determined on the basis of recording the injector coils control voltage course from vehicle tests on a chassis dynamometer[3]. Methodology of determining the characteristics, namely the dependence of dosage from frequency of operation of gas-phase injectors is proposed in the article.

Generally, the gas-phase injectors can be tested experimentally and numerically. Simulation tests are helpful especially during initial stage of the research, when the prototype can be tested in virtual conditions, without necessity of building test stand, which could be expensive. An example of numerical approach to determining of the flow characteristics of the low pressure gas injector is presented in [4]. Firstly, the tested injector was reflected as a CAD model. Then, using specialized software based computational fluid dynamics (CFD) appropriate boundary conditions and mesh has been adopted to start numerical calculations, which allowed to determine pressure distribution along the tested object and its flow characteristics. As it was mentioned in [4], despite of the fact, that numerical determination allows for more than the experimental studies (a qualitative assessment), it is not able to model the real conditions.

The low-pressure gas-phase injector can be treated as pneumatic electro valve, so it can be tested in accordance to JIS B 8390 standard, which specifies determining the flow rate characteristics of elements using compressible fluids [5]. The application of the methodology of determining the flow characteristics of gas injectors by emptying the tank is presented in [6]. The research method involves measuring the pressure in a tank of a specific volume, where compressed air was used as the working medium. Tested gas-phase injector is mounted on a tube, inside which the working medium flows. By means of a mass flow meter, a measurement card and a computer with specific software values of mass flow of working medium is recorded and the flow characteristics is determined. Described method allows to gain the characteristics, but it refers to the situation, when the valve is opened throughout the test. Presented in the next section of the article method uses an opening impulses forcing system, which enables better reflection of real injector working conditions.

2. Materials and methods

The object of the analysis was the injector rail STAG AC W02, which basic technical data is presented in Table 1. Test stand used during research is presented in Fig. 1. The station takes compressed air from the source *1*, sending it further to the preparation system (for pressure stabilization) *2*, and then to the buffer tank *3*, which acts as a pulsation damper. The air flowing from the tank *3*, goes through the mass flow meter *4* to the tested injector *5*, the opening parameters of which are regulated by the pulse generator *6* connected to a computer. Thanks to the use of the voltage connector, whose leads are

connected to the mass flow meter *4* the volumetric flow rate can be counted basing on measured voltage values. The conversion involves taking into account the coefficient provided by the mass flow meter manufacturer.

Table 1. Basic technical data of the tested injector [7]

Parameter	Unit	Value
Maximum flow (at 1.2 bar)	l/min	125
Opening time (at 1.2 bar)	ms	2.0
Closing time (at 1.2 bar)	ms	1.0
Working pressure	bar	0.95…1.2
Performance range (with nozzle 3.5mm)	HP/cyl	45.0
Coil resistance	Ω	1.9 ±0.1
Supply voltage	V	12…16
Operating temperature	˚C	–20…+120
Durability in urban cycle	km	100 000
Durability in extra-urban cycle	km	200 000

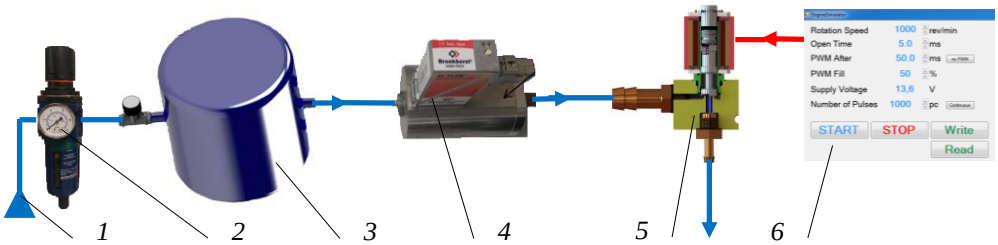

Fig. 1 Test stand: *1* – compressed air source, *2* – air preparation system, *3* – buffer tank, *4* – mass flow meter, *5* – tested gas-phase injector, *6* – pulse generator (based STAG ECU)

3. Results and discussion

The tests on the measurement stand were preceded by a road test carried out on a BMW X3 E83 2.5 i 141kW vehicle using a computer with AC STAG 0.53.6 software. The road test was aimed at determining the maps of the gas controller of the LPG installation of the tested vehicle. After obtaining the necessary data and relating them to the results of similar analyzes [8, 9], test conditions on the measuring station were assumed (Fig. 1): injection time t_{inj} = 5 ms and working medium pressure p = 1.2 bar. The value of the injection time t_{inj} = 5 ms is achieved in the range of average values of the rotational speed of the combustion engine during the driving cycle or non-standard driving [8, 9]. The tested injector was warmed up to the operating temperature by performing at least 5000 injection cycles with an assumed time of t_{inj} = 5 ms, according to the recommendations of the standard [10]. The results of the injector flow tests are presented in Table 2.

Table 2. Wyniki pomiarów stanowiskowych

n, r./min	Nl/min							mg/inj						
	Q_m	d_Q		d_{Qm}	%	s_Q	%	D	d_D		d_{Dm}	%	s_D	%
		–, %	+, %						–, %	+, %				
800	0.8280	5.80	5.07	0.0264	3.19	0.0342	4.13	0.0831	5.80	5.07	0.00265	3.19	0.00343	4.13
1000	1.3980	1.29	0.86	0.0144	1.03	0.0164	1.18	0.1404	1.29	0.86	0.00145	1.03	0.00165	1.18
1500	2.8500	1.05	1.05	0.0120	0.42	0.0212	0.74	0.2862	1.05	1.05	0.00121	0.42	0.00213	0.74
2000	4.6020	0.26	0.39	0.0144	0.31	0.0164	0.36	0.4621	0.26	0.39	0.00145	0.31	0.00165	0.36
2500	5.7060	0.11	0.42	0.0096	0.17	0.0134	0.24	0.5730	0.11	0.42	0.00096	0.17	0.00135	0.24
3000	7.0080	0.26	0.17	0.0144	0.21	0.0164	0.23	0.7037	0.26	0.17	0.00145	0.21	0.00165	0.23
3500	9.1200	0.66	0.33	0.0240	0.26	0.0367	0.40	0.9158	0.66	0.33	0.00241	0.26	0.00369	0.40
4000	10.9320	0.38	0.16	0.0216	0.20	0.0268	0.25	1.0978	0.38	0.16	0.00217	0.20	0.00269	0.25
4500	12.2160	0.29	0.20	0.0192	0.16	0.0251	0.21	1.2267	0.29	0.20	0.00193	0.16	0.00252	0.21
5000	13.1100	0.23	0.23	0.0120	0.09	0.0212	0.16	1.3165	0.23	0.23	0.00121	0.09	0.00213	0.16
5500	15.3780	0.12	0.08	0.0144	0.09	0.0164	0.11	1.5442	0.12	0.08	0.00145	0.09	0.00165	0.11
6000	17.0220	0.25	0.11	0.0216	0.13	0.0268	0.16	1.7093	0.25	0.11	0.00217	0.13	0.00269	0.16

For each of the analyzed cases of engine rotational speed, 5 measurements of the voltage U were made on the electric cables of the mass flow meter (BRONKHORST F-113AC-M50-ABD-00-V, range (0…300) Nl/min, accuracy 0.5%). The values of the volumetric flow Q were determined based on the voltmeter readings, taking into account the conversion factor provided by the flowmeter manufacturer. The mean volumetric output is marked as Q_m. The statistical analysis of volumetric flow Q measurements included the calculation of negative and positive d_Q deviations, mean deviations d_{Qm} and standard deviations s_Q. Each of the statistical calculation values of the volumetric flow measurement results was expressed in Nl/min and converted into percentages for descriptive purposes. Based on measured values of the volumetric flow of the working medium Q, its density ρ = 0.001205 kg/dm^3 (air at temperature +20° and pressure 1.01325 bar) and the injection time

t_{inj} = 5 ms, the values of the fuel dose per injection D were determined. For this value a statistical analysis was carried out in the same way as in the case of volumetric flow Q, calculating negative and positive deviations d_D, mean deviations d_{Dm} and standard deviations s_D expressed in this case in mg/inj and converted into percentages for descriptive purposes. Based on the measurement results, charts were created to assess the influence of the injector operation frequency on its dosage, shown in Fig. 2.

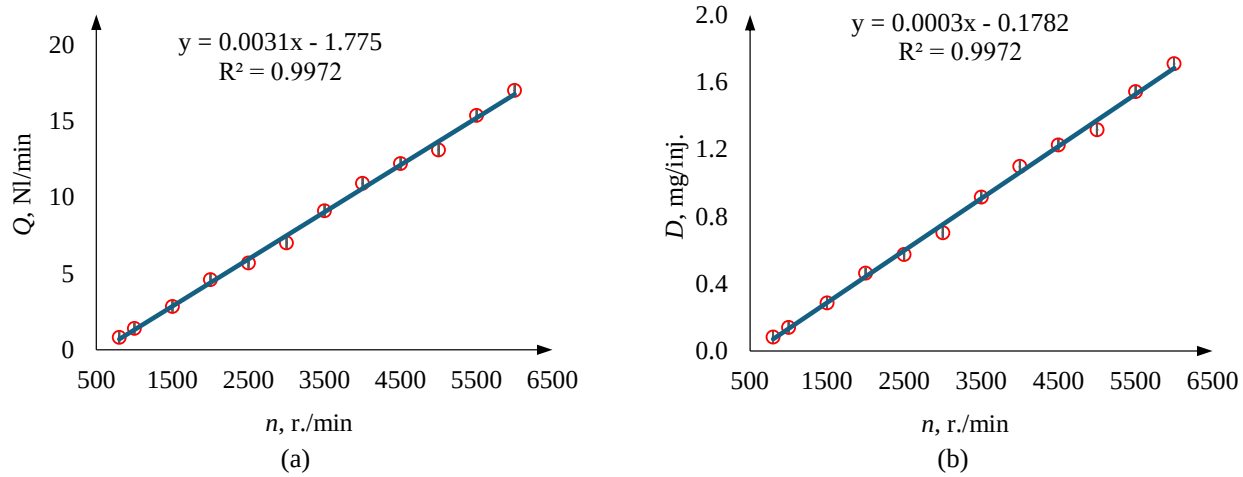

Fig. 2 Graphs of the dependence of: (a) fuel volumetric flow Q on engine rotational speed n, (b) fuel dose D on engine rotational speed n

A spreadsheet was used to process the measurement results. In order to facilitate interpretation the points on both graphs (Fig. 2a and b) have been approximated using a trend line, the method of determining which is described in detail in [11]. The quantity R^2 is called the coefficient of determination. It enables the assessment of the degree of matching of approximate values (points belonging to the trend line) to the points resulting from measurements by assigning a given case a value from 0 to 1 [11]. Both of the determined lines have a high value of R^2 = 0.9972. The volumetric flow characteristics of the STAG AC W02 gas injector are described by the function $y = 0.0031x - 1.775$. Negative deviations d_Q (–) for each series of five measurements were in the range of (0.105…5.797)%, and positive deviations d_Q (+) in the range of (0.078…5.072)%. The mean deviations d_{Qm} were (0.092…3.188)%, and the standard deviations s_Q were (0.107…4.131)%. Even the highest values of each of the given quantities are characterized by a slight level compared to the reference value - the mean volumetric flow Q_m, which proves the high repeatability of the measurement results. The most significant dispersion of the measured flow values Q in relation to the average value Q_m occurs in the case of measurement at the lowest of the considered rotational speeds, n = 800 r./min. The flow of the working medium is then the most unstable due to the relatively long time of closing the injector during its operation. Additionally, the flowmeter operates in the lower measurement range. This relationship is also repeated in the case of rotational speeds n = 1000 r./min and n = 1500 r./min, and the flow begins to stabilize only at the speed n = 2000 r./min, i.e. within the standard rotational speed of the combustion engine. The dependence of the fuel dose per injection cycle on the engine rotational speed is described by the function $y = 0.0003x - 0.1782$. All values of the statistical quantities relating to this relationship are approximately 10 times smaller than the values corresponding to the characteristics in Fig. 2a, and their expressions in percentages are the same as the analogous characteristics of the volumetric flow, which results from the conversion of the volumetric flow Q_m into the fuel dose D based on constant values.

The obtained characteristics illustrate the fuel dosing process during engine operation. The fuel volumetric flow rate increases linearly with the increase in rotational speed. This means that despite the greater demand for fuel at higher rotational speeds, the dose per injection does not increase significantly, as is the case with air supplied to the combustion chamber, but the increased need for fuel is compensated by a greater number of injection cycles per unit of time. Although the straight line on the graph (Fig. 2b) increases with the increase in the engine rotational speed, this increase is insignificant, as evidenced by the slope coefficient of the line a = 0.0003.

4. Conclusions

Based on the calculations and analyzes carried out in the study, the following conclusions were formulated:

1. The applicability of the adopted research method and test stand for determining the volume flow rate during cyclic operation of a gas injector powered by compressed air was confirmed.
2. The aim of the study was achieved, the relationship between the injector dosage and its operating frequency was examined, which may be helpful in configuring the gas supply system.
3. Test conditions, such as injection time and working medium pressure in the measuring station, were assumed based on own experimental research and data from available scientific publications and correspond to various engine operating conditions.

4. Fuel volumetric flow increases linearly with the increase in rotational speed. This means that despite the greater fuel demand at higher rotational speeds, the amount of fuel delivered in one injection does not increase significantly. The indicator of this increase, i.e. the slope coefficient of the line (a = 0.0003), is small, so the characteristics are close to the horizontal line.
5. The results of volumetric flow measurements show high repeatability. The largest dispersion of the measured flow values Q in relation to the average flow value Q_m occurs at the initial considered rotational speeds: n = 800 r./min, n = 1000 r./min and n = 1500 r./min. The flow of the working medium is unstable due to the relatively long time of closing the injector during operation.

5. Further research

The research methodology and conclusions proposed in the study have confirmed their application in determining the characteristics of flow gas injectors. Ultimately, further research will determine the characteristics of various injector designs in order to assess their functional parameters. The results obtained in this way will be helpful in configuring the gas supply system.

References

1. Polish Liquid Gas Association, Raport roczny 2023, Warsaw, **2024**.
2. Polish Liquid Gas Association, 54.5% of Poles use LPG [online]. **2009** [accessed 26 April 2024]. Available online: https://en.pogp.pl/aktualnosci/54-5-polakow-korzysta-z-lpg.
3. Dychto, R.; Leyko, J.; Mitukiewicz, G. Stanowisko do wyznaczania charakterystyk przepływowych wtryskiwaczy benzyny, Publisher: Lodz University of Technology, **2013**. (in Polish).
4. Szpica, D.; Borawski, A.; Mieczkowski, G. Numerical determination of low pressure gas injector flow. *Proceedings of the 19th International Scientific Conference: Engineering for Rural Development*, **2020**, 730-738.
5. Japan Industrial Standard. JIS B 8390:2000. Pneumatic fluid power – components using compressible fluids: determination of flow-rate characteristics.
6. Szpica, D. Numerical determination of low pressure gas injector flow. *Transport Means' 2017: proceedings of 21st International Scientific Conference*, **2017**, 891-896.
7. AC S. A**.** AC W02 [online]. [accessed 26 April 2024]. Available online: https://www.ac.com.pl/products-autogas/injection-rails-lpg-cng/ac-w02/343/.
8. Szpica, D. Operation of a LPG Vapor Phase Fuel System Under the Conditions of Non-Standardized Driving. *Transport Means' 2018: proceedings of 22nd International Scientific Conference,* **2018**, 136-139.
9. Szpica, D.; Dziewiątkowski, M. Analysis of Selected Functional Parameters of the Gas Supply System During NEDC and WLTC Cycles. *Transport Means' 2020: proceedings of 24th International Scientific Conference,* **2020**, 5-10.
10. SAE International, Low Pressure Gasoline Fuel Injector, Warrendale, **2001**.
11. Microsoft, LINEST function [online]. [accessed 8 May 2024]. Available online: https://support.microsoft.com/en-us/office/linest-function-84d7d0d9-6e50-4101-977a-fa7abf772b6d.

The Theoretical Analysis of Nanoplates Using Nonlocal Strain Gradient Theory

Arvydas PALEVICIUS[1], Mostafa SADEGHIAN[1]*

1 Faculty of Mechanical Engineering and Design, Kaunas University of Technology, Studentu 56, 51424 Kaunas, Lithuania
** mostafa.sadeghian@ktu.edu*

Abstract

Nanotechnology is the study of small objects through science and engineering, with an emphasis on objects smaller than 100 nanometres. Many industries are being significantly improved and many of them are even revolutionized by nanotechnology. The prefix nano is derived from the Greek word nanos, which means dwarf. In this investigation, different analyses of nanoplates are studied based on the nonlocal strain gradient theory and discussed and summarized. The nonlocal strain gradient theory finds extensive application in the study of micro- and nanostructures. Both the strain gradient stress field and the nonlocal elastic stress field are considered in the stress field, according to this principle. Also, the differential quadrature technique is one of the common numerical methods which is used for obtaining the results for the nanoplates.

Keywords: Theoretical analysis; nanostructure; nonlocal strain gradient theory.

1. Introduction

The advancement of nanotechnology has ushered in a new era in science. Since the discovery of carbon nanotubes, many researchers have developed an interest in nanostructures. The mechanical properties of nanostructures are different from those of other materials, according to preliminary research. These special properties have led to the widespread use of nanostructures in many different applications, including electric batteries, nanocomposites, nanoactuators, nanosensors, and nanobearings. One kind of nanostructure is the graphene sheet, which is created through the formation of carbon nanotubes. Nanowires, nanorings, and nanorods are some other forms of nanostructures. The primary focus of the study of carbon nanomaterials is therefore the analysis of graphene sheets. Graphene exhibits exceptional mechanical and physical properties such as high tensile strength, high flexibility, and high thermal and electrical conductivity[1].

Experiments have shown us that the mechanical properties of structures can vary at very small scales from those at macroscales. Nanostructure properties cannot be predicted by classical continuum mechanics models because small-scale effects are not taken into account. To overcome these difficulties, several non-classical continuum mechanics models have been created, including couple stress theory, nonlocal elasticity theory, and strain gradient theory. These models provide a more thorough understanding of the mechanical properties of nanoscale structures, overcoming the drawbacks of earlier methods. By developing a nonlocal elasticity model, Eringen expanded classical elasticity theory to include non-local effects. According to this theory, the stress at a specific location is influenced by the entire material domain[2].

In order to account for strain gradient effects, the classical elasticity theory was improved by including the strain gradient component. Furthermore, the couple stress theory was developed, which considers the impact of internal couple stresses on material behaviour, broadening the application of classical elasticity theory. In addition, Yang and associates considered strain gradients from symmetry rotation to develop a couple stress theory. Furthermore, some researchers created the modified strain gradient theory in order to study the effects of strain gradients, including dilatation, symmetry rotation, and deviatoric stretch gradients. The impact of strain gradients or nonlocal factors is taken into account in these theoretical frameworks[3]. The non-local strain gradient theory was created by Lim et al.[4] to take into consideration both of these effects when computing nanostructures.

Based on the nonlocal strain gradient theory, numerous studies on the size-dependent mechanical behaviour of nanostructures have been carried out[5-7]. In this investigation, different analyses of nanoplates are studied based on the nonlocal strain gradient theory and discussed and summarized.

2. The governing equations

Figure 1 a and b depict the graphene sector and circular plates, considering r_i and r_o as the internal and outer radii, respectively. Moreover, the thickness and the angle of the sector plate are defined by h and τ .

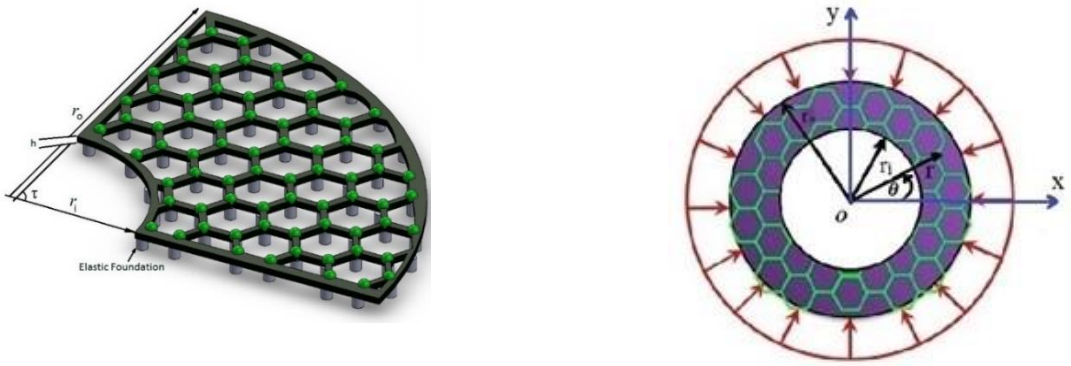

(a) (b)

Fig. 1 (a) The annular sector nanoplate with elastic foundation, and (b) the graphene annular plate

After taking into account the HSDT and incorporating a unique function known as *g(z)*, the displacement field can be represented by the subsequent equations, which are defined by *U*, *V*, and *W* in the *r*, *θ*, and *z* directions, respectively:

$$\begin{aligned} U(r,\theta,z) &= u_0(r) - z\frac{dw_0(r)}{dr} + g(z)\phi(r) \\ V(r,\theta,z) &= v_0(r,\theta) - \frac{z}{r}\frac{\partial w_0(r,\theta)}{\partial\theta} + g(z)\psi(r,\theta) \\ W(r,\theta,z) &= w_0(r) \end{aligned} \tag{1}$$

Where u_0, v_0, and w_0 are the displacement components of the midplane in *r*, *θ*, and *z* axes. Besides, ϕ and ψ are noted as the rotation components of the *θ* and *r* directions. It is viewed that for the circular analyses, the *V* in the displacement field (Eq.1) is equal to zero due to symmetrical assumption. Moreover, the function *g(z)* can be written as follows:

$$g(z) = f(z) + zy^* \tag{2}$$

It is possible to think of *f (z)* and *y** as multiple functions that have been used in various references summarized in Table 1.

Table 1. Several suggested g(z) functions that are introduced in different references

Model	$g(z)$ function
Ambartsumian[8]	$-\frac{1}{6}z^3 + \frac{h^2}{8}z$
Reddy[9]	$-\frac{4}{3h^2}z^3 + z$
Reissner[10]	$-\frac{5}{3h^2}z^3 + \frac{5}{4}z$

Using von Karman assumptions, the nonlinear strain components can be written as:

$$\varepsilon_r = \frac{\partial U}{\partial r} + \frac{1}{2}\left(\frac{\partial W}{\partial r}\right)^2 = \frac{\partial u_0}{\partial r} - z\frac{\partial^2 w_0}{\partial r^2} + g(z)\frac{\partial\phi}{\partial r} + \frac{1}{2}\left(\frac{\partial w_0}{\partial r}\right)^2 \tag{3}$$

$$\varepsilon_\theta = \frac{U}{r} + \frac{1}{r}\frac{\partial V}{\partial\theta} + \frac{1}{2r^2}\left(\frac{\partial W}{\partial\theta}\right)^2 = \frac{1}{r}\left(u_0 - z\frac{\partial w_0}{\partial r} + \frac{\partial v_0}{\partial\theta} - \frac{z}{r}\frac{\partial^2 w_0}{\partial\theta^2} + g(z)\left(\frac{\partial\psi}{\partial\theta} + \phi\right)\right) + \frac{1}{2}\left(\frac{1}{r}\frac{\partial w_0}{\partial\theta}\right)^2 \tag{4}$$

$$\begin{aligned} \gamma_{r\theta} &= \frac{1}{r}\frac{\partial U}{\partial\theta} + \frac{\partial V}{\partial r} - \frac{V}{r} + \frac{1}{r}\frac{\partial W}{\partial\theta}\frac{\partial W}{\partial r} = \\ &\frac{1}{r}\left(\frac{\partial u_0}{\partial\theta} - 2z\frac{\partial^2 w_0}{\partial r\partial\theta} + g(z)\frac{\partial\phi}{\partial\theta} + \frac{\partial w_0}{\partial\theta}\frac{\partial w_0}{\partial r} - v_0 - g(z)\psi\right) + 2\frac{z}{r^2}\frac{\partial w_0}{\partial\theta} + \frac{\partial v_0}{\partial r} + g(z)\frac{\partial\psi}{\partial r} \end{aligned} \tag{5}$$

$$\gamma_{rz} = \frac{\partial W}{\partial r} + \frac{\partial U}{\partial z} = \phi\frac{\partial g(z)}{\partial z} \tag{6}$$

$$\gamma_{\theta z}=\frac{1}{r}\frac{\partial W}{\partial \theta}+\frac{\partial V}{\partial z}=\psi\frac{\partial g(z)}{\partial z} \tag{7}$$

The stress and moment resultants with the nonlocal (*NL*) expression can be written as:

$$\{N_r,N_\theta,N_{r\theta},Q_r,Q_\theta\}^{NL}=\int_{-\frac{h}{2}}^{\frac{h}{2}}\{\sigma_r,\sigma_\theta,\sigma_{r\theta},\sigma_{rz},\sigma_{\theta z}\}^{NL}\,dz \tag{8}$$

$$\{M_r,M_\theta,M_{r\theta}\}^{NL}=\int_{-\frac{h}{2}}^{\frac{h}{2}}\{\sigma_r,\sigma_\theta,\sigma_{r\theta}\}^{NL}\,z dz \tag{9}$$

$$\{R_r,R_\theta,R_{r\theta}\}^{NL}=\int_{-\frac{h}{2}}^{\frac{h}{2}}\{\sigma_r,\sigma_\theta,\sigma_{r\theta}\}^{NL}\,f(z)dz \tag{10}$$

$$\{R_{rz},R_{\theta z}\}^{NL}=\int_{-\frac{h}{2}}^{\frac{h}{2}}\{\sigma_{rz},\sigma_{\theta z}\}^{NL}\,f'(z)dz \tag{11}$$

According to the principle of minimum potential energy, the potential energy variation in an equilibrium state is equal to zero:

$$\delta\Pi=\delta U+\delta\Omega=0 \tag{13}$$

The strain gradient model and nonlocal stresses field can be combined to form the nonlocal strain gradient principle, which was developed by Lim et al. [4] and is expressed as follows:

$$(1-\mu^2\nabla^2)\sigma_{ij}=C_{ijkl}(1-l^2\nabla^2)\varepsilon_{kl},\quad \nabla^2=\frac{\partial^2}{\partial r^2}+\frac{1}{r^2}\frac{\partial^2}{\partial\theta^2}+\frac{1}{r}\frac{\partial}{\partial r} \tag{14}$$

The sector nanoplate's equilibrium equations on the elastic foundation are expressed locally in the following equations:

$$\delta u_0: N_r^L-N_\theta^L+r\frac{\partial N_r^L}{\partial r}+\frac{\partial N_{r\theta}^L}{\partial\theta}=0 \tag{15}$$

$$\delta v_0: \frac{\partial N_\theta^L}{\partial\theta}+r\frac{\partial N_{r\theta}^L}{\partial r}+2N_{r\theta}^L=0 \tag{16}$$

$$\begin{aligned}&\delta w_0: r\frac{\partial^2 M_r^L}{\partial r^2}+2\frac{\partial M_r^L}{\partial r}-\frac{\partial M_\theta^L}{\partial r}+\frac{1}{r}\frac{\partial^2 M_\theta^L}{\partial\theta^2}+\frac{2}{r}\frac{\partial M_{r\theta}^L}{\partial\theta}+2\frac{\partial^2 M_{r\theta}^L}{\partial\theta\partial r}+(1-\mu\nabla^2)\Big((q-k_w w_0)r+\\&rN_r^L\frac{\partial^2 w_0}{\partial r^2}+N_\theta^L\frac{\partial w_0}{\partial r}+\frac{1}{r}N_\theta^L\frac{\partial^2 w_0}{\partial\theta^2}-\frac{2}{r}N_{r\theta}^L\frac{\partial w_0}{\partial\theta}+2N_{r\theta}^L\frac{\partial^2 w_0}{\partial r\partial\theta}\Big)+\\&\mu r\left((\nabla^2 N_r^L)\frac{\partial^2 w_0}{\partial r^2}+(\nabla^2 N_\theta^L)\left(\frac{1}{r}\frac{\partial w_0}{\partial r}+\frac{1}{r^2}\frac{\partial^2 w_0}{\partial\theta^2}\right)+2(\nabla^2 N_{r\theta}^L)\left(\frac{1}{r}\frac{\partial^2 w_0}{\partial r\partial\theta}-\frac{1}{r^2}\frac{\partial w_0}{\partial\theta}\right)\right)=0\end{aligned} \tag{17}$$

$$\delta\phi: y^*\left(r\frac{\partial M_r^L}{\partial r}+\frac{\partial M_{r\theta}^L}{\partial\theta}+M_r^L-M_\theta^L-rQ_r^L\right)+R_r^L-R_\theta^L+r\frac{\partial R_r^L}{\partial r}+\frac{\partial R_{r\theta}^L}{\partial\theta}-rR_{rz}^L=0 \tag{18}$$

$$\delta\psi: y^*\left(r\frac{\partial M_{r\theta}^L}{\partial r}+\frac{\partial M_\theta^L}{\partial\theta}+2M_{r\theta}^L-rQ_\theta^L\right)+2R_{r\theta}^L-rR_{z\theta}^L+r\frac{\partial R_{r\theta}^L}{\partial r}+\frac{\partial R_\theta^L}{\partial\theta}=0 \tag{19}$$

Also, the following equations represent the equilibrium values for a single-layer axisymmetric annular/circular nano-plate on a Winkler-Pasternak elastic foundation:

$$\delta u_0: N_r^L+r\frac{dN_r^L}{dr}-N_\theta^L=0 \tag{20}$$

$$\begin{aligned}&\delta w_0: r\frac{d^2 M_r^L}{dr^2}+2\frac{dM_r^L}{dr}-\frac{dM_\theta^L}{dr}+(1-\mu\nabla^2)\Big((q-k_w w_0+k_p\nabla^2 w_0)r\\&+N_\theta^L\frac{dw_0}{dr}+rN_r^L\frac{d^2 w_0}{dr^2}\Big)+\mu r\left((\nabla^2 N_r^L)\frac{d^2 w_0}{dr^2}+(\nabla^2 N_\theta^L)\left(\frac{1}{r}\frac{dw_0}{dr}\right)\right)=0\end{aligned} \tag{21}$$

$$\delta\phi : y^{*}\left(r\frac{dM_r^{L}}{dr} + M_r^{L} - M_\theta^{L} - rQ_r^{L} \right) + R_r^{L} + r\frac{dR_r^{L}}{dr} - R_\theta^{L} - rR_{rz}^{L} = 0 \tag{22}$$

2. The solution method

One of the highly accurate numerical techniques that comes from the quadratic integration method is the differential quadrature technique. The integral at any one point along the domain in the quadratic integration method depends on every point along that direction.

$$\int_a^b f\,(r)dr = \sum_{k=1}^{n} w_k f_k \tag{23}$$

3. Results and discussions

This section examines various factors to study their role on the results of nanoplates for Clamped (*c*) and simply supported (*s*) and free (*f*) conditions. For this purpose, the following assumptions are considered:

$$\begin{aligned} &k_w = 1.13(GPa/nm)\ ;\ k_p = 1.13(Pa.m)\ , k_0 = 45(GPa/nm), r_o = 5(nm) \\ &E_1 = 1765\ \text{GPa},\ E_2 = 1588\ \text{GPa}, \nu_{12} = 0.3,\ \nu_{21} = 0.27,\ h = 0.34\ \text{nm},\ r_i = 0.2r, \end{aligned} \tag{24}$$

The influence of the number of nodes applied in the DQM to obtain the results of this paper is shown in Figure 2. It is evident that the proper convergence is reached after nine nodes.

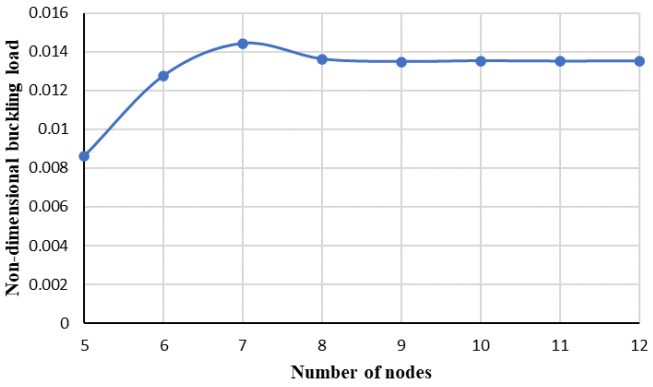

Fig. 2 The role of the number of nodes on the results of nano circular plate

An example of verification of the present study with other references is gathered in Table 2.

Table 2. The results of the present paper compared to the references for the bending of nano sector plates.

r_i / r_o	[11]	Present study
0.25	2.76	2.85
0.5	1.42	1.45
0.75	0.09	0.093

Figure 3 shows how the sector nanoplate's non-dimensional maximum deflection changes with nonlocal parameters under various boundary conditions. It is evident that the non-dimensional deflection decreases as the nonlocal parameter increases.

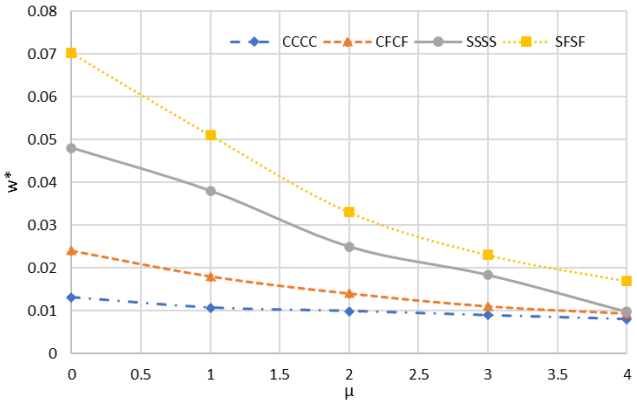

Fig. 3 Variations in the sector nanoplate's dimensionless maximum deflection in relation to the nonlocal parameter

The non-dimensional buckling load is plotted against the radius ratios in Figure 4 for a range of boundary conditions and strain gradient values. Therefore, it can be said that buckling loads decrease as the strain gradient increases.

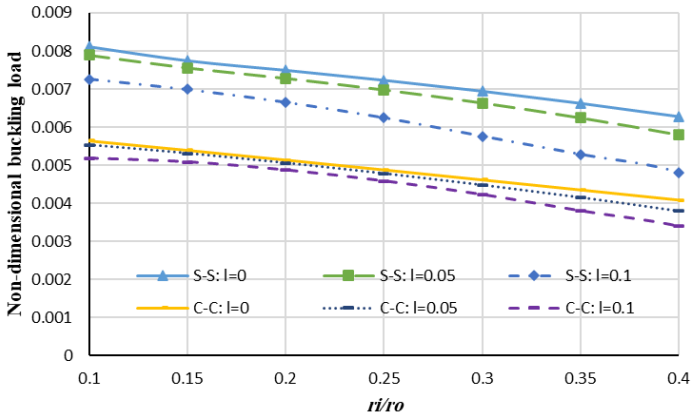

Fig. 4 The annular nanoplate's nondimensional buckling load in relation to radius ratios

4. Conclusions

This paper focuses on the theoretical analyses of the nanoplate with the aid of the nonlocal strain gradient theory with HSDT. The differential quadrature technique is one of the common numerical methods which is used for obtaining the results for the nanoplates. It is viewed that the results of the nanoplates are strongly dependent on small-scale parameters.

References

1. Farajpour, A., M.H. Ghayesh, and H. Farokhi, A review on the mechanics of nanostructures. International Journal of Engineering Science, 2018. 133: p. 231-263.
2. Eringen, A.C., Nonlocal polar elastic continua. International Journal of Engineering Science, 1972. 10(1): p. 1-16.
3. Thai, H.-T., T.P. Vo, T.-K. Nguyen, and S.-E. Kim, A review of continuum mechanics models for size-dependent analysis of beams and plates. Composite Structures, 2017. 177: p. 196-219.
4. Lim, C.W., G. Zhang, and J.N. Reddy, A higher-order nonlocal elasticity and strain gradient theory and its applications in wave propagation. Journal of the Mechanics and Physics of Solids, 2015. 78: p. 298-313.
5. Sadeghian, M., et al. The Nonlinear Bending of Sector Nanoplate via Higher-Order Shear Deformation Theory and Nonlocal Strain Gradient Theory. Mathematics, 2024. 12, DOI: 10.3390/math12081134.
6. Sadeghian, M., A. Palevicius, and G. Janusas Nonlocal Strain Gradient Model for the Nonlinear Static Analysis of a Circular/Annular Nanoplate. Micromachines, 2023. 14, DOI: 10.3390/mi14051052.
7. Sadeghian, M., A. Palevicius, and G. Janusas Nonlinear Thermal/Mechanical Buckling of Orthotropic Annular/Circular Nanoplate with the Nonlocal Strain Gradient Model. Micromachines, 2023. 14, DOI: 10.3390/mi14091790.
8. Ambartsumian, S., On the theory of bending plates. Izv Otd Tech Nauk AN SSSR, 1958. 5(5): p. 69-77.
9. Reddy, J.N., A simple higher-order theory for laminated composite plates. 1984.
10. Reissner, E., On tranverse bending of plates, including the effect of transverse shear deformation. 1974.
11. Mousavi, S.M. and M. Tahani, Analytical solution for bending of moderately thick radially functionally graded sector plates with general boundary conditions using multi-term extended Kantorovich method. Composites Part B: Engineering, 2012. 43(3): p. 1405-1416.

3D Woven Composite Materials and Their Meso-mechanical Modelling

Sumeyye ERDEM[1]*, Mete Onur KAMAN[2]

1 University of Karamanoglu Mehmetbey, Karaman, Turkiye
2 University of Firat, Elazig, Turkiye
** sumeyyeerdem@kmu.edu.tr*

Abstract

Two-dimensional (2D) and three-dimensional (3D) fabrics in order to strengthen composites can provide strong composites. In three-dimensional composites, the fact that the reinforcement materials can be laid in the desired direction and multi-layer and the reinforcement materials have sufficient intersection eliminates the delamination error in composites. Three-dimensional fabrics are produced in two different ways, either by combining two-dimensional fabrics produced in traditional weaving machines with matrix materials or by sewing together or directly on machines that produce three-dimensional woven fabric. Meso-mechanical analysis is important at this point for the analysis of 3D composites. In the presented study, 3D composite modelling was done in the Ansys Workbench program. It has been observed that yarns, especially in the vertical direction, are important in mechanical behaviour.

Keywords: 3D woven, meso-mechanics, finite element method, fiber reinforced composites.

1. Introduction

Scientific and technological advances have accelerated the process of developing new materials in engineering. In defence, automotive, space and many other sectors, the production of low-cost, high-strength and lightweight products has gained importance. This need has triggered the development of composite materials [1]. These materials, which combine in visible dimensions, have a wide range of applications, especially in the defence industry [2]. In the defence industry, the development of light and durable products is of great importance in terms of ease of transport and use [3]. Polymer matrix composites are among the preferred materials in military vehicles and provide weight and cost advantages. In the construction industry, composites are used in areas such as structural reinforcement and insulation [4]. In the health sector, they are preferred in a wide range from dental implants to protective equipment [5]. In pandemic conditions, the potential of composite materials for the development of more effective protective equipment is emphasised [6]. In general, the properties of composites such as lightness and durability make them indispensable in many industries [7].

The production of composite materials has made significant progress with technological advances. Used in a wide range of applications from defence to health, automotive to aerospace, these materials offer superior properties by combining the strengths of different materials [8]. Composites consist of reinforcing materials and matrices; glass, carbon and aramid fibres and vinyl ester, epoxy and polyester resins are included in this structure. Offering advantages such as strength, stiffness and lightness, composites are also resistant to corrosion and abrasion. Fibre-reinforced composites are preferred in applications requiring high performance and the arrangement of fibres can be varied to obtain different mechanical properties [9]. Composites can undergo deformation due to external influences and delamination is an important type of damage in three-dimensional (3D) composites. While two-dimensional (2D) fabrics have low weight strength, 3D fabrics overcome this weakness and reduce delamination damage. However, the cost of 3D fabrics is high and the lack of local production leads to difficulties in composite production [10]. 3D fabrics can be produced on conventional weaving machines or specialised three-dimensional looms. True 3D looms provide a more efficient production and reduce fibre damage. The durability and reliability of composites are determined by the amount and distribution of fibres used. The production of 3D fabrics provides suitable reinforcement materials for high-performance elements and can eliminate delamination damage. 3D composites produced by weaving, knitting and sewing methods can have purpose-built mechanical properties [11]. Traditional woven fabrics have a wide range of applications from defence and aerospace to construction and health sectors. Textile composites, which can compete with ceramics and metals with their low density and high strength properties, offer significant advantages in industrial applications [12]. The lack of strength and delamination problems in the thickness direction of 2D woven composites have led to the development of 3D woven composites. These composites eliminate the problem of delamination and integrate high-strength fibres in the $-x$, $-y$ and $-z$ axes, increasing the fibre-to-volume ratio and thus elasticity and strength due to the low crimp ratio [7]. 3D weaving allows the production of composites with fibres of various thicknesses and strengths such as glass, carbon and basalt. Furthermore, this textile enables direct forming of composite parts, eliminating the need for drilling and cutting operations, reducing material waste and labour costs, and facilitating homogeneous dispersion of resins [13]. 3D woven fabrics are produced using improved conventional looms or specialised 3D looms. The integration of layers by means of vertical warp yarns enables the formation of multilayer composite structures. On special 3D looms, three-dimensional composite weaving is achieved by means of both vertical and horizontal movements of the warp yarns. An illustration of the production of 3D fabrics with horizontal and vertical movements of warp yarns is given in Figure 1.

(a) (b)

Fig. 1 Spout opening system (a) one-way spout mechanism (b) two-way spout mechanism [14]

In 1974, Greenwood produced multilayer woven fabrics with two separate warp groups for the first time. In addition to these two groups, three-dimensional woven fabrics contain a third warp yarn that provides structural integrity. The loom designed by Greenwood is an innovative approach that makes the production of three-dimensional fabrics possible [15]. A visual of the three-dimensional woven fabric production loom developed by Greenwod is shown in Figure 2.

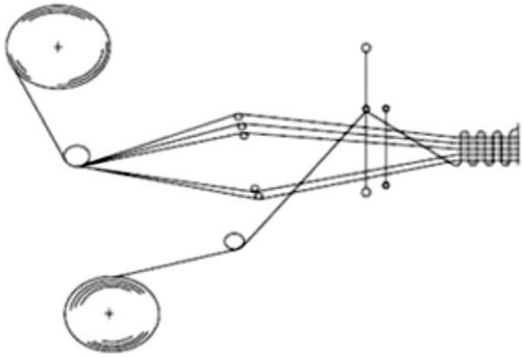

Fig. 2 Greenwood 3D weaving mechanism [15]

3D weaving technology, which is defined as noobed, allows the production of fabrics with up to seventeen layers thanks to the limited connection points of three separate yarn sets [16]. A visualization of the fabrics produced with this method is presented in Figure 3.

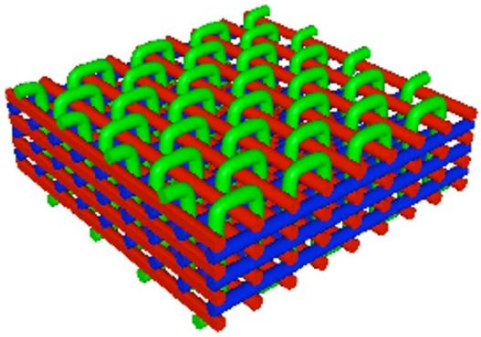

Fig. 3 Noobed 3D fabric production [17]

In 3D fabric weaving system on conventional looms were developed. In this technique, the threads are arranged on the machine according to the profile shape. Some warp yarns are placed linearly, while others move vertically with the frames. The weft yarns are integrated at constant speed to create three-dimensional fabrics with high thickness. Pneumatic systems are applied to prevent electrification and the yarns are threaded through tubing to reduce friction. A visualisation of the loom is shown in Figure 4. Conventional weaving machines developed with modifications can produce 3D fabrics by adding additional layers to 2D fabrics. However, since all structures cannot be processed simultaneously with this method, this system cannot be considered as fully 3D [18]. In real 3D looms, it is possible to produce four types of fabrics: uniaxial and multiaxial, with and without intersection of yarn layers. In uniaxial fabrics, the $-y$ yarns of the unconnected yarn groups lie flat, while the $-x$ and $-z$ yarns are integrated with shuttles. In modified machines, the yarns can only be connected at 90° angles, while real three-dimensional looms increase the cross strength of multiaxial fabrics by providing connection at -45° and +45° angles [18].

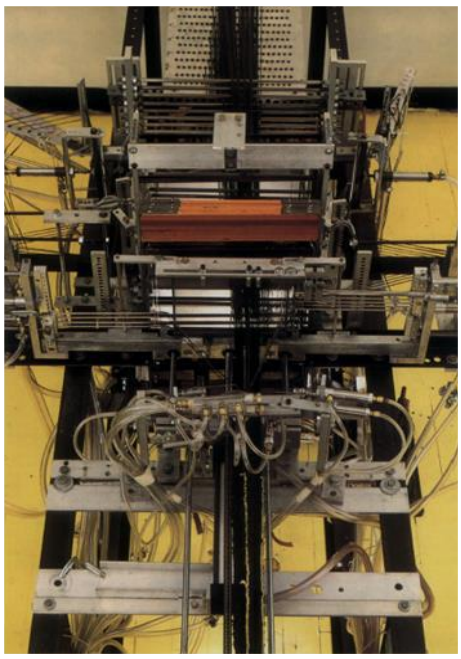

Fig. 4 Modified three-dimensional fabric loom [17]

The aim of this study is able to make a numerical model for predicting the deformations of 3D composites and also to determine the correct boundary condition for unit cell analysis of textile composites. Because of this reason, meso-scale numerical modelling of 3D fabrics drawn in SolidWorks was carried out. Then, the prepared 3D model was imported into the ANSYS Workbench program. Here, boundary conditions are applied to the model. In the final stage, displacement and stress values were obtained on the model.

2. Materials and Method

SolidWorks is a reliable and user-friendly 3D design software that accelerates product design. A schematic view of an orthogonal 3D woven fabric prepared SolidWorks program is shown in Figure 5. Then, the model was analysed in ANSYS Workbench, and fibre and matrix properties were evaluated based on 70% fibre volume fraction. Linear elastic properties and specific moduli of elasticity (E_1 =165000 MPa, E_2 and E_3 =8000 MPa), Poisson's ratios (v_{12} =0.37, v_{23} and v_{13} =0.24) and shear moduli (G_{12} =4500 MPa, G_{23} and G_{13} =3000 MPa) were used with the assumptions of orthotropic material. 1 axis defines parallel to the fiber direction, 2 is perpendicular to the fiber axis, and 3 is defines thickness axis with respect to composite mechanics. 27.8x9.9x5.3 mm unit cell model and local coordinate axes were created to define the fibre directions. There are 17 plies in xy plane. Fiber yarns were modelled as 3D homogeneous volumes. Additionally, yarns were assumed as resin impregnated composites.

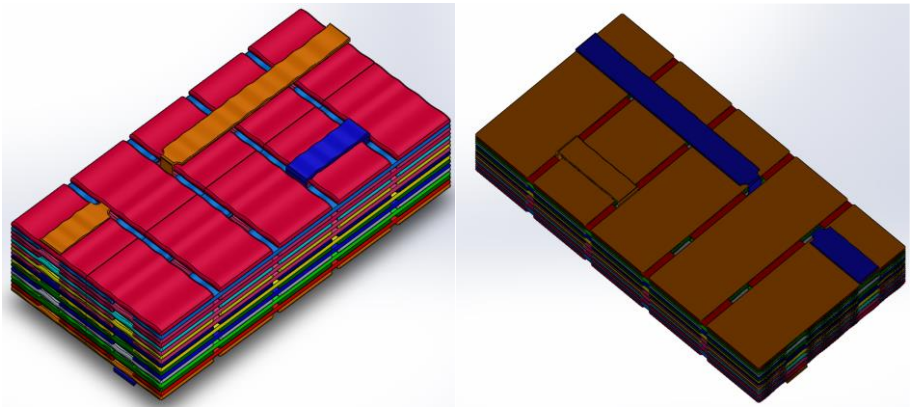

(a) (b)

Fig. 5 Schematic view of 3D woven fabric (a) top view, (b) bottom view

There are three main modelling scales for studying mechanical behaviors of materials: macro, meso and micro. Meso-scale modelling is preferred due to the high computational capacity of today's computers and the high accuracy required in research. For meso-scale analysis of materials such as fabrics, a realistic geometry design is essential. Figure 6 shows the mesoscale unit element model. The finite element model consists of a total of 157527 nodes.

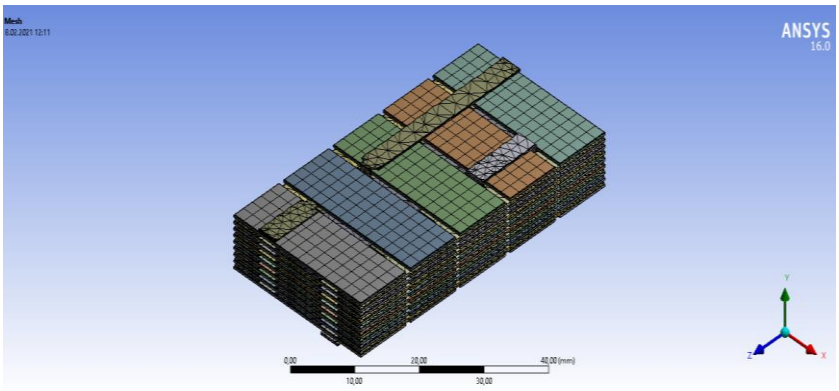

Fig. 6 Mesh model for the fabric examined within the scope of the research

Figure 10 shows the prepared three-dimensional unit cell model. Since the model is symmetrical, a parametric boundary condition was applied to the loaded sections. According to this boundary condition, displacements in parallel planes are equal and opposite to each other. Therefore, a boundary condition of the form

$$u_z(front\ surface) + u_z(back\ surface) = 0 \tag{1}$$

can be written for a loading in the $-z$ axis. In order to do this, two remote points were defined on the opposite edges of the plate and 0.2 mm displacement was applied from the surfaces where remote point 2 is located. The schematic view of the model with the boundary conditions applied is given in Figure 7.

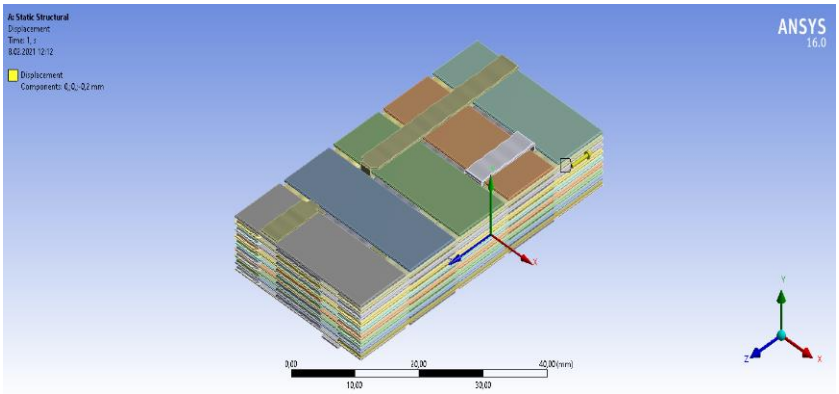

Fig. 7 Solid model of the 3D fabric

3. Results and Discussion

Figure 8 shows the normal stress distribution along the $-z$ axis. It is seen that the stress is uniformly distributed except for the stress concentration points. It is determined that the stresses are higher especially in the vertical yarns.

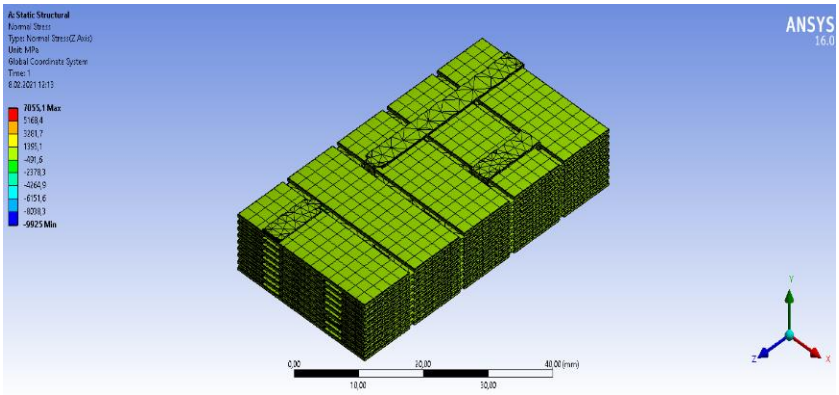

Fig. 8 Static structural normal stress distribution of the fabric

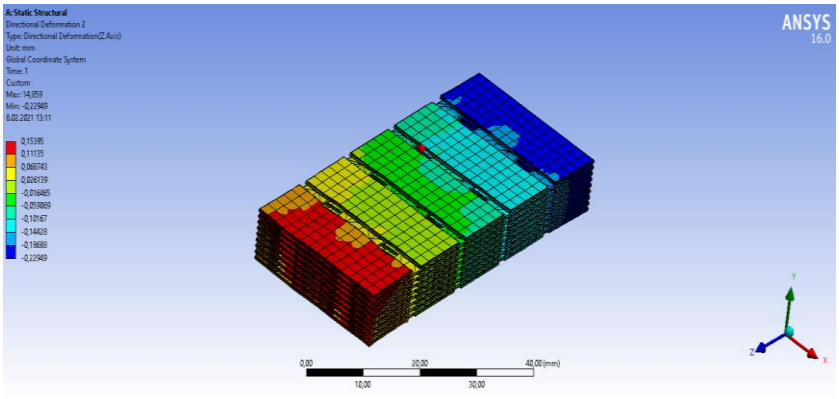

Fig. 9 Displacement result of the modeled 3D composite fabric

In Figure 9, vertical yarns are removed and the periodic boundary condition in orthotropic fibers is examined. It is seen that symmetrical elongation in both directions is obtained for the 0.2. mm elongation given in the $-z$ axis. However, it is seen that the elongation is much larger for the yarns in the vertical direction. While modeling, symmetry in the vertical yarns was avoided in order to create a more realistic model instead of idealization. This affected the displacements (Figure 10).

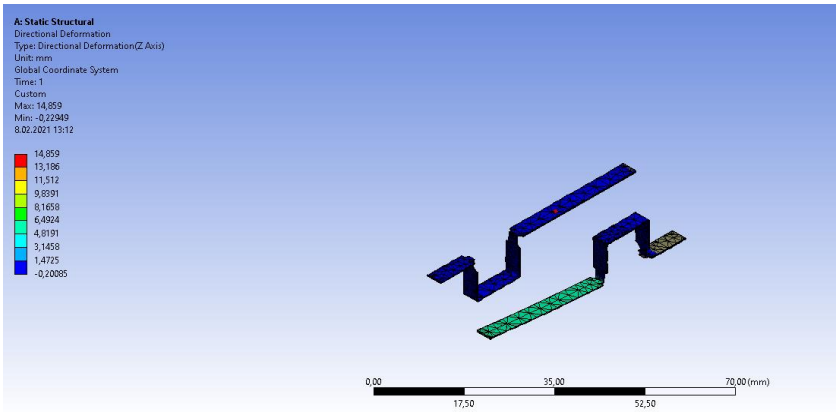

Fig. 10 Displacement result of the $-z$ direction of the modeled vertical yarns

4. Conclusions

In this study, the production and weaving types of 3D composite materials are explained, and then a finite element analysis is performed for a typical orthogonal 3D composite.

- 3D textile composites have a wide range of applications thanks to their advanced properties. These structures are resistant to delamination and tolerant to damage, so they are considered as alternative materials. 3D preforms are produced on customized looms and combine three yarn groups including warp, weft and $-z$ yarn. With this method, composites of the desired thickness are obtained. By modifying conventional looms, the strength of the composites in the thickness direction is increased. The mechanical properties of 3D composites classified according to fiber type and arrangement are affected by factors such as winding speed, inter-yarn distance, $-z$ yarn angle and density. An increase in the $-z$ yarn volume ratio leads to a decrease in in-plane properties, while a decrease in the $-z$ yarn volume ratio leads to localized delamination-type damage.
- Meso-scale dimension was used in the finite element model. Parametric boundary condition was applied to symmetrical surfaces and the stress distribution in the composite was examined in the tensile direction. It has been determined that high displacements and stress concentrations occur in the yarns, especially along the $-z$ axis. Therefore, it can be said that the design of vertical yarns has gained importance in the analysis and calculations to be made. Thus, results are relation with the first paragraph and critical for optimizing the performance of 3D composites.

References

1. Kaw, A.K. *Mechanics of composite materials,* 2nd Edition, çev Okutan Baba, B.; Karakuzu, Efil Yayınevi, İstanbul 2014.
2. Chen, X.; Taylor, L.W.; Tsai, L.J. An overview on fabrication of three-dimensional woven textile preforms for composites. *Textil Research Journal,* 2011, 81, 932–944.
3. Saleh, M.N.; Soutis, C. (2017). Recent advancements in mechanical characterisation of 3D woven composites, *Mechanics of Advanced Materials and Modern Processes,* 2017, 3(12), 1-17.

4. Potyrala, P.B. *Use of fiber reinforced polymers in bridge construction: state of the art in hybrid and all-composite structures*, Universitat Politècnica de Catalunya, Barcelona 2011.
5. Umer, R.; Alhussein, H.; Zhou J.; Cantwell, W.J. The mechanical properties of 3D woven composites. *Journal of Composite Materials*, 2016, 1(2), 1-14.
6. Ning, F.; Cong, W.; Qiu, J.; Wei, J.; Wang, Additive manufacturing of carbon fiber reinforced thermoplastic composites using fused deposition modeling. *Composites Part B: Engineering*, 2015, 80, 369–378.
7. Li, Y.; Li, R.; Lu, L.; Huang, X. Experimental study of damage characteristics of carbon woven fabric/epoxy laminates subjected to lightning strike. *Composites: Part A*, 2015, 79, 164-175.
8. Seltzer, R.; Gonzalez, C.; Munoz, R.; Llorca, J.; Blanco-Varela, T. Xray microtomography analysis of the damage micromechanisms in 3D woven composites under low-velocity impact. *Composites Part A: Applied Science and Manufacturing*, 2013, 7, 49-60.
9. Zhang, D.; Sun, M.; Liu, X.; Xiao, X.; Qian, K. Off-axis bending behaviors and failure characterization of 3D woven composites. *Composite Structures*, 2018, 5, 45-55.
10. EL-Dessouky, H.; Snape, A.; Tew, H.; Scaife, R.; Modi, D.K.; Kendall, K. Design, weaving and manufacture of a large 3d composite structure for automotive applications. *The 7th World Conference on 3D Fabrics and Their Applications*, 2016, 2(4), 16-29.
11. Li, Z.; Guo, L.; Zhang, L.; Wang, Q. In situ experimental investigation on the out-plane damage evolution of 3D woven carbon-fiber reinforced composites. *Composites Science and Technology*, 2018, 101-109.
12. Deepak Patel, K.; Anthony Waas, M.; Yen, C.F. Direct numerical simulation of 3D woven textile composites subjected to tensile loading: An experimentally validated multiscale approach. *Composites Part B: Engineering*. 2018, 152, 102–115.
13. Brandt, J.; Drechsler, K.; Arendts, F.J. Mechanical performance of composites based on various three-dimensional woven-fibre preforms. *Composites Science and Technology*, 2006, 56(3), 381-386.
14. Liu, Y., Labanieh, A.R., Vasiukov, D., Soulat, D., Panier, S. Influence of off-axis in-plane yarns on the mechanical properties of 3D composites. *Composites: Part A*, 2017, 98(8), 45-57.
15. Hu, J. 3D fibrous assemblies, Number 74, Woodhead Publishing Limited, England 2008.
16. Guo, L., Huang, J., Zhang, L., Sun, X. Damage evolution of 3D woven carbon/epoxy composites under tensiontension fatigue loading based on synchrotron radiation computed tomography (SRCT), *International Journal of Fatigue*, 2020, 142, 1-11.
17. Eizaguirre, M.G. Tensile testing of 3D reinforced composites. Master of Science Thesis, Kungliga Tekniska Högskolan Lightweight Structures, Stockholm/Sweeden 2011.
18. Yan, S.; Zeng, X.; Long, A. Experimental assessment of the mechanical behaviour of 3D woven composite T-joints, *Composites Part B: Engineering*, 2018, 3, 108-113.

Characterization of Beta Phase and Piezoelectric Properties of PVDF/HA/$AgNO_3$ Piezoelectric Film

Ieva MARKUNIENE[1]*, Giedrius JANUSAS[1]

1 Faculty of Mechanical Engineering and Design, Kaunas University of Technology, Studentu str. 56, Kaunas, LT 51373, Lithuania
**ieva.markuniene@ktu.edu*

Abstract

Beta *(β)* - phase of PVDF exhibits outstanding electrical characteristics, including piezoelectric, pyroelectric, and ferroelectric properties. These electroactive properties are becoming increasingly important in areas such as energy storage, rotary valve devices, biomedicine, sensors, and smart scaffolds. This article discusses the methods of obtain the main PVDF phase and reviews the applications and properties of *β*-phase PVDF. This study can provide information on the development and application of *β*-phase PVDF films in the field of biosensors. Its use is restricted by the brittleness and low bending strength. To counteract mechanical weakness of HA, several formulas involving HA and polymer composites [1, 6]. Because there is so much HA in the composition as a whole, HA / polymer composites have excellent biocompatibility. When PVDF films are optimized for crystallization, dimethylsulfoxide (DMSO) is used as a solvent to produce films with a high *β*-phase content of up to 98.8%. It can be beneficial to include a conductive phase, such us silver. By facilitating better charge transfer, the conductive phase raises the piezoelectric response sensitivity. These factors influenced the selection of the materials: PVDF, HA, and AGNO3. PVDF films were created using a solvent casting technique in DMSO solvent.

Keywords: biocompatible, electrode, PVDF, HA, $AGNO_3$, d_{33}, piezoelectric, solvent casting.

1. Introduction

Polymer composites and ceramics are used to create biosensors. Ceramics are typically combined with polymers to compensate for mechanical weakness, brittleness, and poor strength or bending.

Low elasticity, low density, low dielectric constant, and low acoustic and mechanical resistance are among the pertinent polymer properties that enhance the sensitivity to high voltage, making them ideal for sensor characteristics. Polymers typically exhibit high field strength and high dielectric degradation. Piezoelectric polymers have excellent applications in technical and engineering fields as well as in a variety of device configurations due to these properties.

Identifying different molecules of microorganisms or biological structures is possible using piezoelectric biosensors. A wide range of materials with good acoustic velocity are used to create piezoelectric biosensors. Piezoelectric sensors are known for their low detection limit, excellent linear response, and good reproducibility. Piezoelectric biosensors are useful for tracking a variety of particular biological processes, including genetic hybridization, which may reveal details about the kinetics of the reaction [2].

In recent times, a multitude of biosensors have surfaced that utilize biocompatible piezoelectric materials. It is possible to incorporate these biological sensors into biological systems. To avoid the toxicity of traditional lead-containing piezoelectric materials, new materials and cutting-edge technologies have been used to develop modern piezoelectric biosensors. There exist biocompatible piezoelectric materials. This could lead to a new era in engineering or medicine in the field of piezoelectric materials and microsystems. Ion shift within the crystals is the basis for piezoelectricity in inorganic materials. A dipole moment is created when a voltage is applied to a piezoelectric material because the crystalline structure of the material changes, shifting the ionic equilibrium within the structure [4, 5].

Piezoelectric materials are sensitive to external stimuli because of their good mechanical and flexible qualities, which is crucial for a variety of medical devices. An important characteristic that makes medical sensors near internal organs useful is their high degree of flexibility.

The following are common measurements made with biosensors and sensors: wrist pulse, hand, joint, cord, pulse, respiration, human voice, breath, pulse, heartbeat, and food swallowing detection, as well as pressure on the brain or eyes. In engineering, electronics, materials science, and other fields, it is also widely used [2].

Its use is limited by the brittleness and low flexural strength of hydroxyapatite. In order to counteract HA's mechanical weakness, several formulas involving HA and polymer composites have been developed. Because there is so much HA in the composition as a whole, HA / polymer composites have excellent biocompatibility.

PVDF films with a high phase content of *β*-phase up to 98.8% are obtained using dimethyl sulfoxide (DMSO) as the solvent in optimized by crystallization [6]. The PVDF film was annealed at 90 °C for 5 hours, according to the XRD curve, during this annealing, the *β*-phase peak is the largest. The same polar solvent can form all three phases of PVDF. When the solution temperature using the polar DMSO solvent, different phases of PVDF can be obtained. The annealing conditions lead to the presence of different phases and the transformation of one phase to another PVDF phase. The *β*-phase, which is important for ferroelectric applications, is obtained using a polar solvent and appropriate annealing. The maximum *β* phase in the films exists when the PVDF films are annealed at 90 °C for 5 h. [7].

Author Jinwoo Choi's PVDF films were prepared using a conventional rod-coating technique. Consequently, the concentrations of BOD and water were mixed with DMF and then heated at 100 °C for 9 h. After cooling to room temperature, PVDF at a concentration of 10 wt% was added to the solution and further heated at 60 °C for 2 h. Finally, PVDF films were prepared using a rod coating technique at around 100 °C. The prepared PVDF/BDS solution was stable and could be stored for a long time without changing the morphology and quality of the films obtained [3].

β-phase PVDF films were prepared by simply casting from a PVDF solution containing a small amount of BOD and water, where H_2SO_3 is generated in situ during the thermal decomposition process and is spontaneously removed during the coating process. H_2SO_3 effectively induced a large β phase in PVDF (β = 95%). Thus, PVDFBDS films exhibited excellent ferroelectric and piezoelectric properties without mechanical stretching or an extensive thermal annealing process. The author's simple and efficient preparation method for β PVDF is promising for a wide range of applications, including various electrical devices, energy harvesters, electrochemical sensors, and transducers [3].

The β phase with all trans conformations (TTTT) has the highest piezoelectric properties. Polymeric fibers are prepared with a polymer solution that rearranges the molecules into the trans conformation. Many studies have investigated different enhancement parameters of the β phase and piezoelectric properties of PVDF fibers, for example, decreasing the evaporation rate increases the amount of β phase [8].

It is noted that the β-phase becomes the main phase in the PVDF film cast from the DMSO solvent, corresponding to the obvious β peak. Diffraction data show that β-phase trends in PVDF films when cast from a solvent with higher dipole moment. The β-phase transition involves the transformation of the molecular chain into the TTTT conformation from the initial α-phase conformation (TGTG) in the PVDF film [6]

The effect of annealing on the transformation of γ-phase PVDF to β and α-phase PVDF was presented by S. Satapathy. PVDF films were annealed at 90 °C in DMSO for 5 hours. Through this annealing process, the PVDF film contains β-phases condition. Author S. Satapathy results of, it is evident that in the PVDF film under annealing conditions 70°C for 5 h corresponds to the β and α phases, respectively. Therefore, under this annealing condition, both β and α phases are contained in a PVDF film. The presence of both β and α-phase in PVDF films when it is annealed. A temperature of 110°C and annealing for 5 hours are also confirmed. When PVDF films are annealed at 130 °C for 5 hours, they shows a decrease and an increase in the values of β-phases in the α-phase content.

PVDF has advantages such as high β phase and suitability for a thin film process. However, PVDF copolymers easily lose ferroelectricity at higher temperatures, as indicated by the Curie temperature. Recently, enhancement of the β-phase by organic/inorganic additives has also been investigated. In this aspect, the method of β-rich pure PVDF is in high demand [3].

The addition of a conductive phase, such as silver, can be beneficial for several reasons. The conductive phase improves charge transfer by increasing the sensitivity of the piezoelectric response. Additionally, the addition of the conductive phase can create a local electric field and inductive charges until the polishing process is complete [8].

2. Preparation process and results

As a result, was chosen Sol Gel method of preparation. The solvent casting method is a very good and efficient way to change the PVDF phase. DMSO was chosen as the solvent because it is biocompatibility and is very suitable for all components.

The result, which presented Xiongjie Li, confirmed that a higher solvent dipole moment is more beneficial for the β-phase formation of the phase in PVDF films. PVDF films with a high β phase content of up to 98.8% are obtained using dimethyl sulfoxide (DMSO) as a solvent at an optimized crystallization temperature of 60°C.

The effect of annealing on the transformation of γ-phase PVDF to β and α-phase PVDF was presented by S. Satapathy. PVDF films were annealed at 90 °C in DMSO for 5 hours.

Dimethylsulfoxide (DMSO) was used as a solvent to create films, and the ideal temperature is 90 °C. First, the DMSO solvent and PVDF beads were combined, and then the mixture was dissolved for four hours at 90 °C to create a homogenous solution. Moreover, room temperature DMSO solvent was used to disperse and mix silver nitrate and hydroxyapatite until they were completely dissolved or distributed. After mixing all ingredients and pouring them onto the base, the film is formed using forming rods and baked for four hours at 60 degrees Celsius. Figure 1 represents the entire preparation procedure.

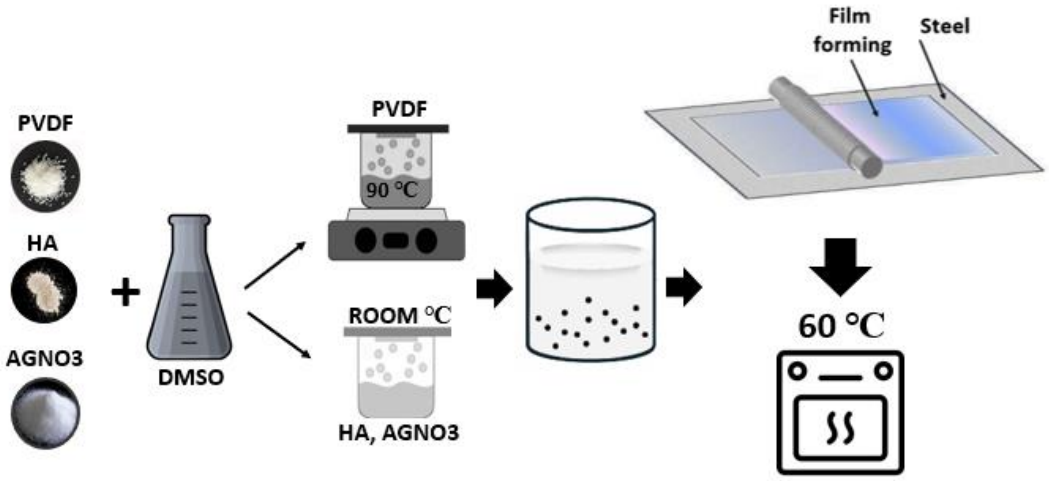

Fig. 1 Preparation of the thin film by, solvent casting method

In Figure 2 composite samples made on steel background. 1. PVDF/0.05HA, 2. PVDF/0.1HA, 3. PVDF/$AgNO_3$, 4. PVDF/HA/$AgNO_3$, 5. PVDF. All components were prepared separately and after thar was mixed together: sample 1: 0.5 g. PVDF in 2 ml. DMSO, 0.05 g. HA in 1 ml. DMSO, sample 2: 0.5 g. PVDF in 2 ml. DMSO, 0.1 g. HA in 1 ml. DMSO, sample 3: 0.5 g. PVDF in 2 ml. DMSO, 0.2 g. $AgNO_3$ in 1 ml. DMSO, sample 4: 0.5 g. PVDF in 2 ml. DMSO, 0.2 g. $AgNO_3$ in 1 ml. DMSO, 0.05 g. HA in 1 ml DMSO, sample 4: 0.5 g. PVDF in 2 ml. DMSO.

Fig. 2 Samples on steel electrode

The samples were morphologically examined using SEM, and the resulting images are shown in Figure 3. As a result, Example 1 captures the growth of HA on PVDF. The similarity of the images of examples 1 and 2 can be explained by their similar composition. It should be emphasized that despite the fact that sample 3 was prepared with a small amount of $AgNO_3$, in this case the penetration of $AgNO_3$ was satisfactory because the particles were evenly distributed throughout the skeleton. The particle size of the cores of sample 4 was smaller due to the $AgNO_3$, PVDF, and HA composites. Sample 5 shows the excellent transformation of PVDF to the beta phase after synthesis.

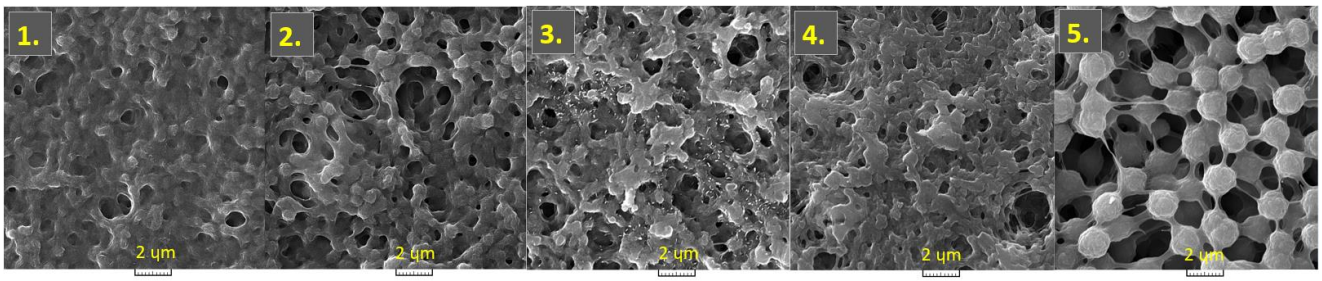

Fig. 3 SEM analysis of samples. 1. PVDF/0.05HA, 2. PVDF/0.1HA, 3. PVDF/$AgNO_3$, 4. PVDF/HA/AgNO3, 5. PVDF

PVDF-based thin films were prepared on previous studies from DMSO solvent at 90 °C. Granular (flake) PVDF was

dissolved in DMSO solvent, HA and $AgNO_3$ were dispersed in DMSO solvent at room temperature and mixed to a homogeneous mass. The solutions are poured together and evenly mixed and poured at room temperature on a metal base, an electrode. The films are dried at a temperature of 60 °C for about 3-4 hours.

For film metering, d_{33} was set to "x0.1" mode. The knob adjusts the distances between the two hemispherical probes to hold the sample firmly enough but not too tightly, to prevent damage to the sample. The meter shows the d_{33} value of the samples, which you can see in Figure 4. The values of meter displayed as d_{33} (A). Then was turned sample 180° and measure the sample again (opposite polling direction). The meter showed opposite polarization and d_{33} (B) values. Positive and negative results should be very close, in another case need to adjust the knob to get correct values. It is difficult to be quantitative for soft polymer film. This is reason why need measured results are qualitative and use the meter to compare different samples with similar thicknesses for comparison purpose.

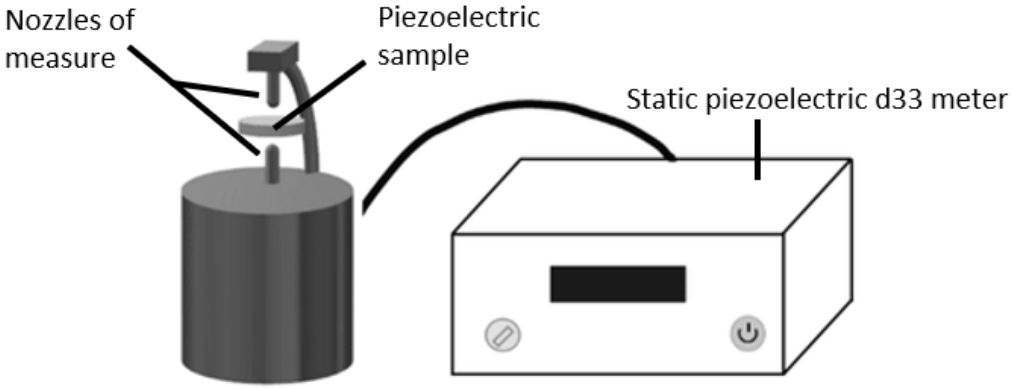

Fig. 4 Schematic of piezoelectric constant d_{33} by Polyk Quasi Satic Piezoelectric d_{33} Meter

The constant d_{33} was measured using a Polyk Quasi Satic Piezoelectric d_{33} Meter. The Polyk d_{33} meter is a special instrument for directly measuring the piezoelectric constant d_{33} values of piezoelectric ceramics, polymers and single crystals. It can also measure the d_{33} value in a very wide range with high resolution and high reliability. Specimens of various sizes and shapes can be easily accommodated and measured. In Figure 2 are presenting the schematic of the test with d_{33} piezoelectric static meter.

Figure 5 shows piezoelectric results. Each sample was measured in the range of forces [2-4 N]. The piezoelectric gauge showed the lowest result for the PVDF sample, which is 5.6 pC/N at a force 2 N and continuously decreased. The best results were shown for the PVDF/HA samples, which are 8.8-9 pC/N with a force of 2 N and continuously decreased. The PVDF/HA/$AgNO_3$ sample also shows good results with a d_{33} constant of 8.3 pC/N at 2 N force. We also see a trend that decrease change is found to be slower in the presence of impurities in the film. The addition of the component HA improves the d_{33} constant and reduces the chance of variation. The best results are obtained at a force load of 2 N in all samples.

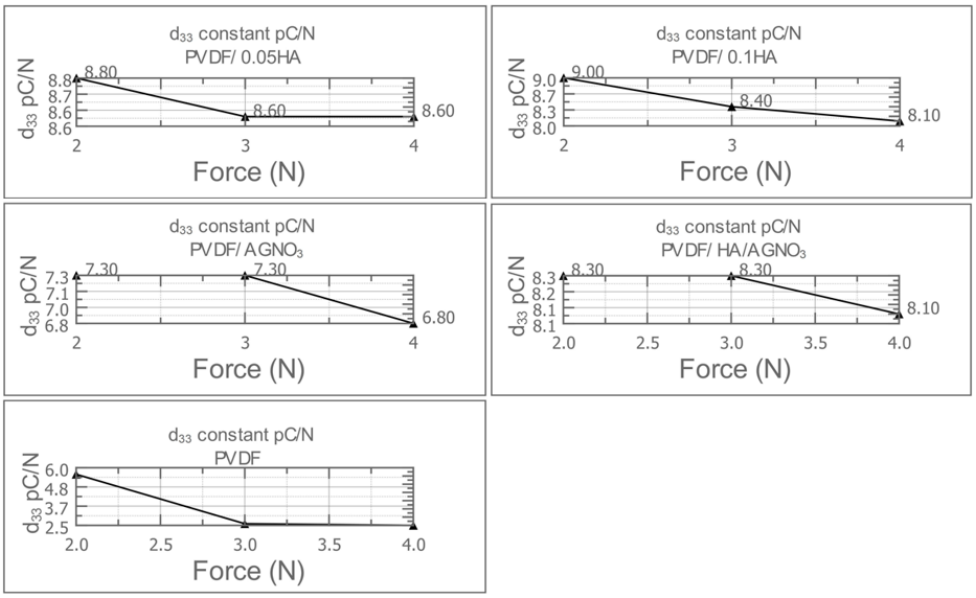

Fig. 5 Dependence of constant d_{33} on static force

4. Conclusions

Due to its well-known excellent ferroelectric characteristics, mechanical properties, flexibility, and biocompatibility, polyvinylidene fluoride (PVDF) polymer was chosen to develop the functional element. In addition, silver nitrate and hydroxyapatite were selected for their suitability for biosensors and their innovation and piezoelectric properties. The non-toxic solvent DMSO and the solvent casting method were chosen for the preparation of the thin film.

The annealing conditions lead to the presence of different phases and the transformation of one phase to another PVDF phase. Because PVDF is in crystalline form and the molecular chains can move freely without a fixed structure, negatively affects the electrical properties, it was necessary to create an amorphous phase for this study.

According to the SEM images, the swelling occurs when the solvent penetrates the amorphous region of PVDF, leaving the crystalline region essentially passive. 5 different concentration samples were made: (1) PVDF/0.05HA, (2) PVDF/0.1HA, (3) PVDF/$AgNO_3$, (4) PVDF/HA/$AgNO_3$, (5) PVDF.

Therefore, the SEM images of samples 1, 2, 3, 4, and 5 show the presence of vaporized DMSO in the pores. The right temperature induces PVDF to form the β phase.

For the PVDF sample (5), the piezoelectric meter yielded the lowest result, 5.6 pC/N at a force of 2 N, which decreased steadily. Samples with PVDF/0.05 HA (1) and PVDF/0.1 HA (2) showed the best results, ranging from 8.8 to 9 pC / N at a force of 2 N and gradually decreasing. Good results are also shown by sample PVDF/HA/$AgNO_3$, where the constant d_{33} at a force of 2 N is 8.3 pC/N. The 2 N of force of the force load that produces the best results. The developed piezoelectric composite material can be used in flexible electronic devices for sensing purposes.

References

1. Liuxia Ruan; Xiannian Yao; Yufang Chang; Liaqun Zhou; Gaowu Qin; Xianmin Zhang. Properties and Applications of the β Phase Poly(vinylidene fluoride). *Polymers* **2018**, 10(3): 228. Available online: https://www.ncbi.nlm.nih.gov/pmc/articles/PMC6415445/
2. Zaszczynska A.; Gradys A.; Sajkiewicz P. Progress in the Applications of Smart Piezoelectric Materials for Medical Devices. *Polymers* **2020**, 12(11), 2754.
3. Jinwoo Choi; Kyuho Lee; Minhwan Lee; Taebin Kim; Sangwon Eom; Jae Hyun Sim; Won Bo LEE; Yongjoo Kim; Cheolmin Park; Youngjong Kang. High β-phase Poly(vinylidene fluoride) Using a Thermally Decomposable Molecular Splint. *Advanced Electronic Materials* **2022**, Volume 9, Issue 1, 2200279. Available online: https://onlinelibrary.wiley.com/doi/full/10.1002/aelm.202200279
4. Scheller F.; Schubert F. Biosensors. *Elvesier* **1992**.
5. Hummady M.; Campitelli A.; Wlodarski W. Acoustic wave sensors:design, sensing mechanisms and applications. Smart Materials and Structures, 197, Volume 6, Number 6, 647. Available online: https://iopscience.iop.org/article/10.1088/0964-1726/6/6/001/pdf.
6. Li X.; He T. Hu Q.;Yang Y. Preparation of PVDF flexible piezoelectric film with high β-phase content by matching solvent dipole moment and crystallization temperature. *Journal of Materials Science: Materials in Electronics*, **2018**, 30 20174-20180. Available online: https://link.springer.com/article/10.1007/s10854-019-02400-y.
7. Satapathy S.; Pawar S.; Gupta P. K.; Varma K. B. R. Effect of annealing on phase transition in poly(vinylidene fluoride) films prepared using polar solvent. Laser Materials Development and Devices Division, Raja Ramanna Centre for Advanced Technology **2010**. Available online: https://www.ias.ac.in/article/fulltext/boms/034/04/0727-0733.
8. Dashtizad S.; Alizadeh P.; Yourdkhani A. Improving piezoelectric properties of PVDF fibers by compositing with BaTiO3-Ag particles prepared by sol-gel method and photochemical reaction. *Journal of Alloys and Compound* **2021**. Volume 883 160810. Available online: https://www.sciencedirect.com/science/article/abs/pii/S0925838821022192.

Optimum Carbon Fibre Reinforced Polymer (CFRP) Design for Increasing Shear Capacity of Reinforced Concrete Beams Using Grey Wolf and Archimedes Optimization Algorithm

Yaren AYDIN[1]*, Gebrail BEKDAŞ[1]*, Sinan Melih NİGDELİ[1]*

1 Istanbul University-Cerrahpaşa, Civil Engineering Department, 34320 Avcılar, Istanbul, Turkey
** yaren.aydin1@ogr.iuc.edu.tr; bekdas@iuc.edu.tr; melihnig@iuc.edu.tr*

Abstract

The main objective in an engineering design is to find the best result that provides both factors of safety and economy. Due to that, optimization is a required process as an engineering problem that has various design variables and is constrained via safety factors. One of the methods that can be applied in order to provide safety against principal tensile stresses resulting from shear forces and bending moments in reinforced concrete structures is to increase the shear capacity with carbon fibre reinforced polymer (CFRP) strip application in this study, the optimum design of carbon fibre reinforced polymer (CFRP) for increasing the shear capacity of reinforced concrete beams is carried out with two different metaheuristic algorithms. The metaheuristic algorithms used are Grey Wolf Optimization (GWO) algorithm and Archimedes Optimization Algorithm Then, the results of different methods were compared. Optimum results were obtained with AOA.

Keywords: reinforced concrete beams, metaheuristic algorithms, grey wolf, archimedes, cost optimization.

1. Introduction

In reinforced concrete structures, shear reinforcements (stirrups) are used to provide safety against the principal tensile stresses resulting from shear forces and bending moments. It may be necessary to increase the cross-sectional shear capacities of structural elements due to reasons such as increasing the cross-sectional capacity in meeting the forces caused by earthquakes, i.e. strengthening work, changing the intended use of the existing building or expanding the area. One of the methods that can be applied in this case is sheathing. Since the weight and stiffness of the section strengthened by sheathing increases, the design analysis should be performed again and the internal forces of the section should be obtained again according to the strengthened condition [1].

Another method that can be applied is to increase the shear capacity with carbon fibre reinforced polymer (CFRP) strip application. Compared to the first method, when CFRP is used in the structure, the shear capacity increases while the weight and stiffness of the section remain the same. In addition, the advantages of the method are that CFRP is easy to apply and has linear deformation behaviour with a large stress capacity. Thus, it may not be necessary to analyse the structural design repeatedly [1]. This study aims to find the best CFRP design in order to increase the shear capacity of T-section beams with effective strain d and width b_w. For this reason, Grey Wolf Optimization (GWO) algorithm and Archimedes Optimization Algorithm (AOA) were used as metaheuristic algorithms.

Optimization is the process of determining the most appropriate solutions to a problem, event or situation, or demonstrating the best performance for such elements [2]. Algorithms that solve optimization problems are optimization algorithms. Metaheuristic algorithms, a type of these algorithms, are used for nonlinear modelling and optimization problems [3]. These algorithms are also effective in the area of structural engineering. In order to find the best solution, new algorithms have been proposed and modified ones have been improved.

GWO is used in various fields such as economic dispatch [4], building energy optimization [5], task scheduling in cloud-fog computing [6]. AOA is used in various fields optimization of a cantilever beam [7], effective design of hybrid renewable energy system [8], optimization of tuned mass damper [9], parameter identification of solar cells [10], truss system optimization [11], feature selection [12] etc. too.

In this study, the Grey Wolf Optimization (GWO) algorithm and the Archimedes Optimization Algorithm (AOA) optimization algorithm are used and compared. The algorithms are briefly described in the paper as seen in the following sections. Each of these algorithms has its own parameters, so these unique features of the algorithms are the main reason to choose these algorithms. Varying these parameters differentiates the local and global search capabilities of the algorithm. According to the results, the algorithms are compared and their performances are evaluated for optimum carbon fibre reinforced polymer (CFRP) design for increasing the shear capacity of reinforced concrete beams.

2. Methodology

2.1 Optimum Carbon Fibre Reinforced Polymer (CFRP) Design with Grey Wolf Optimization (GWO) Algorithm

Grey Wolf Optimization (GWO) was developed by Mirjalili et al. in 2014 [4], inspired by the hunting behaviour of grey wolves in nature and the concept of leadership hierarchy. In the hierarchy, three wolves are identified as alpha (α) (first leader), beta (β) (deputy) and delta (δ) (relaying orders from beta), which control the progress in a pack. The remaining

wolves are called omega wolves (ω) and are the weakest wolves in the pack. To qualify the algorithm as an optimization, a group hunt performed by the wolves is highlighted. First, the group leaders are identified. After identifying their prey, the wolves follow and eventually surround their prey. Meanwhile, the distance ($\vec{D}$) of the prey to the surrounding wolf is given by Equation (1). In addition, each wolf can randomly change its position around its prey as in Equation (2). Here $X_{i,new}$, $X_{i,p}$, and $X_{i,j}$ are the new value, the initial matrix value of the p-th (prey) and j-th (ω) candidate solution, respectively; it is a coefficient factor, a vector describing the state in which the wolf attacks its prey, a vector affecting the prey-gray wolf distance, t is the number of available iterations [5].

$$\vec{D} = \left|\vec{C}X_{i,p} - \left|X_{i,j}\right|\right| \tag{1}$$

$$X_{i,new} = X_{i,p} - \vec{A}\vec{D} \tag{2}$$

$$\vec{C} = 2rand() \tag{3}$$

$$\vec{A} = 2\vec{a}rand() - \vec{a} \tag{4}$$

$$\vec{a} = 2 - 2\frac{t}{stopping\ criteria} \tag{5}$$

After the encirclement, the attack takes place, but the knowledge of the leader wolves is required for this to be successful. The distances of wolves α, β and δ to their prey and the new positions of each of them can be described by Equations 6-8 and 9-11 respectively. The updated final position of the current solution is expressed by Equation 12 (Mirjalili et al., 2014):

$$\overrightarrow{D_\alpha} = \left|\overrightarrow{C_1}X_{i,a} - X_{i,j}\right| \tag{6}$$

$$\overrightarrow{D_\beta} = \left|\overrightarrow{C_2}X_{i,\beta} - X_{i,j}\right| \tag{7}$$

$$\overrightarrow{D_\delta} = \left|\overrightarrow{C_2}X_{i,\delta} - X_{i,j}\right| \tag{8}$$

$$X_{i,\alpha_{new}} = X_{i,\alpha} - \overrightarrow{A_1}\,\overrightarrow{D_\alpha} \tag{9}$$

$$X_{i,\alpha_{new}} = X_{i,\beta} - \overrightarrow{A_2}\,\overrightarrow{D_\beta} \tag{10}$$

$$X_{i,\alpha_{new}} = X_{i,\delta} - \overrightarrow{A_3}\,\overrightarrow{D_\delta} \tag{11}$$

$$X_{i,new} = \frac{X_{i,\alpha_{new}} + X_{i,\beta_{new}} + X_{i,\delta_{new}}}{3} \tag{12}$$

Eventually, finding the new position, the grey wolf attacks its prey. wolves' incentive to approach their prey decreases. In parallel, it is also modified and the rule expressing the realisation of the attack takes the form of Equation 13 [4].

$$X_{i,new} = \left\{\left|\vec{A}\right| < 1, X_{i,p}\right. \tag{13}$$

2.2. Optimum Carbon Fibre Reinforced Polymer (CFRP) Design with Archimedes Optimization Algorithm (AOA)

Archimedes Optimization Algorithm (AOA) is a population-based meta-heuristic algorithm recently developed by Hashim et al. and it is based on a law of physics that is Archimedes' principle. Archimedes' principle is about the law of buoyancy and it states that buoyancy is equal to the weight of the liquid displaced by the sinking body [6]. The algorithm can be described via the following processes:

The O_i presented in Equation (14) are the random solutions of the ith dimension of the ith object. and are the lower and upper bounds of the search space. The initial density (den_i) and volume (vol_i) of each ith object are initialized randomly. Each i. The initial acceleration of the object (acc_i) can be defined by the same calculation as Equation 14, as shown in Equation 15.

$$O_i = lb_i + rand \times (ub_i - lb_i); \quad i = 1,2,\dots,N \tag{14}$$

$$acc_i = lb_i + rand \times ((ub_i - lb_i) \tag{15}$$

Using the initial solutions, the fitness function can be calculated and the best solution (x_{best}), density (den_{best}), volume (vol_{best}) and acceleration (acc_{best}) can be obtained. Updating densities and volumes (Equation 16 and Equation 17):

$$den_i^{t+1} = den_i^t + rand \times (den_{beest} - den_i^t) \tag{16}$$

$$vol_i^{t+1} = vol_i^t + rand \times (vol_{beest} - vol_i^t) \tag{17}$$

The transfer operator (TF) refers to the transition of objects from the discovery phase to the exploitation phase. Here TF gradually increases with time until it reaches the current number of iterations. The density reduction factor (d) helps the algorithm in the global-to-local search.

If TF ≤ 0.5, collisions occur between objects (exploration phase),

$$acc_i^{t+1} = \frac{den_{mr}+vol_{mr}\times acc_{mr}}{den_i^{t+1}\times vol_i^{t+1}} \tag{18}$$

In Equation 18, acc_{mr}, den_{mr} and mol_{vr} are the acceleration, density and volume of the randomly selected object. If TF > 0.5, there is no collision between objects (Use phase). The normalization acceleration is the percentage of the step followed by each object in Equation 19.

$$acc_{i-norm}^{t+1} = u \times \frac{acc_i^{t+1}-\min(acc)}{\max(acc)-\min(acc)} \tag{19}$$

Updating the position: If TF ≤ 0.5, the position of the ith object is shown in Equation 20.

$$x_i^{t+1} = x_i^t + C_1 \times rand \times acc_{i-norm}^{t+1} \times d \times (x_r - x_i^t) \tag{20}$$

If TF ≤ 0.5, the position of the ith object is shown in Equation 8.

$$x_i^{t+1} = x_{best}^t + F \times C_2 \times rand \times acc_{i-norm}^{t+1} \times d \times (T \times x_{best} - x_i^t) \tag{21}$$

In Equations 20 and 21; C_1, C_2, C_3 and C_4 are constants. In Equation 22, F is the flag that changes the direction of movement, and Equation 23 is used to calculate P:

$$F = \begin{cases} +1 \; if \; P \le 0.5 \\ -1 \; if \; P > 0.5 \end{cases} \tag{22}$$

$$P = 2 \times rand - C_4 \tag{23}$$

For all algorithms here, the process is terminated when the maximum iteration is reached, if the maximum iteration is not reached, all operations are repeated.

3. Numerical Example

Optimization aims to minimize the total CFRP area used in 1 meter, and for this purpose, design variables wf (mm) are defined as CFRP width, s_f (mm) are CFRP spacing and β (º) is defined as CFRP angle. Design variables can be seen in Figure 1. The d_f expression in the figure shows the depth of the reinforced concrete element covered with CFRP and can be expressed as a mathematical equation with Equation 24 [1].

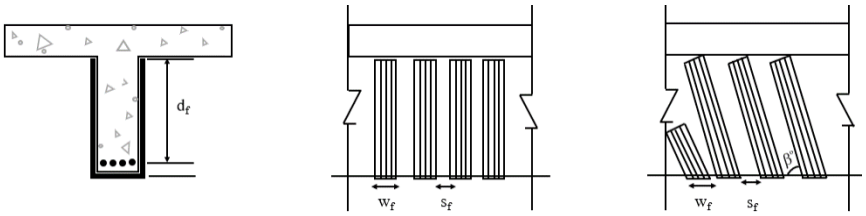

Fig. 1 Beaam and CFRP details and sections

$$d_f = d - h_f \tag{24}$$

h_f here shows the thickness of the reinforced concrete slab. On the other hand, as mentioned before, the objective function related to minimizing the CFRP area (fx) at 1 meter is expressed in Equation 25. The expression b in Equation 25 indicates the effective width of the floor.

$$Area = \; f(x) = \frac{w_f(\frac{2d_f}{sin\beta}+b)}{s_f} \times 1000 \tag{25}$$

The lower and upper variables, that is, the ranges, of the design variables to be optimized are located between Equation 26 and Equation 28.

The constraint functions to be taken into account in the design problem are specified in Equation 29, Equation 30 and Equation 31 and are calculated taking into account ACI 318-05 [16] (Building Code Requirements for Structural Concrete and Commentary).

$$g_1(x): s_f \le \frac{d}{4} \tag{29}$$

$$g_2(x): V_{ek} < 0.7R\frac{(2t_f w_f f_{fe})(sin\beta+cos\beta)d_f}{s_f+w_f} \tag{30}$$

$$g_3(x): V_{ek} < 0.7R\frac{(2t_f w_f f_{fe})(sin\beta+cos\beta)d_f}{s_f+w_f} \le \frac{2\sqrt{f_c}b_w d}{3} - V_s \tag{31}$$

The design constants and their values seen in the equations are explained in Table 1. The values in the table were used in the numerical example considered for the optimization process.

Table 1. Design constants and values of the problem

	Symbol	Unit	Value
Body width of the beam	b_w	mm	200
Beam height	h	mm	500
Effective depth	d	mm	450
CFRP thickness	t_f	mm	0.165
Reduction factor	R	-	0.5
Slab thickness	h_f	mm	100
Compressive strength of concrete	f'_c	Mpa	20
Effective tensile strength of CFRP	f_{fe}	Mpa	3790
Additional sliding capacity	V_{ek}	N	50000
Shear capacity of stirrup	V_s	N	50000

Statistical results such as standard deviations, mean and minimum values were used in all studies to evaluate the quality of the solutions. When the results obtained in Table 2 are examined, it is seen that AOA and GWO algorithms give almost the same minimum value and average value in cost optimization. However, the standard deviation is lower in the GWO algorithm. The number of iterations shown in Table 2 is the number of iterations in which the optimum value was found. The number of iterations in which the AOA algorithm finds the optimum value is less than the GWO algorithm. This shows that the AOA algorithm is faster. AOA reached the optimum point in cost optimization very quickly compared to the GWO algorithm in approximately 3880 iterations.

4. Results

The optimization process was executed 20 times, each running for 40,000 iterations. Table 2 shows the standard deviations, averages, and minimum values of the optimized objective function, along with the number of iterations at which the optimal value was achieved for the algorithms.

Table 2. Results obtained with algorithms

Algorithm	Minimum value	Mean value	Standard deviation	Iteration number
GWO	2.3882e+05	2.3954e+05	1.1457e+03	10427
AOA	2.3881e+05	2.4068e+05	1.3337e+05	3880

5. Conclusions

In general, these two compared algorithms are successful. Although the algorithms show very close performance in finding the values, the number of iterations they find should also be controlled, since the speed of finding the minimum value is an important factor in solving large optimization problems. Comparing the performance of AOA and GWO algorithm, the results show that AOA has a faster convergence ability and tries to find a relatively better optimal solution. This is because AOA has a good balance between exploration and exploitation.

References

1. Bekdaş G., Nigdeli S.M., Yüel, M., & Kayabekir A.E. (**2021**) Artificial Intelligence Optimization Algorithms and Engineering Applications. Seçkin Publishing.
2. Smith, T.F., Waterman, M.S.: Identification of Common Molecular Subsequences. J. Mol. Biol. 147, 195--197 (**1981**)
3. Gandomi, A. H., Yang, X. S., Talatahari, S., & Alavi, A. H. (**2013**). Metaheuristic algorithms in modeling and optimization. Metaheuristic applications in structures and infrastructures, 1.
4. Jayabarathi, T., Raghunathan, T., Adarsh, B. R., & Suganthan, P. N. (**2016**). Economic dispatch using hybrid grey wolf optimizer. Energy, 111, 630-641. https://doi.org/10.1016/j.energy.2016.05.105
5. Ghalambaz, M., Yengejeh, R. J., & Davami, A. H. (**2021**). Building energy optimization using grey wolf optimizer (GWO). Case Studies in Thermal Engineering, 27, 101250. https://doi.org/10.1016/j.csite.2021.101250
6. Saif, F. A., Latip, R., Hanapi, Z. M., & Shafinah, K. (**2023**). Multi-objective grey wolf optimizer algorithm for task scheduling in cloud-fog computing. IEEE Access, 11, 20635-20646. https://doi.org/10.1109/ACCESS.2023.3241240
7. Aydin, Y., Nigdeli, S.M., Bekdaş, G. (**2023**). Archimedes Optimization Algorithm on a Structural Optimization Problem. In: Vasant, P., et al. Intelligent Computing and Optimization. ICO 2023. Lecture Notes in Networks and Systems, vol 854. Springer, Cham. https://doi.org/10.1007/978-3-031-50151-7_17
8. Kharrich, M., Selim, A., Kamel, S., & Kim, J. (**2023**). An effective design of hybrid renewable energy system using an improved Archimedes Optimization Algorithm: A case study of Farafra, Egypt. Energy Conversion and Management, 283, 116907. https://doi.org/10.1016/j.enconman.2023.116907
9. Aydin, Y., Nigdeli, S. M., & Bekdaş, G. (**2024**). Archimedes Optimization Algorithm for Optimization of Tuned Mass Dampers in Structural Control. Available at SSRN 4750319. http://dx.doi.org/10.2139/ssrn.4750319
10. Krishnan, H., Islam, M. S., Ahmad, M. A., & Rashid, M. I. M. (**2023**). Parameter identification of solar cells using improved Archimedes Optimization Algorithm. Optik, 295, 171465. https://doi.org/10.1016/j.ijleo.2023.171465

11. Aydin, Y., Nigdeli, S. M., & Bekdaş, G. (**2024**). Parametric Investigation of Archimedes Optimization Algorithm for a Structural Problem. Available at SSRN 4750288. http://dx.doi.org/10.2139/ssrn.4750288
12. Mengash, H. A., Alruwais, N., Kouki, F., Singla, C., Abd Elhameed, E. S., & Mahmud, A. (**2023**). Archimedes Optimization Algorithm-Based Feature Selection with Hybrid Deep-Learning-Based Churn Prediction in Telecom Industries. Biomimetics, 9(1), 1. https://doi.org/10.3390/biomimetics9010001
13. Mirjalili, S., Mirjalili, S. M., & Lewis, A. (**2014**). Grey wolf optimizer. Advances in engineering software, 69, 46-61.
14. Faris, H., Aljarah, I., Al-Betar, M. A., & Mirjalili, S. (**2018**). Grey wolf optimizer: a review of recent variants and applications. Neural computing and applications, 30, 413-435.
15. Hashim, F.A., Hussain, K., Houssein, E.H. et al. Archimedes optimization algorithm: a new metaheuristic algorithm for solving optimization problems. Appl Intell 51, 1531–1551 (**2021**). https://doi.org/10.1007/s10489-020-01893-z
16. ACI Committee. (**2005**). Building code requirements for structural concrete (ACI 318-05) and commentary (ACI 318R-05). American Concrete Institute.

Seismic Performance Assessment of an Irregular Plan Shape Retrofitted Masonry Building

Baris GUNES[1], Kamran SAMADI[2], Baris SAYIN[1*]

1 Department of Civil Engineering, Istanbul University-Cerrahpasa, 34320, Istanbul, Türkiye
2 Institute of Graduate Sciences, Istanbul University-Cerrahpasa, Istanbul, Türkiye
** barsayin@iuc.edu.tr*

Abstract

The seismic performance of a masonry irregular plan-shaped building was determined according to the applicable seismic codes. The strengthened state of the building was considered in the analyses. A finite element model of the examined building was prepared using 3D "Solid" elements. The DAMAGE TC3D plastic material model was employed to simulate masonry member behaviors. Springs compatible with the soil investigation report data were defined to represent the foundation-soil interaction in the shallow foundations. Soil and related earthquake parameters were acquired through drilling and Multichannel Analysis of Surface Waves (MASW) studies. Subsequently, horizontal elastic design spectra were obtained for DD-2 and DD-3 earthquake ground motion levels. The building model was subjected to linear mode coupling analysis. The model was examined for three different earthquake ground motion levels/performance targets. However, the building was found to meet only the "Pre-Collapse" performance target for the DD-3 earthquake ground motion level. Analysis results indicated that the shallow foundations have sufficient soil bearing strength under static and dynamic effects.

Keywords: Seismic Analysis, Solid Model, Masonry Building, Irregular Structure, Historical building, Existing Structure, Retrofitted Structure, Foundation Performance.

1. Introduction

Today, masonry building stock requires more structural strengthening compared to reinforced concrete, steel, and composite structures, primarily due to their advancing age and brittle behavior. Various structural strengthening methods have been explored in the literature, including individual element strengthening, strengthening of the whole structural system (integrity enhancement), and seismic load reduction [1]. However, the effectiveness and practicality of these methods vary depending on several factors, such as the current status of the building, the targeted performance for a given earthquake level, and the associated costs. Furthermore, considering that some masonry buildings hold cultural and historical significance, as well as the need to preserve the touristic texture of cities, retrofitting these buildings emerges as a critical aspect of city and community management. From this perspective, some important case studies in the literature were reviewed in terms of methodology.

Marino et al. [2] examined the accuracy of nonlinear pushover analysis on existing masonry buildings with irregularity in plan and height. They focused on specific parameters such as load model, damage level, target displacements, and compared the results with those obtained through nonlinear time history analysis. In a similar study, Kalkbrenner et al. [3] showed that multidirectional pushover analysis can provide more possible collapse mechanisms and therefore, more accurate seismic behavior estimation for irregular masonry buildings without box behavior, compared to conventional pushover analysis. They applied the proposed methodology to a highly irregular masonry building in Chile and demonstrated its consistency with the findings of nonlinear dynamic analysis, as well as the damage incurred during the 2010 earthquake. Yildizlar [4] examined the seismic performance of a historic masonry building through linear, nonlinear, and kinematic analyses. The results indicated that the building did not meet target performance, vertical and lateral bending mechanisms were observed, and therefore, a retrofitting project was proposed. Cosgun et al. [5] assessed the seismic performance of a historic masonry building with a wooden slab and proposed a retrofitting project. Their results obtained from linear and nonlinear analyses indicated that the building failed in shear despite having sufficient displacement capacity.

In the current study, the seismic performance of a masonry building, that had incurred damage due to moisture and dampness, was assessed in accordance with both the current Turkey Building Seismic Code (TBEC) and the criteria outlined in the Earthquake Risk Management Guide in Historical Buildings (ERMGHB). The performance evaluation of the strengthened foundation was performed using boring and Multichannel analysis of surface waves (MASW) data. The results suggest that the dynamic linear analysis methodology is adequate in the seismic assessment of retrofitted masonry buildings with historical value. The methodology presented in this study is believed to make a contribution to the current literature.

2. Materials and Methods

2.1. Structural System Before Retrofitting

The examined building is an irregular plan-shaped masonry structure comprising 2 basement levels, 1 ground floor, 1 mezzanine, 4 standard floors, and 1 terrace floor. The floor heights are 2.2 m for the 2nd basement floor, 2.6 m for the 1st basement floor, 3.3 m for the ground floor, 2.4 m for the mezzanine floor, 3.9 m for the 1st standard floor, 3.8 m for the 2nd standard floor, 3.9 m for the 3rd standard floor, 3.9 m for the 4th standard floor, and 2.00-2.52 m for the terrace floor. It is

assumed that the existing foundation system comprises a continuous stone foundation, which is approximately 25 cm wider than the basement masonry walls in both directions and has a height of 170 cm. The vertical load-bearing system of the building was composed of masonry walls/columns and steel columns. However, steel columns were used only on ground and mezzanine floors. The building has reinforced concrete (RC) and steel beams with RC and volta slabs.

2.2. Retrofitting Project

In the retrofitting project, the installation of a 60 cm thick RC plate foundation system between the masonry foundations is proposed. The new RC slab foundation system consists of Ø18 rebars placed at both the top and bottom, with intervals of 15 cm between them. The use of Ø24 anchors is proposed to connect the existing stone foundation with the new slab. Masonry walls are strengthened on either one or both sides using textile-reinforced mortar (TRM). The existing steel beams are strengthened by welding steel plates to the beam headers. Existing RC and wooden slabs are converted to volta slabs. Furthermore, to prevent the separation of the volta slabs from the masonry walls, slabs are secured to the masonry walls using flat steels and pull rods.

2.3. Soil and Earthquake Parameters

As a result of three boreholes and a MASW study, groundwater was encountered at a depth of 8 meters. However, no liquefaction risk is anticipated for the study area. Soil and earthquake parameters, calculated from the soil investigation report or obtained from AFAD, are summarized in Table 1 [8]. The horizontal elastic design spectra for DD-2 and DD-3 earthquake ground motion levels are shown in Figure 1 for various Strength Reduction (R) and Overstrength Factors (D) [6].

Table 1. Soil and earthquake parameters

Parameter	DD-2	DD-3
PGA (g)	0.388	0.1633
PGV (cm/sec)	23.975	9.903
S_S (g)	0.947	0.374
S_1 (g)	0.262	.103
F_S	1.121	1.501
F_1	2.076	2.394
S_{DS}	1.062	0.561
S_{D1}	0.544	0.247
Local Soil Class	ZD	
Ultimate Design Strength of Structural Systems (q_t) kN/m^2	300	
Vertical Bedding Coefficient (K_S) kN/m^3	16800	

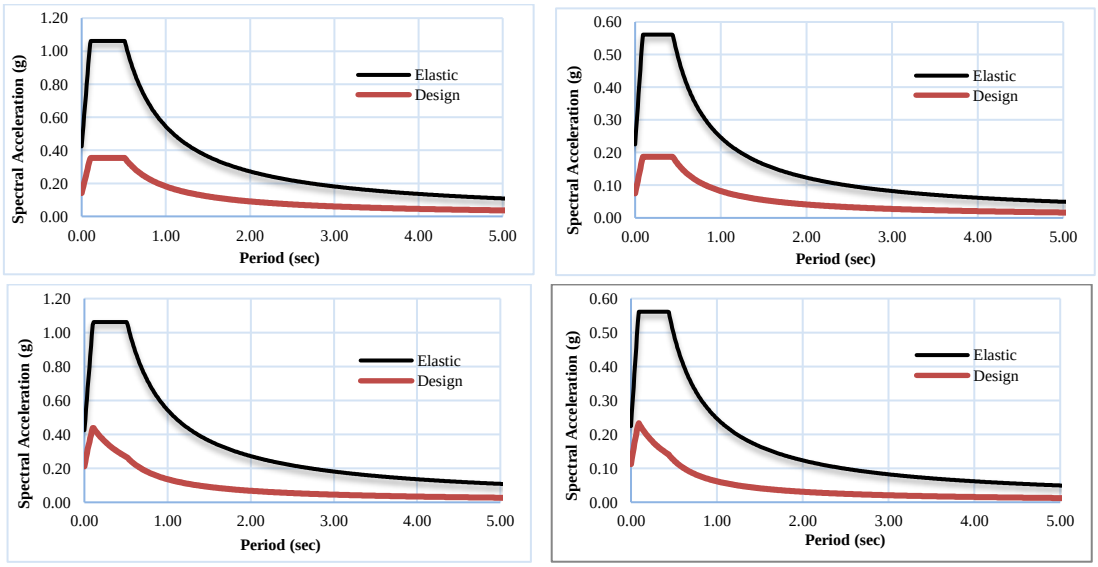

Fig. 1 Horizontal elastic design spectra for DD-2 and DD-3 earthquake ground motion levels; Top: R,D=3; Bottom: R=4, D=2

2.4. Damage Assessment

On-site inspections revealed damages such as moisture and dampness on certain bearing wall surfaces, corrosion on steel voltaic beams and slab rebars, as well as segregation and loss of spacers on RC elements.

2.5. Preparation of the Building Model

The members of the masonry structural system were modeled using 3D "Solid" elements. To represent the behavior of masonry components, the DAMAGE TC3D plastic material model was employed [9]. Mechanical properties of the masonry walls determined according to ERMGHB-2017 and/or TBEC-2018 are shown in Table 2 [6,7]. In the analysis of the strengthened state of the building, certain mechanical properties of the strengthened masonry elements were improved in accordance with the retrofitting method and applicable regulations. In the model shown in Figure 2, masonry elements, foundation components, existing steel columns and beams, and steel strengthening elements were modeled collectively. Springs compatible with the soil investigation report data were defined to represent the foundation-soil interaction in the shallow foundations. The vertical stiffness of the springs functions for both compression and tension in linear analyses, whereas it operates solely for compression in nonlinear analyses.

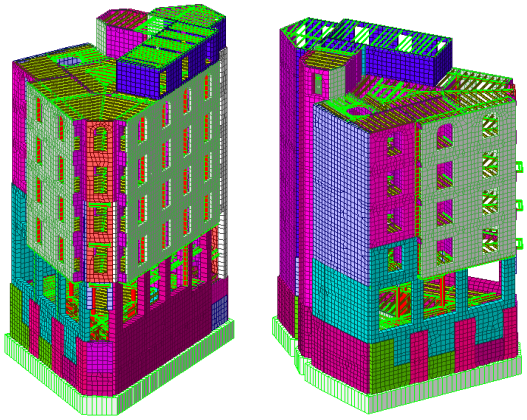

Fig. 2 3D Finite element model of the building from different perspectives

Table 2. Mechanical properties of the masonry elements

Definition	Abbreviation	Pre-strengthened	Strengthened
Masonry unit type	-	Hollow Brick	Hollow Brick
Masonry unit group	-	Group II	Group II
Unit Volume Weight, kN/m^3	-	18	18
Compressive strength of masonry unit, MPa	f_b	5.0	8.0
Compressive strength of mortar, Mpa	f_m	5.1	5.1
Characteristic compressive strength of wall, Mpa	f_k	2.8	5.0
Initial shear strength of wall, Mpa	f_{vk0}	0.1	0.18
Shear strength of wall, Mpa	f_t	0.15	0.27
Modulus of elasticity of wall, Mpa	E_{duv}	2000	3640
Shear modulus of wall, Mpa	G_{duv}	400	728

2.6. Performance Assessment Method

The principles outlined in TBEC-2018 were considered in determining the earthquake loads affecting the structure, while the principles of ERMGHB-2017 were used in determining the target performance level. [6,7]. The building model created using Midas Gen [10] finite element software was subjected to linear mode coupling analysis and the criterion of reaching 95% of the mass participation rate was found to be met for both directions. Parameters and methods related to performance assessment are summarized in Table 3.

Table 3. Parameters and methods related to performance assessment

Parameter	Value / Class
Building Use Class, BUC	3
Building Importance Coefficient, I	1.0
Earthquake Design Class, EDC	1
Building Height Class, BHC	4
Target Performance	Pre-Collapse for DD-2; Controlled Damage for DD-2; Pre-Collapse for DD-3
Design/Assessment Method	Linear Analysis, Strain-based assessment
Strength Reduction and Overstrength Factors for Steel Member Analysis	R=4, D=2
Earthquake Strength Reduction Factor for Masonry and RC Member Analysis	R_a=3
Inter-Story Drift Limits for Masonry Members	1.0% for Pre-Collapse damage; 0.7% for Controlled Damage; (R_a=1)
Building Information Level and Coefficient	Limited; 0.75

3. Results

3.1. Statistical Evaluations

Masonry structural members of the building were found to have sufficient compressive strength under statical effects (vertical loads). Besides, the impact-to-capacity ratios of the steel members in the existing and new steel beams, as well as the existing steel columns on the ground and mezzanine floors were found to be below the limit values. The calculation provided in Eq. (1) demonstrates that the soil bearing capacity of the shallow foundations exhibits adequate strength under static effects (1.4D+1.6L). Displacements in masonry members and shallow foundations under vertical loads are illustrated in Figure 3.

$$q_0 = 14\,mm \times 16800\ {}^{kN}/_{m^3} = 235\ {}^{kN}/_{m^2} \leq q_t \tag{1}$$

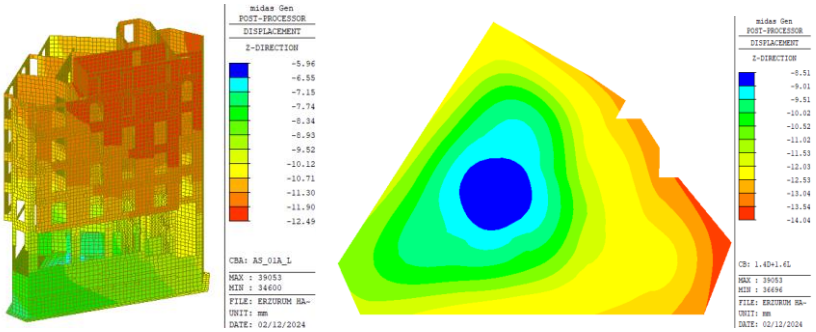

Fig. 3 Displacements in masonry members (left) shallow foundation (right) under vertical loads

3.2. Dynamic Evaluations

The seismic performance of the building was evaluated considering the "Pre-Collapse" performance target for a DD-3 class earthquake ground motion according to the criteria outlined in TBEC-2018 and ERMGHB-2017 codes.

3.2.1. Evaluation of Masonry Structural Members

3.2.1.1. Strength Checks

Shear evaluations were carried out using the finite element model under earthquake loads in the x and y directions in addition to the vertical loads. The ratios of the total shear force acting on the masonry structural members failed in shear to the total shear force in the given story are given in Table 4. These evaluations revealed that the masonry structural members meet the Pre-Collapse" (PC) performance target for a DD-3 class earthquake ground motion in terms of shear.

Table 4. Strength checks

Floor	The ratio of the total shear force carried by vertical structural members with insufficient shear capacity to the total shear force in the given story (%)			Target Performance (PC)
	Masonry	Steel	Total	
2nd Basement	0.32	-	0.32	√
1st Basement	1.94	-	1.94	√
Ground	13.73	0.00	13.73	√
Mezzanine	25.38	0.00	25.38	√
1st Standard	14.30	-	14.30	√
2nd Standard	0.00	-	0.00	√
3rd Standard	0.00	-	0.00	√
4th Standard	0.00	-	0.00	√
Terrace	2.81	-	2.81	√

3.2.1.2. Inter-story drift checks

Inter-story drift checks of the masonry structural system were performed under earthquake effects. The comparison of the inter-story drifts with the limit values corresponding to the target performance is given in Table 5. Accordingly, masonry structural members were found to satisfy the "Pre-Collapse" performance target for a DD-3 level of earthquake ground motion in terms of inter-story drifts.

Table 5. Inter-story drift checks

Floor	Displacement ΔD, (mm)		Inter-Story Drift Ratio, ΔD/H		Limit Value	Result
	x	y	%	%	%	√ / ×
2nd Basement	4.88	6.14	0.22	0.28	1.00 (PC)	√
1st Basement	6.72	7.33	0.24	0.26	1.00 (PC)	√
Ground	15.59	18.00	0.49	0.57	1.00 (PC)	√
Mezzanine	9.89	14.10	0.38	0.55	1.00 (PC)	√
1st Standard	11.85	14.59	0.31	0.38	1.00 (PC)	√
2nd Standard	9.62	13.31	0.25	0.35	1.00 (PC)	√
3rd Standard	8.84	12.63	0.23	0.33	1.00 (PC)	√
4th Standard	7.74	11.71	0.20	0.30	1.00 (PC)	√
Terrace	5.15	3.39	0.17	0.11	1.00 (PC)	√

3.2.2. Evaluation of Steel Structural Members

Strength checks of the steel structural members were carried out using the finite element model under earthquake loads in the x and y directions in addition to vertical loads. The results indicated that the steel structural members satisfy the "Pre-Collapse" performance target for a DD-3 level of earthquake ground motion. Impact-to-capacity ratios for existing steel columns, new steel beams, and existing steel beams are illustrated in Figure 4.

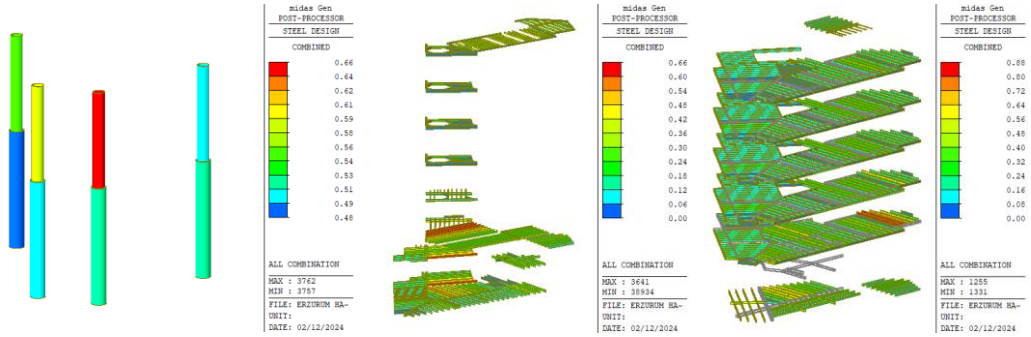

Fig. 4 Impact-to-capacity ratios for existing steel beams (left), new steel beams (middle), and existing steel columns (right)

3.2.3. Evaluation of the Foundation

Strength examinations of the new foundations were conducted under earthquake effects in addition to vertical loads. Figure 5 illustrates the envelope distributions of the bending moments in the foundation. The examinations revealed that new RC foundations meet the strength criteria for a DD-3 earthquake ground motion.

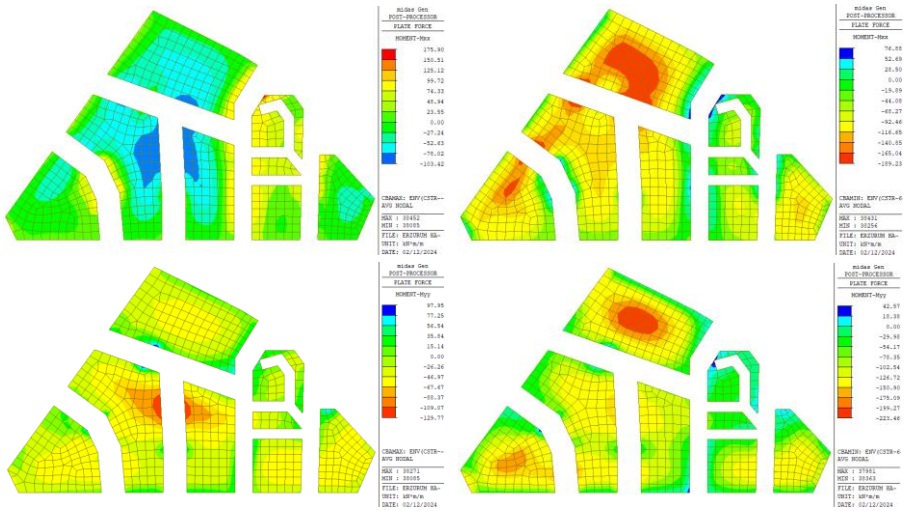

Fig. 5 Foundation moment diagrams; $M_{xx,max}$ (Upper left); $M_{xx,min}$ (Upper-right); M_{yymax} (Lower left); $M_{yy,min}$ (lower right)

3.2.4. Evaluation of shallow foundation for Soil Bearing Strength

Investigations of the foundation settlements and soil bearing capacity were carried out under earthquake effects in addition to vertical loads. The calculations shown in Eq. (2) indicated that the shallow foundations have sufficient soil bearing strength for a DD-3 class earthquake ground motion. Settlements of the shallow foundation are illustrated in Figure 6.

$$q_0 = 15\ mm\ \times 16800\ {}^{kN}/_{m^3} = 252\ {}^{kN}/_{m^2}\ \leq\ q_t \tag{2}$$

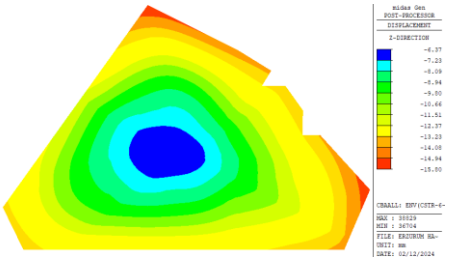

Fig. 6 Settlements of the shallow foundation (mm)

4. Conclusions

A finite element model of the examined masonry building was prepared to represent its strengthened state. The model was examined to determine whether it meets the performance targets of "Controlled Damage" for DD-3 earthquake ground motion level, "Pre-Collapse" for DD-3 earthquake ground motion level, and "Pre-Collapse" for DD-2 earthquake ground motion level according to the principles outlined in TBEC-2018 and ERMGHB-2017. The building was evaluated using the "Strength-Based Assessment" approach.

- The building met only the Pre-Collapse" performance target for the DD-3 earthquake ground motion level.
- The proposed operations in the repair/strengthening project have significantly improved the existing seismic performance of the structure. Axial forces acting on masonry vertical structural members under vertical loads are found to be below the axial force capacities of these members.
- For the considered performance target level, the ratio of the total shear force (resulting from the combined effect of the vertical loads and earthquake effects) carried by vertical structural members with insufficient shear capacity to the total shear force in the given story is below the limit value.
- The building satisfied the inter-story drift control.
- The foundation met the bending requirements and was found to have sufficient strength for soil bearing capacity.

References

1. Gkournelos, P.D.; Triantafillou, T.C.; Bournas, D.A. Seismic upgrading of existing masonry structures: A state-of-the-art review. *Soil Dynamics and Earthquake Engineering*, **2022**;161:1-17.
2. Marino, S.; Cattari, S.; Lagomarsino, S. Are the nonlinear static procedures feasible for the seismic assessment of irregular existing masonry buildings? *Engineering Structures*, **2019**;200:1-16.
3. Kalkbrennera, P.; Pelà, L.; Sandoval, C. Multi directional pushover analysis of irregular masonry buildings without box behavior. *Engineering Structures*, **2019**;201:1-16.
4. Yildizlar, B. Seismic performance analysis and rehabilitation applications for a historical masonry building through field works and experimental investigations. *Structures*, **2021**;34:1811-1833.
5. Cosgun, T.; Ceylan, O.; Manzoor Nasery, M.; Güler Ö.; Sayin, B.; Uzdil, O.; Akcay, C. Seismic performance assessment and retrofitting proposal for a historic masonry school building (Bursa, Türkiye). *Case Studies in Construction Materials*, **2023**;18:1-35.
6. TBEC-2018, Turkey Building Seismic Code: Rules for design of buildings under earthquake effect, Official Gazette, 18.03.**2018**, 30364 (in Turkish).
7. ERMGHB-**2017**, Earthquake Risk Management Guide in Historical Buildings, General Directorate of Foundations (in Turkish).
8. AFAD. (**2019**). Turkey Earthquake Hazard Maps Interactive Web Application. tdth.afad.gov.tr/TDTH/main.xhtml
9. Petracca, M.; Pelà, L.; Rossi, R.; Zaghi, S.; Camata, G. Spacone, E. Micro-scale continuous and discrete numerical models for nonlinear analysis of masonry shear walls. *Construction and Building Materials*, **2017**;149:296-314.
10. Midas Gen (**2021**), Integrated Solution System for Building and General Structures, MIDAS Information Technology Co.

Optimizing Woven Fabric Mechanical Properties for Composite Application: Long and Short Float Analysis

Sultan ULLAH[1], Hassan IFTIKHAR[2], Zeenat AKHTER[3], Giedrius JANUSAS[1*]

1 Faculty of Mechanical Engineering and Design, Kaunas University of Technology, Studentu 56, 51424, Kaunas, Lithunaia
2 Department of Textile Engineering, School of Engineering and Technology, National Textile University,Faisalabad 37610 Pakistan
3 College of Electrical and Mechanical Engineering, National University of Science and Technology, Pakistan
** giedrius.janusas@ktu.lt*

Abstract

This study investigates the influence of long and short floats in weave structures on the mechanical properties of woven fabrics, with a focus on their potential application in composite materials. Plain and 7 end sateen weaves are systematically combined to create various fabric samples. Cotton yarn with a count of 12 Ne is utilized in both warp and weft directions, and desizing is employed to prepare the samples. Using a sample dobby machine, strip weave, alternating, zigzag, and multilayer configurations are generated and subjected to comprehensive mechanical testing. The results demonstrate that the multilayer fabric exhibits superior mechanical properties, including heightened tear resistance, puncture resistance, and air permeability. This research successfully identifies optimal weave combinations that have the potential to enhance the mechanical performance of woven fabrics for composite applications, contributing to the advancement of materials engineering.

Keywords: Woven fabric, Float analysis, Mechanical properties, Composite applications

1. Introduction

Weaving is the process of interlacing two sets of perpendicular yarns in a regular interlacing pattern to make fabric. Weaving not only creates fabrics with traditional designs like plain, twill, and satin but also opens avenues for innovative 3D structures and textures. Weave structure emerges as a critical determinant of woven fabric properties, spanning from mechanical characteristics to thermal behavior. Through systematic analysis, researchers unveil the intricate interplay between weave configurations and fabric attributes, illuminating pathways for tailored material design and performance optimization [1]

Long and short floats emerge as a critical factor in determining the mechanical properties of woven fabrics. Through experimental analysis across various weave structures like plain, twill, and satin, the impact on characteristics such as strength, air permeability, and shrinkage are revealed. These findings underscore the importance of understanding the interplay between floats and weave structure in optimizing fabric performance and durability in materials engineering [2]. Researchers observed greater extensibility of twill weave relative to satin weave is attributed to its higher crimp, while the plain weave exhibits the highest interlacement among the three structures, indicating intermediate properties between plain and satin weaves [3]. Plain woven fabric maximal weave interlacing coefficient contributes to its substantial tensile strength, highlighting its mechanical properties within the fabric structure [4]. The configuration of weave combinations is crucial in shaping the dome structure of dome-shaped fabrics, whereby longer floats in the outer circle and shorter floats in the inner circle contribute to a more pronounced dome effect, with the length of the float directly impacting dome depth, resulting in deeper domes with longer floats, particularly evident in the outer circle of the fabric [5].

A bi-layer-woven fabric was also studied indicating how material type and weave pattern affect physical properties. The textiles with both cotton layers had the highest air permeability, but the thermal resistance of the 3/1 twill samples was lower than that of the 2/2 sample [6]. A statistically significant correlation is observed between the thermal resistance of twill weave and the length of warp float, with an increase in float length resulting in higher thermal resistance [7]. On the other side, elastane count led to enhanced fabric stretch and recovery along the warp, while primarily affecting recovery in the weft direction. Nevertheless, adjustments in elastane count had minimal influence on fabric contraction, with thread density and float size exerting more significant effects on this aspect [8]. The drop weight impact response of hemp/green epoxy composites is significantly influenced by weave pattern and the percentage of glass microspheres (GMS), with satin woven fabric reinforced composites exhibiting the highest maximum force and least central deflection due to their longer yarn float structure [9]. Previous studies have primarily addressed blending longer and shorter floats in weave structures, but there is absence of literature on the integration of these floats. Our research will explore integrated weaves of stripes and alternative combinations to fill this gap. In this experimental study, mechanical properties were investigated with the aim to integrate weaves with longer, middle, and shorter floats through various combinations of two and three weaves for potential composite applications. The tensile, and tear strength, thermal resistance, puncture resistance, air permeability, and stiffness testing are performed on a woven fabric. The results demonstrate that the multilayer fabric exhibits superior mechanical properties.

2. Materials and methods

2.1. Materials

A 12/1 Ne count cotton yarn was utilized to prepare various types of woven fabrics including plain weave, 7-end sateen, strip weave, alternating weave, zigzag fabric, and multilayer fabric. Parameters of fabric samples is shown in Table 1.

Table 1. Parameters of fabric samples

Fabric	Weave	Estimated EPI	Estimated PPI	Actual EPI	Actual PPI	Fabric Weight (gsm)	Fabric Thickness (mm)
Plain weave (S1)	1/1	60	60	59	47	260	0.53
7 end sateen (S2)	1/6	60	60	57	45	280	0.99
Strip weave (S3)	sateen and plain	60	60	56	45	281	0.961
Alternating weave (S4)	alternating sateen and plain	60	60	58	47	291	0.978
Zig Zag fabric (S5)	plain and sateen zig zag	60	60	58	48	287	0.94
Multilayer fabric (S6)	face back	60	60	56	48	302	1.20

2.2. Methods

The study provides the procedural steps undertaken and details the tests performed on these samples, offering a comprehensive insight into the experimental employed. The fabrication of samples on a sample weaving loom as shown in Figure 1 beginning with warping, followed by sizing, weaving, and concluding with desizing. The CCI sample weaving machine was employed to weave six types of fabric variants, each with a length of 1.5 meters, maintaining a constant EPI of 60 and variable PPI. The on-loom width measured 19.5 inches, while the width of the cloth roller was 18 inches, with the machine running at an average RPM of 50 to 60. The specimens underwent various tests, including a tensile test ASTM D5034, tear test BS-EN ISO 13937-2, puncture test EN288, stiffness ASTM D4032, and air permeability D737, to assess their mechanical properties and performance characteristics.

Fig. 1 Sample weaving loom

3. Results and discussion

3.1. Tensile strength testing (ASTM D5034)

Figure 2 demonstrates the tensile strength assessment conducted on fabrics to ascertain their behaviour under stretching or tension forces, providing insights into their strength, elasticity, and elongation characteristics. Plain weave fabrics, characterized by a simple over-and-under interlacing pattern of warp and weft yarns, typically exhibit balanced properties with good tensile strength and moderate elongation due to the presence of crimp in the yarns. However, the study shows that strip weave structures display higher tensile strength compared to plain weave, attributed to a combination of properties from both plain and sateen weaves.

Plain weave fabrics generally demonstrate relatively high tensile strength, the combination of strip and zigzag weaves in multilayer fabrics yields superior tensile properties, surpassing those of individual plain weaves. This phenomenon is attributed to the combined characteristics of both plain and sateen weaves, where the plain weave contributes crimp and stability, while the sateen weave offers less crimp but longer floats. Conversely, sateen weaves typically exhibit lower tensile strength due to reduced interlacements and minimal yarn interaction resulting from longer floats. The multilayer fabric displays the least tensile properties among the tested weaves, primarily due to its structure consisting of two layers and reduced yarn friction. However, it demonstrates increased elongation, attributed to the initial elongation resulting from the combination of crimp from plain weave and reduced crimp from sateen weave within the multilayer structure. Overall, the findings suggest that while plain weave fabrics exhibit good tensile properties (S3>S5>S1>S4>S2>S6), the combination of different weave structures can lead to enhanced mechanical performance in specific applications.

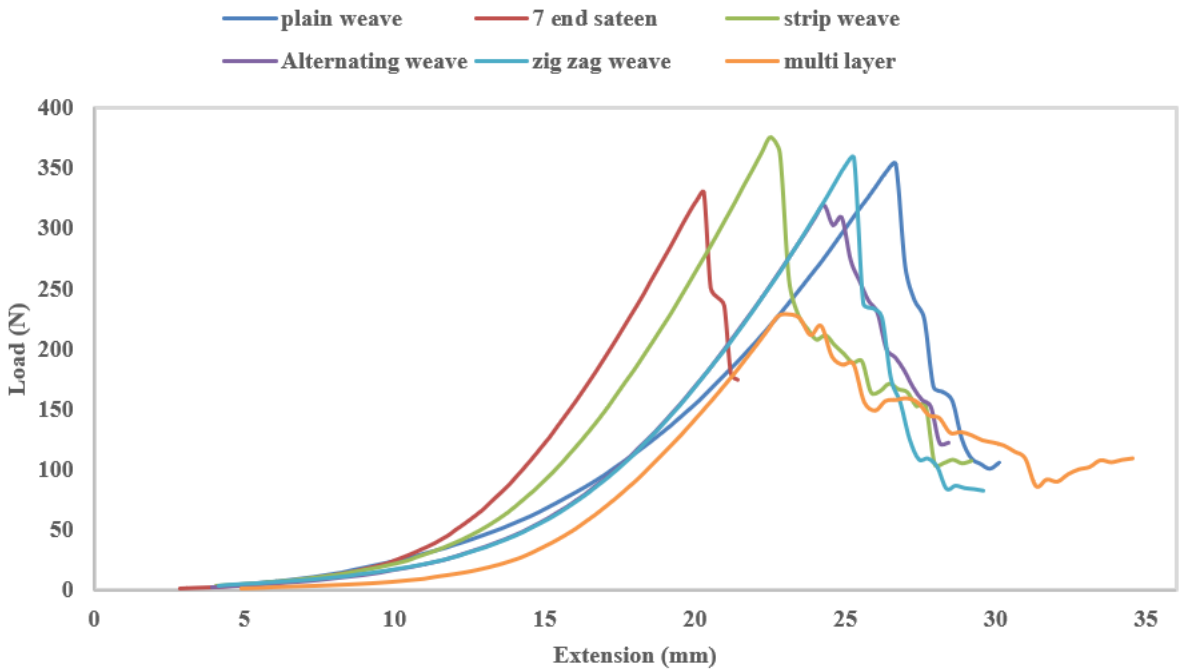

Fig. 2 Tensile strength results for weaved samples

3.2. Tear strength testing (BS-EN ISO 13937-2)

Tear test is instrumental in assessing the fabric toughness and its ability to withstand tearing forces, providing manufacturers with crucial data to determine its tear strength and suitability for various applications. The tear resistance of a fabric is influenced by factors such as weave structure and floats present within the fabric. For instance, fabrics with longer floats, such as seven-end sateen, exhibit greater resistance to tearing due to the increased number of yarn bundles, which effectively resist tearing forces. Conversely, plain weave fabrics, characterized by shorter floats and higher slippage and crimp factors, are more susceptible to tearing. Zigzag and strip weaves demonstrate comparable tear strength, while the alternating weave, with more floats in four quadrants, exhibits higher tear resistance compared to zigzag and strip weaves, despite lower than seven-end sateen. Interestingly, multilayer fabrics display tear resistance beyond the expected range, attributed to limited yarn propagation and high elongation properties, resulting in maximum tear resistance as shown in Figure 3. These findings underscore the intricate relationship between weave structure, float characteristics, and tear strength, influencing the fabric performance in real-world applications.

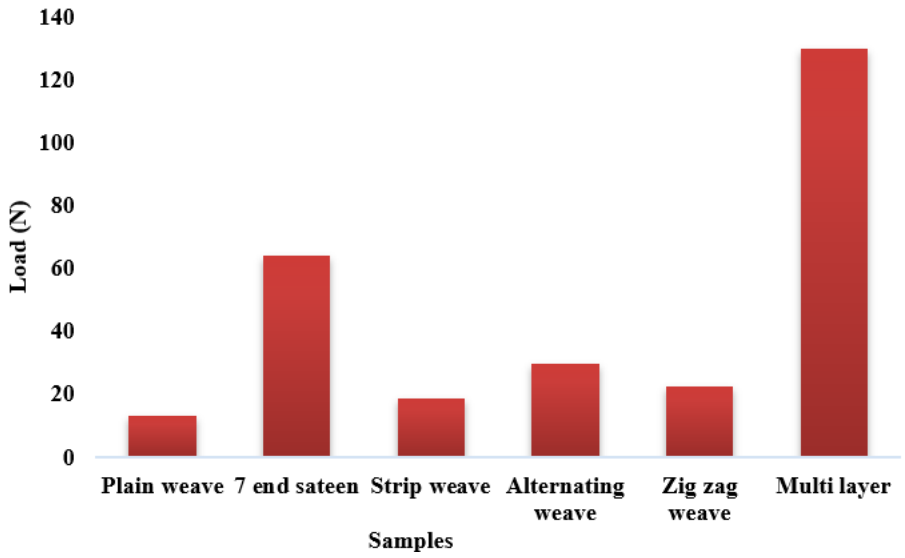

Fig. 3 Tear test results for different weaving samples

Weave structures and their impact on tear resistance is essential for optimizing fabric performance and ensuring its suitability for potential composite applications. By integrating insights from tear tests into material selection processes, manufacturers can enhance product quality and durability, meeting the diverse needs of consumers across different industries.

3.3. Puncture test (EN 288)

The puncture test results are shown in Figure 4, conducted according to EN: 388:2016 standards, plays a critical role in evaluating a fabric ability to withstand piercing forces. Utilizing a stylus made of Steel 60 HRC Rockwell with specific dimensions ensures standardized testing conditions, generating a spherical diameter of 1 mm upon impact. Puncture resistance is influenced by interconnected factors such as fibre type, yarn construction, fabric structure, weight, and finishing treatments, collectively determining the fabric overall resistance to puncturing forces. Fabrics constructed with multilayer and seven-end sateen weaves exhibit the highest puncture resistance, attributed to their layered structure that offers sequential resistance to the needle strike. Additionally, multilayer fabrics demonstrate increased elongation, further enhancing their puncture resistance. In contrast, plain weave fabrics, characterized by shorter floats and higher interlacements, display lower puncture resistance due to compromised structural stability.

Weave structure and compactness significantly impact puncture resistance, with weaves like alternating, zigzag, and strip demonstrating relatively lower resistance compared to seven-end sateen and multilayer fabrics. Combinations of different weaves do not notably improve puncture resistance, as the specific impact point of the needle remains uncertain. Consequently, individual weaves and multilayer fabrics are considered more reliable in providing maximum puncture resistance due to their distinct properties and layered construction.

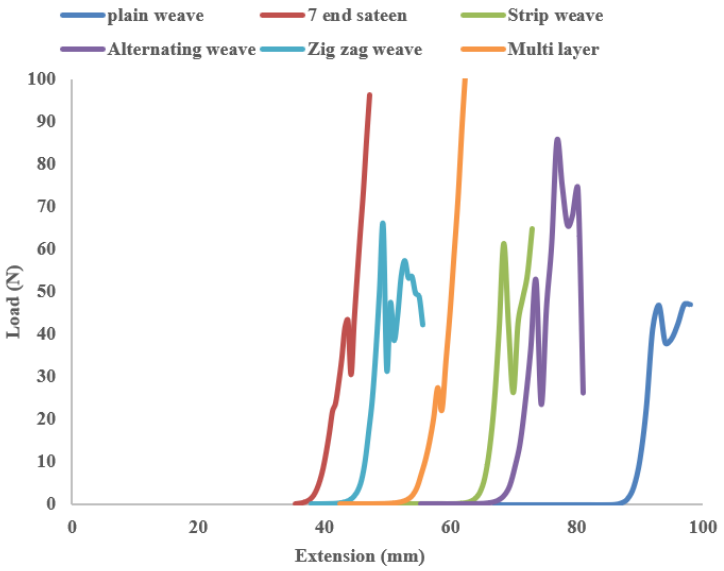

Fig. 4 Puncture test results for different weaving samples

3.4. Stiffness testing (ASTM D4032)

Stiffness, a fundamental property of fabrics, characterizes their resistance to bending or flexibility, defining how easily or rigidly they can be manipulated. Various factors such as fibre content, yarn construction, fabric structure, finishing treatments, and weight contribute to a fabric stiffness. Fabrics manufactured from stiffer fibres like polyester or featuring tight weaves tend to exhibit higher stiffness compared to those made from softer fibres or looser weaves. Stiffness holds significant importance across diverse fields and applications, including textiles and composite materials. In clothing, tougher textiles are preferred for tailored suits or gowns requiring structure, while softer, more flexible fabrics are favoured for draping and casual wear like t-shirts or light dresses. Moreover, stiffness in upholstery and home furnishings influences their appearance, durability, and comfort. The weave or knit structure profoundly impacts fabric stiffness, with tight weaves like plain weave or double-knit fabrics typically displaying higher stiffness. Conversely, looser weaves or knits such as leno or jersey result in softer and more flexible fabrics. Particularly, alternating weaves exhibit higher stiffness compared to plain weave, attributed to their quadrant structure combining features of both plain and sateen weaves.

Strip weaves show comparable stiffness to alternating weaves due to their similar weave structure. Conversely, seven-end sateen weaves individually demonstrate lower stiffness owing to increased spaces and gaps between yarns, resulting in reduced interlacements and less jammed structure. Additionally, the longer floats in sateen contribute to increased gaps, further reducing stiffness. Multilayer and zigzag weave structures display relatively consistent stiffness, with no significant differences observed. However, overall, plain weave fabrics demonstrate more considerable stiffness compared to other weaves, as depicted in Figure 5. This scientific analysis highlights the intricate interplay between fabric composition, weave structure, and stiffness, offering valuable insights for fabric selection and design in potential composite applications.

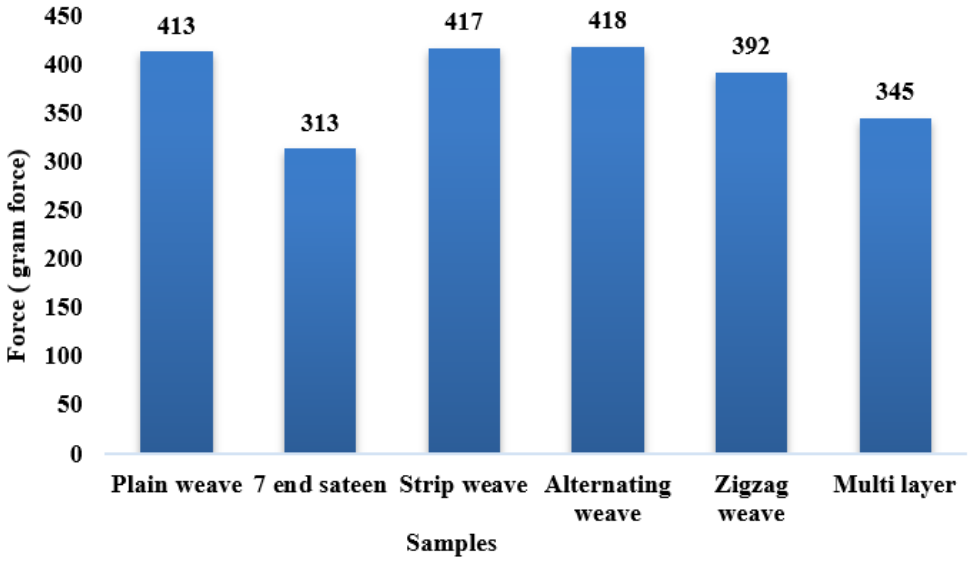

Fig. 5 Stiffness test results for weaving samples

3.5. Air permeability test (D737)

The air permeability of a fabric, denoting its capacity to facilitate airflow, is intricately linked to its pore structure, a characteristic quantifiable through porosity calculations. Fabrics with a plain weave pattern tend to exhibit lower air permeability owing to the denser interlacement of warp and weft yarns, resulting in a more compact grid structure. Conversely, multilayer fabrics showcase heightened air permeability due to the increased gaps between layers resulting from the splitting into two layers upon needle strike. Additionally, seven-end sateen weaves manifest elevated air permeability levels, a consequence of their longer floats, which enhance breathability compared to their plain weave counterparts. In contrast, strip, alternating, and zigzag weaves yield similar air permeability values, reflecting comparable features of plain and sateen weaves within their combined structures. This scientific analysis highlights the detailed interplay between weave structure and air permeability, explaining the diverse factors influencing a fabric ability to facilitate airflow and its implications for breathability and comfort in various applications. The air permeability results for weaved samples are shown in Figure 6.

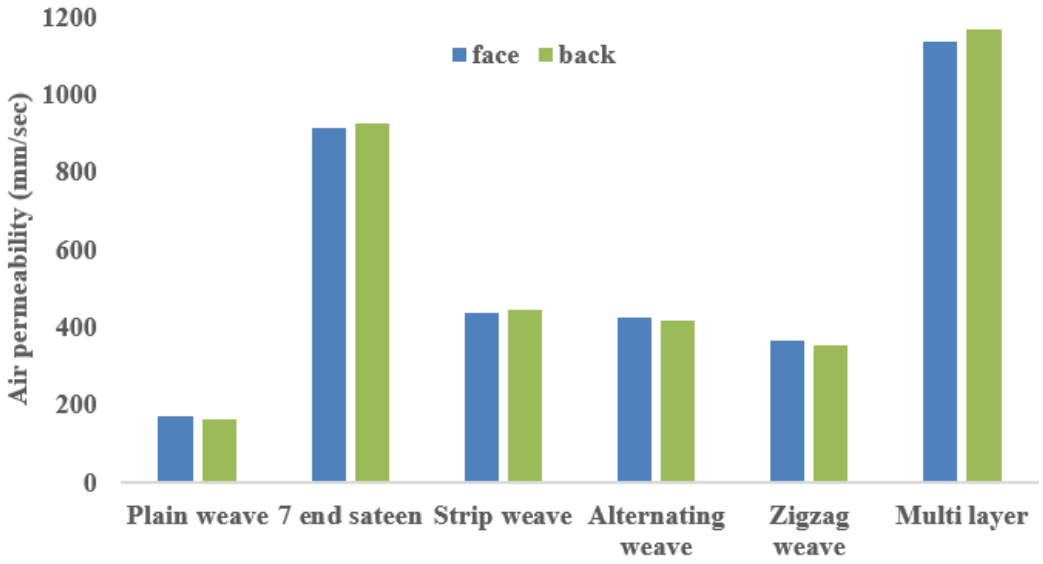

Fig. 6 Air permeability test results for weaving samples

In composite applications, the air permeability of fabric plays a crucial role in determining the performance and quality of the final composite material. The air permeability test helps assess the ability of the fabric to allow air to pass through it, which is essential for various applications such as vacuum bagging, resin infusion, and airflow control in composite structures. The air permeability of fabric serves as a fundamental parameter in composite applications, impacting multiple facets of the manufacturing process and the ultimate quality of composite products, with precise control and management crucial for achieving high-performance and dependable composite structures.

4. Conclusions

In conclusion, the study highlights the distinct performance characteristics of plain and sateen weaves, as well as their combined effects in various fabric combinations. While plain weave exhibits superior tensile strength and stiffness, sateen weave demonstrates enhanced tear resistance, air permeability, and puncture resistance. However, when combined, these individual features do not necessarily yield the expected results. Multilayer fabric emerges as the most promising option, showcasing excellent tensile strength, tear resistance, air permeability, and puncture resistance. This can be attributed to its unique structure, where one layer comprises plain weave and the other layer features sateen weave, effectively leveraging the strengths of both weaves. The high initial elongation of multilayer fabric further underscores its versatility and performance. Future research could explore the use of high-performance fibres to potentially enhance the performance of the fabrics. Additionally, investigating composite materials formed by integrating different weave combinations, such as alternating quadrants, holds promise for yielding novel and improved material properties. In summary, the findings suggest that rather than relying on combinations of individual weaves, the fabrication of multilayer fabrics offers a more effective approach to achieving superior performance across a range of mechanical and physical properties.

References

1. Most. S. Begum and R. Milašius, Factors of Weave Estimation and the Effect of Weave Structure on Fabric Properties: A Review, *Fibers*, vol. 10, no. 9, p. 74, Aug. **2022**, doi: 10.3390/fib10090074.
2. S. Islam, S. Akter, S. Ahmed, S. Islam, S. Akter, and S. Ahmed, Influence of Cover Factor on the Physical Properties of Woven Fabrics, doi: 10.48302/jtp.**2022**.145558.
3. M. Ruhul Amin, M. Haque, and M. Mahbubul Haque, Effect of weave structure on fabric properties annals of the university of oradea fascicle of textiles, leatherwork effect of weave structure on fabric properties, **2011**. [Online]. Available: https://www.researchgate.net/publication/321161966
4. H. Özdemir and E. Mert, The effects of fabric structural parameters on the tensile, bursting, and impact strengths of cellular woven fabrics, *Journal of the Textile Institute*, vol. 104, no. 3, pp. 330–338, Mar. **2013**, doi: 10.1080/00405000.2012.725521.
5. D. Yang, A. E. Tayyar, and X. Chen, Parametric study of the weave combination on the moldability of dome-shaped fabrics, *Textile Research Journal*, vol. 89, no. 2, pp. 150–161, Jan. **2019**, doi: 10.1177/0040517517741157.
6. M. U. Nazir, K. Shaker, Y. Nawab, M. Z. Fazal, M. I. Khan, and M. Umair, Investigating the effect of material and weave design on comfort properties of bilayer-woven fabrics, *The Journal of The Textile Institute*, vol. 108, no. 8, pp. 1319–1326, Aug. **2017**, doi: 10.1080/00405000.2016.1247616.
7. A. Asayesh, M. Talaei, and M. Maroufi, The effect of weave pattern on the thermal properties of woven fabrics, *International Journal of Clothing Science and Technology*, vol. 30, no. 4, pp. 525–535, Aug. **2018**, doi: 10.1108/IJCST-10-2017-0163.
8. M. Maqsood, T. Hussain, M. H. Malik, and Y. Nawab, Modeling the effect of elastane linear density, fabric thread density, and weave float on the stretch, recovery, and compression properties of bi-stretch woven fabrics for compression garments, *The Journal of The Textile Institute*, vol. 107, no. 3, pp. 307–315, Mar. **2016**, doi: 10.1080/00405000.2015.1029809.
9. M. Umair, M. Hussain, Z. Abbas, K. Shaker, and Y. Nawab, Effect of weave architecture and glass microspheres percentage on the low velocity impact response of hemp/green epoxy composites, *J Compos Mater*, vol. 55, no. 16, pp. 2179–2195, Jul. **2021**, doi: 10.1177/0021998320987605.

Effects of Foundation Excavation on the Adjacent Structures and Potential Structural Damage

Baris GUNES[1], Kamran SAMADI[2], Baris SAYIN[1*]

1 Department of Civil Engineering, Istanbul University-Cerrahpasa, 34320, Istanbul, Türkiye
2 Institute of Graduate Sciences, Istanbul University-Cerrahpasa, Istanbul, Türkiye
** barsayin@iuc.edu.tr*

Abstract

The study aimed to investigate whether the damages observed in a three-block school building with a sheared reinforced concrete (RC) frame system were related to the foundation excavation activities on the adjacent parcel. Based on the data obtained from the soil investigation report, a shoring system was designed and implemented for the safety of the excavation process. The conformity of the shoring project was verified through detailed calculations. Damage assessments were conducted based on on-site observational geotechnical and structural investigations and were categorized by damage on the retaining walls, non-structural/structural elements, and ground. In general, it was concluded that the horizontal displacements in Block B of the school building were caused by the rotation of the foundation during the excavation. However, since the amount of rotation in the foundation was limited and the building has a raft foundation, it was concluded that these displacements do not cause structural damage. The load-carrying capacity of the shoring system designed and implemented for the excavation was found to be adequate. However, despite the damages on the retaining walls were not structurally related to the adjacent foundation excavation, it was concluded that the current condition of the retaining walls could potentially endanger life safety.

Keywords: Excavation Effects, Structural Damage, Geotechnical Evaluation, Retaining Structures, Structural Damage Assessment.

1. Introduction

Since the latter half of the twentieth century, deep excavations have become a fundamental phase of construction projects due to several reasons including the rising number of high-rise buildings in megacities, the demand for basements in commercial structures to accommodate car parking and other requirements, and the necessity of underground systems such as subway lines. However, excavation for projects must be conducted with meticulous calculations based on comprehensive geotechnical investigations. And when necessary, the design and implementation of shoring systems are essential to ensure the safety of lives and property. In this regard, it is critical to prioritize the stability and safety of nearby structures during excavation operations.

Some studies have investigated the risks and potential damages to surrounding structures resulting from excavations. In one such study, Castaldo et al. [1] introduced a simplified methodology for evaluating excavation-induced damage to surrounding buildings. They applied this methodology to assess the potential damage in a specific excavation project, particularly for the construction of an underground metro station. Zhang et al. [2] conducted a comprehensive evaluation of damages resulting from foundation excavation on an adjacent building. Their approach involved a combination of field observation, numerical analysis, and experimental investigation. The results demonstrated that the settlement of strata beneath existing buildings during foundation pit excavation is significantly influenced not only by excavation but also by the dewatering of soil masses required for constructing the foundation pit. Ou et al. [3] conducted a series of parametric studies to assess the potential for building damage resulting from excavations, through an advanced soil model and numerical analysis. The authors applied the proposed models to two case studies and observed that the subsurface ground motions were modeled more accurately, leading to a more realistic estimation of the damage potential index. Li et al. [4] examined the risk of deformation and damage to a historic building adjacent to a supported excavation in soft ground, conducted during a subway construction. The authors proposed the use of partition walls to mitigate the corner effect on buildings. Mangir et al. [5] investigated the changes in structural behavior and seismic performance of a thirteen-story reinforced concrete (RC) building following a nearby excavation. They employed field studies, laboratory tests, and numerical simulation modeling. Their results revealed that the building is in a critical state in the event of a possible earthquake post-excavation, characterized by an increase in the number of damaged elements and high displacements under both vertical and seismic loading scenarios.

The current study evaluates the potential risk posed to an adjacent building by the excavation for a building construction, as well as the causation of damages to the building and to determine whether any damages may be attributed to inadequate shoring systems applied during excavation. This evaluation was based on ground project calculations, on-site geotechnical investigations, and structural investigations. According to the results, it is recommended that the existing condition of structures in the vicinity be carefully evaluated as a crucial safety consideration before excavation and throughout the design phase of shoring projects.

2. Materials and Methods

2.1. The Examined Structure and Area

Figure 1 illustrates the layout of the examined school building and the adjacent excavation. The school building features a shear-wall RC frame system and includes a basement, ground floor, three standard floors, and an attic floor. The building consists of three distinct blocks separated by expansion joints. The basement and ground floor have heights of 3.8 meters, while the standard floor heights are 3.3 meters each.

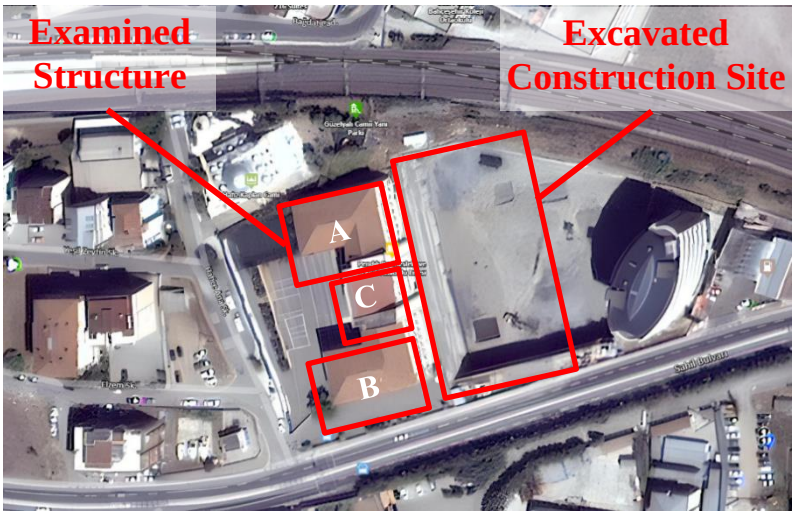

Fig. 1 The layout of the examined building and the excavation site

2.2. Geotechnical Evaluations

The results of the ground investigation and the soil profile analysis for the ongoing construction were used to prepare a ground project and shoring report to support the excavation surfaces during foundation excavations.

2.2.1. Examination of the Soil Investigation Report

During the ground investigation works, a total of 14 soil boreholes were drilled, and seismic refraction Multichannel Analysis of Surface Waves (MASW) measurements were conducted along 6 profiles. According to observations from the boreholes, the soil profile comprises a fill unit with a thickness ranging between 2 and 6.5 meters from the surface. Beneath the fill, there was a layer of weathered claystone (W5) continuing to a depth of 8.5 meters. Below this, there was a fractured claystone (W2) unit extending to the bottom of the borehole. During the investigations, groundwater was encountered at a depth of 8.5-9.0 m. Additionally, based on the seismic measurement results, the local soil class was determined as ZB. Seismic measurement and laboratory test results are summarized in Table 1. The geotechnical design parameters determined for the soil units in the re-inspected soil project are given in Table 2.

Table 1. Seismic measurement results

	Maximum	Minimum	Mean
V_{S30} (m/sec)	972	770	860
Dominant Vibration Period (sec)	0.189	0.227	0.212

Table 2. Geotechnical design parameters determined for soil units

Layer	γ_n kN/m^3	γ_K kN/m^3	C_{u-ort} kN/m^2	C' kN/m^2	Φ (°)	ϕ' (°)	E' kN/m^2
Fill	16.0	15.0	---	3.0	---	25.0	12.000
Weathered claystone W5	20.0	18.5	67.0	10.0	5.0	28.0	35.000
Fractured-Fissured Claystone W2	24.0	23.0	---	50.0	---	35.0	150.000

2.2.2. Examination of the Shoring Project

A temporary shoring project was prepared to support the excavation surfaces during the foundation excavations for the construction. Within this temporary shoring project, 8 sections were created, taking into account the locations and impacts of the surrounding roads, infrastructure facilities, neighboring structures, a state railway, and a tunnel passing beneath the Coastal Road Boulevard. Among these, 4 sections were identified as critical and subjected to analysis. As part of the shoring project, 4-4 sections were evaluated to investigate the interaction between the school building and the excavation. The

idealized soil profile is depicted in Figure 2, and the geotechnical design parameters for soil units are provided in Table 3.

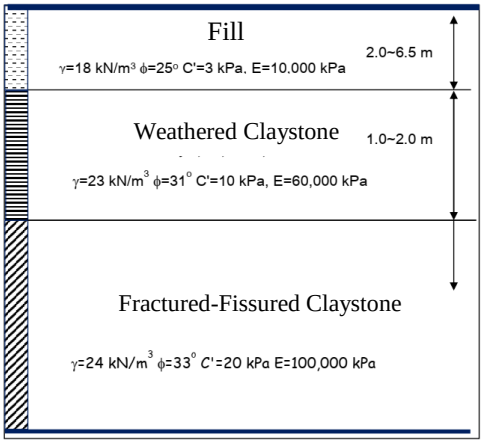

Fig. 2 The idealized soil profile for the 4-4 sections

Table 3. Design parameters selected for idealized soil profile

Soil Unit	γ kN/m3	E_s kN/m3	C' kPa	Φ (°)	υ
Fill	18.0	10.000	3.0	25.0	0.40
Silty Solid Clay	23.0	60.000	10.0	31.0	0.30
Hard Clay	24.0	100.000	20.0	33.0	0.25

As illustrated in Figure 3, the existing land elevation in the cross-section was determined as +9.0, while the final excavation elevation was -3.62. Accordingly, a 12 m excavation was made up to the final excavation level. For the examined 4-4 sections, bored piles with a diameter of 65 cm and a length of L = 14.4 m were designed as shoring elements, with a distance of s = 0.85 m between their centers. The socket length of the piles was 2.4 m. The bored piles were vertically supported by four rows of temporary ground anchors. In the design of the anchors, 3×0.6" ropes were utilized. Taking into account the lower elevation of the basement floor and the foundation of the school building, the anchors were planned to be installed at an angle of 20 degrees. The horizontal spacing of the anchors was 1.7 m, and the root length was calculated as 7 m. The roots of the anchors were planned to remain within the claystone unit, and the tension loads were calculated as 300 kN.

As shown in Figure 3, according to the analysis of the 4-4 sections, the bending moment on the bored piles was calculated as M = 137.34 kNm/m, shear force as Q = 160.8 kN/m, and lateral displacement as u_x = 6.5 mm. The safety of the system against total collapse was obtained as GS = 2.05. For the reinforced concrete design of the piles, it was necessary to utilize 11ϕ16 longitudinal reinforcement and ϕ10/15 cm spiral shear reinforcement.

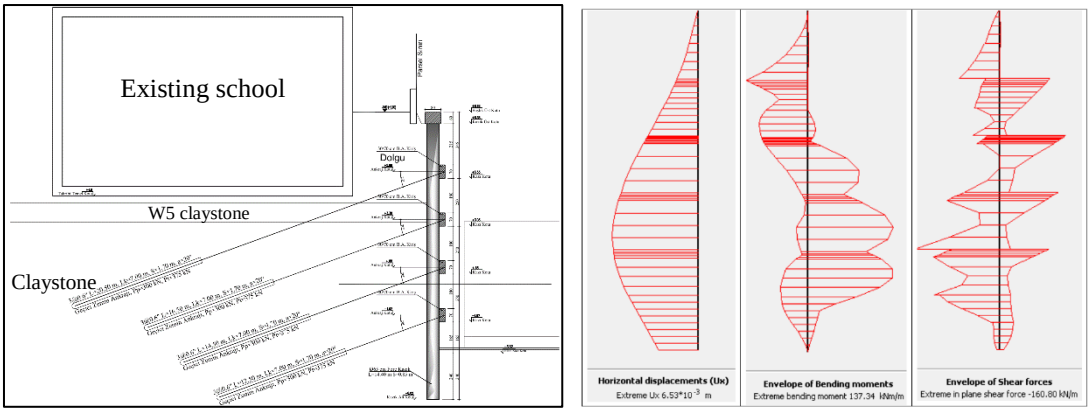

Fig. 3 Details of shoring elements for the 4-4 sections (left) and acting forces on the section (right)

3. Results

3.1. Examination of Retaining Walls Around the School Building

The retaining walls supporting the ground of the mosque and the field at the corner of the school building were investigated. These retaining walls were approximately 3-3.5 meters high and extended along three facades. Observational investigations revealed significant separation and visible slopes between the walls due to ground movement, as well as hairline cracks on the retaining walls (Figure 4).

Fig. 4 Damages on the retaining walls: separation and slopes (Left), hairline cracks (right)

It was determined that the current condition of the retaining walls may pose a risk to life safety. If there is a potential movement, intervention is necessary, and if needed, rebuilding the retaining walls is required. However, it was understood that the damages detected on the retaining walls were not structurally related to the foundation excavation on the adjacent parcel and were not caused by this excavation.

3.2. Examinations of the School Building

In these examinations, it was determined that the middle block of the building (Block B) rotated relatively towards the excavation side in comparison to the side blocks (Blocks A and C) due to the foundation excavation in the adjacent parcel. This movement is clearly visible at the expansion joints. While there was no relative horizontal displacement at the expansion joints of the blocks at the basement floors, a relative horizontal displacement of approximately 0.5 cm between blocks A-B and 1.5 cm between blocks B-C was observed at the top floor.

3.2.1. Non-structural Damages

Non-structural damages are repairable damages that have no or limited effect on the seismic resistance of the structure. As long as they do not affect the structural system and do not spread throughout the entire structure, such damages are not critical for the structural system. The following implications were made based on observational examination of the non-load-bearing elements of the structure:

- Cracking, rupture, and lifting-type damages were observed on the ceramic or tile coating elements on the walls and slabs in the expansion joints between the blocks, primarily on the normal floors of the building. The expansion joints were severely damaged and expansion elements partially detached. No relative displacement and no such damages were observed in the basement. These damages observed on the ceramics occurred in the areas where the blocks were separated by expansion joints and were thought to be caused by the two blocks moving differently due to ground movement.
- On the surfaces of the non-load bearing inner brick walls, various forms of cracks were observed (Figure 5a). The cracks were generally diagonal, horizontal, and vertical. Horizontal and diagonal cracks were observed in some of the non-load-bearing walls near the doors and windows, and partial separation was observed between the windows and the walls/marbles (Figure 5b). Furthermore, partial cracks were observed at the joints of some load-bearing elements and non-load-bearing brick walls throughout the building (Figure 5c). The cracks were limited to the plaster or plaster layer on the wall surface. The cracks were generally not at an advanced level and were repairable.
- Some of the cracks on the brick wall surfaces were observed around architectural, mechanical, or electrical elements (such as cables, ducts, plaster brackets, etc.) and were caused by procedural mistakes in these places. It was thought that the cracks and plaster darkening on the brick walls and surfaces throughout the building were caused not only by ground displacement but also by material and/or workmanship defects, as well as poor adhesion of the plaster to the surface.
- Some interior and exterior walls exhibit blistering and plaster spills due to dampness.
- Water leaks were observed in the attic floor due to faulty insulation application. The leaks have spread to the walls and caused plaster flaking on some slabs and walls. These leaks were observed only in the middle block and it was concluded that they were not caused by the excavation work on the adjacent parcel.

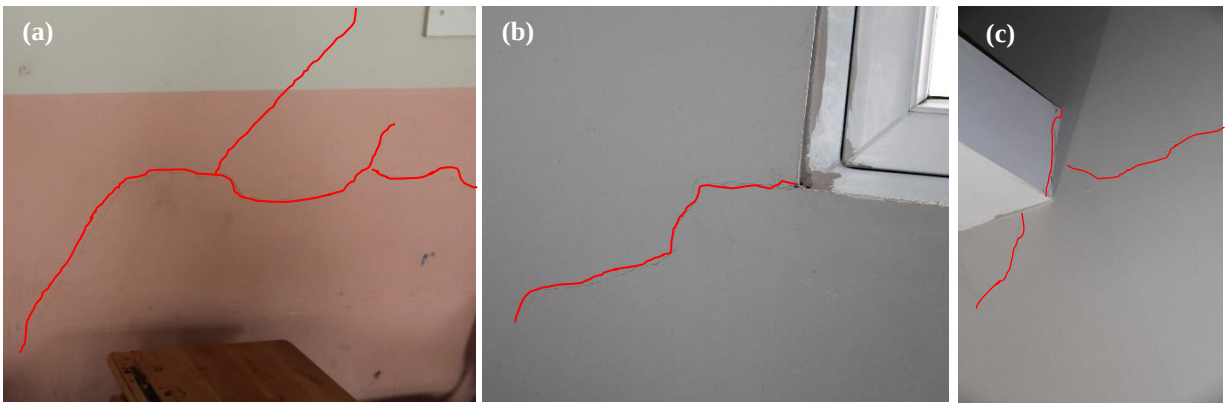

Fig. 5 Damages on the non-load-bearing elements: (a) partition walls; (b) window edge; (c) beam-wall joint

3.2.2. Structural Damages

Structural damages refer to potential damages to columns, walls, beams, and slabs in reinforced concrete buildings. However, depending on the type and distribution of the damage, it can be critical for the structural system. In this study, the following evaluations were made based on observational examinations in the structural elements of the building:

- Vertical and diagonal cracks were observed on the surfaces of some reinforced concrete columns (Figure 6a). To determine whether the cracks had penetrated the reinforced concrete, the gypsum-plaster layer was removed/broken and checked. As a result of the inspection, it was determined that the cracks were only in the gypsum plaster and did not spread to the concrete.
- Visible cracks and damages were observed in RC walls. As an exception, cracks were observed in some of the shear walls on the basement floor and on the sides of the stairs. However, it was observed that the cracks in these walls were limited to the gypsum plaster layer and were superficial (Figure 6b).
- In the basement floor, capillary cracks, which are estimated to be due to corrosion, were found at the lower ends of some columns. Considering the age of the building and the location of the damage on the basement floor, they were evaluated as repairable damage.
- Very few horizontal and vertical cracks were observed in the beams and wall joints (Figure 6c). The thickness of these cracks was very small and only in the gypsum plaster.
- A dilatation joint was left between the blocks of the building. These blocks moved separately due to ground displacement, causing relative rotational movement between them. As a result of this movement, openings/separations were observed between the joint gaps. It was concluded that these separations did not cause any structural damage to the examined parts of the building. Plaster spills in the dilatation areas did not spread to the RC elements.

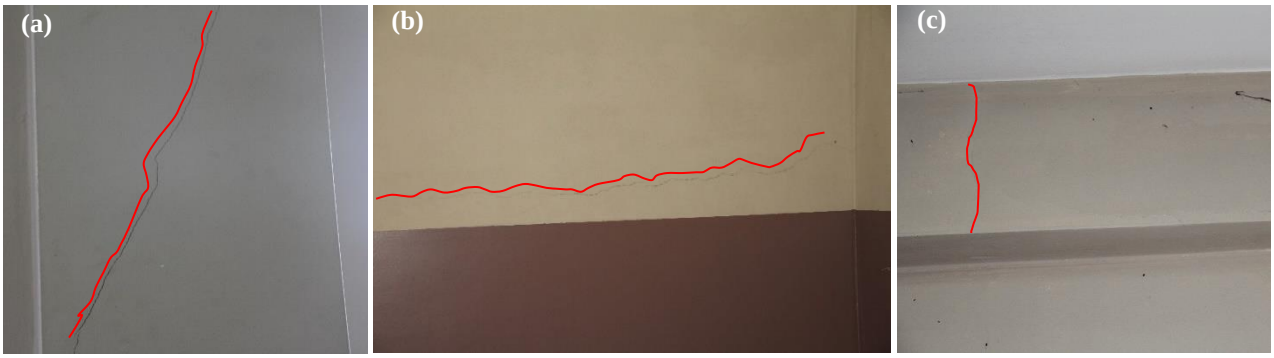

Fig. 6 Damages on the structural elements (a): column; (b): shear wall; (c): beam

3.2.3. Soil Damages

Soil damages are defined as separations between the building and the visible ground surface; pits and crevices indicating ground movement around the building (garden, entrance, etc.); heaves and openings in floor coverings (paving stones, asphalt, concrete, etc.); cracks and splitting in garden walls. Such damages can be critical for the structural system depending on its type and distribution on the ground. The following conclusions were made based on observational investigations of the visible ground surfaces in the perimeter and interior of the structure:

- On the front, rear, and side facades of the building, partial separations were observed between the floor/stair concrete and the facade wall of the building due to differential settlement. During the on-site investigations, the researchers were informed that these separations existed before the excavation process. However, it is believed that these damages further increased after the excavation due to differential settlements (Figure 7a).

- Partial cracks were observed on the facade of the building, on the sidewalks adjacent to the building, on the paved steps, and the concrete and asphalt pavements in the large area (ceremony, sports, playground) (Figure 7b).
- Cracks were observed in the concrete garden wall and detachments in its coatings on the facade of the building adjacent to the excavation (Figure 7c).
- The assessment of the damage observed on the ground surfaces and in the ground concrete-building joints led to the conclusion that there were partial settlements in the surrounding ground concretes/coatings.

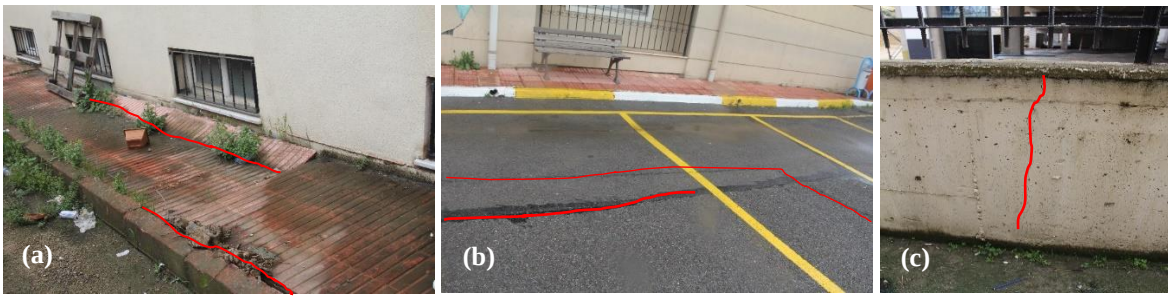

Fig. 7 Soil damages:(a) side ground surfaces; (b) covered ground; (c) garden wall

4. Conclusions

In this study, the damage and relative displacement of an adjacent school building caused by foundation excavation for a building construction were evaluated. Based on on-site observational investigations and evaluation of geotechnical reports, the following results were obtained:

According to the geotechnical evaluations:

- It was concluded that the calculated horizontal displacements in the shoring piles were within acceptable limits, and the system was safe against total collapse.
- According to the calculated forces in the shoring piles, it was decided that the amount of rebars to be used in the piles was sufficient.
- It was observed that the shoring report does not include the axial forces acting on the ground anchors. However, the calculations revealed that the bearing capacity of the anchors to be constructed within the claystone unit is sufficient.
- It was understood that the horizontal displacements that occurred in Block B (middle building) of the school building were caused by the rotation of the building foundation during the excavation. However, since the amount of rotation in the foundation was limited and the building has a raft foundation, it was concluded that these displacements do not cause structural damage.
- It was concluded that the damages detected on the retaining walls did not have a structural relationship with the adjacent foundation excavation and were not caused by this excavation. However, it was revealed that the current condition of the retaining walls may pose a risk to life safety.

According to the structural evaluations:

- Block B rotated and displaced slightly relative to the side blocks (Blocks A and C). However, no structural damage was observed due to this displacement; some non-structural and easily repairable damages occurred.
- In Block C of the school building, on the opposite side of the excavation (collection area), more non-structural damage was observed on the ground floor. It was concluded that these damages were caused by a local soil weakness in that area and that the foundation excavation on the adjacent parcel had no or very limited effect.

References

1. Castaldo, P.; Calvello, M.; Palazzo, B. Probabilistic analysis of excavation-induced damages to existing structures. Computers and Geotechnics, **2013**;53:17-30.
2. Zhang, X.; Yang, J.; Zhang, Y.; Gao, Y. Cause investigation of damages in existing building adjacent to foundation pit in construction. Engineering Failure Analysis, **2018**;83:117-124.
3. Ou, C.Y.; Teng, F.; Li, C.W. A simplified estimation of excavation-induced ground movements for adjacent building damage potential assessment. Tunnelling and Underground Space Technology, **2020**;106: 1-15.
4. Li, Z.; Han, M.; Liu, L.; Li, Y.; Yan, S. Corner and partition wall effects on the settlement of a historical building near a supported subway excavation in soft soil. Computers and Geotechnics, **2020**;128: 1-17.
5. Mangir, A.; Cosgun, T.; Sayin, B.; Okumus, V.; Gunes, B. Determination of the change in the structural performance of an RC building due to a nearby deep excavation. Structures, **2023**;49:792-806.

Effect of Gradient Boosting Algorithm Parameters on Overall Length Minimization of Five Element Truss System

Yaren AYDIN[1]*, Gebrail BEKDAŞ[1]*, Sinan Melih NİGDELİ[1]*

1 Istanbul University-Cerrahpaşa, Civil Engineering Department, 34320 Avcılar, Istanbul, Turkey,
** yaren.aydin1@ogr.iuc.edu.tr, bekdas@iuc.edu.tr, melihnig@iuc.edu.tr*

Abstract

Truss systems are an economical solution for crossing large spans, and the lower head members of the truss system under the effect of vertical load work in tension and the upper head members work in compression. Therefore, overall length optimization is an important issue, provided that safety is ensured. In this study, a dataset containing the total length minimization of a five-element truss system was created by optimization for use in machine learning (ML). Among the ML models, Gradient Boosting Regressor (GBR) is selected. GBR is a powerful prediction method that produces impressive results in regression and classification problems. Parameters are loss, learning_rate, n_estimators, subsample, max_depth and random_state. In this study, how the overall length prediction changes according to the variation of Gradient Boosting parameters is analysed. As a result of the study, it was seen that the parameter that most positively affected the performance of the machine learning model was "max_depth".

Keywords: gradient boosting, parameter effect, optimization, flower pollination, truss system.

1. Layout

Truss systems are one of the types of structural systems used in engineering. It provides a practical and economical solution to many engineering problems, especially in crane, bridge and building projects. A truss system consists of straight-axis rods joined at the nodal points. The elements of a truss system are fragile and cannot carry loads in the direction perpendicular to its axis; therefore, all loads must be applied to the nodal points, not to the bars themselves. When a distributed load is applied between two nodes, the truss is designed so that these loads are distributed to the neighbouring nodes. For various reasons like these, optimization in cage systems is important as long as security is ensured. Optimization is the process of choosing the best among alternatives to a problem. Many algorithms have been proposed for optimization problems. Metaheuristic algorithms are algorithms that can provide near-optimal solutions in an acceptable time for large-sized optimization problems. In this study, a dataset containing the total length minimization of a five-element truss system was created by optimization using a metaheuristic algorithm (Flower Pollination Algorithm (FPA)) for use in machine learning. Gradient Boosting Regressor (GBR) was chosen among the machine learning models. This dataset consists of 900 rows. The inputs are θ_1 and θ_2 angles, and the output is the overall length.

2. Methodology

2.1 Flower Pollination Algorithm (FPA)

FPA was introduced by Yang [1] in 2012 and is a metaheuristic algorithm inspired by the reproduction process of flowering plants to obtain the best result in the shortest time in solving global optimization problems. The algorithm is used in many optimization problems. Examples of these are robot calibration method [2], patient admission scheduling problem [3], optimization of stair casting parameter for the preparation of aluminum matrix composite [4], characteristic wavelength optimization [5], optimal power flow with uncertain renewable energy sources [6], etc.

FPA is widely used in structural engineering as well as in other fields. Bekdas et al. [7] obtained the optimum dimensions of lattice structures using FPA. Nigdeli et al. [8] performed the optimization of pin-jointed plane frames, truss systems, deflection of I-beams, tubular columns and cantilever beams using FPA. Nigdeli et al. [9] used FPA when finding the optimum mass, period and damping ratio of the tuned mass damper. Bekdas et al. [10] carried out the size optimization of lattice structures without grouping the structural elements using FPA. Mergos and Antoglou [11] designed optimum reinforced concrete retaining walls using FPA. Mergos [12] realized the optimum design of 3D reinforced concrete building frames using FPA. Kayabekir et al. [13] realized the optimum design of reinforced concrete T beam using FPA. Aydin et al. [14] optimized the reinforced concrete beam by changing the key probability parameter of FPA. Ocak et al. [15] carried out the optimum design of base isolation systems using FPA.

The main purpose of flower pollination is to ensure optimum viability and optimum biological reproduction phase. Pollination and other factors interact in the best way to propagate plants. Flowers need pollinators to fulfill pollination rules. These pollinators are biotic pollinators such as flies and bees, which can carry the pollen of flowers to long distances, and abiotic pollinators such as water and wind. The pollination process is modeled as divided into two groups: cross-pollination and self-pollination. Cross-pollination (global search) is when flowers of different plants pollinate each other. Self-pollination (local search) is the pollination of a plant's flowers. Since there are factors such as the closeness of flowers and wind in the self-pollination process, local search has more weight than general search.

In global pollination, pollen is carried over long distances because insects can fly for long periods of time. This guarantees the best reproduction. Global pollination is expressed by Equation 1.

$$X_i^{t+1} = X_i^t + L(X_i^t - g^*) \quad if\ sp > r_1 \qquad (i = 1,2,\dots,m) \tag{1}$$

Here Xit is the solution vector in iteration t. $g*$ is the current best solution among all solutions in the current iteration. i is the solution vector index. L represents the Lévy flight distribution. Long distances traveled by biotic pollinators are mimicked by Lévy flight. The Lévy flight distribution can be described by Equation 2.

$$L = \left(\frac{1}{2\pi}\right) \times r^{-1.5} \times e^{\left(\frac{1}{2r}\right)} \tag{2}$$

Abiotic pollination and flower constancy in the algorithm are given in Equation 3.

$$X_i^{t+1} = X_i^t + \varepsilon\left(X_i^a - X_i^b\right) if\ sp \le r_1 \tag{3}$$

In Equation 3, X_i^a and X_i^b are pollen bundles of different flowers of the same plant, that is, different solutions of the solution set. ε is a random local pollination distance and has a value between [0, 1].

2.2 Gradient Boosting Regressor (GBR)

GBR was first mentioned by Friedman [16]. Gradient Boosting Regression is a widely used algorithm in the field of machine learning and provides effective results, especially in regression problems. This algorithm aims to create a strong predictor model by combining many weak predictor models (usually decision trees) [17]. GBM is the process of creating strong learners from weak learners. Gradient Boosting, as the name suggests, uses a gradient descent optimization algorithm. Each predictor is trained by trying to minimize the difference between the actual output values and the predictions. In this way, at each step, the model compensates for the errors of the previous steps and a stronger estimator is created [18]. GBM in turn builds new trees based on the residuals. Trees are trained by adding them sequentially to recreate the residue by taking into account the residues of the previous tree. If there is no further improvement in performance, new trees are added until the number of trees reaches the maximum level. The predictions are updated so that the sum of the residuals is close to 0 or the predicted values are close enough to the actual values [16]. In Gradient Boosting, the estimator is trained by trying to minimize the difference between the actual output values and the predictions, at each step the model compensates for the errors of the previous steps and a stronger estimator is created. This situation is shown in Fig. 1.

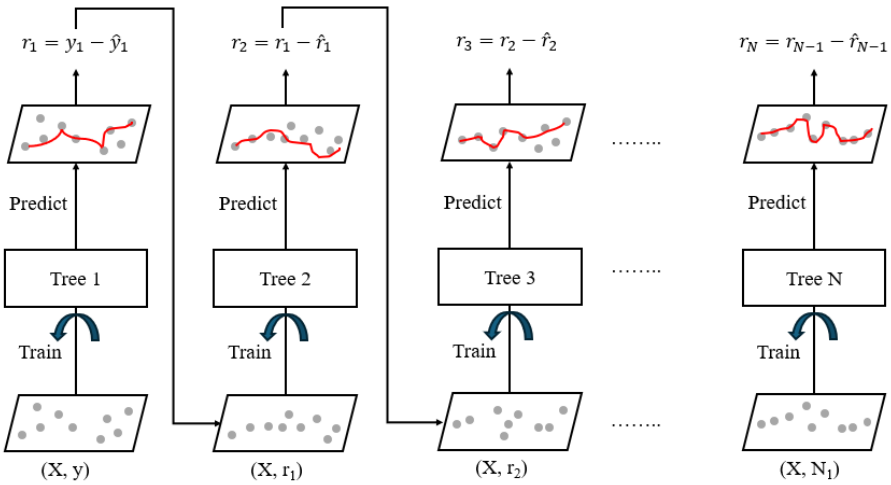

Fig. 1 Working principle of gradient boost regression algorithm [19]

The parameters of Gradient Boosting Regression are loss, learning_rate, n_estimators, subsample, max_depth and random_state. In this study, how the length prediction changes according to the variation of Graident Boosting parameters is analyzed.

2.3 Gradient Boosting Regressor (GBR) Parameters

2.3.1 Loss

With this parameter, the loss function is optimized. Loss has 4 different values. ‘squared_error’ is the squared error for the regression. 'Absolute_error' refers to the absolute error of the regression. 'huber' is a combination of 'square_error' and 'absolute_error'. 'quantile' allows quantile regression. By default, “squared_error” is selected [20].

2.3.2 Learning rate

This parameter determines the impact of each tree on the final result. A lower value generally provides higher performance because it makes the model resistant to certain properties of the tree. 0.1 is selected as default [20, 21].

2.3.3 n_estimators

This parameter refers to the number of ordered trees to be modeled. Gradient boosting is highly resistant to overfitting, so a larger number generally gives better performance. By default, 100 is selected [20].

2.3.4 Subsample

This parameter is the proportion of observations to be selected for each tree. Values must be between 0 and 1. By default, 1 is selected 20, 21].

2.3.5 Max_depth

This parameter expresses the maximum depth of individual regression estimators. The maximum depth limits the number of nodes in the tree. By default, 3 is selected [20, 21].

2.3.6 Random_state

This parameter controls the random seed given to each tree estimator at each iteration of boosting. When the random number is not fixed, different results are obtained in subsequent runs on the same parameters. By default, none is selected [20, 21].

2.3.7 Performance Evaluation

In this study, the coefficient of determination (R^2) was used for performance evaluation. The R^2 value determines how effective the independent variable is on the dependent variable. The higher the R^2 value, the greater the effect of the independent variable on the dependent variable.

3. Numerical Example

Fig. 2 shows a symmetrical truss system consisting of five bar elements and a symmetrical semi-system of this system. In the system, the modulus of elasticity (E) of the material for the structural elements is defined as 200000 MPa and the bar cross-sectional areas (A) are defined as 100 mm^2. The loads applied to the nodal points in the system are 100000 N (P_1) and 50000 N (P_2) respectively and each span (L) is 1000 mm [22].

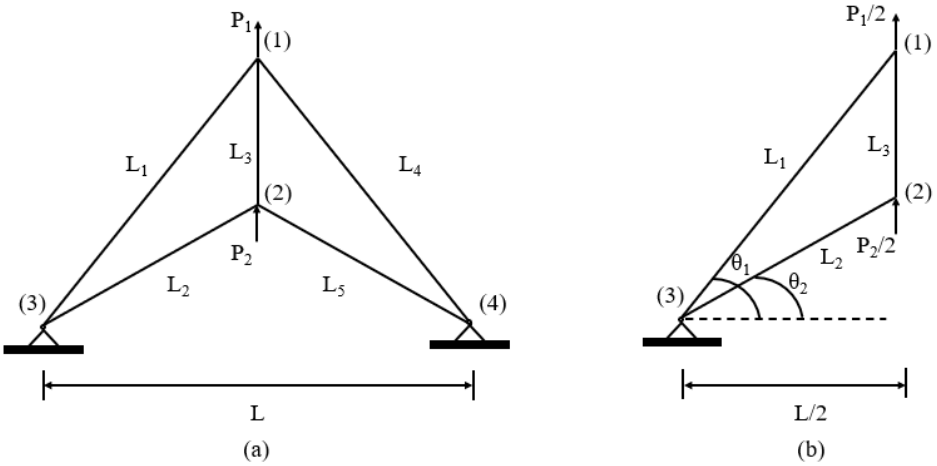

Fig. 2 Five-element truss system (a) and symmetrical semi-system (b) [22]

The objective of the problem is to find the optimum values of design variables θ_1 and θ_2 that will minimise the total bar length in the system. The mathematical expression of the objective function of the problem depending on these design variables is given by Equation 4.

$$Min\ f(\theta_1, \theta_2) = \sum_{i=1}^{3} L_i \tag{4}$$

The lengths of the bars L_1, L_2 and L_3, which are expressed by Li in the equation, can be obtained by utilising the geometrical relations in the following equations (Equations 5-7).

$$L_1 = \frac{L}{2\cos(\theta_1)} \tag{5}$$

$$L_2 = \frac{L}{2\cos(\theta_2)} \tag{6}$$

$$L_3 = \frac{L}{2\cos(\theta_1)\cos(\theta_2)}\sqrt{cos^2(\theta_1) + cos^2(\theta_2) - 2\cos(\theta_1)\cos(\theta_2)\cos(\theta_1 - \theta_2)} \tag{7}$$

The lower and upper limit values of design variables in the problem can be seen below. The vertical displacements (Δ_1 and Δ_2) that will occur at the nodes 1 and 2 of the system (Δ_1 and Δ_2) are defined as the design constraint in the optimization between these limits and these values can be obtained by Equation 8 and Equation 9, respectively. The upper limit of the displacements (MaxΔ) is set as 5 mm.

$$|\Delta_1(\theta_1, \theta_2)| \leq Max\Delta \tag{8}$$

$$|\Delta_2(\theta_1, \theta_2)| \leq Max\Delta \tag{9}$$

To define the problem at this point, optimization is the process of finding the combination of the optimum values of the angles θ_1 and θ_2 between the limits 0 and $\pi/3$ that will minimise the total lengths of the bars in the system according to the maximum vertical displacement condition that will occur at the nodal points. The displacements of these nodal points can be found by utilising the static equilibrium equation $K\Delta=P$. In this expression, K, Δ and P are the global stiffness matrix, displacement vector and load vector of the system, respectively. Where B is the transformation and k is the stiffness matrix in local coordinates [22].

4. Results

6 different GBR parameters were used in the study and their effects on the success of the model are given in 3 tables. In Table 1, the effects of "loss" and "learning_rate" parameters are analysed. When the " loss" parameter is analysed in Table 1, it is seen that "huber" gives the highest R^2 value. When the "learning_rate" parameter is analysed, it is seen that tree different values give very close R^2 values.

Table 1. Effects of the loss and learning_rate parameters

Parameters	Model Architecture	R^2
Default	loss = "squared_error", learning_rate = "0.1", n_estimators = "100", subsample = "1.0", max_depth = "3" and random_state ="None"	0.7782932012302574
loss	loss = "absolute_error", learning_rate = "0.1", n_estimators = "100", subsample = "1.0", max_depth = "3" and random_state ="None"	0.8013087458644967
	loss = "huber", learning_rate = "0.1", n_estimators = "100", subsample = "1.0", max_depth = "3" and random_state ="None"	0.8632505066906953
	loss = "quantile", learning_rate = "0.1", n_estimators = "100", subsample = "1.0", max_depth = "3" and random_state ="None"	0.6052297068035059
learning_rate	loss = "squared_error", learning_rate = "0.2", n_estimators = "100", subsample = "1.0", max_depth = "3" and random_state ="None"	0.7935857655705246
	loss = "squared_error", learning_rate = "0.3", n_estimators = "100", subsample = "1.0", max_depth = "3" and random_state ="None"	0.7856826366025179

In Table 2 the effects of "n_estimator " and "subsample" parameters are analysed. When the "n_estimators" parameter is analysed in Table 2, it is seen that increasing the "n_estimators" value increases R^2. When the “subsample” parameter is analysed, it is seen that as the value of “min_samples_split” increases, the success of the model increases.

Table 2. Effects of the n_estimators and subsample parameters

Parameters	Model Architecture	R^2
Default	loss = "squared_error", learning_rate = "0.1", n_estimators = "100", subsample = "1.0", max_depth = "3" and random_state ="None"	0.7782932012302574
n_estimators	loss = "squared_error", learning_rate = "0.1", n_estimators = "200", subsample = "1.0", max_depth = "3" and random_state ="None"	0.7732459327307178
	loss = "squared_error", learning_rate = "0.1", n_estimators = "300", subsample = "1.0", max_depth = "3" and random_state ="None"	0.7960658531751359
	loss = "squared_error", learning_rate = "0.1", n_estimators = "400", subsample = "1.0", max_depth = "3" and random_state ="None"	0.8099926567558429

subsample	loss = "squared_error", learning_rate = "0.1", n_estimators = "100", subsample = "0.2", max_depth = "3" and random_state ="None"	0.7460412241190434
	loss = "squared_error", learning_rate = "0.1", n_estimators = "100", subsample = "0.4", max_depth = "3" and random_state ="None"	0.7647154381874797
	loss = "squared_error", learning_rate = "0.1", n_estimators = "100", subsample = "0.6", max_depth = "3" and random_state ="None"	0.7937362213012464

In Table 3 the effects of "max_depth " and "random_state " parameters are analysed. When the "max_depth" parameter is analysed in Table 3, it is seen that as the value of "max_depth" increases, the success of the model increases. When the "random_state" parameter is analysed from Table 3, it is seen that two different values give slightly the same R^2 values.

Table 3. Effects of the max_depth and random_state parameters

Parameters	Model Architecture	R^2
Default	loss = "squared_error", learning_rate = "0.1", n_estimators = "100", subsample = "1.0", max_depth = "3" and random_state ="None"	0.7782932012302574
max_depth	loss = "squared_error", learning_rate = "0.1", n_estimators = "100", subsample = "1.0", max_depth = "6" and random_state ="None"	0.8489182986281969
	loss = "squared_error", learning_rate = "0.1", n_estimators = "100", subsample = "1.0", max_depth = "9" and random_state ="None"	0.8556135769627911
random_state	loss = "squared_error", learning_rate = "0.1", n_estimators = "100", subsample = "1.0", max_depth = "3" and random_state ="5"	0.776666025448429
	loss = "squared_error", learning_rate = "0.1", n_estimators = "100", subsample = "1.0", max_depth = "3" and random_state ="20"	0.7799941959124016

5. Conclusions

In this study, firstly, the overall length optimization of the truss system is performed using the Flower Pollination Algorithm (FPA). The Gradient Boosting Regressor (GBR) model is used to predict the overall length optimization of truss system on the 900-row dataset obtained as a result of the optimization and the effect of GBR parameters on performance is examined. The coefficient of determination (R^2) was used in performance evaluation.

The effect of different values of different parameters on the performance of the model is examined, and it is seen that the most effective way to increase the success of the model is to increase the "max_depth" parameter. This is because higher depth allows the model to learn relationships that are very specific to a given sample. The "n_estimators" parameter also significantly affected the performance of the model, but it is not as effective as "max_depth".

References

1. Yang X S (2012) Flower Pollination Algorithm for Global Optimization. In: Unconventional Computation and Natural Computation: 11th International Conference, 3-7 Eylül 2012, Orléan, Fransa, Proceedings 11, Springer Berlin Heidelberg, Germany, 240-249.
2. Cao, H. Q., Nguyen, H. X., Tran, T. N. C., Tran, H. N., & Jeon, J. W. (2021). A robot calibration method using a neural network based on a butterfly and flower pollination algorithm. IEEE Transactions on Industrial Electronics, 69(4), 3865-3875. https://doi.org/10.1109/TIE.2021.3073312.
3. Abdalkareem, Z. A., Al-Betar, M. A., Amir, A., Ehkan, P., Hammouri, A. I., & Salman, O. H. (2022). Discrete flower pollination algorithm for patient admission scheduling problem. Computers in biology and medicine, 141, 105007. https://doi.org/10.1016/j.compbiomed.2021.105007.
4. Adithiyaa, T., Chandramohan, D., & Sathish, T. (2020). Flower Pollination Algorithm for the Optimization of Stair casting parameter for the preparation of AMC. Materials Today: Proceedings, 21, 882-886. https://doi.org/10.1016/j.matpr.2019.07.711.
5. Ong, P., Jian, J., Yin, J., & Ma, G. (2023). Characteristic wavelength optimization for partial least squares regression using improved flower pollination algorithm. Spectrochimica Acta Part A: Molecular and Biomolecular Spectroscopy, 302, 123095. https://doi.org/10.1016/j.saa.2023.123095.
6. Abdullah, M., Javaid, N., Khan, I.U., Khan, Z.A., Chand, A., Ahmad, N. (2020). Optimal Power Flow with Uncertain Renewable Energy Sources Using Flower Pollination Algorithm. In: Barolli, L., Takizawa, M., Xhafa, F., Enokido, T. (eds) Advanced Information Networking and Applications. AINA 2019. Advances in Intelligent Systems and Computing, vol 926. Springer, Cham. https://doi.org/10.1007/978-3-030-15032-7_8.

7. Bekdaş, G., Nigdeli, S. M., & Yang, X. S. (2015). Sizing optimization of truss structures using flower pollination algorithm. Applied Soft Computing, 37, 322-331. https://doi.org/10.1016/j.asoc.2015.08.037.
8. Nigdeli, S. M., Bekdaş, G., & Yang, X. S. (2016). Application of the flower pollination algorithm in structural engineering. Metaheuristics and optimization in civil engineering, 25-42.
9. Nigdeli, S. M., Bekdas, G., & Yang, X. S. (2016). Optimum tuning of mass dampers for seismic structures using flower pollination algorithm. Int. J. Theor. Appl. Mech, 1, 264-268.
10. Bekdas, G., Nigdeli, S. M., & Yang, X. S. (2017). Size optimization of truss structures employing flower pollination algorithm without grouping structural members. Int. J. Theor. Appl. Mech, 1, 269-273.
11. Mergos, P.E., Mantoglou, F. Optimum design of reinforced concrete retaining walls with the flower pollination algorithm. Struct Multidisc Optim 61, 575–585 (2020). https://doi.org/10.1007/s00158-019-02380-x.
12. Mergos, P. E. (2021). Optimum design of 3D reinforced concrete building frames with the flower pollination algorithm. Journal of Building Engineering, 44, 102935. https://doi.org/10.1016/j.jobe.2021.102935.
13. Kayabekir, A. E., Bekdaş, G., & Nigdeli, S. M. (2021). Optimum design of reinforced concrete T-beam considering environmental factors via flower pollination algorithm. International Journal of Engineering and Applied Sciences, 13(4), 166-178. https://doi.org/10.24107/ijeas.1037908.
14. Aydın, Y., Bekdaş, G., Nigdeli, S.M. (2023). Reinforced Concrete Beam Optimization via Flower Pollination Algorithm by Changing Switch Probability Parameter. In: Vasant, P., et al. Intelligent Computing and Optimization. ICO 2023. Lecture Notes in Networks and Systems, vol 852. Springer, Cham. https://doi.org/10.1007/978-3-031-50330-6_7.
15. Ocak, A., Bekdaş, G., & Nigdeli, S. M. (2024). Flower Pollination Algorithm for Optimum Design of Base Isolation Systems under Near-Fault Effect. Available at SSRN 4752577. http://dx.doi.org/10.2139/ssrn.4752577.
16. Friedman, J. H. (2001). Greedy function approximation: a gradient boosting machine. Annals of statistics, 1189-1232.
17. Otchere, D. A., Ganat, T. O. A., Ojero, J. O., Tackie-Otoo, B. N. and Taki, M. Y., "Application of gradient boosting regression model for the evaluation of feature selection techniques in improving reservoir characterisation .predictions", Journal of Petroleum Science and Engineering, 208 (2022). https://doi.org/10.1016/j.petrol.2021.109244
18. Sagi, O., & Rokach, L. (2018). Ensemble learning: A survey. Wiley interdisciplinary reviews: data mining and knowledge discovery, 8(4), e1249. https://doi.org/10.1002/widm.1249.
19. GeeksforGeeks, "Gradient Boosting Regression".[accessed 21 April 2024]. Available online: https://www.geeksforgeeks.org/ml-gradient-boosting/.
20. sklearn.ensemble.GradientBoostingRegressor [accessed 21 April 2024]. Available online: https://scikit-learn.org/stable/modules/generated/sklearn.ensemble.GradientBoostingRegressor.html.
21. Complete Machine Learning Guide to Parameter Tuning in Gradient Boosting (GBM) in Python [accessed 21 April 2024]. Available online: https://www.analyticsvidhya.com/blog/2016/02/complete-guide-parameter-tuning-gradient-boosting-gbm-python/.
22. Bekdaş G., Nigdeli S.M., Yüel, M., & Kayabekir A.E. (2021) Artificial Intelligence Optimization Algorithms and Engineering Applications. Seçkin Publishing.

Evaluation of PEI-PVAc Composite Membranes with Titania Filler for Mechanical and Gas Separation Performance

Asif JAMIL[1]*, Khuram MAQSOOD[2], Giedrius JANUSAS[1]

1 Department of Mechanical Engineering, Kaunas University of Technology (KTU), Kaunas, Lithuania
2 Department of Chemical Engineering, University of Jeddah, Jeddah, Saudi Arabia
** muhammad.jamil@ktu.lt*

Abstract

Composite membranes, ascertain advantages over polymeric and inorganic ones for gas separation. In this study, composite membranes were developed using wet-phase inversion technology. A blend of polyetherimide (PEI) and polyvinyl acetate (PVAc) in ratios of (98 to 2 wt. %) was used as organic phase and inorganic phase comprised of titanium dioxide (TiO_2) was incorporated at 1 and 2 wt. %. The study aimed to assess titania's impact on thermal, surface mechanical, and gas separation properties. TGA and DSC analyzed thermal properties, nano-indentation tests assessed surface mechanical characteristics, and gas permeation experiments determined separation performance. Results showed TiO_2-containing membranes had enhanced thermal properties and surface hardness. Gas permeation (CO_2/CH_4 & CO_2/N_2) experiments revealed superior separation performance, notably in membranes with 2 wt. % TiO_2, improving compatibility between rubbery and glassy phases and enhancing overall membrane performance.

Keywords: Composite membrane, Blend membrane, titania, gas separation, Nanoindentation.

1. Introduction

Membrane technology is gaining traction due to its energy efficiency and economic benefits in gas separation applications. However, commercially available membranes face constraints due to the trade-off between gas permeability and selectivity. Polymer blends offer a promising alternative, but compatibility between paired polymers and maintaining mechanical properties pose challenges. Blending different polymers creates materials with synergistic properties, customizable for specific applications. Nanoscale structures are advantageous, facilitating the solution-diffusion mechanism and considering molecular interactions with gases [1, 2].

Immiscibility in polymer blends affects product properties at the molecular level, leading to unstable phase morphology and inadequate mechanical performance during processing. Compatibilizers, acting as surfactants, improve interfacial interactions and blend properties, commonly derived from matrix polymer monomers [3]. However, complex synthesis and limited applicability prompt exploration of alternatives. Incorporating nanoparticles in immiscible blends reduces phase separation and enhances mechanical and thermal stability. Adding TiO_2 nanoparticles to PEI-PVAc blends improves physiochemical properties, refining the blend's structure. In this study, pure PEI, PEI-PVAc blend and composite membrane comprising of PEI-PVAc with 2 wt. % titania loading were prepared and characterized for mechanical, thermal and gas separation properties.

2. Experimental

2.1 Materials and Methods

In this study, we utilized polymers like PEI and PVAc. N-methyl-2-pyrrolidone (NMP) served as the solvent, while titania nanoparticles with a primary particle size of 21nm were employed. All the mentioned chemicals were acquired from Sigma Aldrich. The dope solutions for PEI, bend and composite membranes were synthesized by opting the methods discussed somewhere else [4].

2.2 Membrane fabrication

The sope solution was dropped onto the glass plate, followed by uniform spreading with the help of a casting knife that to achieve a film thickness of 150 µm. Subsequently the developed membranes were immersed in water bath at ambient conditions, later, air-dried at room temperature to ensure complete solvent removal.

In subsequent references, the different membranes developed in this study will be denoted as follows: Pure PEI as PEI, the PEI-PVAc blend as PP(2) and the PEI-PVAc blend containing 2 wt. % titania nanoparticles as PPT(2) respectively.

2.3 Membrane Characterizations

The developed membranes were characterized for thermal characterizations by using Thermogravimetric analysis (TGA) under nitrogen environment.

The indentation tests were performed using the continuous stiffness measurement technique, which involves monitoring and recording the dynamic load and displacement of a three-sided pyramidal diamond (Berkovich) indenter. Nanoindentation provides a means to measure mechanical properties of thin layers.

The gas permeation performance of developed membranes was carried out by using 99.99 % pure N_2, CO_2 and CH_4 gases at room temperature at 2 bar pressure. The detailed description of the gas permeation tests is discussed somewhere else [5]. The following equations (1 & 2) are used to determine the permeability and selectivity.

$$P_i = \frac{Ql}{A\Delta P}\frac{273.15}{T} \tag{1}$$

$$\alpha_{ij} = \frac{P_i}{P_j} \tag{2}$$

The gas permeability (P_i) is expressed in barrer units. The subscript "i" denotes the penetrating gas, which could be N_2, CO_2, or CH_4. "Q" represents the volumetric flow rate (cm^3/s), while "A" denotes the effective surface area of the membrane (cm^2). ΔP indicates the pressure difference across the membrane (cm Hg), and "T" represents the temperature in Kelvin. The term α_{ij} signifies the ideal selectivity of gas "i" to gas "j".

3. Results and discussions

3.1 Thermal Characterization

TGA was used to study the thermal behavior of the developed membranes. The decomposition curves (Fig. 1) revealed a single major mass loss for all membrane fibers. Notably, no weight loss was detectable below 100°C, indicating the absence of moisture in the developed membranes. The pure PEI membrane demonstrated an onset temperature of around 440°C, aligning with previously published literature [6]. A 10% weight loss served as a reference point for comparing membrane degradation. The weight loss between 100 to 300 °C represents the mass of solvent retained in the membranes and that which evaporated as the temperature increased.

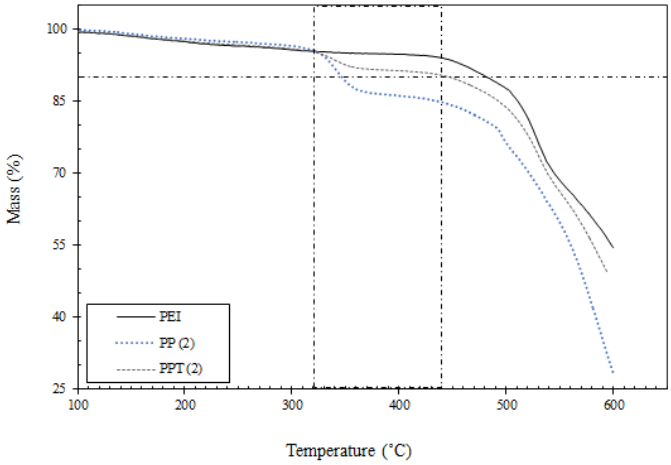

Fig. 1 TGA analysis of developed membranes

Moreover, the addition of PVAc to the PEI matrix led to a decline in thermal properties as the proportion of the rubbery phase increased. Neat PEI displayed a degradation temperature of 482°C, which decreased to 340°C for PP(2), indicating a reduction in thermal properties with the addition of rubbery PVAc to the glassy PEI matrix. However, this trend reversed with the incorporation of titania nanoparticles in the blend membranes. Introducing 2 wt.% of titania nanoparticles in the PEI-PVAc blend resulted in a recovery of the degradation temperature, reaching 450°C, suggesting an enhancement in thermal stability with titanium addition to the blend membrane.

3.2 Surface Mechanical Characterizations

Figure 2 illustrates the compliance curve of the neat PEI, PP (2), and PPT (2) membranes. Each sample underwent nine indents with a spacing of 40 μm between them. A constant load of 15 mN was applied to the membrane samples, resulting in a maximum penetration depth of 15 μm. Following the application of constant force, the unloading phase exhibited a creep region. Creep refers to the change in depth over time while maintaining a constant force, reaching a new limit just before unloading. Subsequently, the indenter begins to unload. The absence of overlap between the loading and unloading

curves suggests that the developed membranes demonstrate both elastic behavior and distinct plastic characteristics [7]. The loading and unloading curves appeared continuous and stable for all the developed membranes.

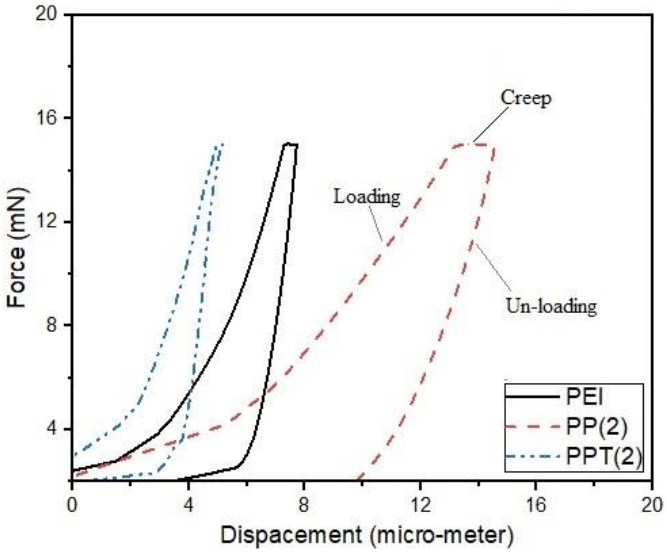

Fig. 2 Load displacement analysis of the casted membranes

The spacing between indents was adjusted to prevent the overlap of internal stresses generated around each indent. In the case of the neat PEI sample, the indenter penetrated to a maximum contact depth of 7.7 μm, while this measurement increased to 14.00 μm for PP(2). However, the value decreased to 5.08 μm for the blend sample incorporating 2 wt.% of titania nanoparticles. It is evident that the presence of PVAc in the PEI matrix reduces the surface hardness and stiffness. Conversely, by integrating titania nanoparticles nanoparticles into the blend sample, the surface becomes stiffer and harder. This change can be attributed to the uniform dispersion of titania nanoparticles nanoparticles within the polymer matrix, which enhances the stiffness of the membranes. These findings are indirectly supported by the thermal analysis discussed in the previous section. Consistent with previous literature, the addition of nanoparticles to the polymer matrix resulted in a stiffer and harder surface [5]. Therefore, ensuring the appropriate dispersion of nanoparticles can enhance membrane hardness and resistance to indenter penetration.

3.3 Gas Separation Performance

Figure 3 illustrates the CO_2 permeance and ideal selectivity (CO_2/CH_4, CO_2/N_2) of the pure PEI, blend, and composite membranes. The figures unmistakably show that the composite membrane outperforms the others in terms of performance. The CO_2 permeance exhibits an increasing trend with the addition of PVAc. In the PEI-PVAc blend membrane, the CO_2 permeance is 26.1% higher than that of the neat PEI membrane at ambient temperature and 2 bar pressure. The inclusion of the rubbery PVAc phase in the blend leads to loosely packed polymer chains, resulting in increased free volume. This loose structure facilitates the diffusion of smaller molecules through the blend matrix, enhancing the permeation of CO_2, CH_4, and N_2. Additionally, CO_2 benefits from higher solubility and a smaller kinetic diameter, giving it an advantage in dissolving and diffusing through the blend membrane matrix. This advantage is reflected in the relative ideal selectivity of the developed blend membrane. Similar observations were reported by Farman et al. when PVAc was added to PES [8], where almost double the value of CO_2 permeance and 3.6 times increase in ideal (CO_2/CH_4) selectivity at 10 bar pressure were observed compared to neat PES.

Conversely, the incorporation of titania nanoparticles also positively impacts the CO_2 permeance of the mixed matrix membrane. CO_2 permeance increases with the titania nanoparticles content in the blend. With a 2 wt. % addition of titania filler in the blend, the permeation is 36% higher compared to the neat sample. Incorporating titania nanoparticles into the PEI-PVAc polymer blend results in nanoparticle aggregation and the creation of voids at the titania-polymer interface, thereby enhancing gas diffusion through the membrane. Similar observations were reported by Abdullah et al. when TiO_2 nanoparticles were incorporated into PES-PVAc blend membranes [9], showing a 32.4% increase in CO_2 permeance and a 65.9% surge in ideal (CO_2/CH_4) selectivity at 10 bar pressure and 25°C. Thus, the addition of titania nanoparticles proves advantageous for both gas selectivity and CO_2 permeance in blend polymeric membranes. A similar behavior can be expected for CO_2/N_2 selectivity since the kinematic diameter of N_2 gas molecules is also larger compared to CO_2 [10].

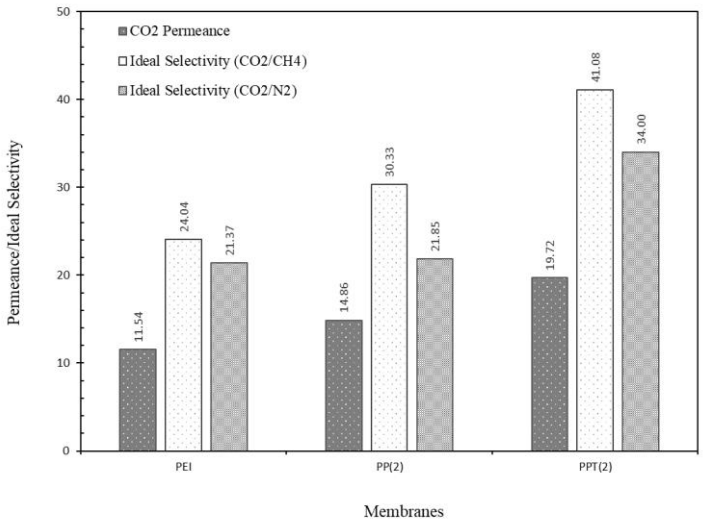

Fig. 3 CO_2 permeance and gas separation performance of the membranes

4. Conclusions

The study investigated the impact of incorporating titania nanoparticles into a PEI-PVAc blend membrane on its thermal, surface mechanical, and gas separation properties. Incorporating titania nanoparticles into the blend membrane enhanced its thermal stability, as evidenced by TGA analysis. Surface analysis revealed a stiffer and harder surface attributed to the uniform dispersion of nanoparticles within the polymer matrix compared to both neat and blend counterparts.

When compared to pure PEI, the PEI-PVAc blend membrane performed better at gas separation, and the addition of titania nanoparticles improved ideal gas separation even more. The optimal results were obtained with a 2 wt. % TiO_2 addition in the PEI-PVAc matrix, achieving high selectivity for CO_2/CH_4 and CO_2/N_2. These findings demonstrate the potential of incorporating nanoparticles to improve the performance of polymer blend membranes in gas separation applications.

Acknowledgement

This research was funded by a grant No. S-PD-24-28 from the Research Council of Lithuania (LMTLT).

References

1. Jamil, A., O.P. Ching, and A.M. Shariff, Polymer-nanoclay mixed matrix membranes for CO2/CH4 separation: A review. Applied Mechanics and Materials, 2014. 625: p. 690-695.
2. Khurram, A.R., et al., Environmental remediation through various composite membranes moieties: Performances and thermomechanical properties. Chemosphere, 2022: p. 136613.
3. Kapantaidakis, G., et al., Gas permeation through PSF-PI miscible blend membranes. Journal of membrane science, 1996. 110(2): p. 239-247.
4. Maqsood, K., Jamil, A., Ahmed, A., Sutisna, B., Nunes, S. and Ulbricht, M., 2023. Effect of TiO2 on Thermal, Mechanical, and Gas Separation Performances of Polyetherimide–Polyvinyl Acetate Blend Membranes. Membranes, 13(8), p.734.
5. Jamil, A., Zulfiqar, M., Arshad, U., Mahmood, S., Iqbal, T., Rafiq, S. and Iqbal, M.Z., 2020. Development and performance evaluation of cellulose acetate-bentonite mixed matrix membranes for CO2 separation. Advances in Polymer Technology, 2020, pp.1-12.
6. Jamil, A., O.P. Ching, and A.M. Shariff, Mixed matrix hollow fibre membrane comprising polyetherimide and modified montmorillonite with improved filler dispersion and CO2/CH4 separation performance. Applied Clay Science, 2017. 143: p. 115-124.
7. Sulaiman, M., Iqbal, T., Yasin, S., Mahmood, H. and Shakeel, A., 2021. Fabrication and nanomechanical characterization of thermoplastic biocomposites based on chemically treated lignocellulosic biomass for surface engineering applications. Frontiers in Materials, 8, p.733109.
8. Farnam, M., H. Mukhtar, and A. M. Shariff. "An investigation on polymeric blend mixed matrix membranes of polyethersulfone/polyvinyl acetate/carbon molecular sieve for CO2/Ch4 separation." Journal of Fundamental and Applied Sciences 9.7S (2017): 612-622.
9. Abdullah, M.A., et al., Polyethersulfone/polyvinyl acetate blend membrane incorporated with TiO2 nanoparticles for CO2/CH4 gas separation. Malaysian J. Fundam. Appl. Sci, 2017. 13(4): p. 774-777.
10. Vaezi, M.J., Babaluo, A.A. and Maghsoudi, H., 2018. Separation of CO2 and N2 from CH4 using modified DD3R zeolite membrane: A comparative study of synthesis procedures. Chemical Engineering Research and Design, 134, pp.347-358.

Investigation of the Effect of Decision Tree Regressor Parameters on the Optimum Section Design of Reinforced Concrete T-Beam Under Simple Bending Effect

Yaren AYDIN[1]*, Sinan Melih NİGDELİ[1]*, Gebrail BEKDAŞ[1]*

1 Istanbul University-Cerrahpaşa, Civil Engineering Department, 34320 Avcılar, Istanbul, Turkey,
** yaren.aydin1@ogr.iuc.edu.tr, melihnig@iuc.edu.tr, bekdas@iuc.edu.tr*

Abstract

Cost optimization is one of the most important issues in structural engineering, provided that safety is ensured. In this study, a dataset of 800 lines was obtained primarily by using optimization with JA. Later, this dataset was used in machine learning and the effect of the parameters of the decision tree algorithm in the calculation of the optimum cost was examined. Machine learning is used in almost all fields today. Decision trees are one of the machine learning models. Decision trees, one of the most widely used methods in classification and regression analysis, are a set of rules that identify statistically significant groups and transform the results into easy-to-read tree diagrams. In this study, how the cost prediction changes according to the variation of Decision Tree Regressor parameters is analysed. The parameters are criterion, splitter, max_depth, min_samples_split, min_samples_leaf and random_state. As a result, it was observed that the parameter that most negatively affects the success of the model is increasing "min_samples_leaf".

Keywords: parameter effect, cost optimization, jaya, decision tree, machine learning.

1. Introduction

Optimization is reaching the best result for solving a problem and is used effectively in many different problems. Examples of optimization types include size optimization, weight optimization, cost optimization. Cost optimization is important today due to the increasing price of every product. As long as safety conditions are met, realizing the optimum design in terms of finance is one of the most basic duties of an engineer. For this reason, in this study, this optimization problem, which is addressed for the optimum section design of a T-section (table) reinforced concrete beam under the influence of bending moment, has been realized using the Jaya Algorithm (JA). In the example in this study, the "TS: 500 Design and construction rules of reinforced concrete structures" regulation was used. The data set obtained from the optimization process was used in machine learning. Machine learning is used in many areas of daily life and is a subset of artificial intelligence. Machine learning is a system that can learn from data through experiences and make decisions with minimal human intervention. Changing the parameters of any ML model affects the model architecture and performance. In this study, Decision Tree Regression, one of the machine learning models, was used in cost prediction and the effects of its parameters on the estimation performance were examined.

2. Methodology

2.1 Jaya Algorithm (JA)

Jaya Algorithm (JA) is a metaheuristic optimization method used in solving optimization problems. JA was first proposed by Rao [1] in 2016 for the optimization of functions with and without limiters. The word Jaya means 'victory' in Sanskrit. The working logic of the Jaya algorithm is to approach the best solution and move away from the worst solution in the search process. JA is a very simple optimization method to implement since it contains only two control parameters: population size and maximum number of iterations. For this reason, JA has been applied in many different areas in a short time. These are the identification of photovoltaic cells and modules [2], dimensional optimization of a micro-channel heat sink [3], workflow scheduling [4], short-term load forecasting [5], etc.

In addition to its applications in different fields, JA has also been used in civil engineering. Degertekin et al. [6] achieved the optimum design of lattice structures using JA. Kayabekir et al. [7] carried out the optimum design of carbon fiber reinforced polymer strips to increase the shear capacity of reinforced concrete beam using JA. Bekdas et al. [8] minimized the vertical deflection by optimizing the dimensions of the I-beam with JA. Kayabekir et al. [9] used JA for optimum design of T beams. Rakıcı et al. [10] carried out the optimal cost design of single-storey reinforced concrete frames using JA. Aslay and Dede [11] carried out 3D cost optimization of a 3-storey reinforced concrete structure using JA. Cakiroglu et al. [12] used JA to minimize CO_2 emissions and concrete and steel production cost. Ding et al. [13] used JA for structural damage detection. Coşut et al. [14] carried out the optimum design of Tuned Mass Damper (TMD) using JA. Cakiroglu et al. [15] used JA in the cross-section optimization of rectangular concrete-filled steel tubular columns. Türkoğlu et al. [16] used JA in the cost optimization of this reinforced concrete foundation.

JA is a single-phase metaheuristic algorithm that uses the worst (gw) and best (g*) solutions in a single equation formulation. The Jaya algorithm starts the optimization process by generating random solutions forming the population in optimization.

Depending on the nature of the optimization problem, the best and worst solutions in the population are determined. Using the best and worst solutions, a new solution is generated using a JA-specific formulation (Equation 1) [1].

$$X_{new} = X_{old} + rand()(g^* - X_{old}) - rand()(g^w - X_{old}) \quad (1)$$

In Equation 2, X_{new} and X_{old} are the updated new and existing solutions, respectively. A new solution is generated using a random number between 0 and 1 (rand(0,1)). The new solution and the previous solution are compared. If the new solution is better than the previous solution, it is assigned to the previous solution. Otherwise, the previous solution is left as it is. These steps are repeated for each solution in the population until the maximum iteration. As a result, the best solution is defined as the optimum solution and the optimization process is finished [1].

The 800-row dataset obtained as a result of optimization with JA was used in machine learning. Decision Tree Regressor (DTR), which is one of the machine learning models and used in this study, is explained in the rest of the paper.

2.2 Decision Tree Regressor (DTR)

Decision trees are predictive models that use a set of hierarchical rules on feature variables arranged in a tree-like structure of the prediction process. Each tree is a fairly simple model with branches, nodes and leaves. The root node is the node corresponding to the best predictor at the top of the tree. It divides the tree into two or more homogeneous clusters. When a child node is split into other child nodes, the node into which it is split is called a decision node. The last node is called the leaf node. The tree structure and levels are shown in Fig. 1 [17].

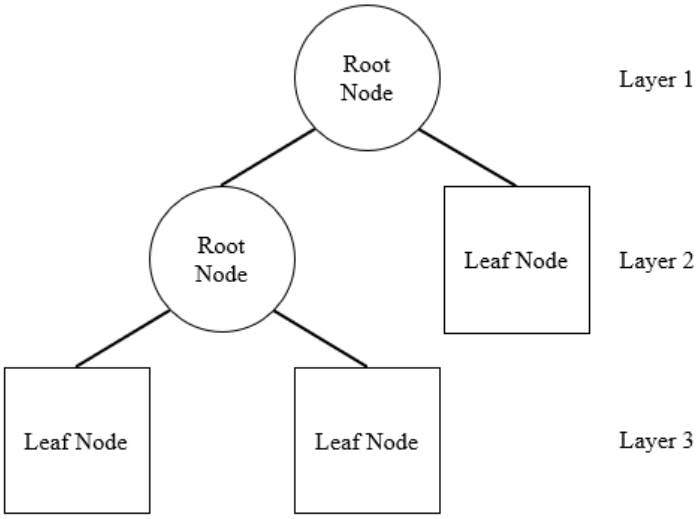

Fig. 1 Tree structure and levels [2]

When performing regression in node calculations, standard deviation (Equation 2) is taken into account. First, the standard deviation of the target cluster is obtained and double standard deviation values (Equation 3) are obtained between the other clusters and the target clusters. Both results are derived from the standard deviation value of the objective set (Equation 3). The cluster with the largest SDR value is determined as the root. These processes are repeated for each node, creating a tree structure [18].

$$S = \sqrt{\frac{\sum(x-u)^2}{n}} \quad (2)$$

$$S(T,X) = \sum c \epsilon X P(c) S(c) \quad (3)$$

$$SDR(T,X) = S(T) - S(T,X) \quad (4)$$

The algorithm stops when it encounters a stopping condition. The stopping condition is applied to the decision tree hyperparameters. Max_depth, which expresses the maximum depth of the decision tree, min_samples_split, the minimum number of samples that a node should have before splitting, min_samples_leaf, the minimum number of samples that a leaf should have, and max_leaf_nodes, the maximum number of leaves, are the most well-known hyperparameters.

In this study, the parameters that affect the prediction performance of the decision tree are criterion, splitter, max_depth, min_samples_split, min_samples_leaf and random_state.

2.2 Decision Tree Regressor (DTR) Parameters

2.2.1 Criteration

With this parameter, the quality of a partition is measured. Criteration has 4 different values. These are “squared_error”, “friedman_mse”, “absolute_error”, “poisson”. “squared_error” selected by default is the mean square error equal to the variance reduction as the feature selection criterion. “absolute_error” uses the median of each terminal node for the average absolute error. “poisson” uses the decrease in Poisson deviance to find divisions [19].

2.2.2 Splitter

The division in the node is selected with the splitter. By default, "best" is used to select the best partition. “random” is used to choose the best random split [19].

2.2.3 Max_depth

Max_depth controls the maximum depth of the tree. The greater the depth of the tree, the more complex the model becomes. By default, “None” is selected. When None is selected, nodes are expanded until all leaves are pure. When max_depth is selected for example 2 the tree will not grow deeper than 2 levels [19].

2.2.4 Min_samples_split

Min_samples_split is the minimum number of samples required to split an internal node (https://scikit-learn.org/stable/modules/generated/sklearn.tree.DecisionTreeRegressor.html). Setting the minimum number of instances required to split a node can prevent the tree from creating overfitting by creating branches with too few instances. By default 2 is selected [20].

2.2.5 Min_samples_leaf

Min_samples_leaf is the minimum number of samples that should be in a leaf node. By determining the minimum number of samples required in the leaf node, the tree can be prevented from creating overfitting by creating branches with too few samples. By default 1 is selected [19].

2.2.6 Random_state

This parameter controls the randomness of the predictor and ensures that the results obtained by the model are repeatable. By default, "None" is selected [19].

2.2.7 Performance Evaluation

In this study, the coefficient of determination (R^2) was used for performance evaluation. This value indicates the strength of the analysis. Being close to 1 indicates that the model is strong.

2.3 Dataset

The dataset consists of 2 inputs and 1 output. The inputs are the web length of the beam (h) and the web width of the beam (b_w). The output is the cost (fx). The dataset contains 800 rows.

3. Numerical Example

The beam model considered in this problem is a continuous beam consisting of a span and a cantilever section as shown in Fig. 2. The fixed load (g) applied to the span and cantilever sections is 10 kN/m and 15 kN/m, respectively, and the live load (q) is 20 kN/m in both sections. The objective of this optimisation problem is to minimise the total material cost consisting of concrete and flexural (longitudinal) reinforcement. The length of the span section (lo) is 6.0 m and the length of the cantilever section (lc) is 1.6 m. The section variables b_w (mm) and h (mm) are the beam width and beam height, respectively. In addition, b (mm) is the effective table width, hf (mm) is the table (slab) thickness and d' is the mat. In the example in this study, "TS:500 Design and construction rules of reinforced concrete structures" regulation was utilised [21].

The characteristic yield strength (f_{yk}) of the flexural reinforcement to be used for the beam model considered in the problem is 420 MPa and the concrete class C25 was chosen. The slab thickness, which is one of the section features, was chosen as 120 mm and the cover as 60 cm.

The length of the beam (h) and the width of the beam (b_w) are design variables. The lower and upper limits of these variables are given in Equations 5 and 6.

$$3 \times h_f \leq h \leq 600 \tag{5}$$

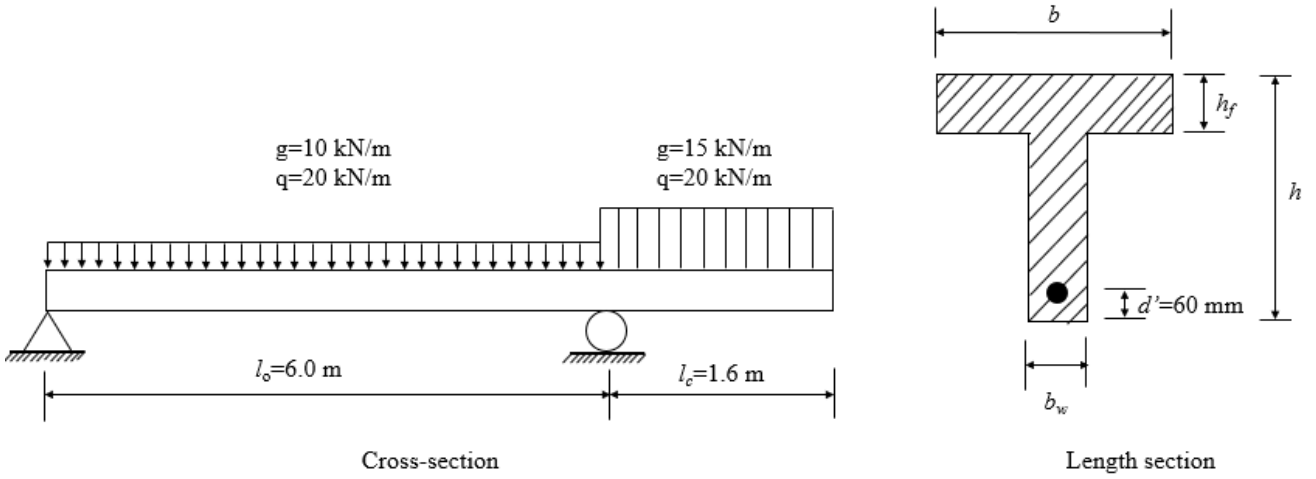

Fig. 2 Reinforced concrete T (Table) beam and section details

$$200 \leq b_w \leq 500 \tag{6}$$

The formula used to calculate the depth of the concrete compression block in reinforced concrete calculations (Equation 7):

$$\sqrt{a} = d^2 - \left(\frac{2 \times M_d \times 10^6}{0.85 \times f_{cd} \times b}\right) \tag{7}$$

The objective function of the problem consists of the sum of the total longitudinal reinforcement cost and the concrete cost (Equation 8).

$$f_x = C_s + C_c \tag{8}$$

The calculations of C_c and C_s in Equation 8 are given in Equations 10 and 11. In Equation 9, V_c is the concrete volume (m^3) used in the beam and in Equation 10, W_s is the weight of the longitudinal reinforcement used in the beam.

$$C_c = V_c \times unit\ cost\ of\ concrete \tag{9}$$

$$C_s = W_s \times unit\ cost\ of\ steel \tag{10}$$

The design constraint defined in TS500 is related to the width of the table that exceeds the cross-section is given in Equation 11. This value cannot be more than 6 times the table thickness.

$$g_1 = \frac{b - b_w}{2} \leq 6 \times h_f \tag{11}$$

4. Results

6 different DTR parameters were used in the study and their effects on the success of the model are given in 3 tables. In Table 1, the effects of "criteration" and "splitter" parameters are analysed. When the "criteration" parameter is analysed in Table 1, very close R^2 values are obtained in 4 different values. When the "splitter" parameter is analysed, it is seen that two different values give very close R^2 values.

Table 1. Effects of the criterion and splitter parameters

Parameters	Model Architecture	R^2
Default	criterion ="squared_error", splitter = "best", max_depth = None, min_samples_split = 2, min_samples_leaf = 1 and random_state = None	0.9954536562356399
criteration	criterion =" friedman_mse ", splitter = "best", max_depth = None, min_samples_split = 2, min_samples_leaf = 1 and random_state = None	0.9954618842578776
	criterion =" absolute_error ", splitter = "best", max_depth = None, min_samples_split = 2, min_samples_leaf = 1 and random_state = None	0.9954590668427414
	criterion = poisson, splitter = "best", max_depth = None, min_samples_split = 2, min_samples_leaf = 1 and random_state = None	0.9954626896107486
splitter	criterion = "squared_error", splitter = "random", max_depth = None, min_samples_split = 2, min_samples_leaf = 1 and random_state = None	0.9936039745386726

In Table 2 the effects of " max_depth" and " min_samples_split" parameters are analysed. When the " max_depth" parameter is analysed in Table 2, setting the value to None provides the highest success, but when it is 1, it has very low success. When the “min_samples_split” parameter is analysed, it is seen that as the value of “min_samples_split” increases, the success of the model decreases.

Table 2. Effects of the max_depth and min_samples_split parameters

Parameters	Model Architecture	R^2
Default	criterion = "squared_error", splitter = "best", max_depth = None, min_samples_split = 2, min_samples_leaf = 1 and random_state = None	0.9954536562356399
max_depth	criterion ="squared_error", splitter = "best", max_depth = 1 , min_samples_split = 2, min_samples_leaf = 1 and random_state = None	0.3940391485317013
	criterion = "squared_error", splitter = "best", max_depth = 2 , min_samples_split = 2, min_samples_leaf = 1 and random_state = None	0.7681419873504783
	criterion = "squared_error", splitter = "best", max_depth = 3 , min_samples_split = 2, min_samples_leaf = 1 and random_state = None	0.9191170880553425
min_samples_split	criterion = "squared_error", splitter = "best", max_depth = None, min_samples_split = 5, min_samples_leaf = 1and random_state = None	0.9953479325985594
	criterion = "squared_error", splitter = "best", max_depth = None, min_samples_split = 50, min_samples_leaf = 1and random_state = None	0.9613946633221433
	criterion = "squared_error", splitter = "best", max_depth = None, min_samples_split = 200, min_samples_leaf = 1and random_state = None	0.8626710582029687

In Table 3 the effects of "min_samples_leaf " and " random_state" parameters are analysed. When the "min_samples_leaf " parameter is analysed in Table 3, it is seen that as the value of “min_samples_leaf” increases, the success of the model decreases. When the “random_state” parameter is analysed from Table 3, is seen that two different values give slightly the same R^2 values.

Table 3. Effects of the min_samples_leaf and random_state parameters

Parameters	Model Architecture	R^2
Default	criterion = "squared_error", splitter = "best", max_depth = None, min_samples_split = 2, min_samples_leaf = 1 and random_state = None	0.9954536562356399
min_samples_leaf	criterion = "squared_error", splitter = "best", max_depth = None, min_samples_split = 5, min_samples_leaf = 1and random_state = None	0.9697875151664161
	criterion = "squared_error", splitter = "best", max_depth = None, min_samples_split = 10, min_samples_leaf = 1and random_state = None	-2031.0925085718009
random_state	criterion = "squared_error ", splitter = "best", max_depth = None, min_samples_split = 5, min_samples_leaf = 1 and random_state = 5	0.995453778500911
	criterion = "squared_error", splitter = "best", max_depth = None, min_samples_split = 10, min_samples_leaf = 1 and random_state = 50	0.9954529643218649

5. Conclusions

Optimization and machine learning have found a wide field of study. In this study, firstly, the cost optimization of the t-table beam is performed with the optimisation process. The Decision Tree Regressor (DTR) model is used to predict the cost of the t-table beam on the 800-row dataset obtained as a result of the optimisation and the effect of DTR parameters on performance is examined.

The parameters "splitter" and "criteration" have no specific effect on the performance of the model. "max_depth" is the maximum depth of the land tree and the increase in its value caused overfitting. "min_samples_split" is the minimum number of samples a node must have before splitting, and an increase in its value indicates that the node will descend further into the lower leaves. The "random_state" value is used to achieve the same result every time the model is run and does not change the result even if it takes different values.

In this study, as a result, it was observed that the parameter that most negatively affects the success of the model is increasing "min_samples_leaf". If the last leaf in the "min_samples_leaf" parameter, which expresses the minimum number of samples that a leaf should have, has fewer samples than the specified number, the nodes will not descend until this leaf and will end at the previous leaf. Therefore, a high value negatively affects the model.

References

1. Rao, R. (**2016**). Jaya: A simple and new optimization algorithm for solving constrained and unconstrained optimization problems. International Journal of Industrial Engineering Computations, 7(1), 19-34. doi: https://doi.org/10.5267/j.ijiec.2015.8.004
2. Yu, K., Qu, B., Yue, C., Ge, S., Chen, X., & Liang, J. (**2019**). A performance-guided JAYA algorithm for parameters identification of photovoltaic cell and module. Applied energy, 237, 241-257. https://doi.org/10.1016/j.apenergy.2019.01.008
3. Rao, R. V., More, K., Taler, J., & Ocłoń, P. (**2016**). Dimensional optimization of a micro-channel heat sink using Jaya algorithm. Applied Thermal Engineering, 103, 572-582. https://doi.org/10.1016/j.applthermaleng.2016.04.135
4. Gupta, S., Agarwal, I., & Singh, R. S. (**2019**). Workflow scheduling using Jaya algorithm in cloud. Concurrency and computation: practice and experience, 31(17), e5251. https://doi.org/10.1002/cpe.5251
5. Ray, P., Salkuti, S.R. (**2023**). Short-Term Load Forecasting Using Jaya Algorithm. In: Salkuti, S.R., Ray, P., Singh, A.R. (eds) Power Quality in Microgrids: Issues, Challenges and Mitigation Techniques. Lecture Notes in Electrical Engineering, vol 1039. Springer, Singapore. https://doi.org/10.1007/978-981-99-2066-2_15
6. Degertekin, S. O., Lamberti, L., & Ugur, I. B. (**2018**). Sizing, layout and topology design optimization of truss structures using the Jaya algorithm. Applied soft computing, 70, 903-928. https://doi.org/10.1016/j.asoc.2017.10.001
7. Kayabekir, A. E., Sayın, B., Nigdeli, S. M., & Bekdaş, G. (**2018**, July). Jaya algorithm based optimum carbon fiber reinforced polymer design for reinforced concrete beams. In AIP Conference Proceedings (Vol. 1978, No. 1). AIP Publishing. https://doi.org/10.1063/1.5043891
8. Bekdaş, G., Nigdeli, S. M., Kayabekir, A. E., & Toklu, Y. C. (**2018**, July). Minimization of vertical deflection of an optimum I-beam by Jaya algorithm. In AIP Conference Proceedings (Vol. 1978, No. 1). AIP Publishing.
9. Kayabekir, A. E., Bekdaş, G., & Nigdeli, S. M. (**2019**). Optimum design of T-beams using Jaya algorithm. In 3rd International Conference on Engineering Technology and Innovation (ICETI).
10. Rakıcı, E., Bekdaş, G., Nigdeli, S.M. (**2021**). Optimal Cost Design of Single-Story Reinforced Concrete Frames Using Jaya Algorithm. In: Nigdeli, S.M., Kim, J.H., Bekdaş, G., Yadav, A. (eds) Proceedings of 6th International Conference on Harmony Search, Soft Computing and Applications. ICHSA 2020. Advances in Intelligent Systems and Computing, vol 1275. Springer, Singapore. https://doi.org/10.1007/978-981-15-8603-3_16
11. Aslay, S. E., & Dede, T. (**2022**, June). 3D cost optimization of 3 story RC constructional building using Jaya algorithm. In Structures (Vol. 40, pp. 803-811). Elsevier. https://doi.org/10.1016/j.istruc.2022.04.055
12. Cakiroglu, C., Islam, K., Bekdas, G., & Apak, S. (**2022**). Cost and CO2 emission-based optimisation of reinforced concrete deep beams using Jaya algorithm. JOURNAL OF ENVIRONMENTAL PROTECTION AND ECOLOGY, 23(6).
13. Ding, Z., Hou, R., & Xia, Y. (**2022**). Structural damage identification considering uncertainties based on a Jaya algorithm with a local pattern search strategy and L0. 5 sparse regularization. Engineering Structures, 261, 114312. https://doi.org/10.1016/j.engstruct.2022.114312
14. Çoşut, M., Nigdeli, S.M., Bekdaş, G. (**2023**). The Sensibility of Jaya Algorithm on Tuned Mass Damper Optimization. In: Vasant, P., et al. Intelligent Computing and Optimization. ICO 2023. Lecture Notes in Networks and Systems, vol 854. Springer, Cham. https://doi.org/10.1007/978-3-031-50151-7_16
15. Cakiroglu, C., Islam, K., Bekdaş, G. (**2023**). Manta Ray Foraging and Jaya Hybrid Optimization of Concrete Filled Steel Tubular Stub Columns Based on CO2 Emission. In: Bekdaş, G., Nigdeli, S.M. (eds) Hybrid Metaheuristics in Structural Engineering. Studies in Systems, Decision and Control, vol 480. Springer, Cham. https://doi.org/10.1007/978-3-031-34728-3_7
16. Türkoğlu, H. K., Bekdaş, G., & Nigdeli, S. M. (**2023**, December). Check for updates Optimum Design of Reinforced Concrete Footings Using Jaya Algorithm. In Intelligent Computing and Optimization: Proceedings of the 6th International Conference on Intelligent Computing and Optimization 2023 (ICO2023), Volume 2 (Vol. 852, p. 86). Springer Nature.
17. Chiu, M. H., Yu, Y. R., Liaw, H. L., & Chun-Hao, L. (**2016**). The use of facial micro-expression state and Tree-Forest Model for predicting conceptual-conflict based conceptual change. Chapter Title & Authors, **2016**.
18. Irmak, M. E., & Aydilek, İ. B. (2019). Using Ensemble Regression Algorithms for Improving the Prediction Success of Air Quality Index. Academic Platform-Journal of Engineering and Science, 7(3), 507-514. 10.21541/apjes.478038
19. sklearn.tree.DecisionTreeRegressor [accessed 21 April 2024]. Available online: https://scikit-learn.org/stable/modules/generated/sklearn.tree.DecisionTreeRegressor.html
20. Decision Trees. [accessed 21 April 2024]. Available online: https://medium.com/@ompramod9921/decision-trees-8e2391f93fa7
21. Bekdaş G., Nigdeli S.M., Yüel, M., & Kayabekir A.E. (**2021**) Artificial Intelligence Optimization Algorithms and Engineering Applications. Seçkin Publishing.

Simulation of the Effect of Composite Iron Acetate Nanoparticles on Polysulfone Membrane Performance in Separating Oil from Water

Javad HASHEMIBENI[1]*

1 Kaunas University of Technology, Department of Mechanical Engineering, Kaunas, Lithuania
** javhas@ktu.lt*

Abstract

The purpose of this research is to model polysulfone membrane and PSF/Iron acetate membrane in order to investigate the effect of adding iron acetate nanoparticles on polysulfone to separate water from oil. A geometric model was considered for water treatment and by entering the parameters that were obtained experimentally in other researches, the effectiveness of adding these nanoparticles to polysulfone was investigated. For the feed and permeate parts, two models of laminar flow and transport of diluted species have been used, and for the membrane part, the porous medium flow model has been used. COMSOL software is used to simulate the desired model. Finally, by comparing the concentration of oil in the tank in the two desired membranes, their performance in separating oil from water is discussed.

Keywords: Membrane Modeling, Polysulfone, Water Treatment.

1. Introduction

Since the second half of the 60s, the first industrial production activities of reverse osmosis membrane manufacturing have started. The manufacturing process, efficiency, layout and operation of membrane systems have been significantly improved. One of the most important environmental problems in the current century is the oil wastes produced by industrial centers, especially refineries and oil distribution centers [1].

Effluents containing petroleum substances and oil-water emulsions are the two main pollutants discharged into the environment [2]. The ultrafiltration process is a low-pressure membrane separation method that is used to separate compounds selected based on their size. Ultrafiltration separates dissolved substances in the range of 0.005-0.1 micrometers, which corresponds to MWCO in the range of 1000-50000 daltons. Ultrafiltration membranes have recently been used in industries such as purification. One of the major problems that limit the various processes of membrane separation technology, including ultrafiltration, and also cause economic problems in the industry is membrane clogging, which seriously limits the use of these methods for large industrial capacities [3]. So far, researches have been conducted to investigate the effect of operating parameters on the flux and efficiency of the membrane process. Most of them have reported a sharp decrease in the flux at the beginning of the process, after a while this decrease becomes very small and almost reaches a steady state. Researchers believe that the excreted components accumulate near the surface of the membrane [4-7]. This accumulation near the membrane surface is called concentration polarization, which has serious consequences in all kinds of membrane processes. This accumulation continues until the concentration near the membrane surface is high enough and provide the necessary potential for the return penetration of these compounds into the fluid mass. High concentrations near the surface of the membrane cause serious problems for the permeation flux due to the concentration polarization phenomenon of the osmotic pressure gradient in the opposite direction of the operating pressure gradient, which has always been the focus of researchers. In this project, two membranes are investigated, one of which is polysulfone and the other is polysulfone composite reinforced with iron acetate particles. By comparing the oil concentration in the tank, we will get the effect of the changed parameters in the desired composite.

2. Geometry of the model

The geometry of our model consists of two parts. The first part includes the feed tank. The feed, which contains water and oil, enters the tank. Then it enters the surface part of the membrane from the tank. Part of the water that passes through the membrane and enters the lower part or permeate. Therefore, the feed geometry includes the tank and the upper part of the membrane. The inlet of the upper part of the membrane is the outlet of the tank and its outlet returns to the tank. The inlet of the permeate section is pure water with very low pressure, which is installed for the output of purified water, and the output is purified water. In Fig. 1, the general schematic of the geometry of the model can be seen.

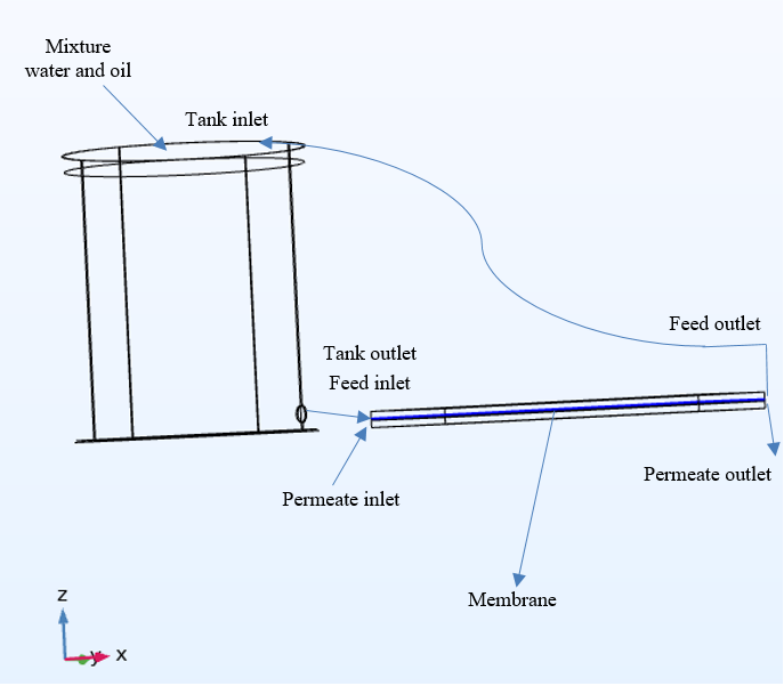

Fig. 1 Geometry of the model

The dimensional parameters can be seen in Table 1.

Table 1. Dimensional parameters

Name	Expression	Value
V_fluid	300[l]	0.3 m3
R_tank	35[cm]	0.35 m
H_fluid	V_fluid/(pi*R_tank^2)	0.77953 m
t_wall	5[mm]	0.005 m
H_tank	V_tank/(pi*R_tank^2)	0.8315 m
V_tank	V_fluid+20[l]	0.32 m3
W_module	1[m]	1 m
D_module	44[cm]	0.44 m
H_module	0.5[cm]	0.005 m
H_permeate	2[cm]	0.02 m
H_feed	2[cm]	0.02 m
R_out	2.5[cm]	0.025 m
H_out	5[cm]	0.05 m

3. Simulation

The simulation was done using the experimental data obtained in [8]. All the parameters related to the pressure and flow rate in the input feed part were considered the same in the modeling of both membranes. We included the parameters of porosity, average fiber diameter and hydrophilicity, which were measured by the contact angle of water with the surface of the membrane, and various values obtained in the experimental research in the article [8] for both membranes, were included in the variable parameters. The properties obtained by adding iron acetate nanoparticles to polysulfone can be seen and compared in Table 2.

Table 2. Properties obtained for membranes

Membrane materials	Porosity (%)	Average fiber diameter	WCA
PSF	75 ± 6	261 ± 50	100° ± 7°
PSF/Iron acetate	79 ± 5	219 ± 20	98° ± 8°

4. Simulation results

By placing the parameters that are considered common for both membranes, such as the pressure and flux of the feed input flow and the initial concentration of the feed input to the tank, as well as the parameters that are considered different for both membranes, have been entered in the parameters section for both modeling. And after the desired meshing, we will perform the simulation for both membranes and investigate the oil and water concentration in the tank in time scale. Fig.2 and Fig. 3 show the concentration of water and oil in the tank on a time scale for the polysulfone membrane (Fig. 2) and the polysulfone membrane containing iron acetate nanoparticles (Fig. 3).

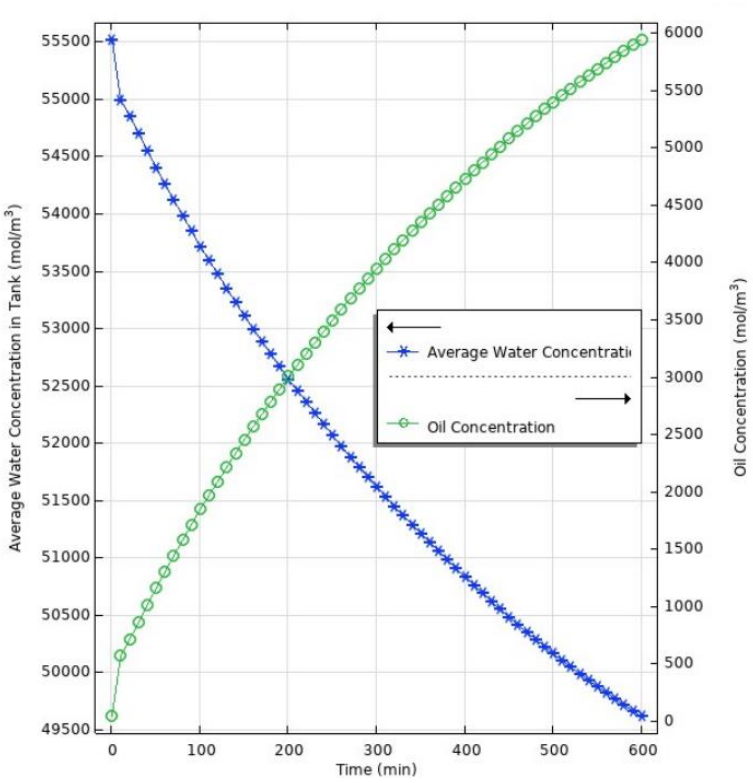

Fig. 2 Water and oil concentration graph in time scale for polysulfone membrane

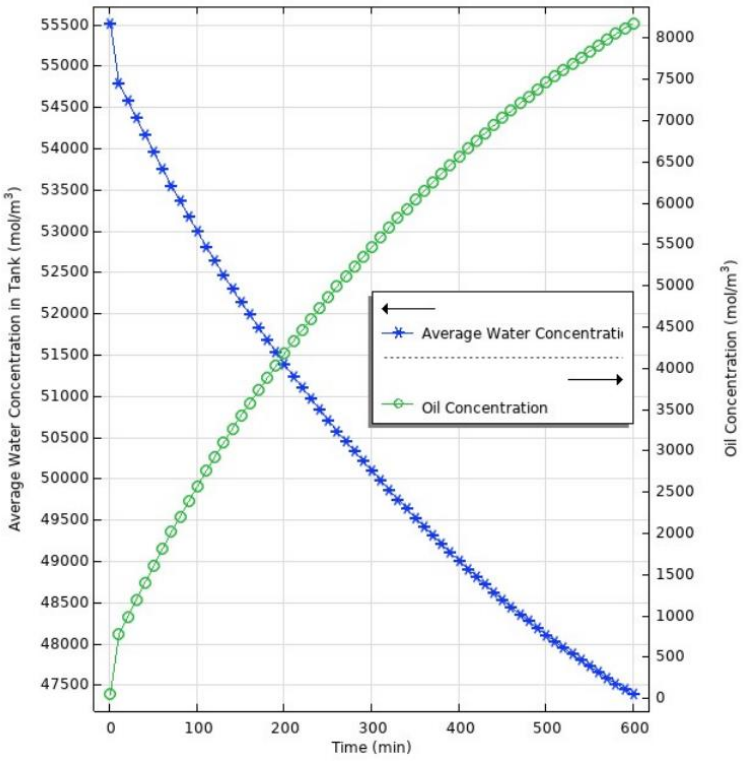

Fig. 3 Water and oil concentration graph in time scale for polysulfone membrane and iron acetate nanoparticles

By comparing the changes in water and oil concentration in the two graphs above, we come to the conclusion that when we use the polysulfone membrane containing iron acetate nanoparticles, we see an increase in the oil concentration in the tank in the time scale, and this is due to the increased efficiency and separation capability of the membrane. be Because when the separation is done better and the membrane flux increases, more water enters the permeate from the feed space and the oil concentration returned to the tank increases, and this generally increases the oil concentration in the tank.

5. Conclusions

Our intention of adding nanoparticles to membrane polymers and making composites is to increase their productivity and efficiency. In this simulation, with the addition of iron acetate nanoparticles in polysulfone, we saw an increase in hydrophilicity and porosity and a decrease in average fiber diameter. The increase in oil concentration and the decrease in water concentration in the time scale show the effect of nanoparticles in the composite membrane.

References

1. Salahi, A., Abbasi, M. and Mohammadi, T. Permeate flux decline during UF of oily wastewater: Experimental and modeling. *Desalination* **2010**, *251*(1-3), 153-160.
2. Abbasi, M., Salahi, A., Mirfendereski, M., Mohammadi, T. and Pak, A. Dimensional analysis of permeation flux for microfiltration of oily wastewaters using mullite ceramic membranes. *Desalination* **2010**, *252*(1-3),113-119.
3. Karakulski, K., Kozlowski, A.A.M.A.W. and Morawski, A.W. Purification of oily wastewater by ultrafiltration. *Separations Technology* **1995**, *5*(4), 197-205.
4. Karakulski, K., Morawski, W.A. and Grzechulska, J. Purification of bilge water by hybrid ultrafiltration and photocatalytic processes. *Separation and Purification Technology* **1998**, *14*(1-3), 163-173.
5. Cheryan, M. and Rajagopalan, N. Membrane processing of oily streams. Wastewater treatment and waste reduction. *Journal of membrane science* **1998**, *151*(1), 13-28.
6. Mueller, J., Cen, Y. and Davis, R.H. Crossflow microfiltration of oily water. *Journal of Membrane Science* **1997**, *129*(2), 221-235.
7. Kołtuniewicz, A.B. and Field, R.W. Process factors during removal of oil-in-water emulsions with cross-flow microfiltration. *Desalination* **1996**, *105*(1-2), 79-89.
8. Mousa, H.M., Alfadhel, H., Ateia, M. and Abdel-Jaber, G.T. Polysulfone-iron acetate/polyamide nanocomposite membrane for oil-water separation. *Environmental nanotechnology, monitoring & management* **2020**, *14*, 100314.

Resistivity Analysis of 3D Printed Biodegradable Conductive PCL/Graphene Composites Manufactured Using Solvent-free Process

M. Usman SIKANDAR[1]*,Rolanas DAUKSEVICIUS[1], Malik Daniyal ZAHEER[1], Valdas GRIGALIUNAS[1]

1 Institute of Mechatronics, Kaunas University of Technology, Kaunas, Lithuania
** muhsik@ktu.lt;*

Abstract

Despite the rapid evolution of 3D printing technology, there is still ongoing research into integrating environmental sustainability. This study explores the electrical resistivity of biodegradable, conductive PCL/rGO (polycaprolactone/reduced graphene oxide) composites produced through a solvent-free hot melt extrusion (HME) method. Unlike the majority of works on 3D printable conductive composites, which are based on solvent processing, this approach offers a scalable and more environment-friendly alternative. HME not only enhances biocompatibility but also supports sustainable manufacturing practices by allowing for the production of intricate structures like scaffolds using the fused filament fabrication (FFF) technique. Theoretical analysis of conductivity in polymer composites highlights the important functional benefits of graphene as a conductive filler in changing the electrical properties of polymeric matrices. Employing the Noztek fusionX extruder, filaments composed of PCL blended with rGO at concentrations of 5, 7.5, and 10 wt% were produced. These filaments were then used to 3D print 1 cm³ cubes and 10 cm filament segments were cut to measure their resistance. Resistance measurements employed a 4-probe method together with silver paste contacts, while resistivity assessments in build direction (z) utilized silver paste and copper foil for full surface contact. The results indicate that the electrical properties improve with higher rGO content, with resistance decreasing nearly 7-fold from 10.3 kΩ at 5 wt% to 1.48 kΩ at 10 wt%, and volume resistivity at 100 °C dropping more than 15-fold from 234.5 Ω-cm at 5 wt% to 15.2 Ω-cm at 10 wt%. Comparative analysis with commercial filaments (conductive PLA-based Protopasta and Fiber Force Nylforce, conductive TPU-based NinjaTek Eel) shows that PCL/rGO composites perform better, particularly at higher nanofiller contents, with resistivities slightly lower than those of existing commercial filaments. These findings suggest that PCL/rGO composites hold promise for 3D-printed electrical components such as resistive sensors and electrode layers.

Keywords: 3D printing, melt compounding, conductive filament, graphene, electrical resistance

1. Introduction

Polymers offer a broad range of functionalities and are known for their lightweight, flexibility, and low cost [1]. However, the widespread production and consumption of synthetic plastics since the 1950s have significantly contributed to environmental pollution, leading to stringent regulatory actions like the EU's 2021 ban on single-use plastics [2]. In response, the focus has shifted towards developing biodegradable polymers, which offer an environmentally friendly alternative without sacrificing the beneficial properties of traditional plastics. In this work, we are developing conductive biodegradable polymer composites. The following paragraphs will elaborate on polymers, biodegradable polymers, conductive polymer composites, and the previous research work.

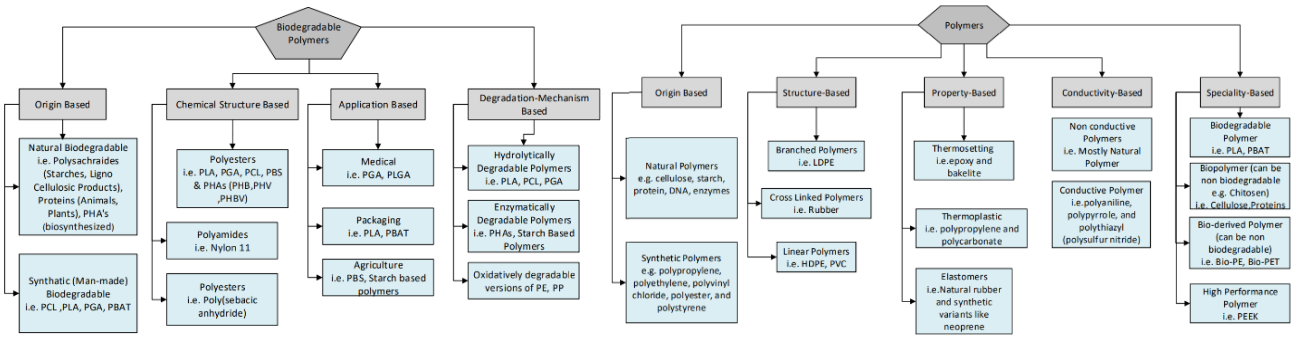

(a) (b)

Fig. 1 Classification (a) polymers (b) biodegradable Polymers

Biodegradable polymers, introduced in 1980, are designed to break down safely in the environment while maintaining reliability. According to ASTM standards, a material is biodegradable if it decomposes by 70% within 30 days under anaerobic conditions (ASTM D5526-18 and D5511-18) or 90% into carbon dioxide within 180 days under aerobic conditions (ASTM D6868-19 and D6400-19)[3].

Polymer composites are defined as high-performance, flexible materials consisting of a mixture of different phases of materials, where at least one phase is a polymer. Due to environmental concerns, recent research has focused on developing

biodegradable composites with low density and good mechanical properties [4]. Polymer composites are valued for their lightweight, corrosion-resistant, and cost-effective qualities. Natural fibers and high-conductivity fillers like graphene and carbon nanotubes enhance these composites, making them more sustainable and efficient [5]. It is possible to produce thermally and electrically conductive polymer composites. Thermally conductive polymer composites use thermally conductive fillers like metals, ceramics, and carbon materials [6]. Before discussing the conductive polymer composites (ECPCs), it's essential to understand conducting polymers (CPs). CPs exhibit excellent stability, are lightweight, workable, and offer corrosion resistance. The development of conducting polymers began with the discovery of polysulfur nitride [7]. Organic conductive polymers such as polyaniline, polypyrrole, and polyacetylene are made conductive through doping and are widely known as intrinsically conductive polymers (ICPs) [8]. Electrically conductive polymer composites (ECPCs) enhanced by fillers like carbon black, conduct electricity differently based on the particle distribution within the polymer matrix. Their extensive use in microelectronics and potential for ecological benefits underscore their importance in advancing both technology and sustainability [9]. Known alternatively as extrinsically conductive polymers, ECPCs are produced through methods such as solvent mixing or melt mixing (hot melt extrusion) that produce conducting blends or by incorporating conductive elements. Some research work on graphene-based conductive polymer composites is discussed in the following paragraph [10].

Reduced Graphene Oxide (rGO), which is graphene oxide that has been reduced to minimize phase separation and aggregation, is employed as a filler to enhance the conductivity of polymers. Composite filament strips for Fused Deposition Modeling (FDM) were fabricated by solvent mixing incorporating rGO into polylactic acid (PLA). The results demonstrated that increasing the rGO content in the composite directly improved the conductivity of the filaments. [11]. Following similar advancements, Wei et al. prepared graphene-reinforced acrylonitrile butadiene styrene (G-ABS) and graphene-reinforced polylactic acid (G-PLA) composites, demonstrating their applicability in FDM 3D printing [12]. While the aforementioned studies utilized solvent-based methods, researchers have investigated electroactive scaffolds made from polycaprolactone (PCL) and thermally reduced graphene oxide (TrGO) using a melt mixing technique for 3D printing. These scaffolds employ TrGO, which not only enhances antibacterial properties but also significantly improves cell viability, with a fourfold increase [13]. Graphene's two-dimensional structure and high surface energy tend to cause agglomeration in polymer matrices, disrupting conductivity. Ecco et al. found that when using FDM printing, CNT/ABS composites outperformed GNP/ABS composites in conductivity across all directions. [14].

In this research work, PCL-rGO composites with rGO content up to 10% by weight are being produced using hot melt extrusion and subjected to resistivity analysis. This method demonstrates superior control over conductivity and maintains biocompatibility compared to techniques such as solvent mixing, in situ polymerization, solvent electrospinning, and spray coating, making it highly suitable for medical applications [15].

2. Materials and Methods

In this section, the materials employed, specifically reduced graphene oxide (rGO) and polycaprolactone (PCL), are discussed, alongside a detailed description of the methodology. This includes three main steps: hot melt extrusion, filament fabrication, and resistance and resistivity analysis, which are described below.

2.1 Materials

rGO is synthesized from graphene oxide (GO) using chemical, thermal, or electrochemical reduction, each affecting its conductivity and structural integrity. [16]. rGO retains a modified graphene lattice with some residual oxygen groups, giving it unique properties distinct from pristine graphene, suitable for applications not requiring perfect structures. Its surface can be covalently or non-covalently functionalized to enhance interactions with substances like polymers and biomolecules, allowing customization for uses ranging from biomedical devices to environmental sensors and as a conductive material in electronics and energy storage devices[17] [18].

PCL is synthesized through the ring-opening polymerization of ε-caprolactone, utilizing catalysts like stannous octanoate. [19]. PCL degrades slowly through hydrolysis of its ester linkages, which can be accelerated by blending with other polymers or additives. This a bit slow degradation rate is beneficial for applications requiring durability [20]. In the medical sector, PCL is used for long-term implantable devices and controlled drug delivery systems. Its properties allow for gradual degradation, aligning with the needs of tissue integration and drug release [21]. Beyond medical applications, PCL's blend with starch and other biodegradable materials is used for creating eco-friendly packaging, contributing to the reduction of plastic waste [20]. PCL is characterized by its hydrophobic, semi-crystalline nature. It has a low melting point which makes it processable at lower temperatures, thereby reducing energy consumption during manufacturing [22], [23].

2.2 Methodology

In this research, we followed a comprehensive three-step methodology for the fabrication and resistivity analysis of 3D printable polymeric composite filaments, focusing on the integration of polycaprolactone (PCL) with reduced graphene oxide (rGO). Each step of the process—hot melt extrusion, filament fabrication, and electrical resistance and resistivity testing—follows a precise protocol to ensure reproducibility and accuracy in results.

The steps are elaborated below.

2.2.1 Step 1: hot melt extrusion (filament fabrication)

The initial phase of the methodology involves the hot melt extrusion process. Here, we blend PCL powder with rGO, followed by palletization and the addition of more rGO to increase its percentage weight. The mixture is extruded through a single-screw Noztek fusionX extruder, whose schematic is given in Figure 2 (a), under parameters as given in Table 1.

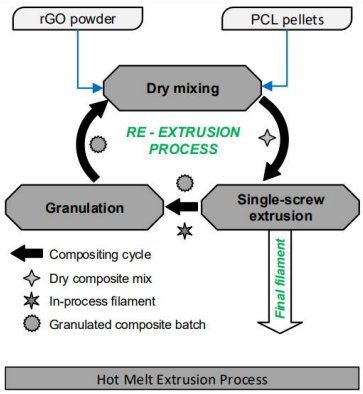

Fig. 2 Filament fabrication using solvent-free process

Table 1. Hot melt extrusion parameters

No.	Homogenizing extrusion	PCL/rGO 5 wt %	PCL/rGO 7.5 wt %	PCL/rGO 10 wt %
1	Extrusion zone temperature	80 °C	85 °C	95 °C
2	Mixing zone temperature	70 °C	75 °C	82 °C
3	Nozzle diameter	1.75 mm	1.75 mm	1.75 mm
4	Motor speed	10-13 RPM	10-13 RPM	10-13 RPM
5	Cooling Type	Water cooling	Water cooling	Water cooling

2.2.2 Step 2: fused filament fabrication

After extrusion, the filaments are used in a fused filament fabrication process, as shown in Figure 3, utilizing a Prusa i3 MK3 3D printer to evaluate their practicality in 3D printing applications. The printing parameters are detailed in Table 2.

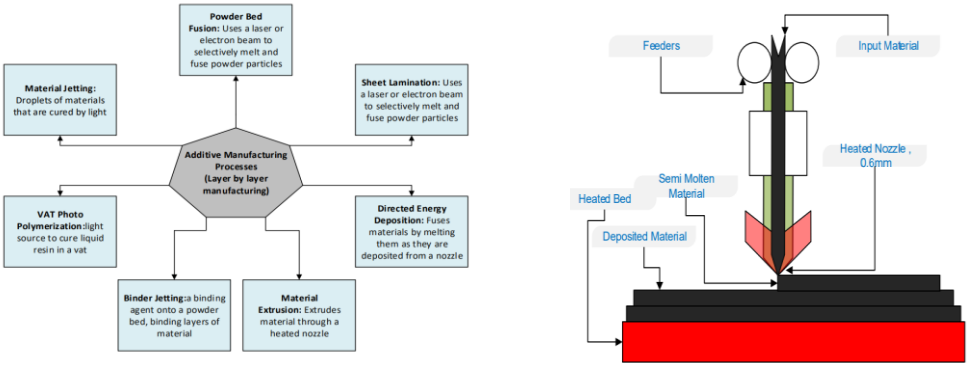

(a) (b)

Fig. 3 (a) Additive Manufacturing Processes (b) Fused Filament Fabrication (FFF)

Table 2. Fused filament fabrication parameters

No.	3D Printing Parameters	Extruded Filament			Commercial Filament		
		PCL/rGO 5%	PCL/rGO 7.5 %	PCL/rGO 10%	Protopasta	Nylforce	NinjaTek Eel
1	Nozzle diameter, material type	0.6 mm, Brass nozzle					
2	Nozzle temperature	80,85,90,100 °C	80,85,90,100 °C	100, 110, 120 °C	215°C	215°C	215°C
3	Bed temperature	60 °C	60 °C	60 °C	50 °C	50 °C	45 °C
4	Printing speed	10.5 mm/sec	10 mm/sec	10 mm/sec	12 mm/sec	12 mm/sec	12 mm/sec
5	Printing time	43 min	46 min	46 min	37 min	37 min	37 min
6	Raster angle & Infill ratio	+45°/-45°, 100% infill					
7	Layer thickness	mm					

2.2.3 Step 3: resistance & resistivity testing

In the four-wire setup, a constant current is passed through the device under test (DUT) via the source leads, and the voltage is measured across the DUT using the sense leads. The separation of current and voltage paths helps minimize errors caused

by the resistance of the measuring leads themselves [24], [25]. It has been found that the four-wire method eliminates probe resistance from the measurements, providing accurate and reliable results [26]. This method can be enhanced by the Van der Pauw technique, which is an extension of the four-wire method. It emphasizes that for accurate measurements, the resistivity values computed from different geometrical factors should be closely matched [27].

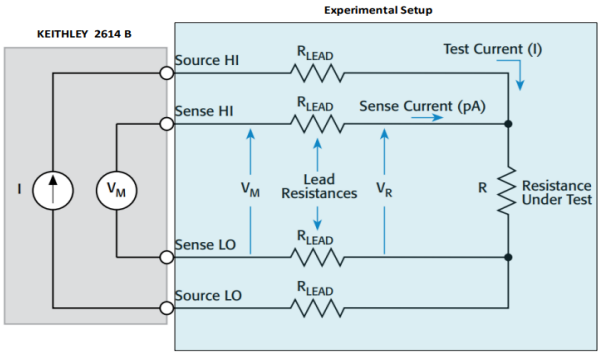

Fig. 4 Four-wire resistance measurement setup [25]

Resistivity expression is given below:

$$R = \rho \frac{L}{A} \tag{1}$$

where: R= Resistance, in ohms (Ω), ρ= Resistivity, in Ω cm, L= Length, in cm, A= Diameter, in cm^2, respectively.

The final step involves the electrical characterization of the fabricated filaments, commercial filaments, and 3D-printed cubes. A 10 cm segment of the filaments and a 1 cm^3 cube are tested for their resistance and resistivity, respectively, using a four-wire resistance measurement setup. The cubes and filaments are shown in the figure below.

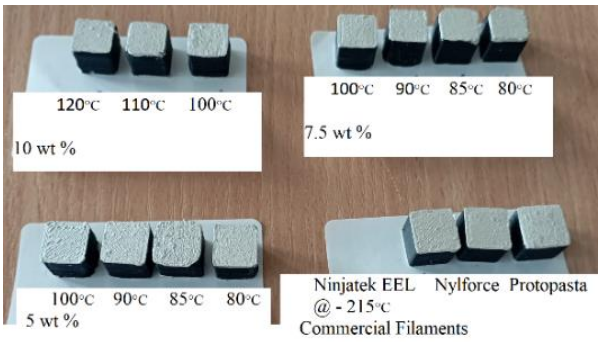

(a)

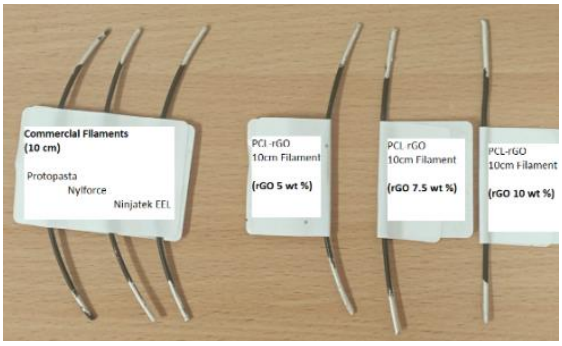

(b)

Fig. 5 (a) 3D Printed Cubes of Filaments (b) Commercial Filaments (10cm)

3. Results and discussion

The experimental data derived from the analysis of three commercial conductive filaments and poly(caprolactone)-reduced graphene oxide (PCL-rGO) filaments with varying concentrations of rGO (5%, 7.5%, and 10% by weight) provides significant insights into their electrical properties. Nylforce displayed superior conductive properties among the commercial options with a resistance of 1.03885 k-Ohm and resistivity of 21.7836 Ohm-cm, while Proto Pasta exhibited a slightly higher resistance of 1.7801 k-Ohm and resistivity of 26.8163 Ohm-cm. Ninjatek EEL showed the highest values, substantially higher at 5.0948 k-Ohm and 265.9713 Ohm-cm.

The PCL-rGO filaments demonstrated a clear trend of decreased resistance and resistivity with increased rGO content, indicating enhanced electrical conductivity. Specifically, at a lower 5% rGO concentration, the resistance was notably high at 10.3225 k-Ohm but decreased to 1.4768 k-Ohm at a 10% concentration with a 7 times decrease to the initial value. This pattern was mirrored in resistivity measurements, which declined from three-digit values in samples with less rGO to approximately 12 Ohm-cm in samples with 10% rGO content. These observations suggest that higher rGO concentrations effectively improve the formation of conductive networks within the filament matrix, enhancing overall electron mobility.

Temperature-dependent resistivity changes were also significant, especially for the PCL-rGO samples. At 80°C, the resistivity for the 5% rGO samples was at 689.3961 Ohm-cm, decreasing to 234.4794 Ohm-cm by 100°C. The 10% rGO samples started at a much lower resistivity and decreased further to 11.6945 Ohm-cm by 120°C showing a 15 times decrease from the results at the 5% rGO sample. These findings are consistent with the behavior expected of semi-conductive materials, where thermal energy assists carriers in overcoming conduction barriers.

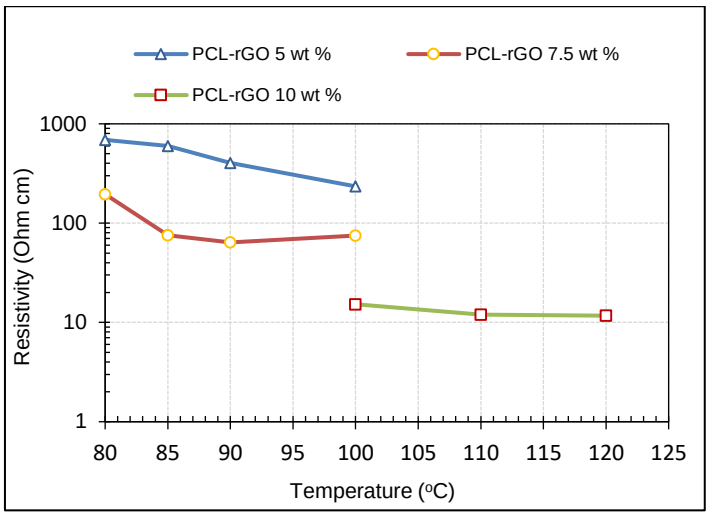

Fig. 6 PCL-rGO 3D printed cubes resistivity vs temperature plot

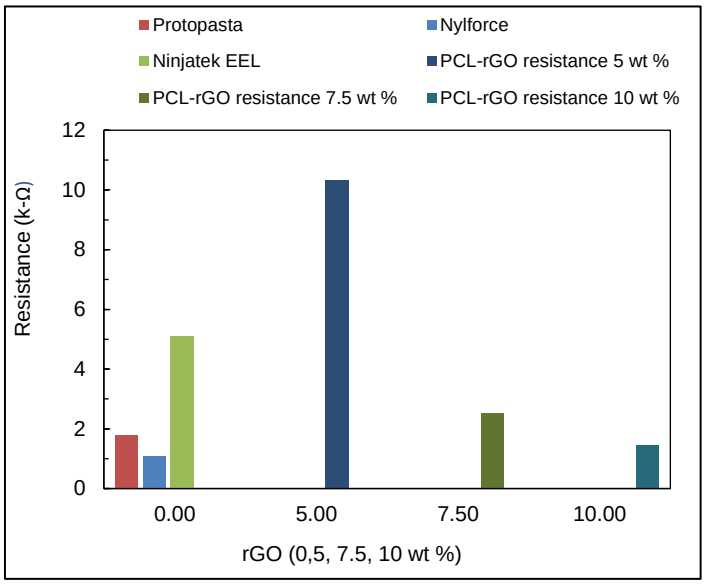

Fig. 7 Resistance of PCL-rGO at 5, 7.5 and 10 wt %

Table 3. Resistance & resistivity results

No.	Filament	Resistivity	Resistance
		Ohm-cm	K -Ohm
Commercial Conductive Filaments			
1	Proto-Pasta	26.8163	1.7801
2	Nylforce	21.7886	1.08385
3	Ninjatek EEL	265.9713	5.0948
Extruded Filaments			
1	PCL-rGO (5%)		
	80°C	689.3961	10.3225
	85°C	600.2431	
	90°C	405.5543	
	100°C	234.4794	
2	PCL-rGO (7.5%)		
	80°C	195.366	2.5278
	85°C	75.2846	
	90°C	63.9497	
	100°C	74.8486	
3	PCL-rGO (10%)		
	100°C	15.2441	1.4768
	110°C	12.0182	
	120°C	11.6945	

4. Conclusions

The comprehensive analysis of the electrical properties of commercial and experimental conductive filaments highlights the significant potential of rGO-enhanced PCL filaments. The non-linear improvements in conductivity with increased rGO concentrations and elevated temperatures suggest that these materials could be particularly useful in applications requiring responsive conductivity changes, such as in resistive sensors, electrode layers, or heating elements. The pronounced decrease in resistivity at higher temperatures also indicates potential utility in heat-sensitive applications.

However, while the low resistivity and enhanced conductivity at high rGO concentrations are advantageous, it is essential to consider the potential impact on the mechanical properties, processing, and durability of the filaments. Further investigations into the long-term stability and performance consistency of these filaments under various environmental conditions are recommended. By addressing these factors, the full potential of PCL-rGO composites in advanced technological applications can be more effectively realized.

Acknowledgment

The author would like to express gratitude to Gopi Kompelli and Saeid Saberi Alkouhi for providing their insights. Their support facilitated the completion of this work.

References

1. H. N. Abdelhamid, “Dielectric, Thermal, and Electrical Conductivity Properties of Biodegradable Polymer Nanocomposites,” **2022**, doi: 10.21203/rs.3.rs-2003331/v1.
2. M. Dusselier and J.-P. Lange, *Biodegradable polymers in the circular plastics economy*. John Wiley & Sons, **2022**.
3. H. Jena, P. Pradhan, and A. Purohit, “Dielectric properties, thermal analysis, and conductivity studies of biodegradable and biocompatible polymer nanocomposites,” in *Biodegradable and Biocompatible Polymer Nanocomposites: Processing, Characterization, and Applications*, Elsevier, **2023**, pp. 113–140. doi: 10.1016/B978-0-323-91696-7.00011-8.
4. R. Reshmy *et al.*, “Biodegradable polymer composites,” in *Biomass, Biofuels, Biochemicals: Biodegradable Polymers and Composites - Process Engineering to Commercialization*, Elsevier, **2021**, pp. 393–412. doi: 10.1016/B978-0-12-821888-4.00003-4.
5. A. Li, C. Zhang, and Y. F. Zhang, “Thermal conductivity of graphene-polymer composites: mechanisms, properties, and applications. Polymers (Basel) 9: 437.” **2017**.
6. Z. Wang *et al.*, “A Roadmap Review of Thermally Conductive Polymer Composites: Critical Factors, Progress, and Prospects,” *Advanced Functional Materials*, vol. 33, no. 36. John Wiley and Sons Inc, Sep. 05, **2023**. doi: 10.1002/adfm.202301549.
7. K. K. Kar, “Handbook of Nanocomposite Supercapacitor Materials I Characteristics,” **2020**. [Online]. Available: http://www.springer.com/series/856
8. M. G. Tadesse, A. S. Ahmmed, and J. F. Lübben, “Review on Conductive Polymer Composites for Supercapacitor Applications,” *Journal of Composites Science*, vol. 8, no. 2. Multidisciplinary Digital Publishing Institute (MDPI), Feb. 01, **2024**. doi: 10.3390/jcs8020053.
9. V. E. Gul′, *Structure and properties of conducting polymer composites*. CRC Press, **2023**.
10. A. Saleem, L. Frormann, and A. Soever, “Fabrication of extrinsically conductive silicone rubbers with high elasticity and analysis of their mechanical and electrical characteristics,” *Polymers (Basel)*, vol. 2, no. 3, pp. 200–210, **2010**.
11. J. Gomez, E. Villaro, J. Perez, and B. A. Haidar, “Preparation of electrically conductive PLA/rGO nanocomposite filaments,” *Graphene Technol*, vol. 5, no. 3–4, pp. 41–48, Dec. **2020**, doi: 10.1007/s41127-020-00031-3.
12. X. Wei *et al.*, “3D Printable Graphene Composite,” *Sci Rep*, vol. 5, Jul. **2015**, doi: 10.1038/srep11181.
13. C. Angulo-Pineda, K. Srirussamee, P. Palma, V. M. Fuenzalida, S. H. Cartmell, and H. Palza, “Electroactive 3D printed scaffolds based on percolated composites of polycaprolactone with thermally reduced graphene oxide for antibacterial and tissue engineering applications,” *Nanomaterials*, vol. 10, no. 3, Mar. **2020**, doi: 10.3390/nano10030428.
14. L. G. Ecco *et al.*, “Rapid prototyping of efficient electromagnetic interference shielding polymer composites via fused deposition modeling,” *Applied Sciences (Switzerland)*, vol. 9, no. 1, Jan. **2019**, doi: 10.3390/app9010037.
15. A. Youssef, S. J. Hollister, and P. D. Dalton, “Additive manufacturing of polymer melts for implantable medical devices and scaffolds,” *Biofabrication*, vol. 9, no. 1, p. 012002, **2017**.
16. S. C. Ray, “CHAPTER 2 2 Application and Uses of Graphene Oxide and Reduced Graphene Oxide.”
17. A. Pandey and P. Chauhan, “Functionalized graphene nanomaterials: Next-generation nanomedicine,” in *Functionalized Carbon Nanomaterials for Theranostic Applications*, Elsevier, **2022**, pp. 3–18. doi: 10.1016/B978-0-12-824366-4.00020-0.
18. S. C. Ray, “Application and Uses of Graphene.”
19. F. J. Buchanan, *Degradation rate of bioresorbable materials : prediction and evaluation*. Woodhead Publishing Ltd, **2008**.
20. L. W. McKeen, “Environmentally Friendly Polymers,” in *Permeability Properties of Plastics and Elastomers*, Elsevier, **2012**, pp. 287–304. doi: 10.1016/b978-1-4377-3469-0.10013-x.

21. L. Jiang and J. Zhang, "Biodegradable Polymers and Polymer Blends," in *Handbook of Biopolymers and Biodegradable Plastics: Properties, Processing and Applications*, Elsevier Inc., **2013**, pp. 109–128. doi: 10.1016/B978-1-4557-2834-3.00006-9.
22. C. Lauchlin, "Biodegradable polymer nanocomposites."
23. M. Kurakula, G. S. N. K. Rao, and K. S. Yadav, "Fabrication and characterization of polycaprolactone-based green materials for drug delivery," in *Applications of Advanced Green Materials*, Elsevier, **2020**, pp. 395–423. doi: 10.1016/B978-0-12-820484-9.00016-7.
24. Keithley, "A Greater Measure of Confidence Two-Wire vs. Four-Wire Resistance Measurements: Which Configuration Makes Sense for Your Application?," **2013**. [Online]. Available: www.keithley.in
25. K. Instruments, "Models 2611B, 2612B, and 2614B System SourceMeter Instruments Quick Start Guide," **2019**.
26. D. Gricius, "Design of Experimental Setup for Measuring Electrical Conductivity of Titanium Composite Samples Master's Final Degree Project."
27. A. J. Majid, "Resistivity Measurements of Conductors and Semiconductors of Different Geometrical Shapes Using Van der Pauw Technique," *Int J Sci Eng Res*, vol. 2, no. 10, **2011**, [Online]. Available: http://www.ijser.org

Weight Optimization of Cantilever Beam Using Machine Learning Models

Yaren AYDIN[1]*, Sinan Melih NİGDELİ[1]*, Gebrail BEKDAŞ[1]*

1 Istanbul University-Cerrahpaşa, Civil Engineering Department, 34320 Avcılar, Istanbul, Turkey,
** yaren.aydin1@ogr.iuc.edu.tr, melihnig@iuc.edu.tr, bekdas@iuc.edu.tr*

Abstract

Optimization is the determination of the most appropriate solutions when reaching a solution to a problem. Metaheuristic algorithms are algorithms developed inspired by the heuristic optimization processes of living things in nature. By using meta-heuristic algorithms, effective and successful results can be obtained in optimization compared to traditional algorithms. In this study, the success of machine learning models in weight prediction is investigated by using the cantilever beam weight minimization dataset obtained by optimization. Firefly Algorithm (FA) was used for the optimization process, Random Forest (RF), Decision Tree Regressor (DTR), K Neighbors Regressor (KNR) and Support Vector Regressor (SVR) were used for the machine learning process. Coefficient of determination (R^2) and negative mean absolute error (NMAE) were used for performance evaluation in machine learning. When machine learning models were compared using the analysis results, Decision Tree Regressor (R^2=1) showed the best performance in weight estimation of the cantilever beam, and Support Vector Regressor (R^2=-0.13) showed the worst performance.

Keywords: weight optimization, metaheuristic, machine learning, cantilever beam, firefly algorithm.

1. Layout

Reinforced concrete beams with one end embedded (anchored) and the other end unsupported (suspended) are cantilever beams. Cantilever beam is a structural element that mainly carries the load applied on it by moment effect. In order to prevent tensile stress in cantilever beams, main reinforcements are placed on top and mounting steels are placed on the bottom. Cantilever beams are used in places such as balconies, building facades, reinforced concrete stairs, roofs and eaves. In addition, in order to enlarge the floor area in buildings, they are usually placed on cantilevered projections after the ground floor [1]. Therefore, cantilever beam members in these structures are deflected. For these reasons, the design and application principles of cantilever beams are important. In this study, the cantilever beam dataset was first obtained by optimisation and then tested with machine learning models for weight estimation.

Optimization is the task of finding the minimum or maximum value of a function and at which independent variable values this value occurs. The use of meta-heuristic algorithms for solving optimization problems helps to solve complex problems more effectively [2]. In this study, the weight function which depends on different parameters of cantilever beam is minimized. Minimization of the weight of the cantilever beam is an important consideration as it will positively affect the total weight and cost of the structure. Metaheuristic algorithms are widely used for the optimisation process. Metaheuristic algorithms are algorithms developed by taking the behaviours of living creatures in nature such as hunting and survival reflexes in the life cycle as an example. There are many studies in the field of civil engineering where problems are solved using metaheuristic algorithms. These are optimization of tuned mass dampers [3-9], optimization of reinforced concrete beams [10-14], optimization of reinforced concrete retaining walls [15,16], RC columns [17,18], optimization of truss structures [19-23], RC members [24], optimum carbon fiber reinforced polymer design [25,26].

2. Methodology

2.1 Firefly Algorithm (FA)

Meta-heuristic optimization algorithms inspired by nature have become more successful and popular in optimization studies in recent years. Fireflies are a type of insect that live in hot and tropical regions. Fireflies perform actions such as reproduction, hunting and protection from enemies by attracting the opposite sex thanks to their chemical ability to generate cold light. At the same time, these insects can search for food and find other fireflies with their biological ability to glow [27]. In 2007, Xin-She Yang developed a firefly algorithm inspired by this natural behaviour of fireflies and their glow patterns. These are:

- It is accepted that fireflies are androgynous. Thus, all fireflies can influence the rest of the fireflies.
- Attractiveness is related to the brightness of the firefly. In this way, the less bright (jth (I_{xj}) firefly) of two light-emitting fireflies moves towards the brighter (kth (I_{xk}) firefly). As the distance between them increases, the brightness decreases. If the brightness level is equal, random movement occurs.
- Brightness is determined by the fitness (objective) function. There is a fitness function that recognises the brightest as the best [28].

When light propagates, a certain amount of light intensity is absorbed. Therefore, by using a constant light absorption coefficient (ɣ), the attractiveness of the firefly is calculated by Equation 1.

$$\beta_{r_{jk}} = \beta_0 e^{-\gamma r_{jk}^2} \tag{1}$$

j and k are two fireflies and their positions in the two-dimensional plane are X_k and X_j respectively. The distance between them (r_{jk}) is calculated by the Euclidean relation as given in Equation 2.

$$r_{jk} = [X_k - X_j] = \sqrt{\sum_{p=1}^{ts} (X_{p,j} - X_{p,k})^2} \tag{2}$$

Thus, the new position (X_j) of a firefly (j) orientated towards the more attractive and brighter one (k) is calculated as in Equation 3.

$$x_{J,new} = \begin{cases} I_{x_k} > I_{x_j}, \ X_{i,k} + \beta_{r_{jk}}(X_{i,j} - X_{i,k}) + \alpha_t(rand - 0.5) \\ I_{x_k} < I_{x_j}, \ X_{i,k} + \alpha_t(rand - 0.5) \end{cases} \tag{3}$$

In the Equation 5, $\alpha \in [0,1]$ is the coefficient parameter that takes a fixed value, rand takes a random value between [0,1] [28].

2.2 Machine Learning (ML) Models

Machine learning is a subset of artificial intelligence (AI) that deals with extracting patterns from data and then using those patterns to enable algorithms to improve themselves with experience.

The cantilever beam dataset obtained as a result of the optimization was tested with ML models. In the dataset, the inputs are θ_1 and θ_2. The output is weight. ML models used in this study are Random Forest (RF), Decision Tree Regressor (DTR), Decision Tree Regressor (DTR), K Neighbors Regressor (KNR) and Support Vector Regressor (SVR) and described below.

2.2.1 Random Forest (RF)

Random Forest (RF) is a machine learning algorithm used for classification, regression and other tasks. Random Forests work by combining multiple decision trees, thereby reducing the overfitting problem that a single decision tree may encounter. Random Forests create a "forest" by randomly selecting both the feature space and the training examples. This allows each decision tree to learn from different datasets and features during training [29].

2.2.2 Decision Tree Regressor (DTR)

A decision tree is a machine learning model that divides the dataset into several subsets, called nodes, to select the best among multiple possible solutions, and then assigns each node a label based on the values of its inputs. From there, the decision tree algorithm proceeds sequentially through the nodes and tests the output of each node against the labels assigned to its child nodes. If the output of a given node matches one of the labels in the dataset, that node is selected as a result of this algorithm; otherwise, it is skipped. This process continues until all nodes have been tested [30].

2.2.3 Decision Tree Regressor (DTR)

Linear regression models a target forecast value based on independent variables. It is mostly used to find the relationship between variables and prediction. The linear regression model is written as Equation 4, where y is the dependent variable, x is the independent variable, β_0 is the intercept (the value of y when x takes the value zero), β_1 is the coefficient (slope of the line) and ε is the random variable representing the noise that causes the true values to deviate from the function [31].

$$y = \beta_0 + \beta_1 + \varepsilon \tag{4}$$

2.2.4 K Neighbors Regressor (KNR)

K Nearest Neighbour algorithm is a versatile algorithm that can be used both in classification and regression. In its working logic, the data with unknown class is compared with other data in the training set and a distance measurement is made. According to the calculated distance, the most optimal class is found for the data that has not yet been assigned to a class. The main idea in the kNN algorithm is that groups of similar points or variables are most likely to belong to the same class. The most commonly used distance measure for distance calculation is the Euclidean distance [32].

2.2.5 Support Vector Regressor (SVR)

Support Vector Machine is a machine learning model based on prediction and generalisation on other data by sampling on training data. In support vector regression (SVR), a linear regression function is calculated in the higher dimensional input space where the input data are mapped from a nonlinear function. Thus, from a nonlinear regression problem in the low-dimensional input space, a linear regression problem in the high-dimensional input space is obtained and the solution is performed in this space [33].

2.3 Performance Metrics

In this study, the coefficient of determination (R^2) and negative mean absolute error (NMAE) were taken as basis for evaluating the performance of the models. When the R^2 value approaches 1 and the error (NMAE) value approaches 0, it indicates that the model is successful. The explanation of R^2 is given in Equation 5, and the expression explaining MAE is given in Equation 6.

$$R^2 = \frac{Variance\ explained\ by\ the\ model}{Total\ variance} \tag{5}$$

$$MAE = \frac{1}{n}\sum_{i=1}^{n}|y_i - \hat{y}_i| \tag{6}$$

In Equation 6, n is the number of observations, y_i i. is the actual value of the i^{th} observation and $\hat{y}_i$ is the predicted value of the i^{th} observation.

3. Numerical example

The cantilever beam model to be used in cantilever beam weight optimization is divided into five separate sections and has a hollow section [34] (Figure 1).

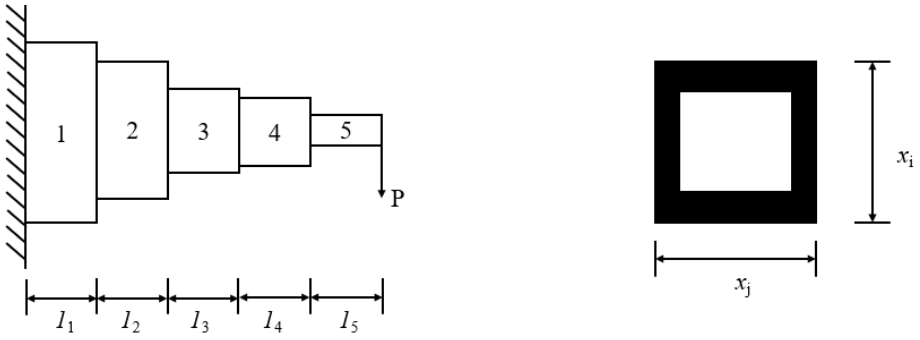

Fig. 1 Cantilever beam model and dimensions of hollow section [35]

The l_1, l_2, l_3, l_4 and l_5 values seen in Figure 1 indicate the length of each beam section. P value is the vertical load applied to the beam end. The dimensions of the hollow section, which is intended to be determined in a way that ensures that the beam weight is minimum, are shown as x_j (j = 1, 2, 3, 4, 5). The equation expressing the minimization of the beam weight and the objective function in the optimization problem is given in Equation 7.

$$Min\ f(x_j) = 0.0624\ (x_1 + x_2 + x_3 + x_4 + x_5) \tag{7}$$

Variation ranges for the width and depth dimensions of hollow beam section are given in Equation 8. These are lower and upper limits design variables.

$$0.001 \leq x_j \leq 100 \tag{8}$$

The only constraint of the optimization problem is given in Equation 9.

$$g_1 = \frac{61}{x_1^3} + \frac{37}{x_2^3} + \frac{19}{x_3^3} + \frac{7}{x_4^3} + \frac{1}{x_5^3} - 1 \leq 0 \tag{9}$$

4. Results

All analyses were carried out on the Python. The parameters in the machine learning models are selected by default. The R^2 and NMAE values obtained as a result of the analysis with machine learning models for weight prediction of cantilever beam are given in Table 1. Table 1 shows R^2 and NMAE values of each model.

Table 1. ML models and their performances

ML Models	R_2	NMAE
Decision Tree Regressor	1.0	-1.5685144500002136e-05
Linear Regression	0.9008	-38999.76131957122
Random Forest Regressor	0.9979	-1399.9981357878994
K Neighbors Regressor	0.9959	-999.9986723735819
Support Vector Regressor	-0.1352	-117987.40706975487

When Table 1 is analysed in terms of R^2, it can be concluded that the Decision Tree Regressor shows the highest success with R^2=1. Random Forest Regressor follows DTR. Support Vector Regressor method showed the worst performance with negative R2 (R2=-0.13). When Table 1 is analysed in terms of NAME, it can be concluded that the Decision Tree Regressor shows the highest success with NMAE=-1.56e-05 error. Random Forest Regressor follows DTR. Support Vector Regressor method showed the worst performance with negative R^2 (R^2=-0.13) and large NMAE (NMAE=-117987.40) value.

4. Conclusions

In this study, the success of machine learning models in weight prediction is investigated by using the cantilever beam weight minimization dataset obtained by optimization. For this purpose, a 1000-row dataset was first generated with the Firefly Algorithm (FA) and the weight of the cantilever beam was predicted using five different machine learning models and the model results were compared. For the machine learning methods used in the analysis, k fold validation was used. According to the results obtained, the Decision Tree machine learning method has come to the forefront by showing the highest performance for cantilever beam weight prediction. The Support Vector Regressor method showed the worst performance.

References

1. Aykaç, S., Aykaç, B., Ekinci, Y., Additional Loads Transferred to Cantilever Beams in BA Structures, *IMO Technical Journal*, **2011**, 5449-5462, Article351.
2. Seyyedabbasi, A., Aliyev, R., Kiani, F., Gulle, M. U., Basyildiz, H., & Shah, M. A. (**2021**). Hybrid algorithms based on combining reinforcement learning and metaheuristic methods to solve global optimization problems. *Knowledge-Based Systems*, 223, 107044. https://doi.org/10.1016/j.knosys.2021.107044
3. Bekdaş, G., & Nigdeli, S. M. (**2011**). Estimating optimum parameters of tuned mass dampers using harmony search. *Engineering Structures*, 33(9), 2716-2723. https://doi.org/10.1016/j.engstruct.2011.05.024
4. Bekdas, G., & Nigdeli, S. M. (**2013**). Optimization of tuned mass damper with harmony search. Metaheuristic *Applications in Structures and Infrastructures*, 14, 345-372.
5. Kaveh, A., Fahimi Farzam, M., Hojat Jalali, H. et al. Robust optimum design of a tuned mass damper inerter. *Acta Mech* 231, 3871–3896 (**2020**). https://doi.org/10.1007/s00707-020-02720-9
6. Prakash, S., & Jangid, R. S. (**2022**). Optimum parameters of tuned mass damper-inerter for damped structure under seismic excitation. *International Journal of Dynamics and Control*, 10(5), 1322-1336. https://doi.org/10.1007/s40435-022-00911-x
7. Aydin, Y., Nigdeli, S. M., & Bekdaş, G. (**2024**). Archimedes Optimization Algorithm for Optimization of Tuned Mass Dampers in Structural Control. Available at SSRN: https://ssrn.com/abstract=4750319 or http://dx.doi.org/10.2139/ssrn.4750319
8. Çoşut, M., Nigdeli, S. M., & Bekdaş, G. (**2024**). Optimizing Tuned Mass Damper According to Mean Efficiency via Jaya Algorithm. Available at SSRN: https://ssrn.com/abstract=4753712 or http://dx.doi.org/10.2139/ssrn.4753712
9. Wang, L., Zhou, Y., & Shi, W. (**2024**). Seismic multi-objective stochastic parameters optimization of multiple tuned mass damper system for a large podium twin towers structure. *Soil Dynamics and Earthquake Engineering*, 177, 108428. https://doi.org/10.1016/j.soildyn.2023.108428
10. Bekdaş, G., & Nigdeli, S. M. (**2012**, December). Cost optimization of T-shaped reinforced concrete beams under flexural effect according to ACI 318. *In 3rd European conference of civil engineering* (pp. 2-4). Paris: France.
11. Bekdaş, G., & Nigdeli, S. M. (**2013**). Optimization of T-shaped RC flexural members for different compressive strengths of concrete. *International Journal of Mechanics*, 7(2), 109-119.
12. Kayabekir, A. E., Bekdaş, G., & Nigdeli, S. M. (**2021**). Optimum design of reinforced concrete T-beam considering environmental factors via flower pollination algorithm. *International Journal of Engineering and Applied Sciences*, 13(4), 166-178. https://doi.org/10.24107/ijeas.1037908
13. Aydın, Y., Bekdaş, G., Nigdeli, S.M. (**2023**). Reinforced Concrete Beam Optimization via Flower Pollination Algorithm by Changing Switch Probability Parameter. In: Vasant, P., et al. Intelligent Computing and Optimization. ICO 2023. *Lecture Notes in Networks and Systems*, vol 852. Springer, Cham. https://doi.org/10.1007/978-3-031-50330-6_7
14. Pierott, R., Hammad, A. W., Haddad, A., Garcia, S., & Falcón, G. (**2021**). A mathematical optimisation model for the design and detailing of reinforced concrete beams. Engineering Structures, 245, 112861. https://doi.org/10.1016/j.engstruct.2021.112861
15. Ghazavi, M., & Bonab, S. B. (**2011**). Optimization of reinforced concrete retaining walls using ant colony method. *Geotechnical Safety and Risk*. ISGSR, 297-306.
16. Kayabekir, A., Bekdaş, G. & Nigdeli S.M. (**2020**). Optimum Design of Post-Tensioned Axially-Symmetric Cylindrical Reinforced Concrete Walls. *IGI Global*. https://doi.org/10.4018/978-1-7998-2664-4.ch009
17. Nigdeli, S. M., Bekdas, G., Kim, S., & Geem, Z. W. (**2015**). A novel harmony search based optimization of reinforced concrete biaxially loaded columns. *Structural Engineering and Mechanics*: *An International Journal*, 54(6), 1097-1109.
18. Kayabekir, A., Bekdaş, G., Nigdeli, S., & Apak, S. (**2022**). Cost and environmental friendly multi-objective optimum design of reinforced concrete columns. *Journal of Environmental Protection and Ecology*, 23(2).
19. Deb, K., & Gulati, S. (**2001**). Design of truss-structures for minimum weight using genetic algorithms. *Finite elements in analysis and design*, 37(5), 447-465. https://doi.org/10.1016/S0168-874X(00)00057-3

20. Bekdaş, G., Nigdeli, S. M., & Yang, X. S. (**2015**). Sizing optimization of truss structures using flower pollination algorithm. *Applied Soft Computing*, 37, 322-331. https://doi.org/10.1016/j.asoc.2015.08.037
21. Jafari, M., Salajegheh, E., & Salajegheh, J. (**2021**, August). Optimal design of truss structures using a hybrid method based on particle swarm optimizer and cultural algorithm. *In Structures* (Vol. 32, pp. 391-405). Elsevier. https://doi.org/10.1016/j.istruc.2021.03.017
22. Khodadadi, N., Harati, E., De Caso, F., & Nanni, A. (**2023**). Optimizing truss structures using composite materials under natural frequency constraints with a new hybrid algorithm based on cuckoo search and stochastic paint optimizer (CSSPO). *Buildings*, 13(6), 1551. https://doi.org/10.3390/buildings13061551
23. Aydin, Y., Nigdeli, S. M., & Bekdaş, G. (**2024**). Parametric Investigation of Archimedes Optimization Algorithm for a Structural Problem. Available at SSRN: https://ssrn.com/abstract=4750288 or http://dx.doi.org/10.2139/ssrn.4750288
24. Bekdaş, G., Nigdeli, S. M., & Yang, X. S. (**2016**). Optimum reinforced concrete design by harmony search algorithm. *Metaheuristics and Optimization in Civil Engineering*, 165-180.
25. Shi, X., Yu, X., & Esmaeili-Falak, M. (**2023**). Improved arithmetic optimization algorithm and its application to carbon fiber reinforced polymer-steel bond strength estimation. *Composite Structures*, 306, 116599. https://doi.org/10.1016/j.compstruct.2022.116599
26. Kayabekir, A. E., Sayın, B., Nigdeli, S. M., & Bekdaş, G. (**2018**, July). Jaya algorithm based optimum carbon fiber reinforced polymer design for reinforced concrete beams. In *AIP Conference Proceedings* (Vol. 1978, No. 1). AIP Publishing. https://doi.org/10.1063/1.5043891
27. Gandomi, A. H., Kashani, A. R., Roke, D. A., & Mousavi, M. (**2015**). Optimization of retaining wall design using recent swarm intelligence techniques. *Engineering Structures*, 103, 72-84. https://doi.org/10.1016/j.engstruct.2015.08.034
28. Yang, X. S. (**2009**, October). Firefly algorithms for multimodal optimization. *In International symposium on stochastic algorithms* (pp. 169-178). Berlin, Heidelberg: Springer Berlin Heidelberg.
29. Breiman, L. (**2001**). Random forests. *Machine learning*, 45, 5-32.
30. Bulutistan (**2023**). What is Machine Learning Decision Tree? https://bulutistan.com/blog/makine-ogrenmesi-karar-agaci-decision-tree-nedir/
31. Kutner, M. H., Nachtsheim, C. J., Neter, J., & Li, W. (**2005**). Applied linear statistical models. *McGraw-hill*.
32. Khan, M., Ding, Q., & Perrizo, W. (**2002**, April). k-nearest neighbor classification on spatial data streams using P-trees. In Pacific-Asia Conference on Knowledge Discovery and Data Mining (pp. 517-528). Berlin, Heidelberg: Springer Berlin Heidelberg.
33. Mohandes, M. (**2002**), Support vector machines for short-term electrical load forecasting. *International Journal of Energy Research*, 26(4), 335-345. https://doi.org/10.1002/er.787
34. Bekdaş G., Nigdeli S.M., Yüel, M., & Kayabekir A.E. (**2021**) Artificial Intelligence Optimization Algorithms and Engineering Applications. *Seçkin Publishing*.
35. Yang, X. S., Bekdaş, G., & Nigdeli, S. M. (Eds.). (**2016**). Metaheuristics and optimization in civil engineering. *Cham: Springer International Publishing.*

Influence of Mesh Size of the Osteoporotic Vertebra L1 Finite Element Model on the Convergence of the Strain Calculations Result

Olga CHABAROVA[1], Oleg ARDATOV[2], Jelena SELIVONEC[1]*, Muhammad Imam AMMARULLAH[3]

1 Department of Applied Mechanics, Vilnius Gediminas Technical University, LT-10223 Vilnius, Lithuania
2 Department of Biomechanical Engineering, Vilnius Gediminas Technical University, LT-10223 Vilnius, Lithuania
3 Department of Mechanical Engineering, Universitas Pasundan, Indonesia
** jelena.selivonec@vilniustech.lt*

Abstract

Finite element analysis is commonly employed in studying human biomechanics, allowing for quantitative assessment of skeletal stresses and deformations. A critical aspect in developing finite element models is solution convergence. The aim of this study is to investigate mesh convergence for comparative analysis of the vertebra of lumbar spine. A three-dimensional model of an osteoporotic vertebra L1 with varying mesh sizes was developed. Mesh sizes ranging from 1 mm to 3 mm with a step size of 0.5 mm were utilized. The authors designed the vertebra geometry using Solidworks and conducted a static analysis of deformation changes depending on mesh size using ANSYS. The results demonstrate how mesh size impacts the obtained deformations in modelling thin cortical bone and endplate of vertebra.

Keywords: osteoporotic vertebra, mesh size, convergence

1. Introduction

Finite Element Analysis (FEA) is frequently utilized for studying human biomechanics [1]. Using this method (due to the complexity of geometric and mechanical behaviour), skeletal stresses and strains are quantified [2-4]. Biomechanical models are often developed based on computed tomography, which provides insight into human bones to predict responses when bone properties change [5].

The lumbar spine is extensively studied due to the increasing incidence of vertebral fractures worldwide, attributed to the rapid rise in osteoporosis cases. The strength of lumbar vertebrae has been investigated using FE analysis in studies [6, 7] aimed at establishing a more reliable method for predicting vertebral fractures compared to densitometric assessments or by supplementing bone mineral density (BMD) measurements with geometry derived from radiological scans or structural strength obtained through FEA, to enhance current osteoporosis diagnostics and consequently predict vertebral fractures. Verification and validation are indispensable requirements in the development of a reliable FE model [8, 9]. In vertebrae, where material heterogeneities and geometric shapes can influence the predicted outcome, mesh convergence holds particular significance [10]. Unfortunately, mesh convergence is often overlooked in finite element modelling of spinal segments. Relatively few studies have attempted to explicitly demonstrate mesh convergence [11, 12], but these studies did not analyse the influence of the mesh on the deformation of individual vertebrae, which may impact stability outcomes.

The aim of this study is to investigate mesh convergence for a comparative analysis of the lumbar vertebra in terms of deformation of the thin cortical layer. The study utilizes variations in mesh sizes during modelling. According to FEA theory, a finer mesh yields higher accuracy compared to a coarser mesh. Parameters can be obtained to derive error coefficients, demonstrating the influence of mesh size on modelling results. Such an approach should be well-prepared and deliberated both prior to and during the analysis process to enhance clinical forecasting capabilities [12].

2. FE Setting and Configuration

For this study, a three-dimensional model of an osteoporotic L1 vertebra was developed. The internal geometry of the vertebral body was constructed to reflect osteoporotic degradation, incorporating a cortical bone thickness of δ_{cor} = 0.2 mm [6] and trabecular bone density of 0.45 g/cm^2 [13]. In this study, the shell is modelled as a linearly elastic isotropic material with a Young's modulus E_{cor} = 8000 MPa and a Poisson's ratio v_{cor} = 0.3 [14, 15]. The properties of other constituent parts of the vertebra are as follows: Cancellous bone E_{can} = 95.6 MPa and v_{can} = 0.3 [13], Vertebral bony endplate thickness is δ_{pl} = 0.5 mm, with a Young's modulus E_{pl} = 24 MPa and v_{pl} = 0.4 [16], Posterior Bone E_{pb} = 3500 MPa and v_{pb} = 0.25 [17].

The above properties of particular parts of the vertebra L1 are entered into ANSYS software for static analysis. For designing the vertebra geometry, SolidWorks software is utilized. The 3D model of the L1 vertebra is presented in Fig. 1. Subsequently, the 3D geometric model is imported into ANSYS with varying mesh sizes (L_{size}) for each experiment. The mesh size used is multiples of 0.5, as indicated in Table 1, starting from a mesh size of 1 mm and ending with a mesh size of 3 mm.

To obtain results comparable to those of comparative tests, it is necessary to equate boundary conditions and loading during vertebra modelling. Under a compressive load of 4636 N applied to the vertebra, a strain of 5.14% was observed [13].

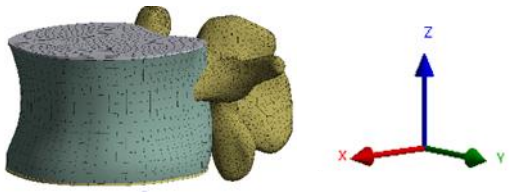

Fig. 1 3D design of the vertebra L1

3. Results and discussion

3.1. Strain ratio

To ensure the reliability of the obtained results, the deformation of the third vertebra model with a mesh size of 2.0 mm was compared with experimental data. The deformed L1 vertebra body is shown in Fig. 2. The resulting strain is 5.10%, which is 0.8% lower than the experimental data obtained by Kurutz et al. [13]. It can be argued that the model corresponds well to the reference.

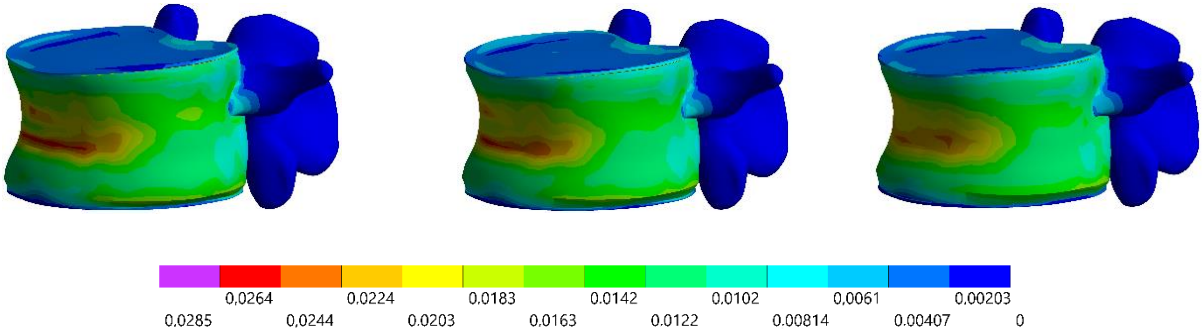

Fig. 2 Strain of the vertebra L1: (a) mesh size 1.5 mm; (b) mesh size 2.0 mm and (c) mesh size 2.5 mm

It is claimed that FE models assess deformation more accurately than static calculations [18]. The results of the cortical bone strain ($\varepsilon_{cor,x}$) ratio and endplate strain ($\varepsilon_{pl,z}$) ratio from five simulations show a varying ratio, as presented in Table 1.

Table 1. Strain ratio of the cortical bone and endplate

Lsize (mm)	Elements	Nodes	Strain εcor,x (%)	Benchmark εcor,x (%)	Ratio εcor,x	Strain εpl,z (%)	Benchmark εpl,z (%)	Ratio εpl,z
1.0	174 694	339 050	2.536	2.040	1.243	0.933	1.304	0.716
1.5	107 747	207 035	2.185	2.040	1.071	1.121	1.304	0.860
2.0	100 076	173 693	2.024	2.040	0.992	1.293	1.304	0.992
2.5	97 409	163 200	1.938	2.040	0.950	1.194	1.304	0.916
3.0	95 851	156 447	1.775	2.040	0.870	1.063	1.304	0.816

The ratio of horizontal deformation of the cortical bone in the first variation is 1.263, while the vertical deformation ratio of the endplate is 0.716. In the second variation, the deformation coefficients are 1.071 and 0.860, respectively. In the third variation, the deformation ratio of the cortical bone and endplate is 0.922 each. In the fourth variation, the overall deformation coefficients of the cortical bone and endplate are 0.950 and 0.916, respectively. In the fifth variation, the deformation coefficients are 0.870 and 0.816, respectively.

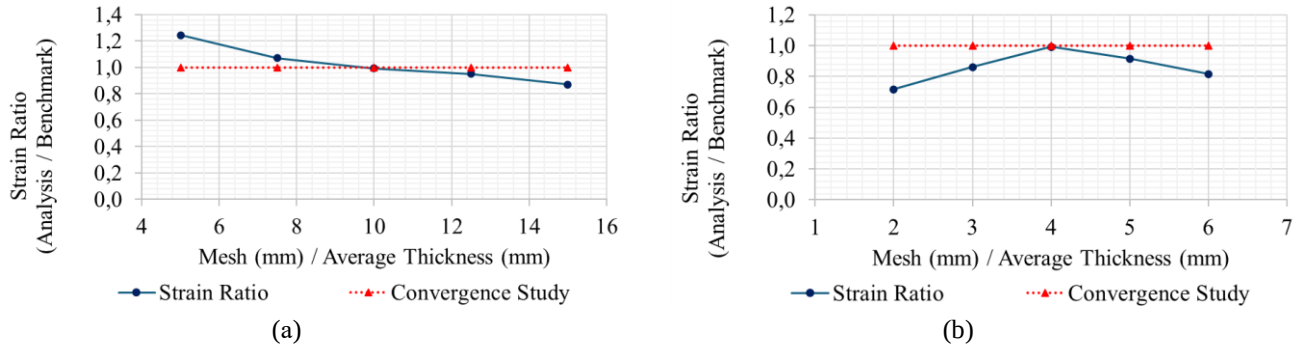

Fig. 3 Mesh convergence study with strain ratio: (a) cortical bone (b) endplate

The convergence study of the cortical bone is graphically depicted in Fig. 3a, where the second variation with a mesh size of 1.5 mm and a strain ratio of 1.071 is close to convergence, with 107,747 elements and 207,035 nodes. In the third variation, with a mesh size of 2.0 mm, the strain ratio is 0.992, with 100,076 elements and 173,693 nodes. In the fourth variation, with a mesh size of 2.5 mm, the strain ratio is 0.950, with 97,409 elements and 163,200 nodes. The convergence results of the endplate are graphically presented in Fig. 3b, where the convergence-like strain ratio is achieved only in the third variation with a mesh size of 2.0 mm and a strain ratio of 0.992. Views of the total deformation of the vertebra for each mesh size that converge are shown in Fig. 2.

3.2. Error ratio

Ayturk and Puttlitz [11] showed that a mesh can be considered converged if the error coefficients obtained from two consecutive mesh resolutions have a difference of less than 0.05 [11, 19]. The overall error coefficient is calculated by comparing the strain ratios of the L1 vertebral cortical bone and endplate with a reference study of strain values, as shown in Table 2.

Table 2. Error ratio of the cortical bone and endplate

Lsize (mm)	δcor (mm)	Lsize / δcor	δpl (mm)	Lsize / δpl	Error Ratio εcor,x	Error Ratio εpl,z
1.0	0.2	5.0	0.5	2.0	-0.243	0.284
1.5	0.2	7.5	0.5	3.0	-0.071	0.140
2.0	0.2	10.0	0.5	4.0	0.008	0.008
2.5	0.2	12.5	0.5	5.0	0.050	0.084
3.0	0.2	15.0	0.5	6.0	0.130	0.184
				Average	-0.025	0.140
				Minimum	-0.243	0.008
				Maximum	0.130	0.284
				Standard of deviation	0.142	0.103
				Coefficient of variance	-5.625	0.743

The strain error coefficient (see Table 2) for the first variation of cortical bone strain is -0.243, while for endplate strain, it is 0.284. In the second variation, the strain error coefficient for cortical bone is -0.071, and for endplate, it is 0.140. In the third variation, the strain error coefficients for cortical bone and endplate are 0.008. In the fourth variation, the strain error coefficient for cortical bone is 0.050, and for endplate, it is 0.084. In the last variation, the strain error coefficients are 0.130 and 0.184, respectively.

As shown in Table 2, the average error ratio is the sum of error ratios divided by the number of simulations, where the average deformation error is -0.025 and 0.140, respectively. The minimum error ratio represents the smallest value of error ratios among the simulations, where the minimum error ratio for cortical bone deformation is -0.243, and for endplate deformation, it is 0.008. The maximum error ratio represents the largest value of error ratios among the simulations, where the maximum error ratio for cortical bone deformation is 0.130, and for endplate deformation, it is 0.284. The standard deviation of the error coefficient is the variance of the error coefficient across the simulations. The standard deviation of the error coefficient for cortical bone deformation is 0.142, and for endplate deformation, it is 0.103. The coefficient of variation of the error is the ratio of the standard deviation of the error coefficient to the average coefficient. The coefficient of variation of the error for cortical bone deformation is -5.625, and for endplate deformation, it is 0.743.

4. Conclusions

The static analysis aims to determine the deformations of the cortical bone and endplate resulting from the study. Then, the magnitude of deformations was assessed using closely spaced mesh sizes with variations in parameters such as the deformation coefficient. As demonstrated in Table 2 above, it was proven that mesh size influences modelling results, as evident from the different modelling outcomes for each mesh size. Convergence can be achieved by comparing each existing mesh size for subsequent modelling.

Based on the results, the modelled lumbar spine vertebra L1 with error percentages shows the closest results with a mesh size of 1.5 mm and a cortical bone deformation coefficient of -0.071. With a mesh size of 2.0 mm, the deformation error coefficients for cortical bone and endplate are 0.008. With a mesh size of 2.5 mm, the deformation error coefficient for cortical bone is 0.050. The deformation error coefficients for cortical bone and endplate have average values of -0.025 and 0.140, minimum values of -0.243 and 0.008, maximum values of 0.130 and 0.284, standard deviations of 0.142 and 0.103, and coefficients of variation of -5.625 and 0.743, respectively.

When evaluating the differences between the values of error ratios, it can be observed that as the deviation value decreases, more accurate computation results are obtained, and vice versa. In the study of biological materials, it is important to assess the convergence of the mesh and the methods of error estimation of discretization, as evidenced by the obtained results. They demonstrate that the accuracy of the results obtained is influenced by the size of the mesh.

References

1. Phellan, R.; Hachem, B.; Clin, J.; et al. Real-time biomechanics using the finite element method and machine learning: Review and perspective. *Medical Physics* **2021**, 48, 7–18. https://doi.org/10.1002/MP.14602Hibbeler, R. *Engineering mechanics: Statics*, 14th ed., Publisher: Pearson, **2015**, 740 p.
2. Vogel, D.; Klimek, M.; Saemann, M.; Bader, R. Influence of the Acetabular Cup Material on the Shell Deformation and Strain Distribution in the Adjacent Bone—A Finite Element Analysis. Materials 2020, 13, Page 1372 13:1372. https://doi.org/10.3390/MA13061372
3. Mishra, RN.; Singh, MK.; Kumar, V. Biomechanical Analysis of Human Femur using Finite Element Method: A Review Study. *Materials Today: Proceedings* **2022**, 56, 384–389. https://doi.org/10.1016/J.MATPR.2022.01.222
4. Oku, N.; Demura, S.; Tawara, D.; et al. Biomechanical investigation of long spinal fusion models using three-dimensional finite element analysis. *BMC Musculoskeletal Disorders* **2023**, 24, 1–8. https://doi.org/10.1186/S12891-023-06290-4/FIGURES/5
5. Imai, K. Computed tomography-based finite element analysis to assess fracture risk and osteoporosis treatment. *World Journal of Experimental Medicine* **2015**, 5:182. https://doi.org/10.5493/WJEM.V5.I3.182
6. Maknickas, A.; Alekna, V.; Ardatov, O.; et al. FEM-Based Compression Fracture Risk Assessment in Osteoporotic Lumbar Vertebra L1. *Applied Sciences* **2019**, 9, Page 3013 9:3013. https://doi.org/10.3390/APP9153013
7. Naoum, S.; Vasiliadis, A.V.; Koutserimpas, C.; et al. Finite Element Method for the Evaluation of the Human Spine: A Literature Overview. *Journal of Functional Biomaterials* **2021**, 12, Page 43 12:43. https://doi.org/10.3390/JFB12030043
8. Oefner, C.; Herrmann, S.; Kebbach, M.; et al. Reporting checklist for verification and validation of finite element analysis in orthopedic and trauma biomechanics. *Medical Engineering and Physics* **2021**, 92, 25–32. https://doi.org/10.1016/J.MEDENGPHY.2021.03.011
9. Wong, DWC.; Chen, TLW.; Peng, Y.; et al. An instrument for methodological quality assessment of single-subject finite element analysis used in computational orthopaedics. *Medicine in Novel Technology and Devices* **2021**, 11:100067. https://doi.org/10.1016/J.MEDNTD.2021.100067
10. Marks, LW.; Gardner, TN. The use of strain energy as a convergence criterion in the finite element modelling of bone and the effect of model geometry on stress convergence. *Journal of Biomedical Engineering* **1993**, 15, 474–476. https://doi.org/10.1016/0141-5425(93)90061-3
11. Ayturk, UM.; Puttlitz, CM. Parametric convergence sensitivity and validation of a finite element model of the human lumbar spine. *Computer Methods in Biomechanics and Biomedical Engineering* **2011**, 14, 695–705. https://doi.org/10.1080/10255842.2010.493517
12. Xu, M.; Yang, J.; Lieberman, IH.; Haddas, R. Lumbar spine finite element model for healthy subjects: development and validation. *Computer Methods in Biomechanics and Biomedical Engineering* **2017**, 20, 1–15. https://doi.org/10.1080/10255842.2016.1193596
13. Kurutz, M.; Donáth, J.; Gálos, M.; et al. Age- and sex-related regional compressive strength characteristics of human lumbar vertebrae in osteoporosis. *Journal of Multidisciplinary Healthcare* **2008**, 1, 105–121. https://doi.org/10.2147/JMDH.S4103
14. Finley, SM.; Brodke, DS.; Spina, NT.; et al. FEBio finite element models of the human lumbar spine. *Computer Methods in Biomechanics and Biomedical Engineering* **2018**, 21, 444–452.
15. Kim, YH.; Wu, M.; Kim, K. Stress Analysis of Osteoporotic Lumbar Vertebra Using Finite Element Model with Microscaled Beam-Shell Trabecular-Cortical Structure. *Journal of Applied Mathematics* **2013**, 1–6.
16. Monteiro, NMB.; da Silva, MPT.; Folgado, JOMG.; Melancia, JPL. Structural analysis of the intervertebral discs adjacent to an interbody fusion using multibody dynamics and finite element cosimulation. *Multibody System Dynamics* **2011**, 25, 245–270.
17. Zahaf, S.; Habib, H.; Mansouri, B.; et al. The Effect of the Eccentric Loading on the Components of the Spine. *Global Journal of Researches in Engineering: A Mechanical and Mechanics Engineering Global Journals Inc* **2016**, 16, 2249–4596.
18. Ashford, SA.; Sitar, N. Effect of element size on the static finite element analysis of steep slopes. *International Journal for Numerical and Analytical Methods in Geomechanics* **2001**, 25, 1361–1376. https://doi.org/10.1002/NAG.184
19. Jones, AC.; Wilcox, RK. Finite element analysis of the spine: Towards a framework of verification, validation and sensitivity analysis. *Med Eng Phys* **2008**, 30, 1287–1304.

Enhancing the Performance of Mark7 Mod1 Arresting Gear System through Genetic Algorithm Optimization

İbrahim ŞENASLAN[1*], Doğukan AYGÜN[2] and Boğaç BİLGİÇ[1]

1 Department of Mechanical Engineering, Istanbul University-Cerrahpasa, Istanbul, Türkiye.
2 Turkish Aerospace Industries Inc., Ankara, Türkiye.
** ibrahim.senaslan@hotmail.com*

Abstract

This study is centered around the optimization of the coordinates of the Mark7 Mod1 Arresting Gear system using the Genetic Algorithm method. After obtaining new Cam coordinates, the system was subjected to tests involving various aircraft models characterized by different masses and speeds. The results demonstrate a significant improvement in the performance of the Mark7 Mod1 system subsequent to optimization using the Genetic Algorithm, thereby showcasing promising outcomes. This research underscores the potential of genetic algorithms in enhancing the efficiency of arresting systems utilized in both military and civilian aviation.

Keywords: Arresting gear, aircraft carrier, genetic algorithm, optimization

1. Introduction

Given the pivotal role of aircraft carriers in modern warfare, the complexities of aircraft operations, especially during take-off and landing, have garnered significant attention from researchers and engineers [1,2,3]. The successful landing of aircraft onto moving carrier decks, often amidst challenging weather conditions and dynamic operational scenarios, showcases remarkable feats of engineering and precision.

Central to this endeavor is the Mark7 arresting gear system, a cornerstone in safely halting and securing landing aircraft on carrier decks [1]. Representing the apex of engineering ingenuity, this system employs hydraulic mechanisms and precision-engineered components to gradually decelerate incoming aircraft, ensuring a controlled stop [4,5].

Moreover, the seamless integration of the Mark7 system with carrier operations underscores its pivotal role in bolstering fleet readiness and mission effectiveness. Through relentless research and innovation, engineers continually refine these critical systems, fortifying the dominance of aircraft carriers as indispensable assets in modern naval warfare.

Genetic Algorithm and its derivative Multi Object Genetic Algorithm are generally used in optimization problems [6,7]. This method is may be longer than others but achieves nearly optimized results.

In this article, we delve into the mathematical underpinnings of the Mark7 Mod1 system, probing into the intricacies of its design and the influence of the cam coordinates on its performance. By dissecting the dynamics of this system, our aim is to bolster its efficiency and reliability, thereby advancing naval aviation technology to new heights.

2. Mathematical model

Mark7 arresting system structure is simply consisting of the hydraulic system that in aircraft carrier and damper sheave system that on aircraft carrier. The hydraulic system absorbs the energy of aircraft and gives force in the opposite direction of aircraft motion for stop the aircraft safely. The damper sheave system transfers the forces that produced in hydraulic system and compresses the hydraulic system for absorption of energy. A simplified representation of the Mark 7 Arresting Gear system is given in Figure 1 [1].

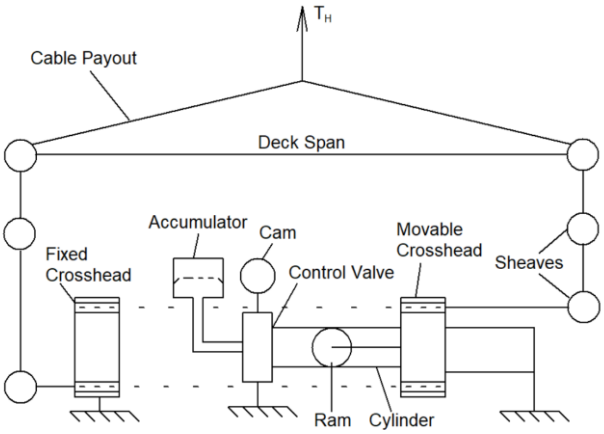

Fig. 1 Simplified Mark7 Arresting Gear Layout

Before the mathematical model of the Mark7 Mod1 arresting gear system, assumptions are important in calculating the mathematical model. Because without assumptions, mathematical calculations become impossible. The assumptions of this study are given below.

1) The aircraft accepted as a point mass. The weight of the ram and the crosshead is neglected.

2) The fluid considered as incompressible between cylinder to accumulator. The thrust coefficient of aerodynamic force is accepted constant.

3) The braking force of aircraft is neglected. The damper influence of movable sheave and cable anchor is also neglected.

4) It is assumed that the aircraft caught the rope at its midpoint and made a one-way movement perpendicular to the rope.

These assumptions ensured that the mathematical model being computable.

$$x = x_{t-\Delta t} + v_{t-\Delta t}\,\Delta t \tag{1}$$

In this equation, Δt represents time step, x represents the aircraft position at t time step, $x_{t-\Delta t}$ represents the aircraft position at previous time step, $v_{t-\Delta t}$ represents the velocity of aircraft at previous time step.

$$L = \sqrt{x^2 + L_p^2} \tag{2}$$

$$x_p = L - L_p \tag{3}$$

$$S = \frac{x_p}{2n_{sheave}} \tag{4}$$

In these equations, L represents cable length from point of engagement to the sheaves on deck, L_p represents half of deck pendant length, x_p represents amount of cable fed from the engine, S represents stroke of ram, n_{sheave} represents number of movable sheaves.

$$cos\theta = \frac{x}{L} \tag{5}$$

$$v_c = \frac{v_t}{cos\theta} \tag{6}$$

$$v_R = \frac{v_c}{2n_{sheave}} \tag{7}$$

In these equations, θ represents half of cable angle in engagement point, v_c represents velocity of the cable, v_t represents velocity of aircraft at t time step, v_R represents velocity of ram.

$$A_c = 1.1107f(2d - f) \tag{8}$$

In this equation, A_c represents control valve area, f represents valve stem lift, d represents valve set diameter.

The valve stem lift refers to the conversion of the cam's radial coordinates into movements of the valve stem, which plays a key role in regulating cylinder pressure and shutting the control valve. It is also a function of the ram stroke [1].

$$C_v = 3.126M^{-0.111} \tag{9}$$

$$C_c = CA_c^{-0.217} \tag{10}$$

In this equation, C_v represents velocity coefficient, Mrepresents the weight of aircraft, C_c represents contraction coefficient, C represents flow equation constant. The contraction coefficient is experimentally determined for Mark7 Mod1 arresting gear system.

$$C_d = C_c C_v \tag{11}$$

For convenience in fluid equations, a new variable named C_d is defined as the product of C_c and C_v.

The fluid equations are obtained with Bernoulli equations.

$$p_1 - p_2 = \frac{\rho V_1^2}{2}\frac{A_1^2}{A_c^2}\frac{1}{C_d^2} \tag{12}$$

$$p_2 = \frac{p_{f0} * V_{f0}^{\gamma}}{(V_{f0} - S_K y)^{\gamma}} \tag{13}$$

$$p_1 = \frac{\rho V_1^2}{2}\frac{A_1^2}{A_c^2}\frac{1}{C_d^2} + \frac{p_{f0} * V_{f0}^{\gamma}}{(V_{f0} - S_K y)^{\gamma}} \tag{14}$$

In these equations, p_1 represents main hydraulic cylinder pressure, p_2 represents accumulator pressure, ρ represents specific weight of fluid, V_1 represents fluid velocity in valve seat, A_1 represents valve seat area, p_{f0} represents initial pressure in gas cylinder, V_{f0} represents initial volume in gas cylinder, γ represents adiabatic coefficient, S_K represents calculated dummy variable, y represents ram stroke of main hydraulic cylinder.

$$F_{ram} = p_1 A_{ram} \tag{15}$$

In this equation, F_{ram} represents the ram force. Considering that the ram force originates from 36 purchase cables, the tension of each purchase cable is determined 1/36 of the ram force.

Another force, known as friction drag, operates within the system as well. This force arises from factors such as cable drag, cable bounce, slipper friction, and the like.

$$F_{drag} = \frac{(1-C_{eff})E_{tot}}{2L_{out}} \tag{16}$$

$$C_{eff} = 0.201E_{tot}^{0.084} \tag{17}$$

$$E_{tot} = 0.5MV_{AK}^2 + T_H R_{out} \tag{18}$$

$$R_{out} = \sqrt{(L_{out} + L_A)^2 - L_A^2} \tag{19}$$

In these equations, F_{drag} represents drag force, C_{eff} represents mechanical efficiency, E_{tot} represents total energy of the engagement, V_{AK} represents velocity of aircraft engagements, T_H represents thrust force, R_{out} represents final position of aircraft hook, L_{out} represents cable payout.

$$T_C = \frac{F_{ram}}{36} + F_{drag} \tag{20}$$

$$F_H = 2T_C cos\theta \tag{21}$$

In these equations, T_C represents cable tension, F_H represents hook load.

This simulation computing not only hook forces but also computing aerodynamic forces. The aerodynamic forces are being as:

$$T_H = k * M \tag{22}$$

In this equation, T_H represents thrust force, k represents thrust coefficient.

The final equations of motion are,

$$a = \frac{(T_H - F_H)}{M} g \tag{23}$$

$$v_{t+1} = v_t + a\Delta t \tag{24}$$

In these equations, a represents aircraft acceleration, $a_{t-\Delta t}$ represents aircraft acceleration at previous time step.

The parameters of the Mark7 Mod1 Arresting Gear system are given in Table S1.

Table 1. Mark7 Mod1 arresting system 118" Stroke K-5 cam parameters [1]

Parameter	Symbol	118" Stroke K-5 cam
Initial accumulator volume	V_{f0}	84000 cu in
Initial accumulator pressure	p_{f0}	400
Maximum ram stroke	S_{max}	118 in
Half of deck pendant	L_p	95 ft
Reeve ratio	RR	18:1
Ram area	A_{ram}	314.16 sq in
Valve seat diameter	d	4 in
Sheave of crosshead number	n_{sheave}	9
Ethylyne Glycol spesific weight	ρ	0.0403
Constant of Flow eq.	C	1.1
Dummy variable accumulator pressure	S_K	210
Thrust coefficient	k	0.4
Adiabatic coefficient	γ	1.4
Cable payout	L_{Out}	2124 ft

The Genetic Algorithm serves as a widely utilized optimization method in control or optimization studies. Essentially, this algorithm employs random numbers within specified bounds, treating each number as an individual within a given population. Once a predetermined number of populations is generated, the algorithm evaluates the Goal Function value of each individual within the population. It identifies and records traits closely aligned with the desired objective as genes. Genes closer to the optimized value are passed on to the next generation, while distant genes are discarded and replaced with new ones to prevent being stuck at local minimums. Additionally, new individuals are introduced in each population independently from previous genes, ensuring that the algorithm continues to explore the search space and avoids premature convergence. In this study, the goal function is determined by the final position of the aircraft.

The flowchart of Genetic Algorithm is given in Figure 2.

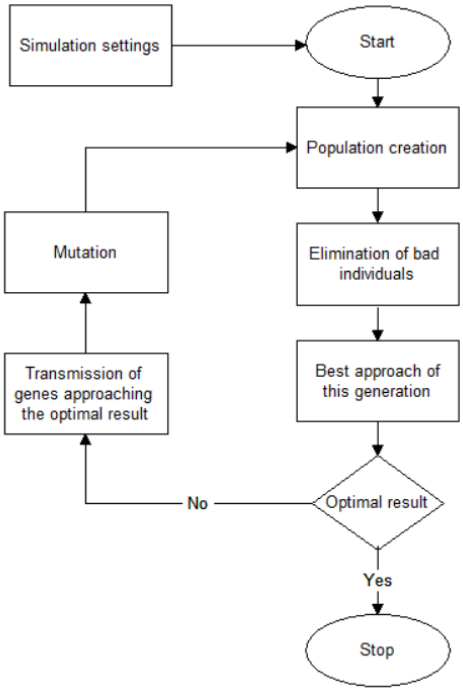

Fig. 2 Genetic Algorithm Flowchart [7]

In this study, the lower limit of the stem lift is determined as 0 and the upper limit was determined as 1.1. The cam coordinates separated with 7 part and the Genetic Algorithm is used. The optimal value is determined as [0 0.089; 20 0.523; 40 0.299; 60 0.273; 80 0.491; 100 0.01; 120 0.011].

The results of new cam coordinates are given in Figure 3. The old cam Coordinate boundaries were preserved and the optimization was carried out within the limits of reality.

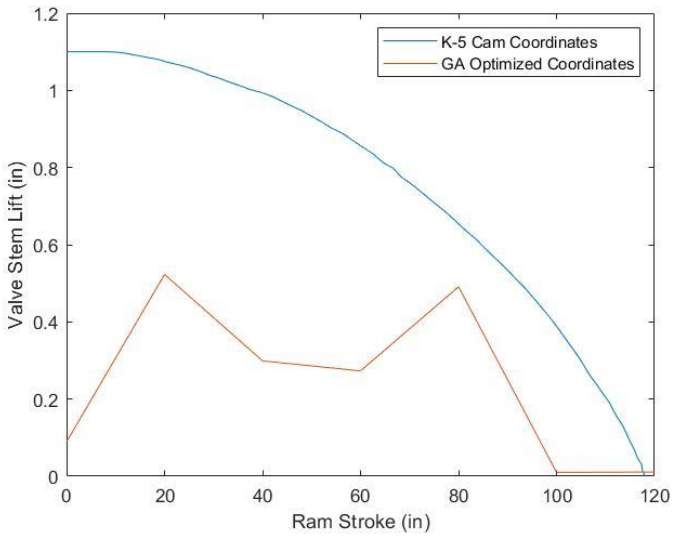

Fig. 3 Cam coordinates

3. Result and analysis

The results show that optimization of cam coordinates with genetic algorithm is effective for aircraft landing. The Figure 4 shows the new cam coordinates is highly successful than conventional cam coordinates.

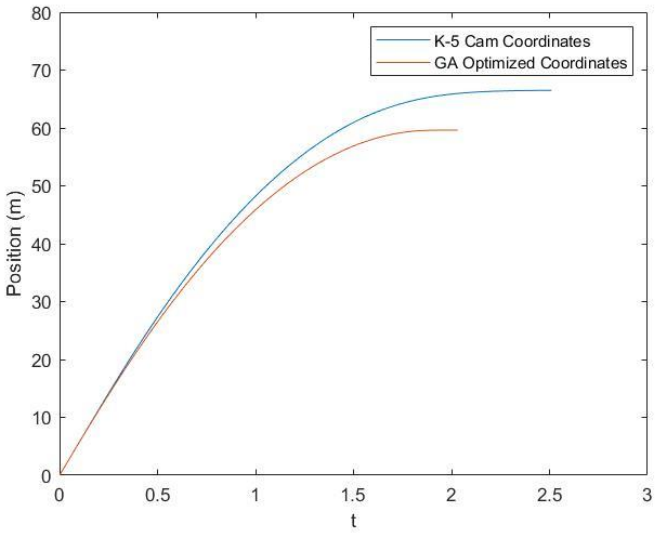

Fig. 4 F4-J Position-Time graph for all coordinates

The new cam coordinates also give robust characteristics for different mass and engaging velocities. Three different aircraft model and engaging velocity is tested for make this study comprehensive. Table 2 shows when mass or engaging velocity upgrading, the new cam coordinates is being more successful.

Table 2. All aircraft models and results

Aircraft Properties			Position (m)	
Name	Mass (lbs)	Engaging Velocity (Knots)	K-5 cam Coordinates	GA Optimized Coordinates
F4-J	50000	110	66.49	59.63
Hürjet	25000	150	63.01	56.55
F-35C	35000	130	65.37	57.62
F-16	40000	125	66.01	59.79

4. Conclusions

In this study, the Mark7 Mod1 Arresting Gear system cam coordinates were optimized using the Genetic Algorithm optimization method. The system and the new cam coordinates have been tested with aircraft models of different masses and velocities. The results obtained show that the performance of the Mark7 Mod1 system has significantly improved with the new cam coordinates optimized with the Genetic Algorithm.

Acknowledgements

This study was funded by Turkish Aerospace Industries Inc. (TUSAŞ), LIFTUP Grant No 6504437b53f85, and the Scientific and Technological Research Council of Turkey (TUBITAK), 2209-B Grant No 1139B412301922.

References

1. Louise, M. F. A Study of the effect of different Cam Designs on Mark 7 Mod 1 Arresting Gear Performance, *AD-A061486*, **1978**.
2. Lv, K.; Zhu, Q.; Li, X. Modeling and Simulation for Arrested Landing of Carrier-based Aircraft. *International Conference on Mechatronics and Automation* **2011**.
3. Leask, G.M. Development of a Mathematical Performance Prediction Model for Rotary-Hydraulic Type Arresting Gear, *AD893157*, **1972**.
4. Hao, J.; Wang, Y.; Peng, Y.; Ma, H.; Wei, X. Design and Structure Optimization of Arresting Gear Based on Magnetorheological Damper. *Aerospace* **2023**, 10(12), 1019.
5. Shen, W.; Zhao, Z.; Ren, G.; Liu, J. Modeling and Simulation of Arresting Gear System with Multibody Dynamic Approach. *Mathematical Problems in Engineering* **2013**, 1-12.
6. Özer, H.Ö.; Hacıoğlu, Y.; Yağız, N. Controlling the Building Model Using High Order Sliding Mode Control Optimized by Multi Objective Genetic Algorithm. *Periodicals of Engineering and Natural Sciences*, 5(3), 256-262.
7. Şenaslan, İ.; Bilgiç, B. Control of the Quarter Vehicle Model with an Innovative Delayed Resonator Optimized by Genetic Algorithm. *Afyon Kocatepe University – Journal of Science and Engineering*, **2024**, 24(1), 189-196.

Prediction of Post-Operative and Pre-Operative Hemodynamic Characteristics of Carotid Artery with Machine Learning and Numerical Analysis

Murad KUCUR[1]*, Banu KÖRBAHTİ[1], Ozan Onur BALKANAY[2]

1 İstanbul University-Cerrahpaşa, Faculty of Engineering, Mechanical Engineering Department, İstanbul, Türkiye
2 İstanbul University-Cerrahpaşa, Faculty of Medicine, Cardiovascular Surgery Department, İstanbul, Türkiye
** kucur@iuc.edu.tr*

Abstract

The aim of this study is to predict post-op and pre-op hemodynamic characteristics of the blood flow in the carotid artery with the machine learning (ML) and computational fluid dynamic analysis (CFD). The use of artificial intelligence algorithms has a significant impact on the accurate prediction and assessment of carotid artery blood flow for hemodynamic parameters, both pre- and post-operations. Machine learning predictions provide clinicians with valuable information about the impact of carotid artery disease on blood flow, which will be important in clinical decision-making. The augmentation of patient data sets enables more precise predictive models to be developed for machine learning. The integration of ML and computational fluid dynamics (CFD) analyses significantly enhances clinical decision-making and patient outcomes. This is achieved by enabling the analysis and prediction of hemodynamic parameters, such as blood flow rate, pressure and wall shear stresses, both before and after surgical operations. Furthermore, ML provides a solution as an alternative to CFD, reducing the burden on CFD resources. In this study, CFD results of average velocity compared with the machine learning results of the patient-specific carotid artery for the pre-operation case as contour view. The velocity values for the contour graphics are obtained by point cloud method. Also, for the post-operation case the predicted average velocity values compared with CFD analysis for eight different cross-sections. The DNN model predicts the average velocity values with a good accuracy. The model was written in Python and used the Keras library. The open-source software OpenFOAM was used for analyzing computational fluid dynamics.

Keywords: blood flow, carotid artery, machine learning, DNN, OpenFOAM

1. Introduction

Hemodynamic parameters, such as wall shear stress and flow disturbances, are known to play a crucial role in the onset and progression of vascular diseases such as atherosclerosis in the carotid artery. The ability to accurately predict and monitor these parameters is essential for understanding disease progression and evaluating the effectiveness of surgical interventions. Computational fluid dynamics simulations are promising approach for studying and predicting hemodynamic parameters in the carotid artery before and after surgery. These simulations can help to identify key flow metrics, including pressure, velocity, and wall shear stress, with high temporal and spatial resolution. Furthermore, the use of deep learning models, such as neural networks, can enhance the prediction accuracy of hemodynamic parameters by analyzing large amounts of data and learning complex patterns. By training neural networks with multimodal datasets, including imaging and computational fluid dynamics results, researchers can develop models that accurately predict hemodynamic parameters before and after surgery. These models can provide valuable insights for clinicians in making informed decisions regarding surgical interventions and assessing the success of these procedures. The integration of computational fluid dynamics and deep learning techniques holds great promise in the prediction of hemodynamic parameters in carotid artery blood flow before and after the operation. Overall, the prediction of hemodynamic parameters of carotid artery blood flow before and after surgery is critical for understanding disease progression and evaluating the effectiveness of surgical interventions. The integration of computational fluid dynamics simulations and deep learning models provides a powerful approach to accurately predict and monitor these parameters. Although computational fluid dynamics is a useful tool, determining patient-specific boundary conditions in order to obtain accurate results for the patient emerges as a challenge. In addition, higher computer capacity and analysis time are required for complex structured arteries.

In the literature, studies are carried out to demonstrate the compatibility of machine learning and computational fluid dynamics in the carotid artery. Taebi [1] also reviewed recent work on combining deep learning (DL) with computational fluid dynamics (CFD). He discussed how this approach can be used to solve hemodynamic problems such as blood flow behavior in the aorta and cerebral arteries. This review shows that efforts to integrate CFD with DL may be a new method for treatment planning of patients [1]. In their study, Wang et al. [2] pointed out the capacity and importance of deep learning-based hemodynamic prediction for pre-and postoperative carotid artery stenosis. In their study, three-dimensional CFD models were created from 280 subjects, and a deep learning network was implemented with point cloud data sets. For both preoperative and postoperative data sets, deep learning algorithm showed good agreement with CFD simulations in terms of velocity and pressure in the stenotic region. Yu et al. [3] developed machine learning models to detect carotid atherosclerosis in asymptomatic adults. They showed that classification models built by using machine learning algorithms based on physical examination results can monitor the carotid atherosclerosis in asymptomatic adults without the need for examination. Latha et al. [4] used machine learning and deep learning approaches to classify 361 ultrasound images in order

to understand whether people had symptomatic or asymptomatic carotid atherosclerosis. Ottokath et al. [5] presented a comprehensive review of the existing literature on ultrasound image analysis methods to detect and characterize plaque formation in the carotid artery. They also compared deep learning and different machine learning algorithms in plaque measurement, characterization, classification and stenosis grading. Savaş et al. [6] proposed a methodology based on deep learning for decision support for intima media thickness classification. They used 501 ultrasound images of 153 patients to test the model, and the deep learning model achieved 89.1% accuracy in intima media thickness classification. Ergün et al. [7] showed that Doppler ultrasound images can be classified by neural network. They used a traditional statistical method based on logistic regression and a Multilayer Perceptron (MLP) neural network, to classify the ultrasound images from carotid arteries of 168 individuals with diabetes. They concluded that the neural network is more effective than logistic regression analysis when the degree of stenosis increases. Übeyli and Güler [8] classified the internal carotid artery stenosis and the internal carotid artery occlusion by using neural network with an accuracy of over 90%.

In this study, the average velocity values for the pre-operative and post-operative cases of the patient-specific carotid artery were obtained by CFD analysis using OpenFOAM [9]. Then, the machine learning algorithm that was created in Python [10] and the average velocity values were estimated. The results were compared with each other, and the success of machine learning was discussed.

2. Problem formulation and methodology

Navier-Stokes and continuity equations were solved for CFD simulations. The blood flow behavior is assumed to be incompressible, Newtonian and laminar. The dynamic viscosity and the blood density of the blood is $\mu = 3.71 \times 10^{-3}$kg/m s and $\rho = 1060$ kg/m^3, respectively. Navier-Stokes and continuity equations are;

$$\nabla.\mathbf{u} = 0 \tag{1}$$

$$\rho\left(\frac{\partial \mathbf{u}}{\partial t} + \mathbf{u}.\nabla\mathbf{u}\right) = -\nabla P + \mu\nabla^2\mathbf{u} + \mathbf{f} \tag{2}$$

In this study, patient specific geometry is obtained from CT Angio scans as DICOM file. The geometric model of the carotid artery for pre-operation and post-operation cases are constructed with Slicer [11] from DICOM files and shown in Fig. 1. The mesh sizes for the pre-operative and post-operative geometries are 842490 and 834766, respectively. Patient' data were anonymized and used after the approval of the local ethics committee approval of the Istanbul University-Cerrahpaşa.

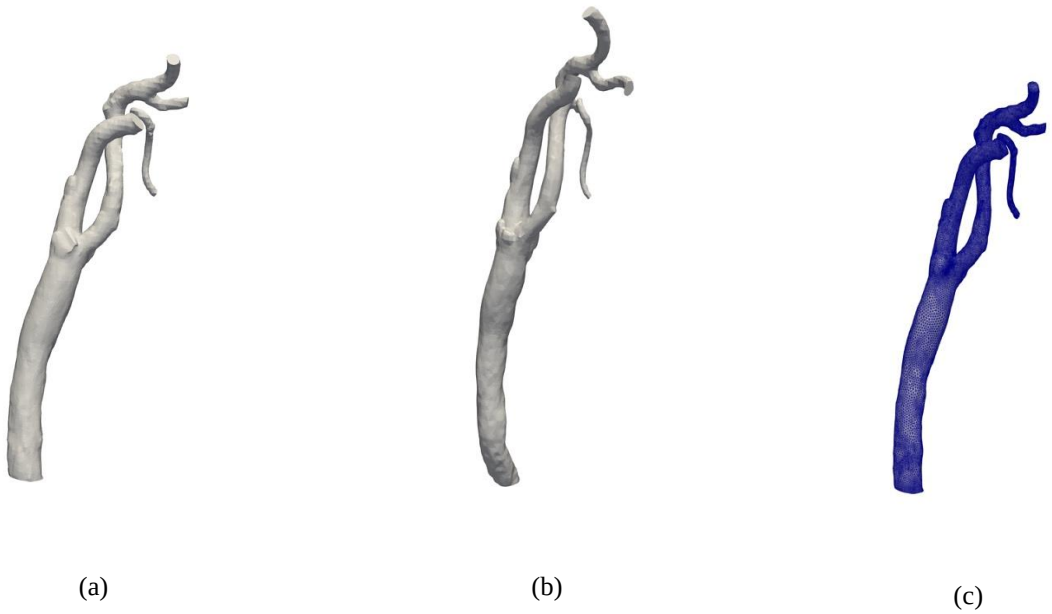

(a) (b) (c)

Fig. 1 Carotid artery geometry (a) Pre-operation (b)Post-operation (c) Mesh structure

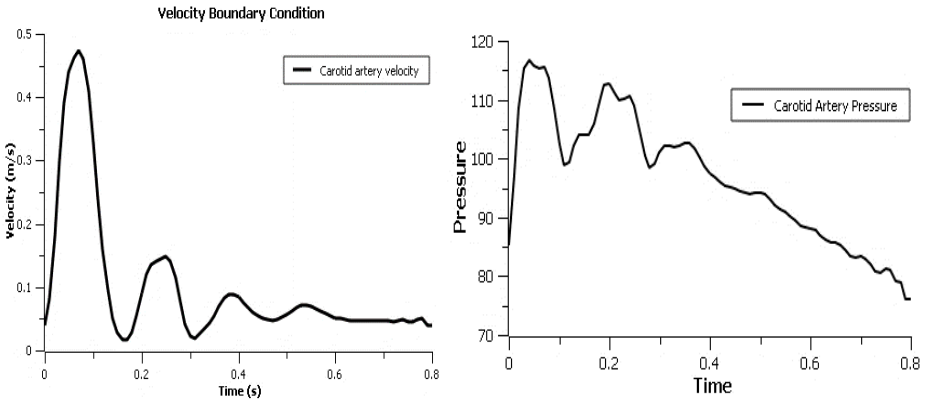

Fig. 2 Pulsatile velocity and pressure cycles as boundary conditions

The pulsatile velocity cycle shown in Figure 2 was taken from the literature [12, 13], then the pressure cycle was generated by the help of 4-Element Windkessel model [14].

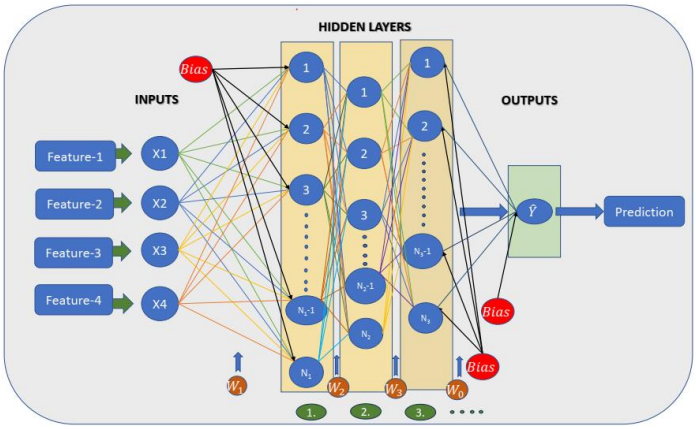

Fig. 3 DNN algorithm

In this study, Python and Keras library were used for neural network construction. ADAM optimizer was used with a learning rate of 0.001. "RELU" (Rectified Linear Unit) was selected as the activation function. 3 layers were used and values such as position, pressure, cross-sectional area were used as input features. In general, the ANN model output is expressed as follows [15]:

$$Y = F\left[\sum_{j=1}^{n} W_{kj}\left[F\left(\sum_{i=1}^{m} W_{ji}X_i + b_j\right)\right] + b_k\right] \tag{3}$$

The response provided by the ANN can be represented by the letter Y, while the number of hidden neurons is denoted by "n". The subscript "k" is associated with the output layer, and the transfer function F is utilized to normalize the output of the neuron. The coefficient of determination, represented by the R-squared value, is determined using Eq. 4.

$$R^2 = 1 - \frac{\sum_1^n (ytr_i - ypr_i)^2}{\sum_1^n (ytr_i)^2} \tag{4}$$

where, n is the overall number of the data, ypr is the predicted data which is based on DNN outputs, ytr is the true value that is coming from CFD. The Mean Squared Error (MSE) is defined in Eq. 5.

$$MSE = \frac{1}{n}\sum_{i=1}^{n}(y_i - \hat{y}_i)^2 \tag{5}$$

3. Results

Figure 4 presents the comparison of the results for machine learning (ML) and computational fluid dynamics (CFD) analyses. The deep neural network (DNN) model was employed as the machine learning algorithm.

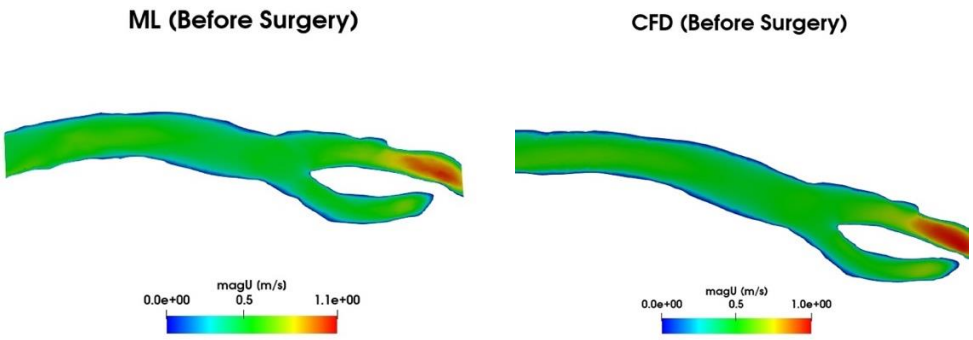

Fig. 4 ML and CFD results for pre-operation

The velocity distribution for the preoperative condition shows that the values were quite similar to those obtained from the DNN model with an r-squared value of 94.49%. The difference is apparent in the stenosis area at the exit of the carotid sinus before the surgical procedure on the internal carotid artery (ICA).

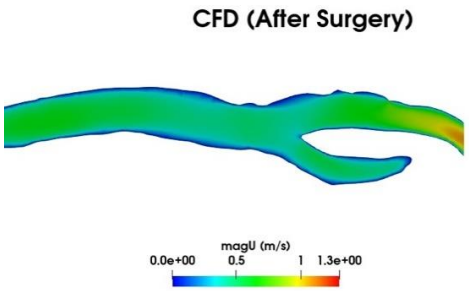

Fig. 5 Post-operation velocity distribution from CFD

Figure 5 illustrates the velocity distribution of the internal carotid artery (ICA) in the post-operative state. It can be observed that the narrowing of the ICA branch in the region posterior to the carotid sinus was eliminated as a consequence of the surgical procedure, resulting a reduction in the flow in the region.

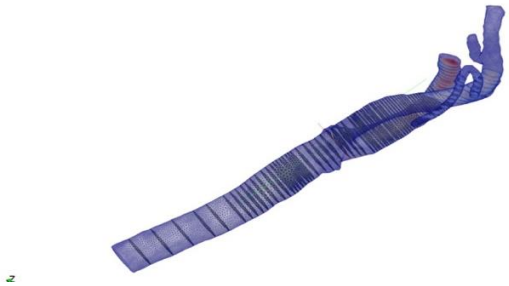

Fig. 6 Slices for ML prediction at the pre-operation geometry

Figure 6 illustrates the positions of the slice sections taken in the preoperative artery geometry. The sections were taken specifically in the proximal, bifurcation, carotid sinus and distal regions. A dataset was constructed using the points, pressure and cross-sectional area values obtained from these sections. This dataset was used to train the DNN model to be used for machine learning. As illustrated in Figure 3, the ML algorithm, which was developed and validated using preoperative CFD values, was employed in a similar manner in this instance.

Table 1. The comparison of the post-operation velocity results for CFD and ML

Slice number	I	II	III	IV	V	VI	VII	VIII
Velocity from CFD	0.427655	0.48132	0.251406	0.388729	0.499419	0.541221	0.679244	0.271886
Predicted velocity from DNN	0.397066	0.453591	0.283843	0.417632	0.528432	0.582446	0.634556	0.328882

The Deep Neural Network (DNN) model achieved an accuracy of 94.4977% in predicting preoperative velocity values. When utilized to predict velocity values for postoperative patients, the Mean Squared Error (MSE) value varies between 5%

and 10% when comparing velocity values from Computational Fluid Dynamics (CFD) analyses in Table 1. The R^2 is calculated as 93.0456%. for postoperative. This suggests that the DNN model can be enhanced by training it with a larger dataset, including additional postoperative values and velocity values from other patients. This is likely to result in higher accuracy rates. It was observed that incorporating area and pressure values as input feature levels yielded more promising results in predicting postoperative hemodynamic data.

4. Conclusions

This study shown that the use of deep learning methodologies can effectively predict hemodynamic parameters especially velocity of carotid artery blood flow for pre- and post-operative conditions. These methods have demonstrated their ability to reduce computational costs while maintaining accuracy, making them valuable tools for clinical applications. If the dataset is more the prediction's accuracy would likely improve, further enhancing the clinical utility of deep learning-based predictions of hemodynamic parameters. CFD simulation has traditionally been the gold standard for predicting hemodynamic parameters, but its complex operation and high computational cost hinder its clinical application. By developing a deep learning network and utilizing cardiovascular hemodynamic point datasets, the researchers were able to overcome these challenges and achieve accurate predictions with reduced computation time and increased computational efficiency. This result is shown that deep learning methods can be a valuable and practical solution for predicting hemodynamic parameters of carotid artery blood flow in clinical settings. The boundary conditions is important for these simulations, so the real and patient specific boundary conditions will give more reliable and accurate predictions.

References

1. Taebi, A. Deep learning for computational hemodynamics: A brief review of recent advances. *Fluids* 2022, 7 (6), 197.
2. Wang, S.; Wu, D.; Li, G.; Zhang, Z.; Xiao, W., Li, R.; Qiao, A.; Jin, L.; Liu, H. Deep learning based hemodynamic prediction of carotid artery stenosis before and after surgical treatments. *Frontiers in Physiology* 2023, 13, 1094743.
3. Yu, J.; Zhou, Y.; Yang, Q.; Liu, X.; Huang, L.; Yu, P.; Chu, S. Machine learning models for screening carotid atherosclerosis in asymptomatic adults. *Scientific Reports* 2021, 11 (1), 22236.
4. Latha, S.; Muthu, P.; Lai, K.W.; Khalil, A., Dhanalakshmi, S.; Performance analysis of machine learning and deep learning architectures on early stroke detection using carotid artery ultrasound images. *Frontiers in Aging Neuroscience* 2022, 13, 828214.
5. Ottakath, N.; Al-Maadeed, S.; Zughaier, S.M.; Elharrouss, O.; Mohammed, H.H.; Chowdhury, M.E.H.; Bouridane, A. Ultrasound-based image analysis stenosis risk: A comprehensive review of the problem, techniques, datasets, and future directions. *Diagnostics* 2023, 13, 2614.
6. Savaş, S.; Topaloğlu, N.; Kazcı, Ö.; Koşar, P.N. Classification of carotid artery intima media thickness ultrasound images with deep learning. *Journal of Medical Systems* 2019, 43, 273.
7. Ergün, U.; Serhatlıoğlu, S.; Hardalaç, F.; Güler, İ. Classification of carotid artery stenosis of patients with diabetes by neural network and logistic regression. *Computers in Biology and Medicine* 2004, 34 (5), 389-405.
8. Übeyli, E.D.; Güler, İ. Neural network analysis of internal carotid arterial doppler signals: predictions of stenosis and occlusion. *Expert Systems with Applications* 2003, 25 (1), 1-13.
9. OpenFOAM Trademark. OpenCFD Ltd. **2004** [accessed: 25 August 2011]. Available from: https://www.openfoam.com
10. Python Software Foundation. **2001** [accessed: 12 March 2022]. Available from:https://www.python.org.
11. 3D Slicer image computing program. **2005** [accessed: 22 June 2022]. Available from: https://www.slicer.org
12. Charlton, P.H.; Harana, J.M.; Vennin, S.; Li, Y.; Chowienczyk, P.; Alastruey, J. **2019** [accessed: 15 January 2022]. Available from: http://doi.org/10.5281/zenodo.3275625
13. Charlton, P.H.; Harana, J.M.; Vennin, S.; Li, Y.; Chowienczyk, P.; Alastruey, J. Modelling arterial pulse waves in healthy aging: a database for in silico evaluation of hemodynamics and pulse wave indexes. *Am J Physiol Heart Circ Physiol.* **2019**, 317 (5), 1062-1085.
14. Kucur, M.; Körbahti, B. Fluid-structure interaction analysis of carotid artery blood flow with machine learning algorithm and OpenFOAM. *Sakarya University Journal of Science* **2022**, 26 (6), 1131-1141.
15. Beigzadeh, R., Ozairy, R., 2019. Developing predictive models for analysis the heat transfer in sinusoidal wavy channels. *Thermal Science and Engineering Progress* **2019,** 14, 100425.

Experimental Analysis of Dragonfly *Aeshna Cyanea* Lift Force

Kamilė Gabrielė ZURLYTĖ[1]*, Rimvydas GAIDYS[1]*

1 Kaunas University of Technology, Faculty of mechanical engineering and design, E-mail:
** kamile.zurlyte@ktu.edu, rimvydas.gaidys@ktu.lt*

Abstract

In this study, 3 individuals of the dragonfly species *Aeshna Cyanea* were studied to investigate how the force they generate during flight changes as their flight cycle changes. The study was carried out by tying the two rear legs of the dragonfly with a fishing line, with weights on the other end of the line, which are placed on a jewellery scale. The readings of the scales were recorded for 9 seconds and the changes in the scale readings were observed over that time interval. Calculations were then performed to produce graphs to monitor the changing flight cycles of the dragonfly and the force generated during flight. This study will be useful for the future development and modelling of a dragonfly-inspired micro aerial vehicle.

Keywords: dragonfly, Aeshna Cyanea, lift force, experiment.

1. Introduction

Dragonflies can move in 6 directions during flight: left, right, forward, backward, upwards and downwards, and their flight can be divided into 4 types: gliding, flying forward, accelerating and hovering [1].

When a dragonfly is hovering, the front wings beat 180 degrees out of phase with the hind wings, creating an effective lift. When the dragonfly flies forward, the rear wings beat 90 degrees ahead of the front wings. This produces more thrust, but less lift compared to the hovering type of flight. During acceleration, thrust is maximised by the synchronised beating of both the front and rear wings of the dragonfly, which helps to accelerate and change the direction of the flight rapidly. When the dragonfly is gliding, the wings are fully extended and there is no beating [1, 2].

Dragonfly wings are distinguished from other insects by the fact that their flight muscles are attached directly to the tips of the wings rather than to the thorax. Dragonflies also have a high power-to-weight ratio - they can accelerate by 4G when flying straight and as much as 9G when making a sharp turn [2].

When a dragonfly is gliding, the wing pairs (a pair of front wings and a pair of rear wings) move in a figure-of-eight trajectory. This wing trajectory is almost vertical and at high angles of attack the wing pairs move independently [3].

During the experiments it was observed that dragonflies are characterised by a sudden instantaneous increase in lift, which can be 15-20 times the weight of the insect. During flight, dragonflies maintain an average lift of 2-3 times their body weight. When a dragonfly flies forward, it can reach a maximum speed of up to 100 body lengths per second [4].

When a dragonfly flies at high speed, it often synchronises the front and rear wing pairs so that the phase difference is zero [2, 5]. This alignment of the wing pairs provides sufficient thrust and lift to achieve high speeds [3]. However, this type of flight is energy intensive, so it is only used for a very short period of time (when catching up with prey or during a sudden take-off) [4]. Conversely, when gliding or hovering, the dragonfly either hovers in one place or flies a very short distance with each stroke of its wings. The main aspect of these types of flight is the changing phase relationship between the front and rear wing pairs. When the wing pairs move in the same direction during phase-shifted strokes, aerodynamic performance is enhanced. Whether this effect occurs during ascent or descent depends on the specific impact parameters and the nature of the manoeuvre [6].

The type of gliding flight is characterised by the movement of the fore and hind wings with no relative motion [7]. A dragonfly can fly up to 40 chord lengths in one complete period of wing movement[8]. This type of flight is low-energy, and is often observed on hot summer days [9–11].

The structural components of the dragonfly wing can be divided into two categories depending on their purpose: supporting elements and mobilising elements [12]. Supporting elements are those elements that add stiffness to the wing as it rotates and bends [12]. This type of element includes the membrane and veins [12]. The veins are filled with resilin, a protein that gives the veins elasticity and helps with the deformation of the wing that occurs in flight as the wing flexes and twists [13, 14]. The mobilising elements are the ones that help with wing deformation [12]. One good example of a mobilising element is nodus. This wing component is located approximately in the middle of the leading-edge vein [15].

A rigid wing generates less lift than a flexible wing with more deflection [16]. However, the ability of wings to be flexible is only useful up to certain environmental conditions. When a wing is extremely flexible, it may not be able to withstand the loads experienced in flight. For this reason, a balance between flexibility and stiffness is required [17].

The dragonfly is one of the world's top predators, with a 97% chance of catching its prey [18]. This good result is due to their extraordinary flight. Dragonflies have the ability to control each of their wings individually, varying the frequency and amplitude of their wing movements. This insect species has great potential for micro aerial vehicle development in the future.

2. Studied species of the dragonfly

The experimental study was carried out in Southern Lithuania. Dragonflies were observed on the banks of water bodies and in the fields adjacent to them. After capture, the length of the dragonfly's body, the distance between the wing tips and the mass were measured. Identification of the species of dragonfly caught was also made. Figure 1 shows a photograph of a male *Aeshna Cyanea* dragonfly taken during the experiment.

Fig. 1 Aeshna Cyanea, male

Aeshna Cyanea (commonly known as a Southern hawker) is one of the most common species of the family Aeshnidae in Lithuania. It is characterised by bright blue and green spots on the body and chest. The body length reaches up to 75 mm and the width between the spread wing tips up to 100 mm. This species often flies over rough water where there are no other individuals of the same family.

3. Experiment

A digital scale and a home-made experimental stand were used for the experiment to determine the lifting force. Weights are placed on one end of it, and a dragonfly is tied on the other. At the end where the dragonfly is tied, there is a 0.5 meter long fishing line. The two back legs of the dragonfly are tied with string. The experimental stand is shown in Figure 2.

Fig. 2 Experimental stand

During the experimental study, the magnitudes of the force generated by the dragonfly were recorded, which changed on average three times per second. Since the lift generated by the dragonflies' during flight was recorded for about 9 seconds, it was chosen to record a total of 28 data changes during each exoeriment. As can be seen in Figure 3, in some time intervals the change in force is very sudden, which may indicate a relationship between changes in flight type. Time intervals in which an increase in force is observed indicate the insect's elevation or movement away from the experimental bench. Meanwhile, ime intervals of stable or little changing force magnitudes indicate hovering in place. When the magnitude of the force decreases, the dragonfly descends or approaches the experimental bench.

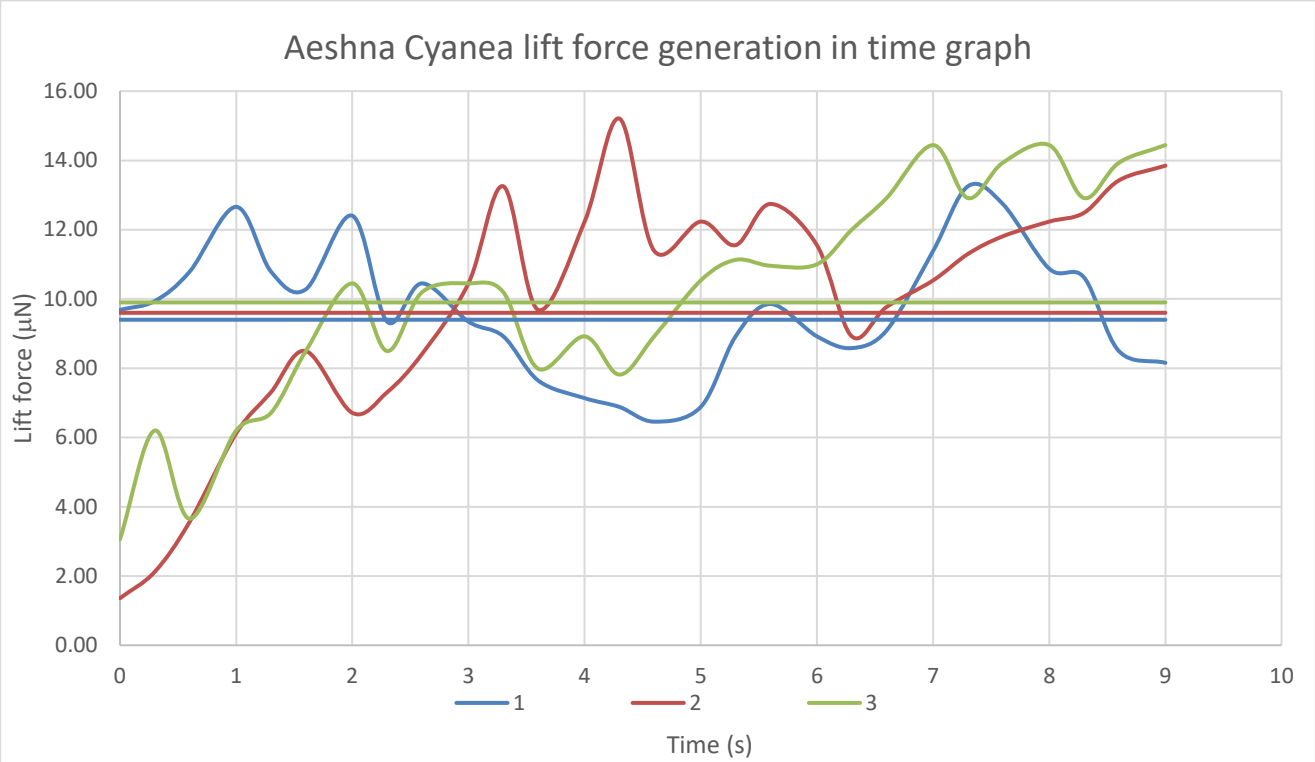

Fig. 3 Dragonfly Lift Force change in time graph

The first graph, marked in blue in Figure 3, shows that the force generated by the dragonfly remains at the lowest levels during the entire measured time interval. The maximum force generated was at 7.3 seconds and was equal to 13.25 mN. The smallest force generated was equal to 6.14 mN and was recorded at 4.6 seconds. During the entire time interval, the dragonfly either rose consistently or descended consistently, and no sudden changes in the trajectory were observed.

In the second graph, highlighted in red, it is evident that the lift generated by the dragonfly increases steadily for the initial 1.6 seconds, subsequently decreases by approximately 7 mN, and then rises once moreuntil 3.3 seconds. Over the following 3 seconds, the induced force fluctuates irregularly, and from 6.3 seconds until the conclusion of data acquisition, it ascends smoothly.

The third dragonfly, highlighted in green in Figure 3, exhibits a highly erratic flight pattern and demonstrates abrupt changes in the lift it generates during flight. The most significant change in the force produced occurs between 5.6 and 6.3 seconds, where the force drops from approximately 11 mN to nearly 0, before sharply rising to an even higher value. The third dragonfly, highlighted in green in Figure 2, exhibits a highly erratic flight pattern and demonstrates abrupt changes in the lift it generates during flight. The most significant change in the force produced occurs between 5.6 and 6.3 seconds, where the force drops from approximately 11 mN to nearly 0, before sharply rising to an even higher value.

As can be seen in the first table, the mass of the dragonfly does not necessarily affect the amount of force produced, as dragonfly 3, which has a mass of 0.67 g, produced more force than the first dragonfly, even though it weighed 0.1 g more.

Table 1. Parameters of a dragonfly

Speciment No.	Mass of a dragonfly:	Distance between wingtips:	Wing area:
1	0.77 g	96.6 mm	375.56 mm^2
2	0.87 g	103.7 mm	435.24 mm^2
3	0.67 g	97.5 mm	395.42 mm^2

In Figure 3, the horizontal lines represent the averages of the generated force. The average force produced by each dragonfly is presented in the same color as the force produced curves in the graph. As can be observed in Figure 3, the average values of the generated forces are very similar for all dragonflies. The average value of the lifting force of the 1st dragonfly is 9.4

mN, the second - 9.6 mN, the third - 9.9 mN. Thus, the average force produced by all dragonflies is 9.63 mN. Meanwhile, dragonflies have an average wing area of 402.07 mm^2.

Figure 4 shows the data variance of all three specimens collected data. The total amount of data is 84.

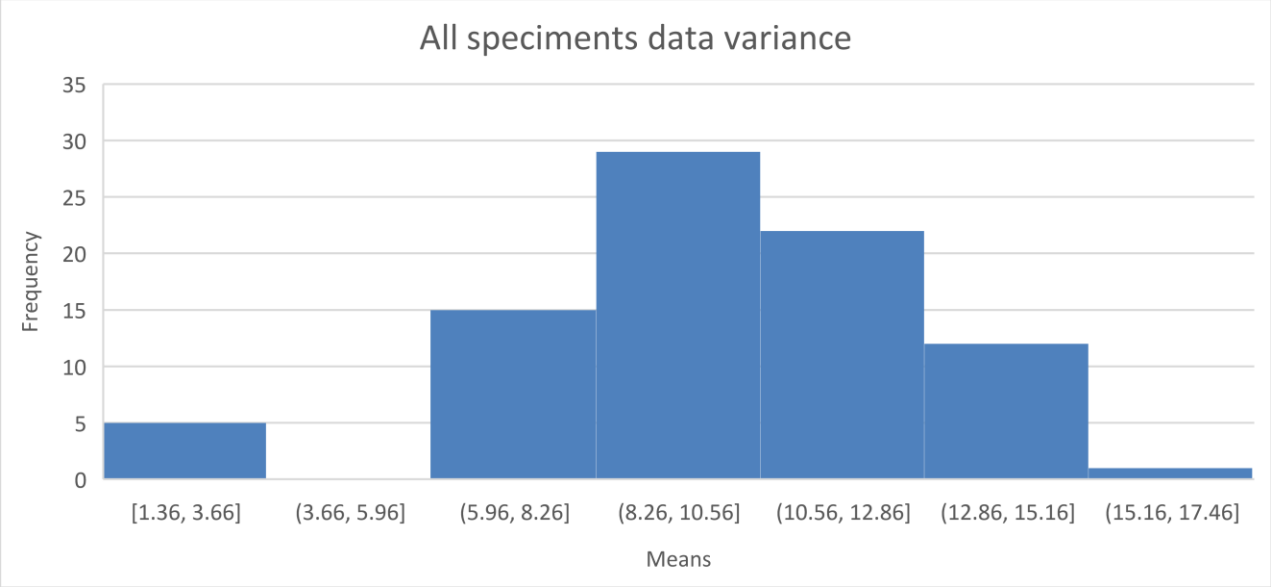

Fig. 4 Dragonfly Lift Force data variance

The variance of the data shows that the most common value of the induced force was in the range of 8.26-10.56 values. There was no data value in the interval of values 3.66-5.96, and only one value occurred in the interval from 15.16-17.46.

4. Conclusions

During this study, 3 specimens of the dragonfly species *Aeshna Cyanea* were observed. During the study, the force generated by the dragonfly was monitored for 9 seconds and the magnitude of the force generated was monitored over that time interval. The magnitude of the force generated was observed to change very rapidly over some time intervals. This may be due to changes in the direction of flight or the different type of the flight. In the time intervals where an increase in force was observed, it can be assumed that the insect flew further away from the experimental stand or upwards. In intervals where the magnitude remained the same or changed only slightly, the dragonfly may be assumed to have flown in one place. A decreasing magnitude of force overtime intervals indicates a downward movement or an approach towards the experimental stand. The study found that mass is not one of the main parameters influencing the force generated during flight, as the dragonfly with the highest mass generated the lowest force and the dragonfly with the second highest mass generated the second highest force. The study also showed that various wing damages of unknown origin have an effect on the magnitude of the force generated by the dragonfly.

References

1. SALAMI, Erfan, WARD, Thomas A, MONTAZER, Elham ir GHAZALI, Nik Nazri Nik. A review of aerodynamic studies on dragonfly flight. Proceedings of the Institution of Mechanical Engineers, Part C: Journal of Mechanical Engineering Science. rugsėjo **2019**. Vol. 233, no. 18, p. 6519–6537. DOI 10.1177/0954406219861133.
2. TAKAHASHI, Hidetoshi, CONCORDEL, Alice, PAIK, Jamie ir SHIMOYAMA, Isao. The Effect of the Phase Angle between the Forewing and Hindwing on the Aerodynamic Performance of a Dragonfly-Type Ornithopter. Aerospace. 25 sausio **2016**. Vol. 3, no. 1, p. 4. DOI 10.3390/aerospace3010004.
3. VAN DOKKUM PIETER. Dragonflies: Magnificent Creatures of Water, Air, and Land. **2015**.
4. MAY, Michael L. Dragonfly Flight: Power Requirements at High Speed and Acceleration. Journal of Experimental Biology. 1 liepos **1991**. Vol. 158, no. 1, p. 325–342. DOI 10.1242/jeb.158.1.325.
5. WANG, Hao, ZENG, Lijiang, LIU, Hao ir YIN, Chunyong. Measuring wing kinematics, flight trajectory and body attitude during forward flight and turning maneuvers in dragonflies. Journal of Experimental Biology. 15 vasario **2003**. Vol. 206, no. 4, p. 745–757. DOI 10.1242/jeb.00183.
6. RÜPPELL, G. Kinematic Analysis of Symmetrical Flight Manoeuvres of Odonata. Journal of Experimental Biology. 1 liepos **1989**. Vol. 144, no. 1, p. 13–42. DOI 10.1242/jeb.144.1.13.
7. SUN, Xiaojing, GONG, Xinyu ir HUANG, Diangui. A review on studies of the aerodynamics of different types of maneuvers in dragonflies. Archive of Applied Mechanics. kovo **2017**. Vol. 87, no. 3, p. 521–554. DOI 10.1007/s00419-016-1208-7.
8. WAKELING, J. M. ir ELLINGTON, C. P. Dragonfly Flight: I. Gliding Flight and Steady-State Aerodynamic Forces. Journal of Experimental Biology. 1 vasario **1997**. Vol. 200, no. 3, p. 543–556. DOI 10.1242/jeb.200.3.543.
9. WERNER NACHTIGALL. Insects in Flight: A Glimpse Behind the Scenes in Biophysical Research. 1973.

10. MAY, Michael L. Thermoregulation and Adaptation to Temperature in Dragonflies (Odonata: Anisoptera). Ecological Monographs. gruodžio **1976**. Vol. 46, no. 1, p. 1–32. DOI 10.2307/1942392.
11. MAY, Michael L. Dependence of Flight Behavior and Heat Production on air Temperature in the Green Darner Dragonfly Anax Junius (Odonata: Aeshnidae). Journal of Experimental Biology. 1 lapkričio **1995**. Vol. 198, no. 11, p. 2385–2392. DOI 10.1242/jeb.198.11.2385.
12. RUDOLF, J., WANG, L.-Y., GORB, S.N. ir RAJABI, H. On the fracture resistance of dragonfly wings. Journal of the Mechanical Behavior of Biomedical Materials. lapkričio **2019**. Vol. 99, p. 127–133. DOI 10.1016/j.jmbbm.2019.07.009.
13. APPEL, Esther ir GORB, Stanislav N. Resilin-bearing wing vein joints in the dragonfly Epiophlebia superstes. Bioinspiration & Biomimetics. 1 gruodžio **2011**. Vol. 6, no. 4, p. 046006. DOI 10.1088/1748-3182/6/4/046006.
14. DONOUGHE, Seth, CRALL, James D., MERZ, Rachel A. ir COMBES, Stacey A. Resilin in dragonfly and damselfly wings and its implications for wing flexibility. Journal of Morphology. gruodžio **2011**. Vol. 272, no. 12, p. 1409–1421. DOI 10.1002/jmor.10992.
15. RAJABI, H., GHOROUBI, N., STAMM, K., APPEL, E. ir GORB, S.N. Dragonfly wing nodus: A one-way hinge contributing to the asymmetric wing deformation. Acta Biomaterialia. rugsėjo **2017**. Vol. 60, p. 330–338. DOI 10.1016/j.actbio.2017.07.034.
16. Flow Phenomena in Nature Volume 2. [interaktyvus]. [Žiūrėta 1 lapkričio 2022]. Prieiga internete: https://www.witpress.com/books/978-1-84564-095-8
17. RAJABI, H. ir GORB, S.N. How do dragonfly wings work? A brief guide to functional roles of wing structural components. International Journal of Odonatology. 2 sausio **2020**. Vol. 23, no. 1, p. 23–30. DOI 10.1080/13887890.2019.1677515.
18. AZUMA, Akira ir WATANABE, Tadaaki. FLIGHT PERFORMANCE OF A DRAGONFLY. . P. 32.

Modeling of Piezoelectric Tubular Structure under Pulsatile Pressure for Application in Smart Vascular Implants

Saeid SABERI [1]*, Rolanas DAUKSEVICIUS [1]

1 Kaunas University of Technology, Institute of Mechatronics, Kaunas, Lithuania
** saeid.saberi@ktu.edu*

Abstract

The objective of this contribution is to computationally explore the feasibility of generating electrical energy through a piezoelectric vascular implant, made of biocompatible ferroelectric PVDF copolymer (PVDF-TrFE), subjected to a pulsatile pressure load. Artificial vascular implants (grafts) are flexible tubular structures (conduits) designed to replace damaged blood vessels. The incorporation of direct piezoelectric effect into vascular implants can bring about significant benefits, including sensing biomechanical forces, diagnosing medical problems and improving tissue regeneration through endogenous electrical stimulation. In this work, a piezoelectric finite element model is implemented in ABAQUS to estimate the electro-mechanical responses of the PVDF-TrFE tubular structure under dynamic internal load that mimics the effect of actual pulsatile blood pressure. A small diameter tubular structure is simulated by applying a realistic harmonic pressure load of 12.2 kPa with a frequency corresponding to 66 bpm. A parametric study is conducted to reveal the influence of blood pressure on the generated piezoelectric voltage output.

Keywords: piezoelectric conduit, multiphysics FEM, electromechanical FEA, smart implants, biomechanical sensors

1. Introduction

Implantable medical devices have garnered substantial interest for both diagnostic and therapeutic capabilities, significantly improving the quality and duration of life for countless patients, especially those afflicted with cardiovascular ailments. Cardiovascular disease stands as a predominant cause of death worldwide, with a rising trajectory from approximately 17.5 million fatalities in 2012 to around 18 million in 2016, projected to surpass 22 million by 2030. The treatment options for cardiovascular disease range from lifestyle changes and adopting healthier dietary habits to medical interventions and surgical procedures. Utilizing artificial blood vessels to replace damaged or blocked vessels presents a promising approach in treating these conditions. At present, artificial blood vessels with diameters larger than 6 mm have been effectively utilized in clinical settings. However, the integration of smaller diameter artificial blood vessels remains largely unexplored, due to challenges such as thrombosis and intimal hyperplasia. Consequently, it is still crucial to undertake different studies on these implants [1,2].

Advancements in technology have recently paved the way for the development of innovative smart vascular implants, such as piezoelectric vascular implants. They represent a remarkable emerging advancement in the field of biomedical engineering, particularly in the domain of cardiovascular treatment. These implants harness the piezoelectric effect, converting mechanical energy from blood flow and the host tissue into electrical energy (direct effect), thus enabling self-powering capabilities without the need for external energy sources. The electrical signals generated by piezoelectric vascular implants can also be utilized for various diagnostic and therapeutic purposes. Furthermore, these smart implants present strategies to promote regeneration of damaged vascular tissues [3].

Piezoelectric polymers with large piezoelectric coefficients such as polyvinylidene fluoride (PVDF) and its copolymer polyvinylidene fluoride-trifluoroethylene (PVDF-TrFE) offer a compelling path for the development of smart vascular implants capable of harvesting mechanical energy and sensing, by responding to mechanical stimuli owing to their structural stretchability and flexibility, biocompatibility and processing simplicity [4]. Several studies have investigated PVDF and its composites as a sensing element in cardiovascular systems. Zhang et al. designed an implantable and flexible piezoelectric generator involving PVDF film which is able to harvest energy from the pulsation of the ascending aorta and performed both in vitro and in vivo studies [5]. Sharma et al. fabricated thin flexible pressure sensors based on piezoelectric PVDF-TrFE to measure the real-time flow in catheter applications. The sensor was developed using low-temperature fabrication methods and simply integrated with the catheter for intravascular measurements [6]. Gil et al. presented a piezoelectric force sensor based on PVDF-TrFE film to monitor the intraluminal pressure and the sensor was fixed into the tip of catheter. The pressure sensing range of the sensor was found below 40 kPa with a signal responsivity of 0.63 μV/Pa [7]. Recently, Chang et al. developed a soft self-powered micro-pressure sensor using PVDF/ZnO piezoelectric nanofibers. This sensor was implanted on the cardiovascular walls of the heart and femoral artery in pigs for the aim of monitoring internal blood pressure. The sensor showed accurate recording and monitoring capabilities for micro-pressure changes during different physiological conditions [8].

This research aims to model a piezoelectric tubular structure made of PVF-TrFE under pulsatile pressure for application in smart vascular implants. First, a FE model of the structure is modeled using ABAQUS. Subsequently, that will be subjected to a harmonic load mimicking pulsatile blood pressure conditions. Following this, the biological forces exerted on the simulated vascular implant due to internal pressure will be estimated and validated against the thick-walled cylindrical shell theory. Finally, the electrical output generated by the piezoelectric implant will be determined.

2. Finite Element Modelling

In order to conduct the finite element analysis, ABAQUS software package is used and the following steps will be implemented. After designing a cylindrical tube with an inner diameter, thickness and length of 5 mm, 0.5 mm and 50 mm, respectively, in the 'Part' module provided in Fig. 1, in the 'Property' module, the mechanical and piezoelectric properties should be defined according to Table 1. PVDF-TrFE 75/25% mol (Piezotech, France) was used in this work.

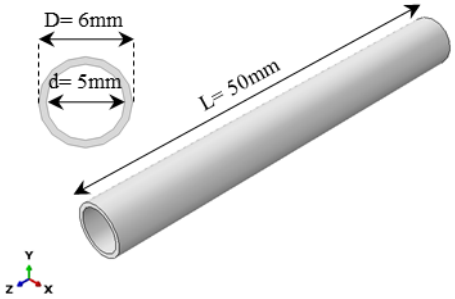

Fig. 1 A schematic representation of the tubular implant designed using ABAQUS

Table 1. Material properties of PVDF-TrFE 70/25

Property	Value
Young's modulus, E, GPa	1.1
Poisson's ratio, υ	0.33
Density, ρ, m^3/kg	1850
Absolute permittivity, pF/m	115
d_{13}, pC/N	12
d_{33}, pC/N	-38

In the 'Step' module, the 'Dynamic-Implicit' step is selected to simulate the effects of the pulsatile blood pressure on the tubular implant. In the 'Load module, the pulsatile blood pressure and boundary conditions of the implant are defined. A new coordinate system is created using 'Create Datum Plane' so that it help us to define the boundary conditions in the cylindrical system. As shown in Fig. 2, the desired boundary conditions are applied at the both ends of the tube using 'XASYMM' option so that it can only deform radially. It should be mentioned that ground electric potential boundary condition was defined on the internal surface using 'Electrical/Magnetic' option.

Regarding the loading condition, blood pressure vessels in normal resting state are generally subjected to a stress ranging from 9 kPa to 13 kPa with a rate from about 50 to 90 beats per minute (bpm). In this research work, the pulsatile blood pressure is approximated as a harmonic force with an amplitude of 0.24 *N* and a frequency of 66 bpm, corresponding to the blood pressure of 12.2 kPa exerted on the internal surface of the cylindrical vessel [9]. This harmonic actuation can be defined using ''Periodic'' option in ABAQUS.

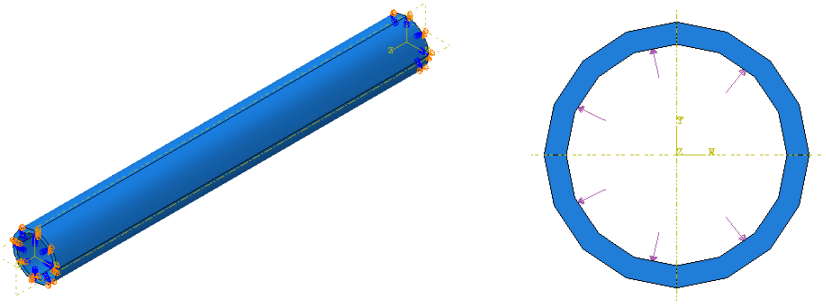

(a) (b)

Fig. 2 (a) Boundary conditions at the ends of the tube (b) applied internal pressure

The simulated implant is meshed using linear hexahedral elements of type C3D8E (8-node linear piezoelectric brick), comprising 6000 elements and 8320 nodes. The elements that are used in this case contain both displacement degrees of freedom and the electric potential as nodal variables. To opt the best mesh size, a mesh convergence analysis is also performed.

3. Results

Using the developed FE model, the main biomechanical stresses applied to vascular implants are predicted and then verified against the theoretical method. After validation the model, the mechanical and electrical responses of the implant under the pulsatile blood pressure will be determined.

3.1. Biomechanical Stresses

Physiological forces play a critical role in the biomechanics of blood vessels, influencing their structural integrity and function. Among the primary forces acting on blood vessels are hoop, radial, and axial stresses. Hoop stress, also known as circumferential stress, refers to the tension exerted tangentially to the tube circumference, primarily due to blood pressure generated during cardiac contraction. This stress is crucial for maintaining vessel integrity and preventing dilation or rupture. Radial stress, occurring perpendicular to the hoop stress, contributes to vessel wall thickness and compliance, influencing its ability to accommodate changes in blood volume and pressure. Axial stress, running along the longitudinal axis of the vessel, arises from factors such as blood flow pulsatility and vessel curvature [10].

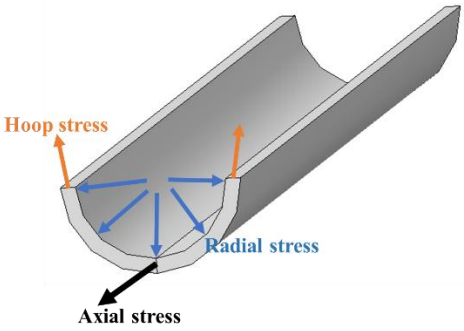

Fig. 3 Physiological stresses applied to a tubular implant

Fig 4 illustrates the variation of Hoop stress in the cross section of the tube, ranging from 65.61 kPa in the internal surface to 56.55 kPa in the external surface, determined using ABAQUS for a constant pressure of 12.22 kPa.

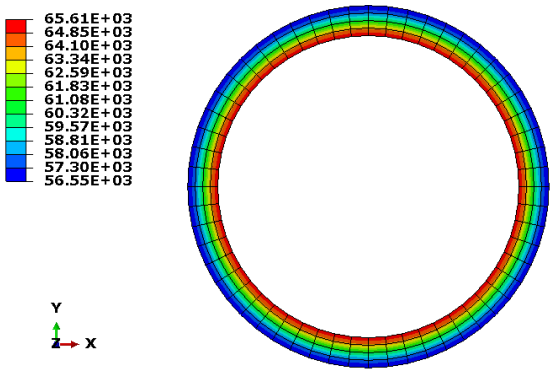

Fig. 4 Hoop stress produced in the tube

As the ratio of the internal diameter to the thickness is not more than 20, the tube is considered as a thick-walled cylinder. Hence, according to Lamé's equations, Hoop, radial and axial stresses are defined as follows [11]:

$$\sigma_\theta = \frac{P_i}{\left(\frac{r_o}{r_i}\right)^2 - 1}\left(1 + \frac{{r_o}^2}{r^2}\right)$$

$$\sigma_r = \frac{P_i}{\left(\frac{r_o}{r_i}\right)^2 - 1}\left(1 - \frac{{r_o}^2}{r^2}\right) \tag{1}$$

$$\sigma_a = \frac{P_i}{\left(\frac{r_o}{r_i}\right)^2 - 1} 2\upsilon$$

where P_i=12.22 kPa, r_o=3 mm, r_i=2.5 mm and $\upsilon = 0.33$.

The values of Hoop stress (σ_θ) determined using the equation in the internal and external surfaces are 67.74 kPa and 55.5 kPa, respectively, which constitutes a very good agreement with FEM with an error of 1.9-3%.

Regarding the axial stress (σ_a), it is constant through the thickness and equal to 18.3 kPa, determined using the equation, which closely concurs with the FEM result shown in Fig 5.

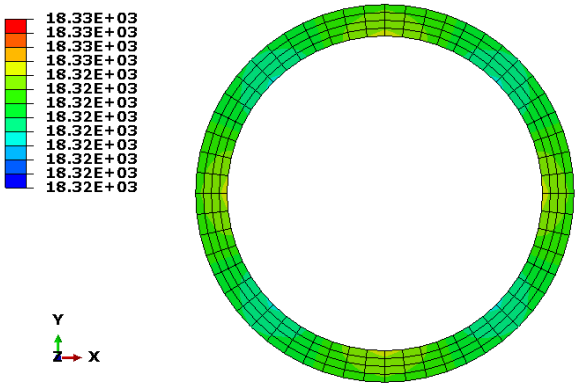

Fig. 5 Axial stress generated in the tube

The radial stress theoretically varies from 12.21 kPa in the internal surface to zero in the external surface. The FEM result for this stress is provided in Fig 6.

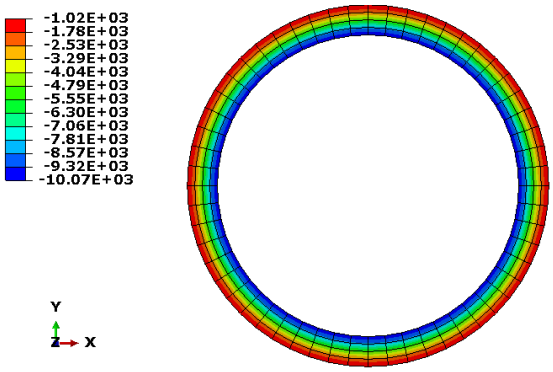

Fig. 6 Radial stress induced in the tube

Hence, the developed model can accurately estimate the stresses exiting on the tubular structure due to the pulsatile pressure.

3.2. Mechanical and Electrical Responses

The radial displacement of the tubular implant under the internal pressure is demonstrated in Fig 7. That shows the tube is deformed by producing radial displacements up to 87 nm under the pulsatile pressure.

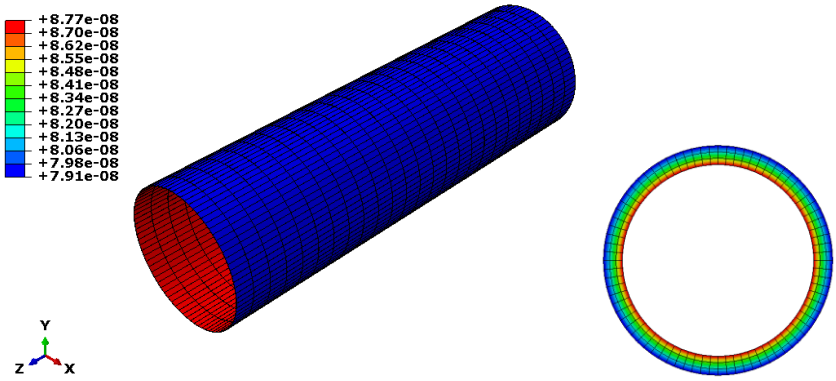

Fig. 7 The radial displacement of the tubular implant

The electrical voltage generated by the piezoelectric vascular implant under the pulsatile blood pressure is demonstrated in Fig 8.

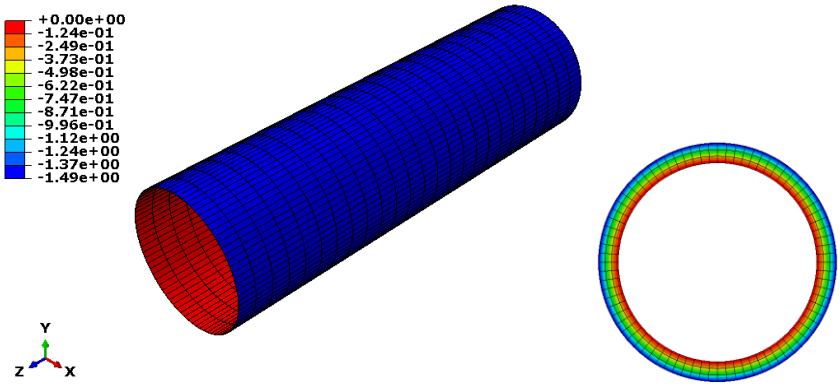

Fig. 8 The electrical voltage generated by the piezoelectric vascular implant

According to Fig. 8, the piezoelectric graft can generate 1.49 V electrical voltage, which can be employed for biomedical purposes.

4. Conclusions

This study utilized numerical analysis to explore the utilization of a cylindrical tube composed of PVDF-TrFE piezoelectric material as a tubular vascular implant. The designed implant can produce an electric voltage of 1.49 V in response to the pulsatile blood pressure. The FE model accurately predicted the biomechanical forces applied to the implant due to the blood pressure oscillations with a maximum error of 3%. This small-calibre implant has potential applications in the medical field, including sensing biomechanical forces, harvesting biomechanical energy or enhancing tissue regeneration through wireless electrical stimulation.

References

1. Khan A, Joshi R, Sharma MK, Ganguly A, Parashar P, Wang T-W, et al. Piezoelectric and triboelectric nanogenerators: promising technologies for self-powered implantable biomedical devices. *Nano Energy* **2023**:109051.
2. Mishra S, Mohanty S, Ramadoss A. Functionality of flexible pressure sensors in cardiovascular health monitoring: a review. *Acs Sensors* **2022**;7:2495–520.
3. Nain A, Chakraborty S, Barman SR, Gavit P, Indrakumar S, Agarwal A, et al. Progress in the development of piezoelectric biomaterials for tissue remodeling. *Biomaterials* **2024**:122528.
4. Oladapo BI, Zhao Q. Enhancing tissue regeneration with self-healing elastic piezoelectricity for sustainable implants. *Nano Energy* **2023**:109092.
5. Zhang H, Zhang X-S, Cheng X, Liu Y, Han M, Xue X, et al. A flexible and implantable piezoelectric generator harvesting energy from the pulsation of ascending aorta: in vitro and in vivo studies. *Nano Energy* **2015**;12:296–304.
6. Sharma T, Aroom K, Naik S, Gill B, Zhang JXJ. Flexible thin-film PVDF-TrFE based pressure sensor for smart catheter applications. *Ann Biomed Eng* **2013**;41:744–51.
7. Gil B, Li B, Gao A, Yang G-Z. Miniaturized piezo force sensor for a medical catheter and implantable device. *ACS Appl Electron Mater* **2020**;2:2669–77.
8. Chang G, Pan X, Hao Y, Du W, Wang S, Zhou Y, et al. PVDF/ZnO piezoelectric nanofibers designed for monitoring of internal micro-pressure. *RSC Adv* **2024**;14:11775–83.
9. Sinek A, Mesek M, Rojczyk M, Juszczyk J, Adamczyk WP, Sturdy J, et al. Evaluating the precision and reproducibility of non-invasive deformation measurements in an arterial phantom. *Measurement* **2023**;216:112904.
10. Camasão DB, Mantovani D. The mechanical characterization of blood vessels and their substitutes in the continuous quest for physiological-relevant performances. A critical review. *Mater Today Bio* **2021**;10:100106.
11. Annaratone D. *Pressure vessel design*. Springer; **2007**.

A Numerical Study of a New Standard Tandem Wind Turbine Performance for Rural Use

Adjlout AKRAM[1]*, Ladjedel OMAR[1], Adjlout LAHOUARI[1], Imine OMAR[2]

1 Naval Aero-Hydrodynamics Laboratory, Department of Maritime Engineering, University of Sciences and Technology of Oran Mohamed Boudiaf, USTO-MB, Oran, Algeria
2 Aeronautics and Propulsion Systems Laboratory, Department of Mechanical Engineering, University of Science and Technology of Oran Mohamed Boudiaf, USTO-MB, Oran, Algeria
** adjloutgm@gmail.com*

Abstract

The present study presents a numerical simulation of a novel three-bladed horizontal axis wind turbines for producing electricity for rural use. Numerical tests were conducted on a single NWT and a typical standard tandem NTWT blade horizontal axis wind turbine. The various meshes and parameters were generated and determined using the Gambit and Fluent 19.2 code, respectively. A finite volume method was used to resolve the averaged Navier-Stokes equations (RANS). The turbulence computation used the k-ε realisable two-equation model. The obtained results were compared with some experimental data from the literature. The maximum power coefficient reaches a value of 0.47 for the NTWT. It has also been observed that the flow on this tandem configuration exhibits a complex phenomenon on both surfaces of both blades.

Keywords: Horizontal wind turbine, tandem, power coefficient, numerical simulation,

1. Introduction

Power line installation is not usually evident in rural areas, especially in those with a high concentration of agricultural activities. In these places, rugged terrain and low population densities sometimes limit access. One option that is accessible for producing electricity locally is wind power. Both vertical and horizontal axis wind turbine performance have been the subject of numerous research [1–6]. Wind energy is still neglected despite being abundant and accessible to all. Nevertheless, since 1973, both industrialized and developing countries have made great strides in the development of affordable wind energy conversion devices for a variety of uses.

Abdelsalam et al. [7] studied wake characteristics of a horizontal-axis wind turbine both experimentally and numerically utilizing a Navier-Stokes solver and the k-ε model adjusted for atmospheric flows. They evaluated the computational model by contrasting projected and measured velocities at specified downstream locations at various upstream wind speeds, obtaining a relationship between wind speed and wake recovery.

Kaya et al. [8] examined the aerodynamic performance of horizontal axis wind turbines (HAWTs) with forward- and backward-swept blades, concluding that forward-swept blades can improve performance while backward-swept blades typically result in a drop in the thrust coefficient.

Krogstad et al.[9] conducted experimental and numerical investigations on the performance of a 0.9 m diameter model wind turbine using the S826 airfoil profile, employing blade element momentum theory (BEM) in the geometric layout and obtaining a peak power coefficient of Cp = 0.448. Their study demonstrated the accuracy of estimation of wind turbine performance using Fluent CFD software and the predictive capability of the BEM method.

In the present study, a numerical investigation of the flow around a single NWT and a tandem NTWT horizontal axis wind turbines for rural use is performed. A new configuration for the horizontal blade is tested.

2. Governing Equations

This section aims to present the various mathematical and physical concepts associated with fluid flow, namely the equations describing fluid motion and the various turbulence parameters. The Navier-Stockes equations govern flows of incompressible fluids. They are given as equations that translate the concepts of momentum and mass conservation, Advances in CFD and numerical modeling have made it possible to address these issues and offer effective solutions for a variety of industrial issues. The fluid's velocity (ui, uj) and pressure (p) at each flow point are expressed to formulate the Navier-Stockes equations, which are (1) (2):

- Mass conservation:

$$\frac{\delta\rho}{\delta t} + \frac{\delta}{\delta x_i}(\rho u_i) \tag{1}$$

- Conservation of momentum:

$$\frac{\partial}{\partial t}(\rho u_i) + \frac{\partial}{\partial x_j} = -\frac{\partial p}{\partial x_i} + \frac{\partial}{\partial x_j}\left[\mu\left(\frac{\partial u_i}{\partial x_j} + \frac{\partial u_j}{\partial x_i} - \frac{2}{3}\delta_{ij}\frac{\partial u_l}{\partial x_l}\right]\right] + \frac{\partial}{\partial x_j}(-\rho\overline{u_i' u_j'}) \tag{2}$$

In addition to the power and torque coefficients laws (3), (4) and the specific speed ratio (5)

- Power Coefficient :

$$\mathrm{Cp} = \frac{\mathrm{Power}}{\frac{1}{2}\rho \mathrm{A} {V_\infty}^3} \tag{3}$$

- Torque Coefficient :

$$\mathrm{Ct} = \frac{8\,\mathrm{Torque}}{\rho \pi {V_\infty}^2 {D_\mathrm{P}}^3} \tag{4}$$

- Specific speed ratio:

$$\mathrm{TSR} = \frac{2\,\pi\,\mathrm{n}\,\mathrm{R}}{V_\infty} \tag{5}$$

- The realizable k−ε turbulence model was chosen for this study because to its higher accuracy for flows involving rotation.

The modeled transport equations for k and Ɛ in the realizable k- Ɛ model are:

$$\frac{\partial}{\partial \mathrm{t}}(\rho \mathrm{k}) + \frac{\partial}{\partial \mathrm{x}_j}\left(\rho \mathrm{k} u_j\right) = \frac{\partial}{\partial \mathrm{x}_j}\left[\left(\mu + \frac{\mu_t}{\sigma_k}\right)\frac{\partial \mathrm{k}}{\partial \mathrm{x}_j}\right] + \mathrm{Gk} + \mathrm{Gb} - \rho\varepsilon - \mathrm{Y}_M + \mathrm{S}_k \tag{6}$$

and

$$\frac{\partial}{\partial \mathrm{t}}(\rho\varepsilon) + \frac{\partial}{\partial \mathrm{x}_j}\left(\rho\varepsilon u_j\right) = \frac{\partial}{\partial \mathrm{x}_j}\left[\left(\mu + \frac{\mu_t}{\sigma_\varepsilon}\right)\frac{\partial \varepsilon}{\partial \mathrm{x}_j}\right] + \rho \mathrm{C}_1 \mathrm{S}_\varepsilon - \rho \mathrm{C}_2 \frac{\varepsilon^2}{k + \sqrt{\nu\varepsilon}} + \mathrm{C}_{1\varepsilon}\frac{\varepsilon}{k} + \mathrm{C}_{3\varepsilon}\mathrm{G}_b + \mathrm{S}_\varepsilon \tag{7}$$

2. The computational procedure

2.1 Blade geometry

The blade used in this investigation is a 1012 mm long, with round camber sections cut out of a 200 mm diameter tube. The cutting angle of the blade from the tube is angled so that the extreme profiles have a 25 degree difference in twist angle. It is noted that the pitch angle, Φ, equals zero at the tip of the blade. As for the thickness of the blade the distribution of NACA 0012 is used, the wind turbine's blade is attached to the conical hub by a stem, as shown in Fig. 1, giving it a radius, Rp, of 1295 mm. the term "Novel Tandem wind turbine" refers to the generated wind turbine (NTWT).

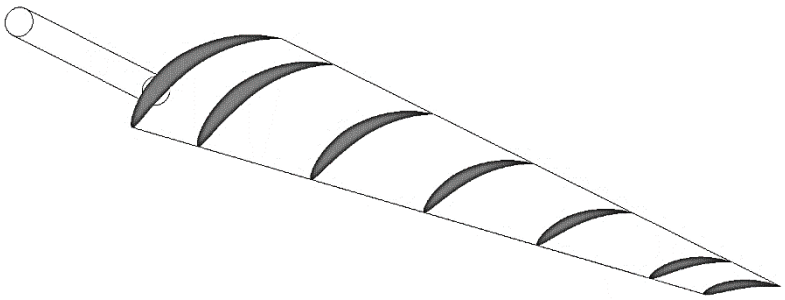

Fig. 1 Profile sections of NWT configuration

To improve the effectiveness of three bladed wind turbines, a tandem configuration NTWT has been investigated, a distance of 80 mm between the two blades have been taken. The tandem distance is measured from the stem center and the stem is rotated to determine the pitch angle Φ to the blade, which for the second blade is 4 degrees.

2.2 Computational domain

The Origin of the Cartesian coordinate system is located at the center point of the wind turbine. the computational domain extended 3.1D downstream and 0.77D upstream from the rotor, with a 1.16D distance from lateral boundaries. As seen in figure 2, the approaching wind's direction was parallel to the y axis. In the current study, the inflow turbulence intensity is 5%.

The following boundary conditions were taken:

- An axial wind speed of 10 m/s is the velocity condition applied at the inlet.
- The disturbance caused by the wind turbine decreases at the outlet and away from the wind turbine, bringing the absolute pressure up to par with the atmospheric air pressure.
- At the side faces (wall), the flow velocity is close to the unperturbed wind velocity. In these regions, the fluid flow is inviscid and free of shear, and a zero shear stress condition is imposed.

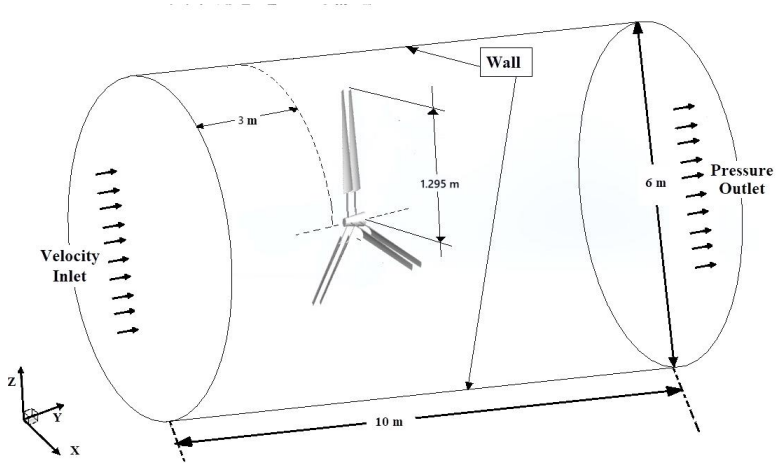

Fig. 2. The computational domain used in this study

A tetra mesh has been created using GAMBIT as shown in the figure 3**,** the 3-D air flow surrounding the wind turbine is simulated using the ANSYS Fluent 19.2 program. The moving reference frame method was used for testing a rotating tandem wind turbine, and it performs appropriately in this situation. The momentum and turbulence equations were discretized using the second-order upwind scheme; the pressure was discretized using the second-order interpolation technique; and the pressure-velocity coupling was handled by the SIMPLE algorithm. The calculation parameters are based on changing the rotating speed while keeping the inflow velocity at 10 m/s constant.

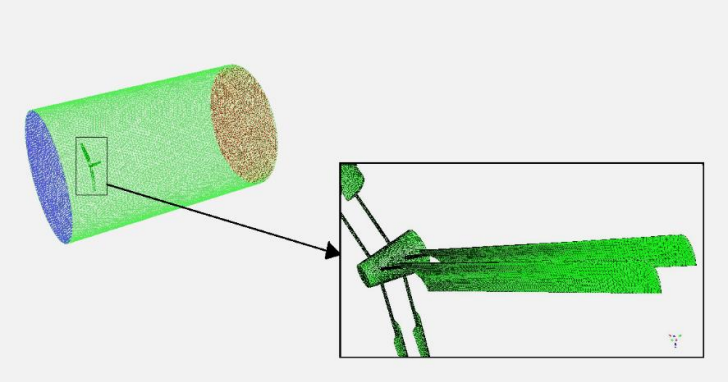

Fig. 3. Mesh of the tandem wind turbine

3. Results and discussions

3.1 Grid convergence study

The torque coefficient for the NTWT was calculated for four grid sizes: fine, two medium meshes and a coarse mesh. Figure 4 shows the grid dependence. It is apparent that although the result for the coarse mesh is different, the torque is about the same for the two refined meshes.

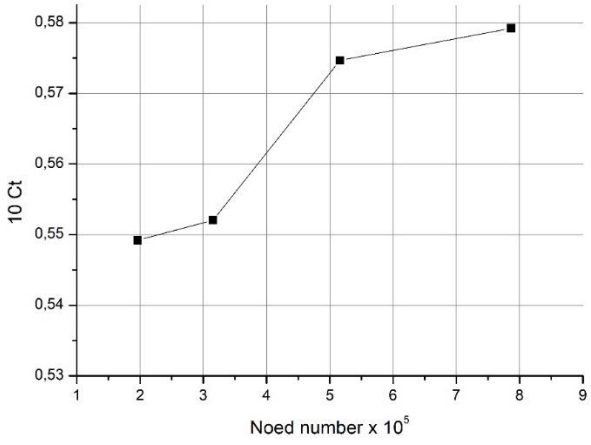

Fig. 4 Comparison of calculated torque for different grid resolutions for the NTWT at a wind speed of 10 m/s

The objective of the calculation was to evaluate the performance of the designed single and tandem wind turbines. The impact of rotation speed on the turbine was examined across a range of specific speed ratios from 1.5 to 9. The analysis focused on the power coefficient and torque. Figure 5 and 6 illustrate how rotational speed influences both the power coefficient and the generated driving torque.

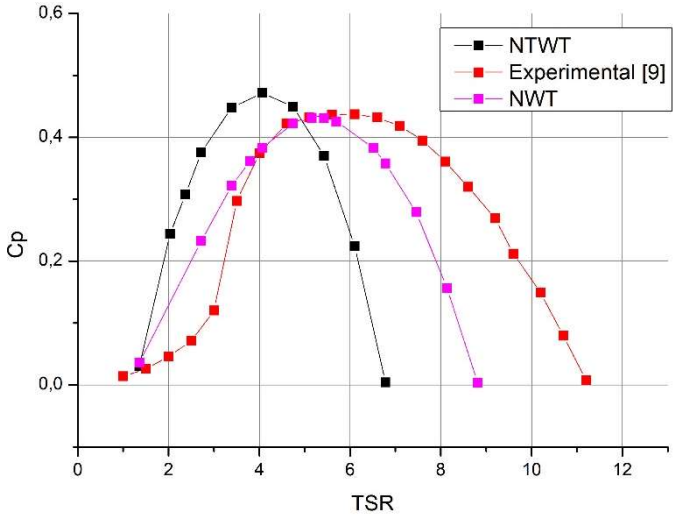

Fig. 5 Power coefficient for NWT, NTWT and ref. [9]

The obtained results for the power coefficient for NWT and NTWT are compared with the experimental results from reference (9) measure in a wind tunnel for 0.9m model wind turbine. The trend for the three curves seems the same. In the range of 2<TSR<4, the NTWT has higher values of Cp than the two other configurations and has a maximum power coefficient of 0.47 for TSR = 4. However the maximum Cp of 0.43 for the NWT is obtained at TSR = 5.5 and Cp max = 0.437 of reference (9) is at TSR = 6. It can also be observed that the working range of NWT and NTWT for TSR is respectively between 1.3 and 9, and 1.3 and 7. While for wind turbine of reference (20) this range is between 1 and 11.5.

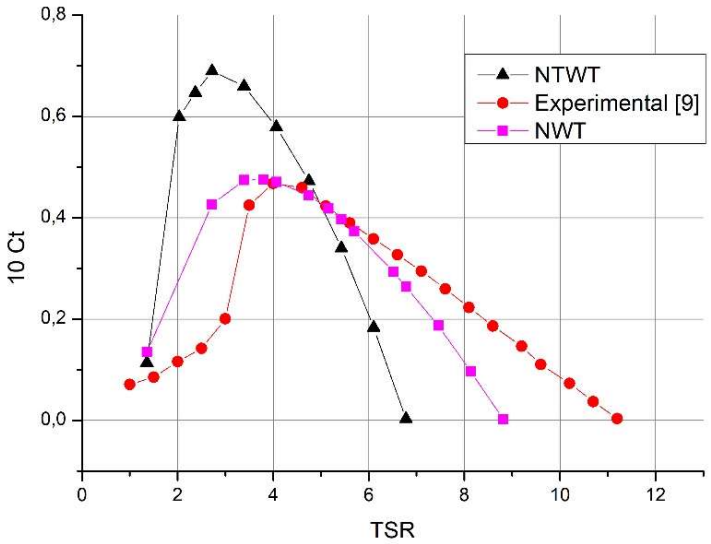

Fig. 6 Torque coefficient for for NWT, NTWT and ref. [9]

Figure 6 presents a comparison between the torque coefficient for the two tested configurations and the reference [9]. It is clearly seen a difference between the tandem wind turbine and the other two turbines in the range of 2<TSR<4. However, this coefficient drops after TSR 5 rapidly for The NTWT compared to the two others. A maximum value of 6.9 is obtained for the tandem configuration.

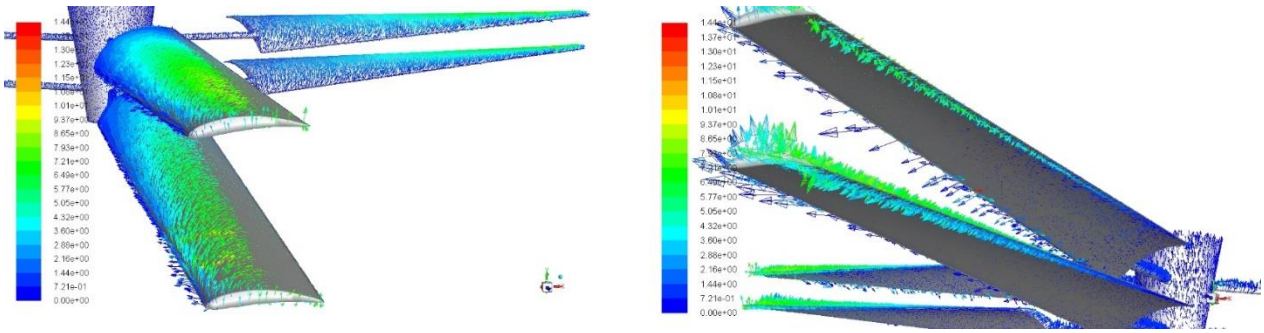

(a) (b)

Fig. 7 Wall shear stress vector distributions on the NTWT (a) Extrados and (b) Intrados.

Figure 7 exhibits the wall shear stress vectors distributions on the pressure and suction surfaces of NTWT. The presence of a clear separation bubble on the suction surface for both blades is clearly seen. A reattachment line is situated in the aft part of the blade. The separation in this case occurs before the mid-chord of the blade

4. Conclusions

A numerical investigation of the flow around a single NWT and a typical standard tandem NTWT blade horizontal axis wind turbine has been performed. The ANSYS Fluent 19.2 software was used to simulate the 3-D airflow around the wind turbine and the turbulence model realizable K-Ɛ was chosen.

The main conclusions drawn from the present study are as follows.

1- The obtained Cp max for the tandem configuration is greater than the experimental results found in reference [9] and the Cp max of the tested single configuration. An increase of Cp max of 7% is obtained compare to ref. [9].
2- The torque coefficient of the tandem configuration has increased by 32% compared to the maximum torque coefficient of reference [9].
3- A clear separation bubble on the suction surface for both blades is observed on the wall shear stress vector distributions
4- The flow on this new tandem turbine exhibits a complex phenomenon on both surfaces.

References

1. Marini, M.; Massardo, A.; Satta, A. Performance of Vertical Axis Wind Turbines with Different Shapes. *J. Wind Eng. Ind. Aerodyn.* **1992**, *39*, 83–93, doi:10.1016/0167-6105(92)90535-I.
2. Ferreira, C.J.S.; Bijl, H.; Bussel, G. van; Kuik, G. van Simulating Dynamic Stall in a 2D VAWT: Modeling Strategy, Verification and Validation with Particle Image Velocimetry Data. *J. Phys. Conf. Ser.* **2007**, *75*, 012023, doi:10.1088/1742-6596/75/1/012023.
3. Beri, H.; Yingxue, Y. Numerical Simulation of Unsteady Flow to Show Self-Starting of Vertical Axis Wind Turbine Using Fluent. *J. Appl. Sci.* **2011**, *11*, doi:10.3923/jas.2011.962.970.
4. Singh rathore, A.; Ahmed, S. Design and Analysis of Horizontal Axis Wind Turbine Rotor. *Int. J. Eng. Sci. Technol.* **2011**, *3*.
5. Azad, K.; Kaysar, M. Design of a Horizontal Axis Wind Turbine for Electricity Generation in Low Speed Windy Sites. *Int. J. Adv. Renew. Energy Res.* **2012**, *1*, 363–373.
6. Pratama, H.; Paranchis, M. The Wind Turbine Design and Test. *Teknomekanik* **2022**, *5*, 13–27, doi:10.24036/teknomekanik.v5i1.12672.
7. Abdelsalam, A.M.; Boopathi, K.; Gomathinayagam, S.; Hari Krishnan Kumar, S.S.; Ramalingam, V. Experimental and Numerical Studies on the Wake Behavior of a Horizontal Axis Wind Turbine. *J. Wind Eng. Ind. Aerodyn.* **2014**, *128*, 54–65, doi:10.1016/j.jweia.2014.03.002.
8. Kaya, M.N.; Kose, F.; Ingham, D.; Ma, L.; Pourkashanian, M. Aerodynamic Performance of a Horizontal Axis Wind Turbine with Forward and Backward Swept Blades. *J. Wind Eng. Ind. Aerodyn.* **2018**, *176*, 166–173, doi:10.1016/j.jweia.2018.03.023.
9. Krogstad, P. -Å.; Lund, J.A. An Experimental and Numerical Study of the Performance of a Model Turbine. *Wind Energy* **2012**, *15*, 443–457, doi:10.1002/we.482.

Seismic Performance Evaluation of a Strengthened RC Building

Baris GUNES[1], Kamran SAMADI[2], Baris SAYIN[1*]

1 Department of Civil Engineering, Istanbul University-Cerrahpasa, 34320, Istanbul, Turkey
2 Institute of Graduate Sciences, Istanbul University-Cerrahpasa, Istanbul, Türkiye
** barsayin@iuc.edu.tr*

Abstract

This study numerically examines the pre- and post-strengthened states of a low-rise RC building. Material characteristics were obtained through on-site examinations and laboratory tests. Damages in certain columns, beams, and slabs resulting from moisture and dampness, as well as cracks in the columns due to reinforcement corrosion, were identified. Numerical models created to represent both states of the building were subjected to non-linear static push-over analysis. While the pre--strengthened building was found not to satisfy the "Controlled Damage" performance level criterion for a DD-2 ground motion, the strengthened building met this criterion. Based on the moment distribution analysis of the strengthened foundation, it was concluded that the foundation reinforcement is adequate. As a result of the soil investigation parameters and static analysis of the foundation, it was determined that the foundation safety was ensured for soil pressures.

Keywords: Seismic Performance, Push-Over Analysis, Strengthened Structure, Foundation Performance, Existing RC Buildings.

1. Introduction

Most of the building stock constructed in the twentieth century comprised reinforced concrete (RC) structures. However, with the emergence of new regulations and specifications worldwide that impose stricter conditions to enhance earthquake resistance, seismic assessment and retrofitting of existing structures, particularly old and neglected RC ones, have become imperative to mitigate potential risks to life and property. Today, retrofitting public and private buildings to withstand earthquakes stands as one of the most crucial strategies in urban management. The initial phase of a retrofitting project involves conducting a seismic assessment of the building, and evaluating whether the structure meets the target performance criteria at a specified ground motion level. Subsequently, an economical strengthening plan is proposed based on the available materials and strengthening techniques. If the strengthening project primarily aims to enhance the ductility of the existing structure, strengthening individual elements might be sufficient. However, local element enhancements aimed at improving the overall structural seismic capacity may not be cost-effective. Local element strengthening techniques applied in RC structures include RC jacketing, steel jacketing, FRP/TRM jacketing, and hybrid jacketing. On the other hand, examples of whole-building strengthening techniques are implementing a bracing system, adding shear walls, adding infill walls, and seismic isolation [1].

Research on retrofitted reinforced concrete buildings typically focuses on element-level or whole-building performance assessments, as well as evaluating the impact of the chosen retrofitting method. Among studies on element-level strengthening and performance assessment, Truong et al. [2] compared the effect of partial strengthening in the plastic hinge region or full strengthening in the column spacing using four different non-seismic strengthening techniques and two different retrofit approaches for RC columns. They modeled flexure-shear and shear collapse mechanisms by setting two different longitudinal reinforcement ratios. They observed that the initial elastic stiffness increased by approximately 109.5% in one group of reinforced samples and by approximately 72.1% in another group of reinforced samples, compared to the control samples. El-Sokkary and Galal [3] evaluated the effectiveness of four different rehabilitation techniques for improving the seismic performance of non-ductile reinforced concrete frame structures using Incremental Dynamic Analysis. Their modeling results indicated that selecting the most appropriate rehabilitation method should take into account the building's properties, seismic risk, and the desired improvement in performance parameters. In a similar study, Zhao et al. [4] investigated the effect of different retrofitting strategies on the seismic behavior of RC buildings with various fundamental periods using nonlinear time history analysis. They revealed the advantages and disadvantages of various strategies based on the analysis results, depending on the structure's characteristics and earthquake parameters. Samadian et al. [5] investigated the effectiveness of retrofitting projects in Iranian schools. They used vulnerability and fragility curves to determine the earthquake resistance of a reinforced concrete school retrofitted with shear walls 10 years after its construction. Their findings showed that vulnerability curves produce more realistic results in estimating the seismic resilience index. For the same school building, Shamsoddin et al. [6] determined the seismic resilience index under carbonation-initiated corrosion considering two different hazard levels of 10% and 2% over 50 years with near-fault pulse-type and without pulse-type ground motions through vulnerability curves. Their results indicated that the resilience index due to corrosion decreased by 3% at the hazard level of 10% and by 58% in 2% over 50 years under the influence of near fault. Consequently, they found that the building was unsafe.

In the current study, the seismic performance assessment of a previously strengthened RC building was conducted. Structural elements of the building suffered damage due to moisture and dampness, as well as reinforcement bar (rebar) corrosion. For this purpose, the design and strengthening projects of the building were reviewed and the condition of the building was

assessed before and after strengthening in terms of materials, damage assessment, and soil investigation. Second, finite element models of the pre- and post-strengthening building were analyzed according to the principles suggested in TBEC-2018 [9] and target seismic performance, foundation performance, and soil bearing capacity were assessed for pre- and post-strengthening states. It was determined that a damaged and previously strengthened structure with the risk of pounding effect met the target performance specified in the current seismic codes.

2. Materials and Methods

2.1. The Examined Building

The building under examination comprises 2 basement floors, 1 ground floor, and 5 normal floors. The floor heights were 2.50 m for the 2nd basement floor, 2.8 m for the 1st basement floor, and 2.9 m for the 1st to 5th normal floors. The foundation system had RC continuous foundations. Properties of the structural members are given in Table 1.

Table 1. Properties of the structural members

Structural member	Longitudinal Rebar (mm)	Transverse Rebar (mm)
Continuous Foundation Beams	Φ10, Φ12, Φ14, and Φ16	Φ6 and Φ8 @ 20~25 cm
Column	Φ14 and Φ16	
Beam	Φ10, Φ12, Φ14, and Φ16	Φ6 and Φ8 @ 20~25 cm
Slab	Φ6 and Φ8 @ 13~30 cm	

2.2. Strengthening Technique

According to the strengthening project, the building consisted of 2 basement floors, 1 ground floor, and 5 normal floors + penthouse. The height of the penthouse was 1.8 m. Table 2 shows the properties of newly added members. Rebar properties of the existing structural elements are given in Table 3.

Table 2. Properties of newly added structural elements for strengthening purposes

Floor	Member	Dimensions (cm)	Longitudinal Rebar (mm)	Transverse Rebar (mm)
Basement	Well Foundation	Footing: 120, Shear: 30	Footing: Φ16 (lower and upper) @10cm, Shear: Φ16@15cm + Φ16@30cm (Backside)	Shear wall: Φ12@10cm
	Slab Foundation	Thickness: 100	Φ22 (lower and upper) @15cm	
2nd Basement	Column	40×45; 40×65; 40×70; 60×50;	Φ16 and Φ18	Φ10@10cm
	Shear wall	Thickness: 25 and 30	Φ16 and Φ18	Φ10, Φ12 and Φ14@10cm
	Beam	30×50;	Φ12 and Φ16	Φ10@10cm
	Slab	Thickness: 15	Φ10 and Φ12 @ 20cm	
1st Basement	Shear wall	Thickness: 25 and 30	Φ16 and Φ18	Φ10, Φ12 and Φ14@10cm
Ground	Beam	25×50; 30×50;	Φ12, Φ16 and Φ20	Φ10@10cm
1st and 2nd	Slab	Thickness: 15	Φ10, Φ12 and Φ16 @ 20 ~ 25cm	
3 – 5	Shear wall	Thickness: 25 and 30	Φ16 and Φ18	Φ10 and Φ12 @10cm
	Beam	25×50; 30×50;	Φ12, Φ16 and Φ20	Φ10@10cm
	Slab	Thickness	Φ10, Φ12 and Φ16 @ 20 ~ 25cm	
Penthouse	Shear wall	Thickness: 25 and 30	Φ16 and Φ18	Φ10 and Φ12 @10cm
	Beam	25×50;	Φ12, Φ16 and Φ20	Φ10@10cm
	Slab	Thickness: 15	Φ10 @ 15 ~ 20cm	

Table 3. Strengthening properties of existing structural elements

Floor	Member	Jacketing Thickness (cm)	Longitudinal Rebar (mm)	Transverse Rebar (mm)
2nd Basement	Column	15 and 20	Φ16	Φ10@10cm
	Shear wall	15	Φ16 and Φ18	Φ10 and Φ12@10cm
1st Basement	Column	15 and 20	Φ16	Φ10@10cm
Ground 1 – 5	Beam	13 ~ 20	Φ14	Φ10@10cm

2.3. Assessment of Structural Damage and Risk Status of the Building

During on-site examinations, it was observed that some columns, beams, and slabs exhibited blistering caused by moisture and dampness, as well as the presence of plaster spills. The investigations conducted by stripping concrete cover revealed that the rebars were exposed to corrosion, resulting in cracks in the columns. It was observed that the building is adjacent to neighboring structures, but the floor slabs are not aligned with them. This discrepancy may potentially lead to pounding damage during an earthquake.

2.4. Material Assessments

According to the laboratory tests, the average unconfined concrete compressive strength was found to be 14.11 MPa. During the undamaged and damaged rebar examinations, longitudinal rebars and stirrups were found to be non-ribbed rebar (S220). In the strengthened elements, C35 concrete and B420C rebar were used.

2.5. Soil and Earthquake Parameters

Soil and earthquake parameters for the building's location were determined based on the Geotechnical report and data from AFAD [7], as presented in Table 4.

Table 4. Soil and Earthquake Parameters

Parameter	Value/Class
Average Shear Wave Speed: $V_{s(30)}$ (m/sec)	313
Local Soil Class	ZD
Earthquake Map Spectral Acceleration Coefficients (g)	DD-3: S_s = 0.387, S_1 = 0.106
	DD-2: S_s = 0.986, S_1 = 0.272
	DD-1: S_s = 1.717, S_1 = 0.481

2.6. Analysis Method

As shown in Figure 1, pre- and post-strengthened states of the building were modeled using Midas Gen [8] finite element software. In both models, slabs were defined to represent in-plane rigidity and slab loads were transferred to beams. The performance analysis parameters for the un-strengthened building according to TBEC-2018 [9]. are given in Table 5.

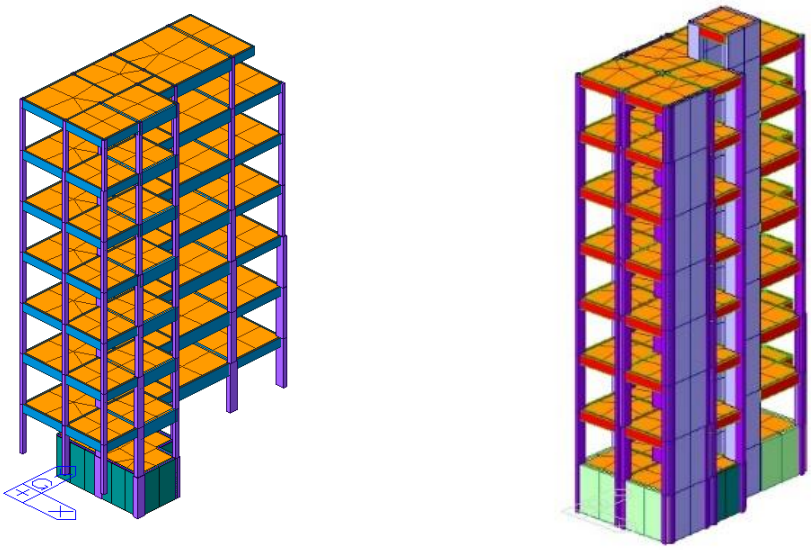

Fig. 1 3-D finite element models for the pre- (left) and post-strengthened (right) states of the building

Table 5. Performance Assessment Parameters

Parameter	Value/Class
Ground Motion Level / Target Performance	DD-2 / Controlled Damage
Performance Assessment Method	Nonlinear push-over analysis
Building Information Level and Coefficient	Existing Members (Limited) 0.75
	Strengthening Members (Comprehensive) 1.00
Earthquake Strength Reduction (R) and Overstrength (D) Factors	DD-2: R=1; D=1

3. Results

The analysis results were evaluated in compliance with TBEC-2018 regulations using a post-processing software developed by the authors in C# [10] programming language [9].

3.1. Performance Analysis Results for the Pre-Strengthened Building

Analysis results obtained from the model representing the pre-strengthened state of the building and performance analysis results for vertical and lateral load-bearing members are given in Table 6 and Table 7, respectively.

Table 6. Performance Analysis Results for Vertical Load-Bearing Members

Floor	Vertical Load-Bearing Members (Columns and Shear walls)			Target Performance (Controlled Damage)
	Strain Check for Article 15.8.4 (b)	Strain Check for Article 15.8.4 (c)	Stiffness Check for Article 15.8.4	
	RC	RC	RC	
2nd Basement	√	√	√	√
1st Basement	×	×	√	×
Ground	×	×	√	×
1st	×	×	√	×
2st	×	×	√	×
3rd	×	×	√	×
4th	×	√	√	×
5th	×	×	√	×

Table 7. Performance Analysis Results for Lateral Load-Bearing Members

Floor	Lateral Load-Bearing Members (Beams)		Performance (Controlled Damage)
	Strain Check for Article 15.8.4 (b)	Strain Check for Article 15.8.4 (c)	
	RC	RC	
2nd Basement	-	-	-
1st Basement	×	×	×
Ground	×	×	×
1st	×	√	×
2st	×	√	×
3rd	√	√	√
4th	√	√	√
5th	×	√	×

3.2. Performance Analysis Results for the Post-Strengthened Building

Analysis results obtained from the model representing the strengthened building and the performance analysis results for vertical and lateral load-bearing members are presented in Table 8 and Table 9.

Table 8. Performance Analysis Results for Vertical Load-Bearing Members

Floor	Vertical Load-Bearing Members (Columns and Shear walls)			Target Performance (Controlled Damage)
	Strain Check for Article 15.8.4 (b)	Strain Check for Article 15.8.4 (c)	Stiffness Check for Article 15.8.4	
	RC	RC	RC	
2nd Basement	√	√	√	√
1st Basement	√	√	√	√
Ground	√	√	√	√
1st	√	√	√	√
2st	√	√	√	√
3rd	√	√	√	√
4th	√	√	√	√
5th	√	√	√	√

Table 9. Performance Analysis Results for Lateral Load-Bearing Members

Floor	Lateral Load-Bearing Members (Beams)		Performance (Controlled Damage)
	Strain Check for Article 15.8.4 (b)	Strain Check for Article 15.8.4 (c)	
	RC	RC	
2nd Basement	√	√	√
1st Basement	√	√	√
Ground	√	√	√
1st	√	√	√
2st	√	√	√
3rd	√	√	√
4th	√	√	√
5th	√	√	√

3.3. Performance Assessment of the Foundation

3.3.1. Bending Examinations of the Foundation

As shown in Figure 2, envelope moment diagrams of the foundation were obtained by bending examinations conducted based on the foundation details given in the strengthening project. Following the assessments conducted by considering the moment distributions in the building's foundation, it was concluded that the foundation rebars were adequate.

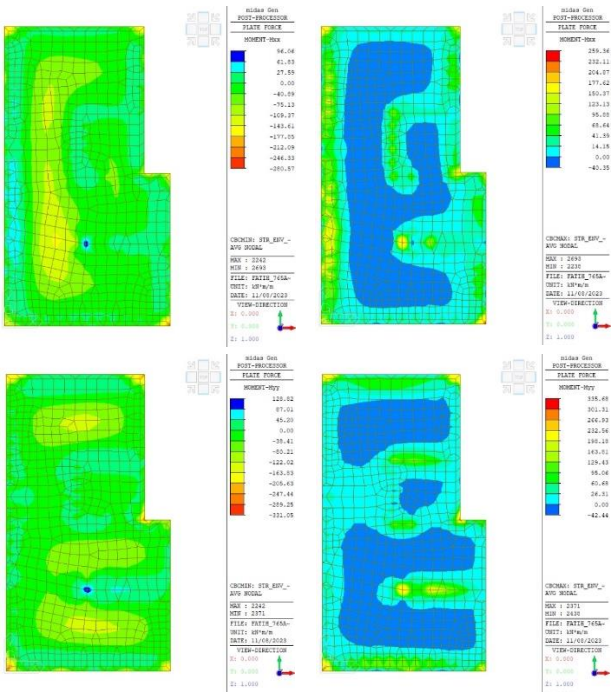

Fig. 2 Bending effects on the foundation; Mxx Minimum Moment (upper-right), Mxx Maximum Moment (upper-left), Myy Minimum Moment (lower-right), Myy Maximum Moment (lower-left). (kN.m/m)

3.3.2. Soil Pressure Examinations

The soil pressure data corresponding to 1.4G+1.6Q and G+Q+E combinations under the foundation are presented in Figure 3, respectively. The highest soil pressure obtained from the analyses was found to be q_0= 327 kPa < q_t. Consequently, the soil strength safety was achieved.

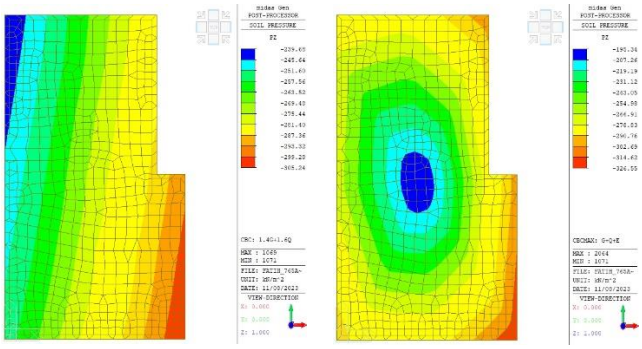

Fig. 3. Soil pressures under foundation; 1.4G+1.6Q (left), G+Q+E (right) (kPa)

4. Conclusions

A seismic assessment of a building for pre- and post-strengthened states was performed based on the criteria envisaged in TBEC-2018 [9].

- Pre-strengthened state: The building was found not to satisfy the criteria outlined in TBEC-2018 for the “Controlled Damage” performance level [9]. Except for secondary beams, which are not part of the lateral load-bearing system, the primary RC beams fell in the “Limited Damage,” “Significant Damage,” “Advanced Damage,” or “Collapse.” categories. The proportion of primary RC beams in the “Advanced Damage” state was below the limit value. However, some primary RC beams were in the “Collapse” state. The RC vertical structural members fell in the “Limited Damage,” “Significant Damage,” “Advanced Damage,” or “Collapse” states. In some stories, the contribution of the vertical structural members in the “Advanced Damage” state to the shear force carried by all vertical structural members

in the given floor was above the limit value. Furthermore, some vertical RC structural members were in the "Collapse" state. In certain stories, some RC vertical structural members in both upper and lower sections exceeded the "Significant Damage" limit. The ratio of the shear force carried by these elements to the shear force carried by all vertical structural elements on that floor was above the target limit. Consequently, the building failed to meet the brittleness criterion outlined in the code. Some RC elements exhibited "brittle" damage.

- Strengthened state: The building met the criteria in TBEC-2018 for the "Controlled Damage" performance level [9]. The primary RC beams, except for secondary beams, fell in the "Limited Damage," or "Significant Damage," states." None of the primary RC beams were in the "Advanced Damage" or "Collapse" states". All vertical structural members fell in the "Limited Damage" zone. None of the vertical RC elements were in the "Significant Damage," "Advanced Damage," or "Collapse." states. No RC vertical structural members in both upper and lower sections exceeded the "Significant Damage" limit. Consequently, the building meet the brittleness criterion in the code. No RC elements exhibited "brittle" damage.

References

1. Gkournelos, P.D.; Triantafillou, T.C.; Bournas, D.A. Seismic upgrading of existing reinforced concrete buildings: A state-of-the-art review. *Engineering Structures*, **2021**;240:1-20.
2. Truong, G.T.; Kim, J.C.; Choi, K.K. Seismic performance of reinforced concrete columns retrofitted by various methods. *Engineering Structures*, **2017**;134:217-235.
3. El-Sokkary, H.; Galal, K. Analytical investigation of the seismic performance of RC frames rehabilitated using different rehabilitation techniques. *Engineering Structures*, **2009**;31(9):1955-1966.
4. Zhao, J.; Qiu, H.; Sun, J.; Jiang, H. Seismic performance evaluation of different strategies for retrofitting RC frame buildings. *Structures*, **2021**;34:2355-2366.
5. Samadian, D.; Ghafory-Ashtianyb, M.; Naderpour, H.; Eghbali, M. Seismic resilience evaluation based on vulnerability curves for existing and retrofitted typical RC school buildings. *Soil Dynamics and Earthquake Engineering*, **2019**;127:1-30.
6. Shamsoddin, Z.; Raissi Dehkordi, M.; Eghbali, M.; Samadian, D. Evaluation of seismic resilience index for typical RC school buildings considering carbonate corrosion effects. *International Journal of Disaster Risk Reduction*, **2020**;46: 1-23.
7. AFAD. (**2019**). Türkiye Earthquake Hazard Maps Interactive Web Application. Retrieved from https://tdth.afad.gov.tr/TDTH/main.xhtml
8. Midas Gen (**2021**), Integrated Solution System for Building and General Structures, MIDAS Information Technology Co.
9. TBEC-2018, Turkey Building Seismic Code: Rules for design of buildings under earthquake effect, Official Gazette, 18.03.**2018**, 30364 (in Turkish).
10. C# Programming language, Microsoft that runs on the NET Framework.

Assessment of an RC Building's Seismic Performance during Construction

Baris GUNES[1], Kamran SAMADI[2], Baris SAYIN[3*]

[1] *Department of Civil Engineering, Istanbul University-Cerrahpasa, Istanbul, Türkiye*
[2] *Institute of Graduate Sciences, Istanbul University-Cerrahpasa, Istanbul, Türkiye*
[3] *Department of Civil Engineering, Istanbul University-Cerrahpasa, Istanbul, Türkiye*
** barsayin@iuc.edu.tr*

Abstract

The seismic performance of a structure during construction was examined in this study. The structure consisted of two RC buildings with shear walls designed as one basement, one ground, two normal and attic floors, but only the basement floor was constructed. Water accumulation was observed in the basements of the buildings, leading to moisture and dampness in the load-bearing elements. Additionally, partial corrosion damage was detected on some rebar rods in the exposed parts of the carriers. In accordance with TBEC seismic regulation, it was examined whether the structures met the "Controlled Damage" performance level for DD-2 ground motion. The buildings were subjected to nonlinear analysis under static loading and the obtained results were considered the initial state of earthquake loadings. Using the scaled earthquake records, nonlinear time-history analyses were performed. The findings revealed that the examined block buildings A and B satisfy the target performance criteria.

Keywords: seismic performance, nonlinear behavior, time-history analysis, foundation performance, existing RC buildings.

1. Introduction

The earthquake performance of existing reinforced concrete (RC) buildings can vary depending on many factors related to the characteristics of the building and the earthquake. Recently, many studies have been conducted on this subject using different parameters and analysis methods. These studies are generally aimed to determine the seismic safety of structures and to propose retrofitting projects if necessary. For example, Aragona et al. compared two simplified models for the rapid evaluation of moment-resisting infilled frames subjected to seismic loading. These models are suitable for large-scale evaluations. Their results showed that the typological model, which can be defined by a few geometrical and mechanical parameters, can significantly reduce the computational burden [1]. Ugalde and Garcia assessed the seismic capacities of three existing 5, 17, and 26-story RC buildings that were not damaged during the 2010 Chilean earthquake using linear and nonlinear analyses. They found that even in the absence of observable damage, the nonlinear time history method provides more accurate results for the analysis of RC buildings subjected to large seismic demands [2]. Cosgun et al. evaluated the effectiveness of the retrofitting technique and the seismic performance of two active reinforced concrete buildings of medium height, which have not been used for a long time, through numerical analysis supported by field studies and laboratory tests. However, their nonlinear pushover analysis results showed that the ductility of the building was reduced with new shear walls. As a solution, the authors suggested that the centers of mass and stiffness should be as close as possible so that the shear walls are not subjected to excessive shear forces [3]. Gunes et al. prepared a model of a university building constructed in the 1940s and presented a methodology based on nonlinear pushover analysis for seismic performance evaluation of RC buildings with masonry infills before and after retrofitting [4]. Badal and Morta compared the performance of reinforced concrete buildings before and after the 2015 Gorkha earthquake. Their incremental dynamic analysis results revealed that the earthquake performance of even the newest buildings did not adequately meet the performance stipulated in the codes for design-level earthquakes [5]. Ibrahim et al. investigated the seismic capacity and collapse mechanisms of damaged RC structures with shear walls, considering the vertical component of the catastrophic Turkey/Syria earthquake that occurred on 6 February 2023. Their results revealed that the spectrum acceleration of this earthquake exceeded significantly the spectrum stipulated in the available design codes. Displacements and shear forces increased substantially, and the axial compressive force of the column/wall transformed into tensile force at a certain moment during the earthquake. In the case of the 18-story building, they found that the dominant collapse mode in the simulation, where the vertical component of the earthquake was considered, was torsional [6]. In the current study, RC concrete buildings under construction were modeled to approximate the static project over the existing status of the basement floors. The novelty of this study is that the structure and modeling process differs from other classical building studies. In other words, the ongoing construction process of the building introduces an increased uncertainty factor, which must be managed correctly in the analysis process.

2. Materials and Methods

2.1. The Examined Building

The buildings examined were designed as 1 basement floor + ground floor + 2 normal floors + attic floor, with each floor having a height of 3.00 m. Basic details of the structural system of the buildings are provided in Table 1. In the existing parts of the building, undamaged rebars were surveyed, and a visual inspection of the rebars was conducted by removing the

concrete cover from the structural elements. As shown in Table 1, the rebar properties were determined, revealing that the longitudinal rebars and stirrups were ribbed rebar (S420). In addition, core samples were extracted and were subjected to laboratory tests. Accordingly, the average uncoated concrete compressive strength was determined to be 37.85 MPa for block A and 45.01 MPa for block B. As an important detail, although laboratory studies revealed that the concrete class was higher than envisaged in TBEC-2018, the concrete strength specified in the static project, namely C25, was considered in the performance analysis [7].

However, during on-site inspections, water accumulation was observed in the basements of the buildings, leading to moisture and dampness in the load-bearing elements. Additionally, partial corrosion damage was detected on some rebar rods in the exposed parts of the carriers.

Table 1. Properties of structural elements and rebars

Structural elements	Longitudinal Rebar (mm)	Transverse Rebar (mm)	Strengthening
Column	ϕ16	ϕ8 and ϕ10 / 10~19 cm	-
Basement shear	ϕ16	ϕ10 / 25 cm	CFRP (1.4 mm) plate
Shear wall	ϕ16	ϕ10 and ϕ12 / 10~20 cm	-
Beam	ϕ12 and ϕ14	ϕ8, ϕ10 and ϕ12 / 8~16 cm	-
Slab	ϕ8 /18 cm		-
Ribbed Beam	ϕ10 and ϕ12	ϕ8 / 20 cm	-

2.2. Soil Investigation Report

According to the information obtained from drilling and MASW (Multi-channel Analysis of Surface Waves) studies, the following findings and recommendations were made regarding the soil parameters underlying the buildings:

- Groundwater level was observed at 3 meters. Necessary measures should be taken to prevent the effect of groundwater and surface water on the foundation.
- Buildings have raft foundations and it is advised that the foundations should not exceed the Design Strength q_t = 1.70 kg/cm^2 for D_f = 2.50 m. Soil bearing capacity was found to be 952 tons/m^3.
- No liquefaction potential is expected on the site.
- The local soil class was determined as ZE.

2.3. Earthquake Effects

2.3.1. Earthquake Response Spectrum

The spectrum values considered in earthquake performance analyses are provided in Table 2. The horizontal elastic design spectrum is illustrated in Figure 1.

Table 2. Elastic design spectrum values for a DD-2 ground motion

Parameters	Value / Class
Earthquake Map Spectral Acceleration Coefficients (g)	S_s = 1.518, S_1 = 0.417
Peak Ground Acceleration (g)	PGA = 0.618
Local Ground Impact Coefficients	F_s = 0.800, F_1 = 2.366
Spectral Acceleration Coefficients	S_{DS} = 1.214, S_{D1} = 0.987

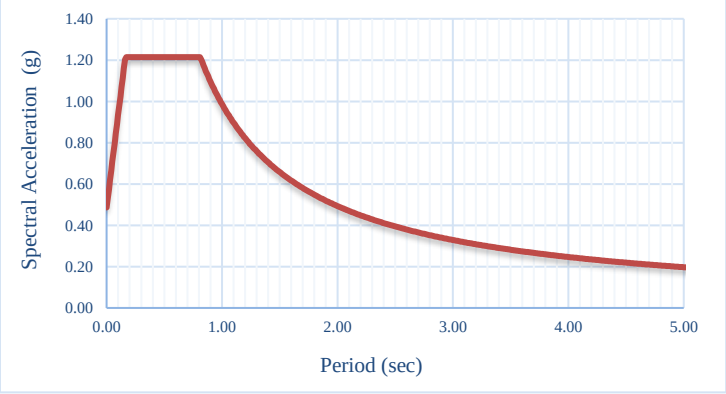

Fig. 1 Elastic design spectrum for DD-2 ground motion

2.3.2. Selection and Scaling of the Records

To determine the earthquake loads acting on the structure, time-domain analysis was preferred. Accordingly, 11 earthquake records were selected and scaled [7]. Basic information about the selected records is presented in Table 3. The records were

chosen from the PEER strong ground motion database (PEER, 2023), considering the characteristics of the faults, the distance of the region to the fault line, and the soil structure [8]. The document "Quantification of Building Seismic Performance Factors, FEMA P695, 2009" was also utilized [9].

Table 3. Basic information about selected earthquake records

Record		Year	Earthquake	Station	Magnitude	V_{s30} (m/s)
01		1999	Kocaeli, Turkey	Duzce	7.51	281.86
02		1979	Coyote Lake	Gilroy Array #2	5.74	270.84
03		1999	Duzce, Turkey	Bolu	7.14	293.57
04		1990	Manjil, Iran	Abbar	6.95	213.44
05		1999	Hector Mine	Hector	7.13	726.00
06		1961	Hollister-01	Hollister City Hall	5.6	198.77
07		1966	Parkfield	Cholame - Shandon Array #5	6.19	289.56
08		1940	Imperial Valley-02	El Centro Array #9	6.95	213.44
09		1987	Superstition Hills-02	El Centro Imp. Co. Cent	6.54	288.62
10		1989	Loma Prieta	Capitola	6.93	545.66
11		1992	Landers	Coolwater	7.28	352.98

The records selected based on the acceleration spectrum of the structure were scaled to the DD-2 Earthquake Ground Motion spectrum in SeismoMatch software using the simple scaling method as prescribed in TBEC-2018 [7,10]. The comparison of the scaled average acceleration spectra with the target DD-2 Ground Motion spectra is shown in Figure 2.

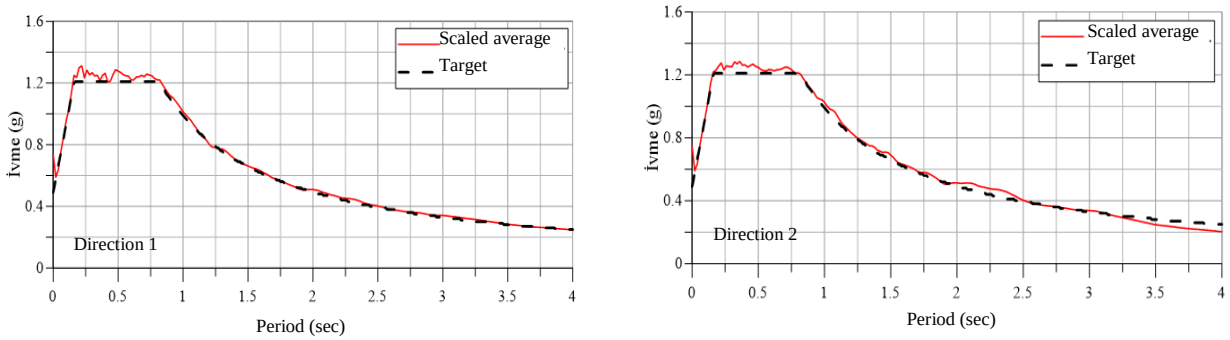

Fig. 2 The comparison of Average Spectrum – Target Spectrum

2.4. Determination of Design/Assessment Method

The evaluation of the structure under static and earthquake loads was based on the "Turkish Building Earthquake Code (TBEC-2018)" [7]. The selected parameters and analysis principles are summarized in Table 4.

Table 4. Performance-based analysis and design method

Parameters	Value / Class
Building Use Class, BUC	3
Building Importance Coefficient, I	1.0
Earthquake Design Class, EDC	1
Building Height Class, BHC	7
Target Performance	Controlled Damage for DD-2
Design/Assessment Method	Nonlinear Analysis, Strain-based assessment,
Building Information Level and Coefficient	Comprehensive, 1.00
Local Soil Class	ZE

2.5. Modeling Approach

2.5.1. Fiber Element Modeling of RC and Steel Elements

Stacked plastic hinges are employed in the finite element model to assess the performance level of reinforced concrete and steel structures, as well as to simulate the nonlinear behavior of column, beam, brace, and shear elements. Stacked plastic hinges are based on the fiber element formulation [11]. To simulate nonlinear behaviors, the Mander concrete model was utilized for concrete material, and the two-curve steel model was employed for rebars and steel [12]. Wrapping effects are taken into account in the model for concrete materials. Figure 3 illustrates examples of sections modeled with fiber elements.

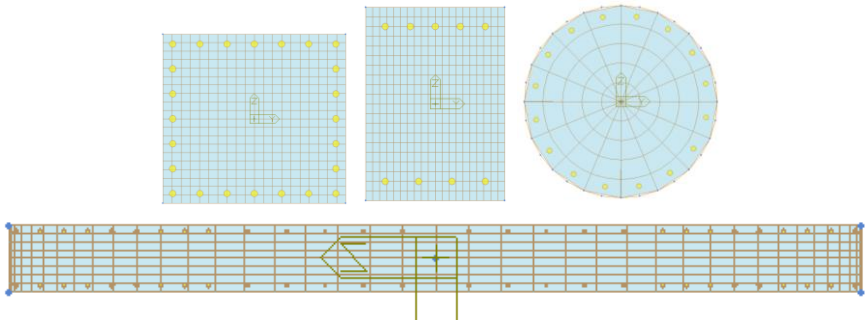

Fig. 3 Fiber model samples for RC elements

2.5.2. Modeling the Structural System

The examined structures were modeled using the Midas Gen finite element program to approximately represent the existing condition of the basement story and the condition given in the static project for the other stories. Subsequently, seismic performance analysis of the buildings was conducted [13]. The slabs were defined only for in-plane stiffness, and the slab loads were assigned to the beams. Figure 4 illustrates the three-dimensional static analysis model of Block A.

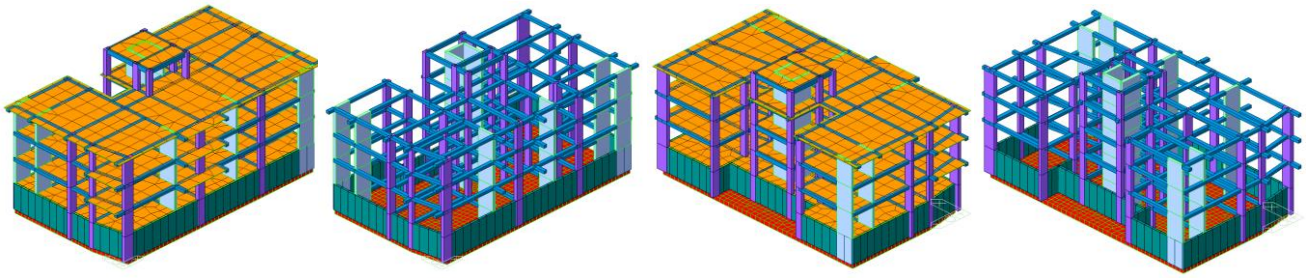

Fig. 4 Three-dimensional finite element model of Block A

3. Results

The compliance of the examined buildings with the "Controlled Damage" (CD) performance level for DD-2 ground motion in accordance with TBEC-2018 was examined [7]. The structures were initially subjected to nonlinear analysis under static effects. The results obtained in this analysis were considered as the initial state of earthquake loading. Using scaled earthquake records, 11 × 2 = 22 nonlinear analyses in the time domain were then performed for each structure.

3.1. Analysis Results for the Superstructure

The main strains and sectional forces used in the assessment were obtained by averaging the absolute maximum values of the sectional forces that occurred in all earthquake records, as recommended in TBEC-2018 [7]. The analysis results for all floors of Block A and the performance assessments of the structure are presented in Table 5 and Table 6 for vertical and lateral load-bearing elements, respectively.

Table 5. Performance Analysis Results of Block A for Vertical Structural Elements

Floor	Vertical Structural Elements (Columns and Shear walls)			Target Performance (CD)
	Article 15.8.4 (b) Strain Check	Article 15.8.4 (c) Strain Check	Article 15.8.4 Stiffness Check	
	RC	RC	RC	
1st Basement Floor	√	√	√	√
Ground Floor	√	√	√	√
1st Normal Floor	√	√	√	√
2nd Normal Floor	√	√	√	√
Attic Floor	√	√	√	√

Table 6. Performance Analysis Results of Block A for Lateral Structural Elements

Floor	Lateral Structural Elements (Beams)		Target Performance (CD)
	Article 15.8.4 (b) Strain Check	Article 15.8.4 (c) Strain Check	
	RC	RC	
1st Basement Floor	√	√	√
Ground Floor	√	√	√
1st Normal Floor	√	√	√
2nd Normal Floor	√	√	√
Attic Floor	√	√	√

3.2. Analysis Results for the Foundation

The final sectional forces used in the assessment were obtained by averaging the absolute maximum values of the sectional forces that occurred in all earthquake records, as suggested in TBEC-2018 [7]. The analysis results for all stories of Block A and the performance assessments of the structure are presented in Table 5 and Table 6 for vertical and lateral load-bearing elements, respectively. Figures 5 and 6 show the bending and shear forces on the foundations for each earthquake record for Block A, respectively [7].

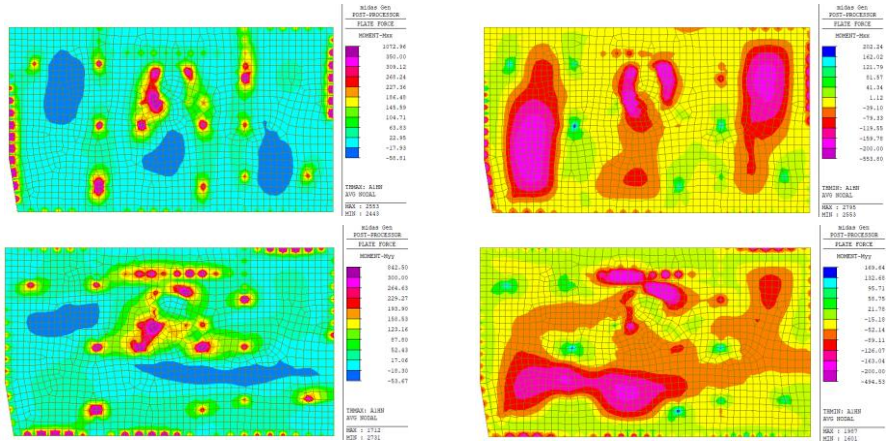

Fig. 5 Bending forces on the foundation of Block A; Maximum (upper-right) and Minimum moments (upper-left) in the long side of the foundation plate; Maximum (lower-right) and Minimum moments (lower-left) in the short side of the foundation plate. (Moment unit: kNm/m)

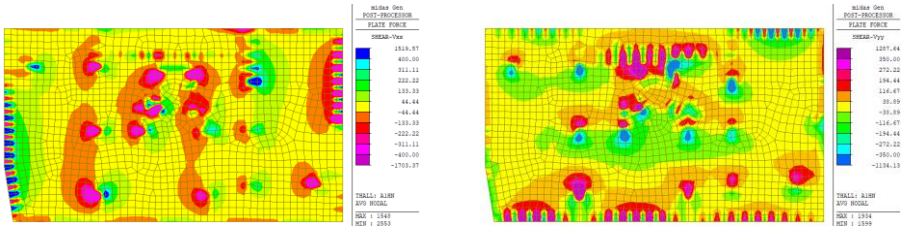

Fig. 6 Shear force envelope distribution in the long side (right) and short side (left) of the foundation of Block A. (Moment unit: kNm/m)

3.3. Analysis Results for Soil Bearing Capacity

The main displacements used in the assessment were obtained by averaging the absolute maximum values of the vertical displacements observed in all earthquake records, as suggested in TBEC-2018 [7]. Figure 7 displays the vertical displacements that occurred in the shallow foundation in an earthquake record for Block A.

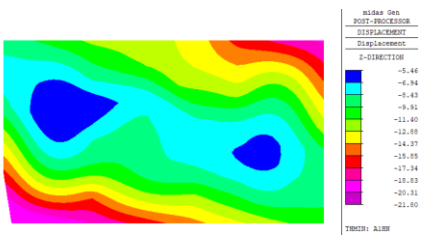

Fig. 7 Vertical displacements (mm) that occurred in the shallow foundation of Block A.

Soil bearing capacity was checked using Eq (1) below:

$$q_0 = 18.0\,mm \cdot 9500\,kN/m^3 \cong 170\,kN/m^2 \leq q_t \tag{1}$$

4. Conclusions

The seismic analysis model of a partially completed building was successfully created. An uncommon assessment methodology was utilized, and the seismic performance of the unfinished building was determined. The key findings obtained from the analyses and evaluations are as follows:

- The proportion of RC main beams in the "Excessive Damage" zone was below the limit value. Additionally, no RC main beam was in the "Collapse" zone.
- Considering the conditions stipulated in TBEC-2018 [7], Article 15.8.4 (b) and (c), no vertical RC load-bearing members of the structure were in the "Advanced Damage" or "Collapse" zone, nor have they exceeded the "Significant Damage Limit".
- No RC elements of the structure displayed brittle damage.
- It was concluded that shallow foundations provide the necessary bending/shear demand and have sufficient strength in terms of soil bearing capacity.

In conclusion, the examined blocks A and B were found to satisfy the “Controlled Damage” performance criteria for a DD-2 ground motion with a 10% probability of exceedance in 50 years (recurrence period of 475 years) as stipulated in TBEC-2018 [7].

References

1. Aragona, M.G.; Polese, Prota, M.A. Stick-IT: A simplified model for rapid estimation of IDR and PFA for existing low-rise symmetric infilled RC building typologies. *Engineering Structures*, **2020**, 223, 111182, 1-17.
2. Ugalde, D.; Garcia, D.L. Analysis of the seismic capacity of chilean residential RC shear wall buildings. *Journal of Building Engineering*, **2020**, 31, 101369, 1-17.
3. Cosgun, T.; Sayin, B.; Gunes, B,; Mangir, A. Retrofitting technique effectiveness and seismic performance of multi-rise rc buildings: A case study. *Case Studies in Construction Materials*, **2022**, 16, e00931, 1-19.
4. Gunes, B.; Mangir, A.; Cosgun, T.; Sayin, B.; Akcay, C. Seismic performance assessment of a historical masonry-infilled RC building located in the historical peninsula of Istanbul (1940s). *Structures*, **2022**, 45, 951-968.
5. Badal, P.; Motra, G. Post-2015 Earthquake vulnerability of typical RC buildings in Kathmandu Valley. *Structures*, **2023**, 57, 105111, 1-15.
6. Ibrahim, A.R.; Makhloof, D.A.; Ren, X. Seismic performance and collapse analysis of RC framed-wall structure excited with turkey/syria destructive earthquake. *Structures*, **2024**, 59, 105774, 1-21.
7. TBEC-2018, Turkey Building Seismic Code: Rules for design of buildings under earthquake effect, Official Gazette, 18.03.2018, 30364 (in Turkish).
8. PEER (2023) Strong Ground Motion Database. Available at: peer.berkeley.edu/products/strong_ground_motion_db.html.
9. FEMA P695. (2009). *Quantification of Building Seismic Performance Factors*.
10. SeismoMatch: An application capable of adjusting earthquake records, through wavelet addition, to match a specific target response spectrum, Seismosoft Ltd.
11. Spacone, E.; Filippou, F.; Taucer, F. Fiber beam-column model for nonlinear analysis of R/C frames. Part I: Formulation. *Earthquake Engineering & Structural Dynamics*, **1996**, 25(7), 711-725.
12. Mander, J.B.; Priestley, M.J.; Park, R. Theoretical stress-strain model for confined concrete. *Journal of Structural Engineering*, **1988**, 114(8), 1804-1825.
13. Midas Gen (2021), Integrated solution system for building and general structures, MIDAS Information Technology Co.

Analysis of Various Waste Plastics Reactors: A Comparative Study

Surya, RAJENDRAN[1]*, JordanNATHANSOLOMON[1], Kristina BAZIENE[1]

1Department of Mechanical and Material Engineering, Vilnis Tech, Saulekis av.11, Vilnius, Lithuania
** surya.rajendran@stud.vilniustech.lt;*

Abstract

Managing waste plastics is one of the world's biggest environmental challenges. Because they can turn waste plastics into useful goods, thermal treatment techniques like pyrolysis and gasification have drawn a lot of attention among the different waste plastic management strategies. This research offers a comparison of several waste plastics reactors—such as rotary kilns, fluidized bed reactors, and fixed bed reactors—that are used in thermal treatment procedures. Reactor design, operating conditions, product yields, energy efficiency, and environmental effects are only a few of the important topics covered in the analysis. The study also assesses each reactor type's performance in terms of economic feasibility, process scalability, and product quality. This comparative analysis attempts to clarify the advantages and disadvantages of each reactor configuration by combining the body of current literature with empirical data, offering guidance for the choice and improvement of waste plastics treatment methods. The results of this study advance our knowledge of waste plastics management techniques and may help in the formulation of sustainable waste management policies.

Keywords: reactors, pyrolysis, pyro-oil, condenser, plastic waste.

1. Introduction

Plastic waste has become a major environmental concern, with its accumulation leading to pollution and resource depletion [1]. The use of pyrolysis to convert plastic waste into fuel offers a promising solution to these challenges. Different types of pyrolysis reactors have been used and developed to use waste plastics for industrial uses. These reactors can be broadly classified into three categories: batch, semi-continuous, and continuous reactor [8]. The choice of reactor type depends on various factors including the scale of operation, desired product output, energy efficiency, and process control. In this study, analysis of the efficiency of these different types of reactors in terms of energy and exergy during the pyrolysis process [13].

Reactor Configuration. Several types of reactors are used for thermal treatment of waste plastic. They include fixed bed reactors, fluidized bed reactors, rotary kilns, and entrained flow reactors. [2]. Fixed bed reactors are characterized by easy operation but poor heat transfer and scalability. Fluidized bed reactors have high heat transfer rates and uniform temperatures due to bed agitation, which allows use for different waste plastic types but requires close bed dynamic control. Rotary kilns are used for continuous operation and effective heat transfer, which is perfect for large-scale operations, but the presence of solid gas may be hard to operate. Finally, entrained flow reactors provide high heating rates and good product yield but need precise control mechanisms, which limits their application to certain feedstock [4].

Fixed Bed Reactors. Fixed bed reactors are a type of chemical reactor where the reactants are stationary within the reactor while the fluid (usually a gas) flows over the stationary bed of solid material. In the context of waste plastic pyrolysis, fixed bed reactors involve passing a gas, typically a hot inert gas, through a stationary bed of waste plastics as shown in Fig 1. This process initiates the pyrolysis reaction, breaking down the plastic into smaller molecular components [3].

Advantages of fixed bed reactors include their simplicity of operation and ease of implementation. However, they also have certain limitations. One major challenge is heat transfer within the stationary bed of waste material, which can result in non-uniform processing and incomplete pyrolysis. Additionally, the scalability of fixed-bed reactors may be limited due to issues such as heat distribution and mass transfer limitations. Despite these limitations, fixed bed reactors can still be effective for smaller-scale operations or for processing specific types of waste plastic [11]. It's mostly used in the research and development sector or for different applications where ease of use and operation are prioritized over scalability and efficiency.

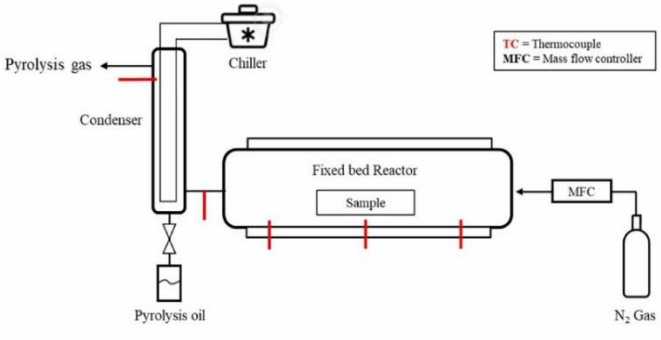

(b) Fixed-bed

Fig. 1 Schematic diagram of Fixed Reactor [3]

Fluidized Bed Reactors. Fluidized bed reactors are another type of chemical reactor commonly used in waste plastic pyrolysis. In a fluidized bed reactor, the solid particles (in this case, waste plastic materials) are suspended and behave like a fluid when a gas (usually air or another gas) is passed through the bed from the bottom. This fluidization of the solid particles enhances heat transfer rates and ensures a more homogeneous temperature distribution throughout the reactor. One of the key advantages of fluidized bed reactors is their efficient heat transfer, which helps to promote uniform and thorough pyrolysis of the waste plastics. This makes them suitable for processing various types of waste plastics, including mixed or heterogeneous feedstocks. [3]. In Fig 2. the fluidized bed sketch is presented.

However, controlling the dynamics of the fluidized bed is crucial for maintaining optimal performance. Variations in particle sizes, densities, and other factors can disrupt the fluidization process and affect the efficiency of the reactor. Therefore, careful monitoring and control systems are required to ensure stable operation. Despite these challenges, fluidized bed reactors are widely used in waste plastic pyrolysis due to their ability to handle diverse feedstocks and their efficient heat transfer properties. They are mainly suited for medium to large-scale operations where high amounts and consistent processing are important considerations [10].

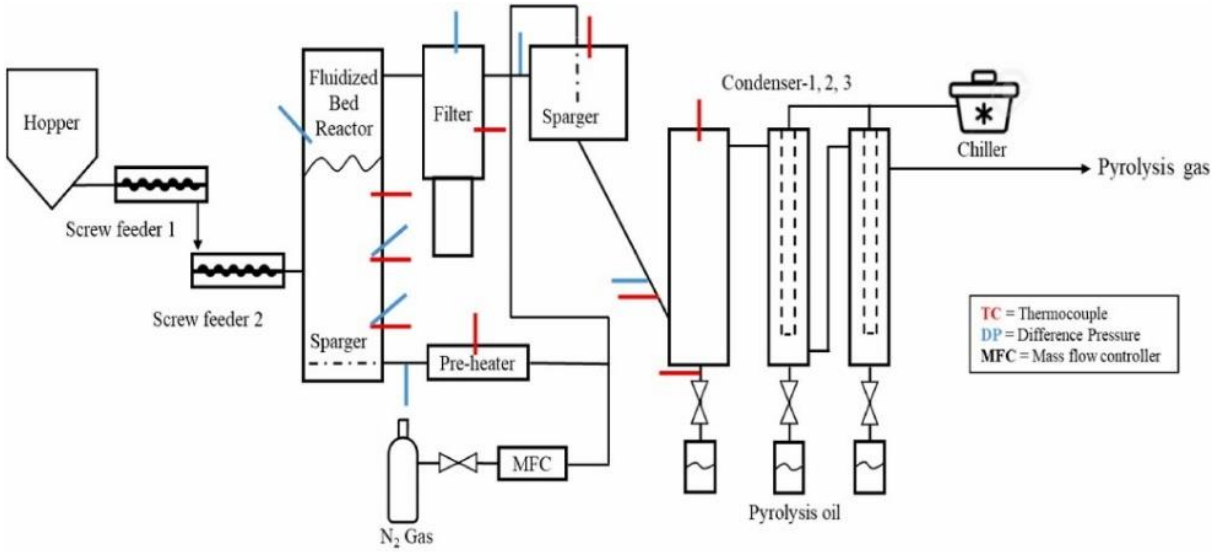

Fig. 2 Schematic diagram of Fluidized reactor [3]

Rotary Kilns. Rotary kilns are cylindrical, inclined, rotating drums used in various industrial processes, including waste plastic pyrolysis. In the context of waste plastic pyrolysis, rotary kilns are utilized to thermally decompose plastic materials at high temperatures in the absence of oxygen, leading to the production of valuable products such as liquid fuels, gases, and char [2]. As shown in the Fig 3.

The key characteristics and advantages of rotary kilns in waste plastic pyrolysis: Continuous Operation: Rotary kilns offer continuous operation, allowing for a steady feed of waste plastic materials into the reactor while the pyrolysis process occurs continuously within the rotating drum. This continuous operation contributes to efficient processing and a high amount [12].

Efficient Heat Transfer: Rotary kilns are known for their efficient heat transfer capabilities. The rotation of the kiln drum ensures thorough mixing and contact between the waste plastic materials and the heating medium (usually hot gases or combustion products), promoting rapid and uniform heating of the feedstock [8].

Scalability: Rotary kilns are suited for large-scale applications due to their ability to handle substantial quantities of feedstock. They can be designed and scaled up to accommodate the processing needs of industrial-scale waste plastic pyrolysis facilities.

Despite these advantages, rotary kilns also present certain challenges and considerations:

Complex Gas-Solid Mixing: Achieving efficient gas-solid mixing within the rotary kiln can be challenging due to the complex flow patterns and dynamics within the rotating drum. Proper design and optimization of the kiln internals are necessary to ensure optimal mixing and heat transfer efficiency.

Energy Consumption: Rotary kilns require significant energy input to maintain the high temperatures necessary for waste plastic pyrolysis. Energy-efficient heating methods and process optimization strategies are essential to minimize energy consumption and operational costs.

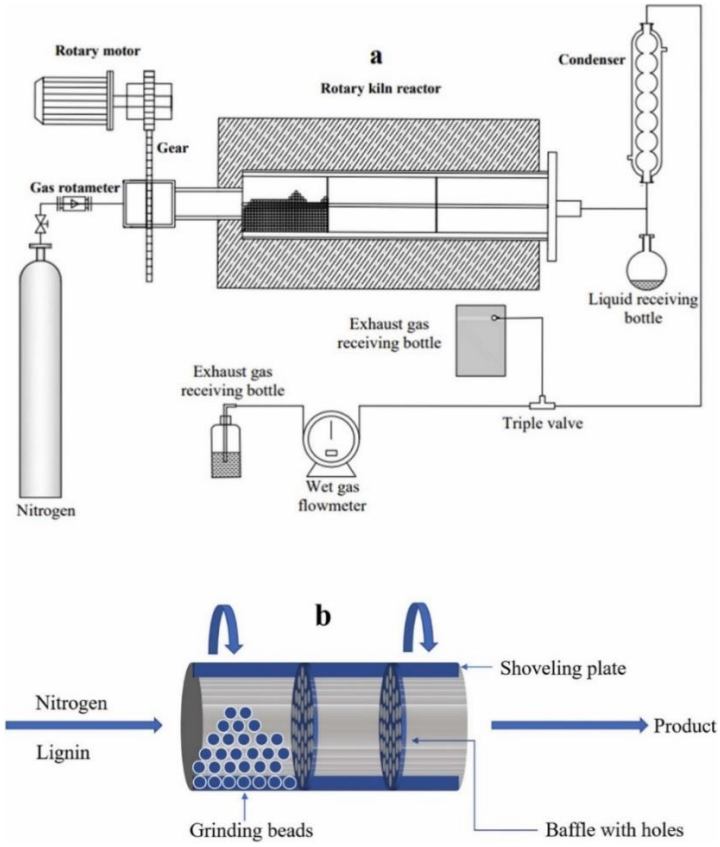

Fig. 3 Schematic diagram of two different Rotary Klin reactor using in industries [3]

Entrained Flow Reactors. Entrained flow reactors are specialized types of chemical reactors commonly used in high-temperature processes such as waste plastic pyrolysis. In these reactors, a finely divided solid or liquid feedstock is suspended and carried by a high-velocity gas stream, typically oxygen or an inert gas, through a reaction zone where thermal decomposition occurs. The high heating rates and short residence times characteristic of entrained flow reactors result in rapid pyrolysis and high yields of desired products [7]. The detailed sketch is shown in Fig. 4. It could also be used for other purposes of pyrolysis processes.

The key characteristics and advantages of entrained flow reactors in waste plastic pyrolysis:

a. High Heating Rates: Entrained flow reactors provide extremely high heating rates due to the intense mixing of feedstock particles with hot gases. This rapid heating promotes fast pyrolysis reactions, leading to high conversion rates and product yields.
b. Short Residence Times: The short residence times in entrained flow reactors, typically on the order of milliseconds to seconds, minimize secondary reactions and promote selective production of desired pyrolysis products. This can improve the quality and composition of the resulting products.
c. High Product Yields: Entrained flow reactors often yield high quantities of valuable products such as liquid fuels, gases, and chemicals due to their efficient pyrolysis kinetics and short residence times. This makes them attractive for waste plastic valorisation and resource recovery.

Although these advantages, entrained flow reactors also present some challenges and considerations:

a. Advanced Control Systems: The fast reaction environment and short residence times in entrained flow reactors require sophisticated control systems to ensure optimal process performance and product quality. Precise control of operating conditions such as temperature, gas flow rates, and residence time distribution is essential.
b. Limited Feedstock Compatibility: Entrained flow reactors may be limited to certain types of feedstocks or require preprocessing to achieve optimal performance. Factors such as feedstock particle size, moisture content, and composition can affect reactor operation and product yields.
c. Equipment Complexity: Entrained flow reactors are typically more complex and expensive to design, construct, and operate compared to other reactor types. Proper engineering and maintenance are necessary to ensure safe and efficient operation.

The entrained flow reactors offer unique advantages for waste plastic pyrolysis, including high heating rates, short residence times, and high product yields. However, their application requires careful consideration of feedstock characteristics, process control requirements, and equipment design to achieve optimal results.

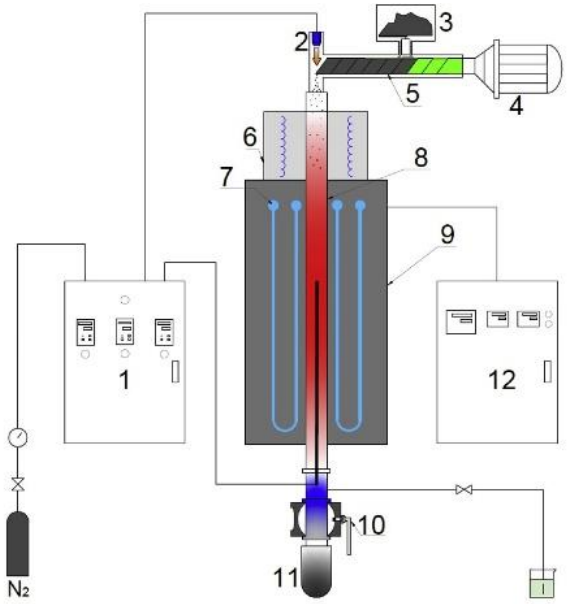

Fig. 4 Schematic diagram of Entrained flow reactors

1. Display Data, 2. Gas Jet, 3. Feedstock, 4. Variable frequency motor, 5. Spiral feed rod, 6. Preheating, 7. Molybdenum Silicide bar, 8. Reaction tube, 9. Heating insulation, 10. Ball Valve, 11. Char chamber 12. Controller for temperature [7].

The reactors can also be classified based on the purposes and use of the reactor. There are three types of pyrolysis reactors namely used in the industries. Batch pyrolysis, Semi-continuous, and fully continuous reactors. The major purposes are to improve the efficiency and efficiency of using the energy for producing the pyro-oil. Every reactor has its advantages and disadvantages. In some cases, the requirement of using these reactors cannot be replaced. Batch pyrolysis is the process used to produce very low output it's mostly suitable for all types of reactors. On the other hand, the Semi-continuous/semi-automatic can be used for a higher average than the batch but the shredded plastics loading into the reactors of fluidized or to the fixed bed reactors can be done automatically without any hassles. It also has better efficiency compared to fixed beds and it can operate nearly 20 tons per day on average. The last and most important role in the stream of efficiency is the fully continuous/automatic reactors mainly consisting of rotary kilns or screw-type reactors. Importantly the process of producing pyro-oil from the automatic process reactors is working without huge manpower for the production. But the arrangements of that need very high investments. The main considerations for selecting the reactors are given in the table based on the different aspects of the working requirements.

Table 1. Reactor and its properties

Reactor Type	Batch Pyrolysis Process	Semi-Continuous Process	Fully Continuous Process
Operation	Discontinuous	Semi-continuous	Continuous
Capacity	6-10 tons/cycle	15-20 tons/cycle	20-24 tons/cycle
Efficiency	Moderate	High	Very High
Operation Cost	High maintenance, Low initially	Moderate for initially and maintenance	Higher for initially and lower for maintenance
Ideal for	Small scale	Medium Scale	Large Scale

Condenser systems analysis. A condenser is a device where steam condenses, and latent heat of evaporation released by the steam is absorbed by cooling water [22].

Types of condenser systems. The main parameters that determine the operating mode of the condenser are cooling water flow rate, cooling water temperature, heat exchange area, and steam flow into the condenser [35]. These classifications can be further broken down into flowing basic parts which in turn make up the Ideal condenser. Types of systems based on several passes: (condensers can be classified based on the number of inlets and outlets in the system to move the fluids).

Single pass condenser system. As the name suggests, a one-pass condenser system only allows the fluids to pass through one another once. This setup is perfect for uses where there is an abundance of cooling water, such as cooling marine engines (Fig. 5).

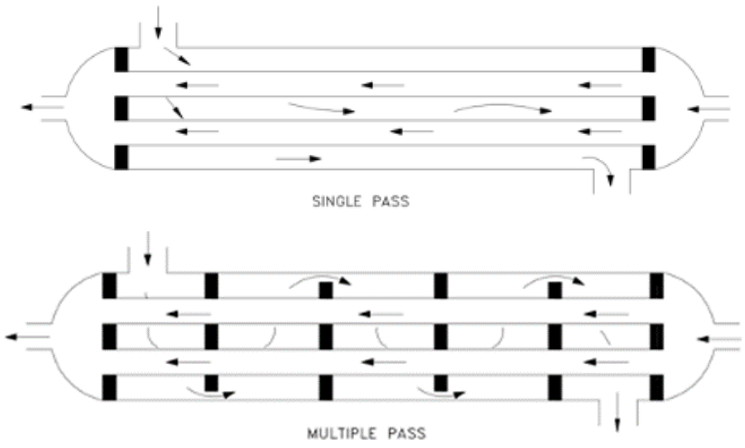

Fig. 5 Types of different pass condensers [21]

Multi-pass condenser system. The fluids pass through each other more than once using U tubes or baffles. A multi-pass condenser enhances the contact duration between the steam and the cooling medium (often water or air) by using numerous passes for the steam, which improves the efficiency of heat transfer. By maximizing steam condensation, this design enhances the power plant's or industrial process's overall efficiency.

Types based on flow arrangements (the condenser systems can be further classified based on the flow direction of the liquids inside the system).

Parallel flow condenser. In parallel flow condensers – both hot and cold fluids, flow in the same direction, parallel to each other. Both fluids enter the condenser at a common end with a high-temperature difference [22]. Hu [20] with other scientists has established a model of a parallel flow condenser to predict the refrigerant pressure drop based on multiple two-phase flow regimes, where the heat transfer performance was obtained by the method of analogy. When lower power consumption and the smaller refrigerant volume are important, parallel flow condensers are used [31]. Multi-pass parallel flow condenser (MPFC) has been widely used in the automotive industry because of its merits in thermal performance, structural robustness, compactness, and weight reduction [36].

Counter Flow Condenser. In a counter-flow condenser – the two fluids i.e. steam vapor and cooling water flow in opposite directions to each other. The flow of each fluid occurs at opposite ends of the steam condenser [23]. As per an experiment conducted by [25], it was demonstrated that the condensation effectiveness of counter-current flow is typically 15% higher than that of parallel flow. The ratio of water to air mass flow determines the condenser's efficiency, as it is not affected by the temperature or humidity of the air entering the system. Also, counter flow heat exchange steam condenser design is the most efficient when the heat transfer rate per unit surface area is considered. It is because of the average temperature difference (ΔT) between the two fluids over the length that the heat exchange processing is maximized [23].

Cross Flow condenser. In cross-flow condensers – fluids flow perpendicular to each other. Cooling water flows through the tubes and steam flows around these tubes at an angle of 90° [23]. Crossflow plate condensers are an efficient means to recover heat from moist exhaust gases [17]. Because the cooler fluid exits the counter-flow heat exchanger at the end where the hot fluid enters the heat exchanger, the cooler fluid will approach the inlet temperature of the hot fluid.

Types based on construction features. The final classification of the condenser is the overall design itself.

Tube and shell. The most basic and the most common type of heat exchanger construction is the tube and shell. This type of heat exchanger consists of a set of tubes in a container called a shell. The fluid flowing inside the tubes is called the tube side fluid and the fluid flowing on the outside of the tubes is the shell side fluid. Contact between the cool and hot liquids will naturally exchange heat from the hotter to the colder [28; 29].

In systems where the two fluids are at vastly different pressures, the higher-pressure fluid is typically directed through the tubes, and the lower-pressure fluid is circulated on the shell side. The shell and tube heat exchanger provides a comparatively large ratio of heat transfer area to volume and weight. It provides this surface in a form that is relatively easy to construct in a wide range of sizes and which is mechanically rugged enough to withstand normal shop fabrication stresses, shipping and field erection stresses, and normal operating conditions [28]. Shell and Tube condensers (Fig. 6) are designed and constructed based on TEMA (Tubular Exchanger Manufacturers Association) standards (TEMA,1999) [32].

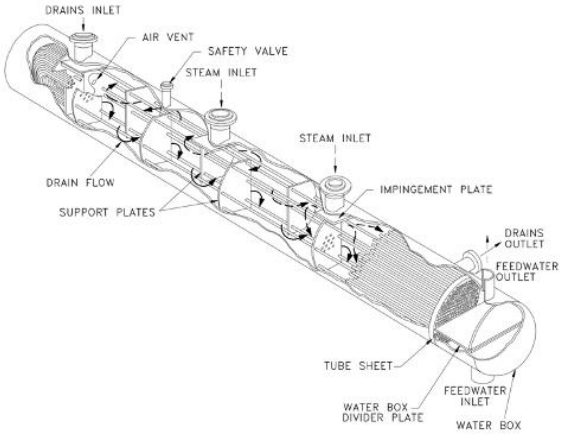

Fig. 6 Tube and shell Condenser design [32]

Plate-type condenser. A plate-type heat exchanger consists of plates instead of tubes to separate the hot and cold fluids. The hot and cold fluids alternate between each of the plates. It is known for high heat exchange efficiency [36] also a major advantage over a conventional heat exchanger as the fluids are exposed to a much larger surface area because the fluids spread out over the plates [37]. But this type (Fig. 7) of heat exchanger can't take huge pressure and is also not suitable for lower-density gas-gas applications [32]. The effectiveness of a plate heat exchanger with a finite number of plates is affected by the end channels, and the channels between two adjacent passes [30].

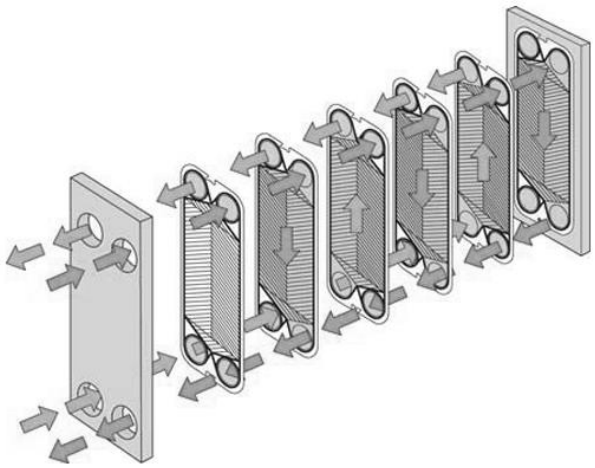

Fig. 7 Plate Type Condenser [32]

2. Methodology

Design and analysis of reactor. The main objective of the study is to create a design of the reactor that is going to be used for experimental purposes. SolidWorks is used to create the model for the analysis of the reactor that is going to be used for the experiment. The whole study consists of fixed bed reactors with cyclone separators for design and analysis. The main moto is to study the temperature that can be withheld by the reactor for producing the pyro oil from the plastics. Fig 8 and Fig 9, Fig 10 shows the model created for testing.

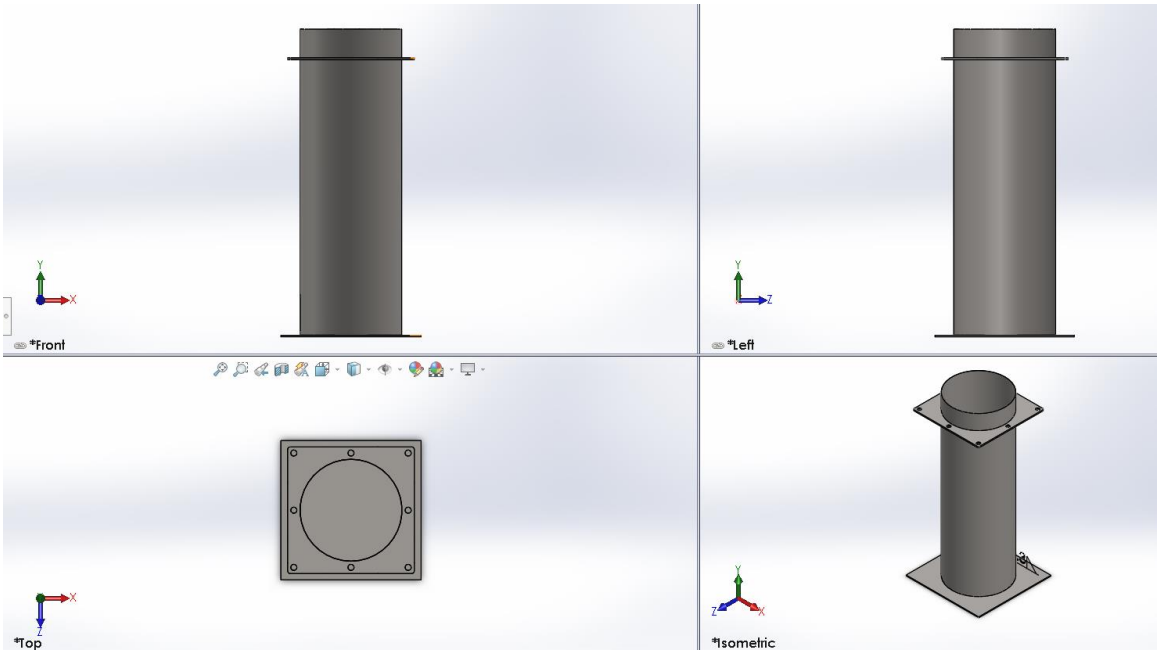

Fig. 8 The reactor body model

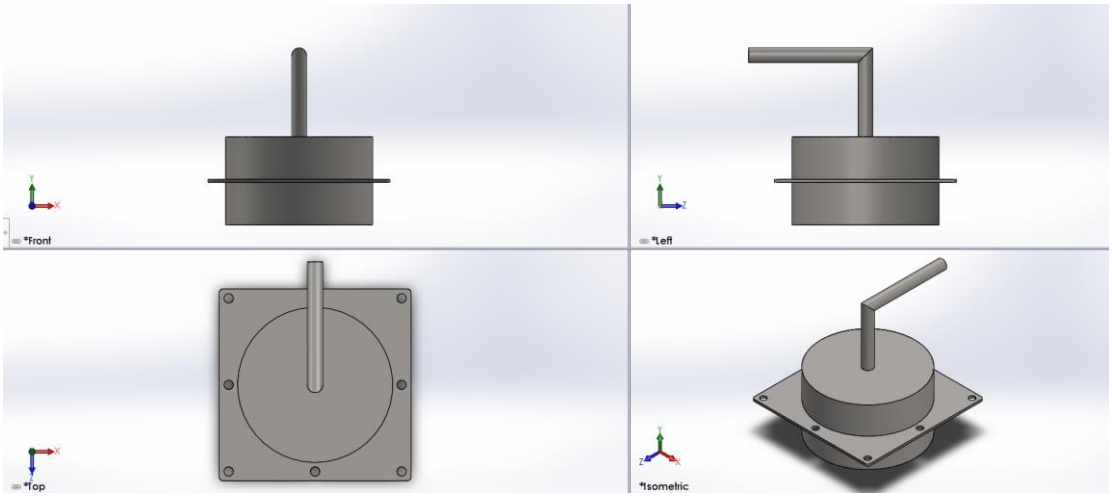

Fig. 9 The reactor cover model

Table 2. The parameters of the reactors

Total Height	700mm
Width of base pate	450 x 450
Diameter of Reactor	200mm
Diameter of Gas exit pipe	20mm

Based on the table given above the reactor body and cover is created.

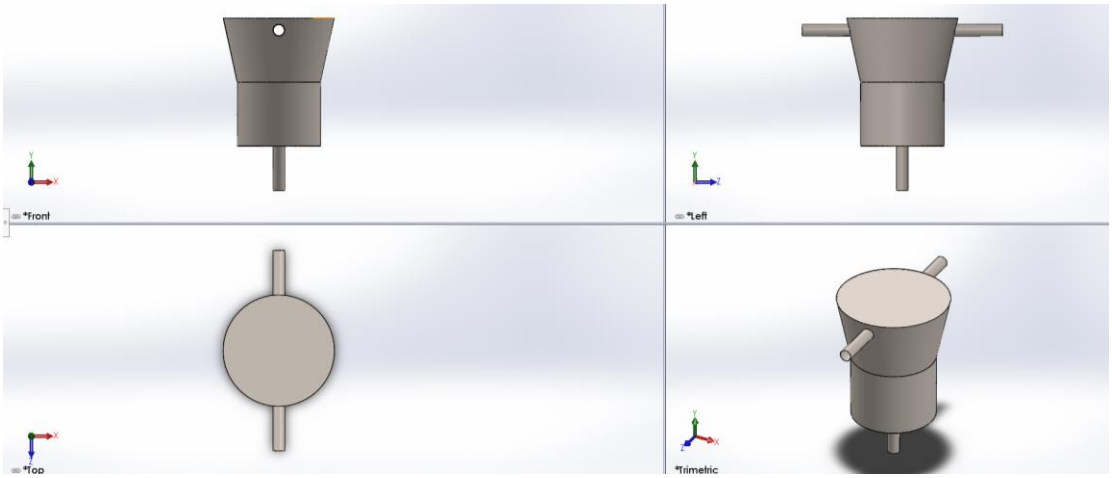

Fig. 10 Cyclone separator model for separating the pyro-gas from the reactor

The Reactor Body and the Cover are made from 2mm of Cast carbon steel, for better conduction of heat. The main sub-part as cyclone separator which is made from AISI 316 stainless steel is used to separate the heavy and weighted pyro-oil. The important factor of the cyclone separator is not to create a wax formation suddenly from the reactor to the condenser. The wax formation is one of the biggest measures to consider

Design of the condenser system.

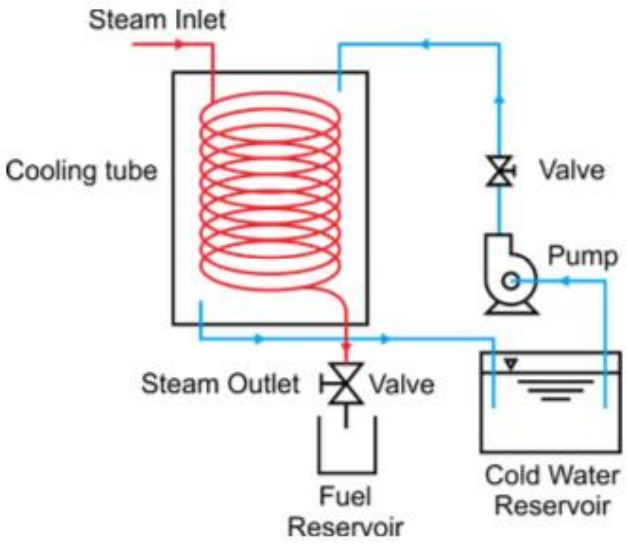

Fig. 11 Final design of the condenser system [26]

Fig. 11 shows the flow control system used is the parallel flow regime where hot steam flows in the inner pipe while the cooling fluid flows on the annular side [26]. The condenser's steel shell has a diameter of 150 mm and a height of 400 mm. The tube is constructed from 0.5-inch-diameter copper tubing that has been coiled spirally to a length of 1000 mm. As a liquid tar, the product leaves the condenser.

The cold fluid from the condenser goes to storage to cool down and to be used again. The inlet temperature of the condenser is 300°C, while the temperature of the cooling fluid is kept constant in the temperature range of 15°C - 20°C.

A theoretical calculation was made to find the temperature differences and the heat transfer rate of the designed system and the following results were obtained.

Table 3. The parameters of the condenser

Properties	Inner pipe	Annulus
Inlet temperature (T_{in})	300°C	30 °C
Outlet temperature (T_{out})	35°C	20 °C
Mass Flow	0.01 kg/s	0.38kg/s

3. Results

After the designing of the reactor analysis is done which is presented on SolidWorks. We assume that there is no heat loss in our system. So that we can find the temperature withhold in our system. The temperature load of 450°C due to the reactor fills with the LDPE plastics. So that the pyro-vapor starts to produce at the temperature of 400°C.

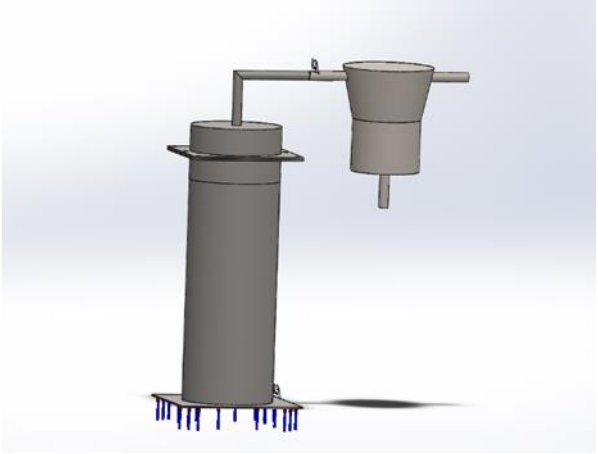

Fig 12. The reactor assembly with the heat transfer points

Table 4. The parameters used for experimental simulation [18, 19]

Variant	Temperature	Input materials	Melting Temperature	Temperature of pyrolysis
I	450	LDPE	110°C	250-380
II	500	HDPE and PP	131°C and 168-176°C	390-500
III	600	Mixed(unsorted)	Depends on mixing	380-525

The above table states LDPE- Low-Density Polyethylene, HDPE-High Density Polyethylene, and PP- Polypropylene.

A temperature of 450°C is given to the base plate of the reactor body shown in Fig 13. For better heat holding capacity the reactor plate is placed under the body of the reactor. So as an outcome, the heat can significantly improve the gas without wax formation. The pyro-vapor will be at a temperature of nearly 430°C, from the reactor the hot gas mixed with impurities flows through the next chamber of the cyclone separator. Then the hot vapor flows through the condenser to cool down the vapor and changes into a liquid.

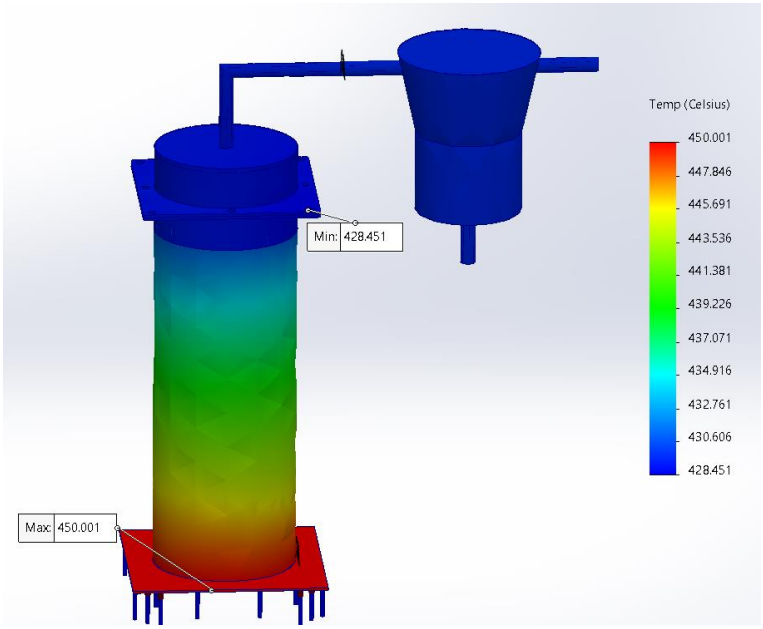

Fig. 13 Shows the overall analysis of temperature changes for 450°C

The result shows that the temperature is starting to melt the plastics that are packed inside the reactor. The heating starts to melt the plastics from the bottom neck of the reactor to the top. Thus, it shows the result of it can withhold the temperature

needed for the pyrolysis process to do as an experimental setup.

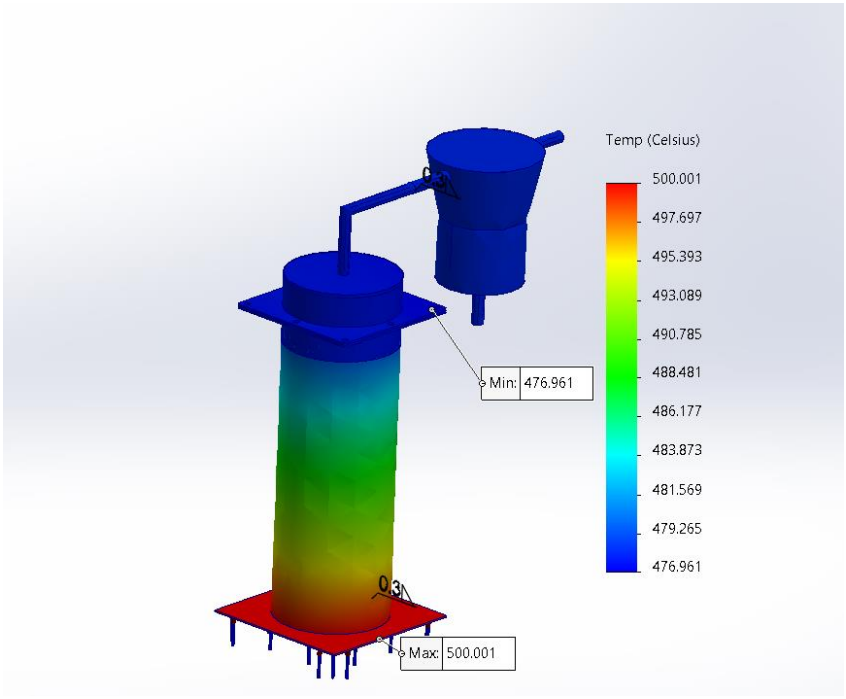

Fig. 14 The overall analysis of temperature changes for 500°C

\On the above the temperature has shown for 500°C which is used for the HDPE and PP plastics which have the higher temperature for melting and producing the pyro-vapor to the reactor to the cyclone reactor. The temperature of 470°C pyro-vapor passes through the cyclone separator chamber to split less density and higher density gas.

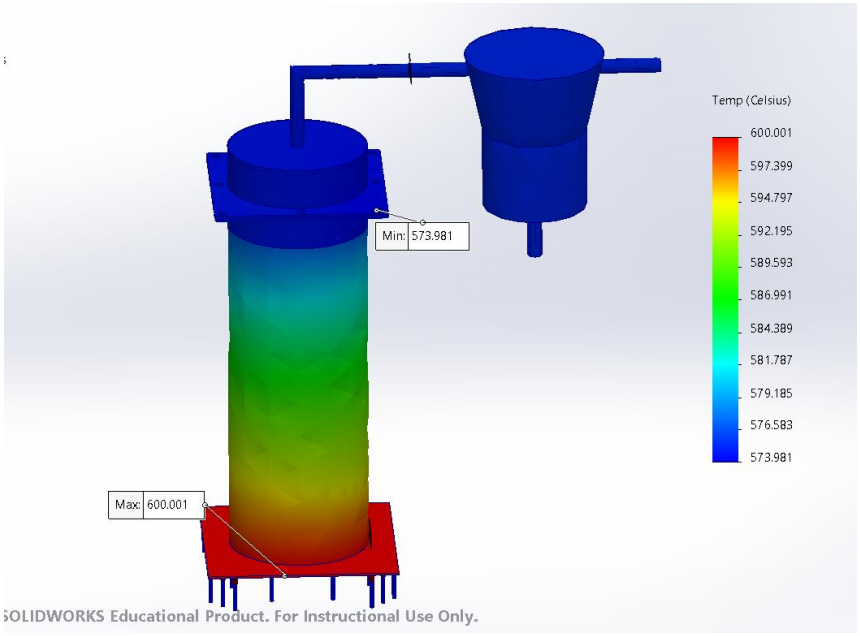

Fig. 15 The overall analysis of temperature changes for 600°C

Fig. 15 shows the temperature of minimum where the gas exits from the reactor at 574°C to the cyclone separator, the temperature of 600°C is used to produce the pyro-gas from the mixed plastics which can contain more contamination than the specific plastics used in the previous analysis. So 600°C of input heat is chosen.

The entire plastic pyrolysis system for producing the pyro-oil from the LDPE has been successfully verified by the designing and the analysis using SolidWorks. The data from the different analyses and the research articles clearly states that this type and this model can work perfectly for experimental purposes to do as lab experiments. The places of the temperature drops are clearly shown in this study of analysis.

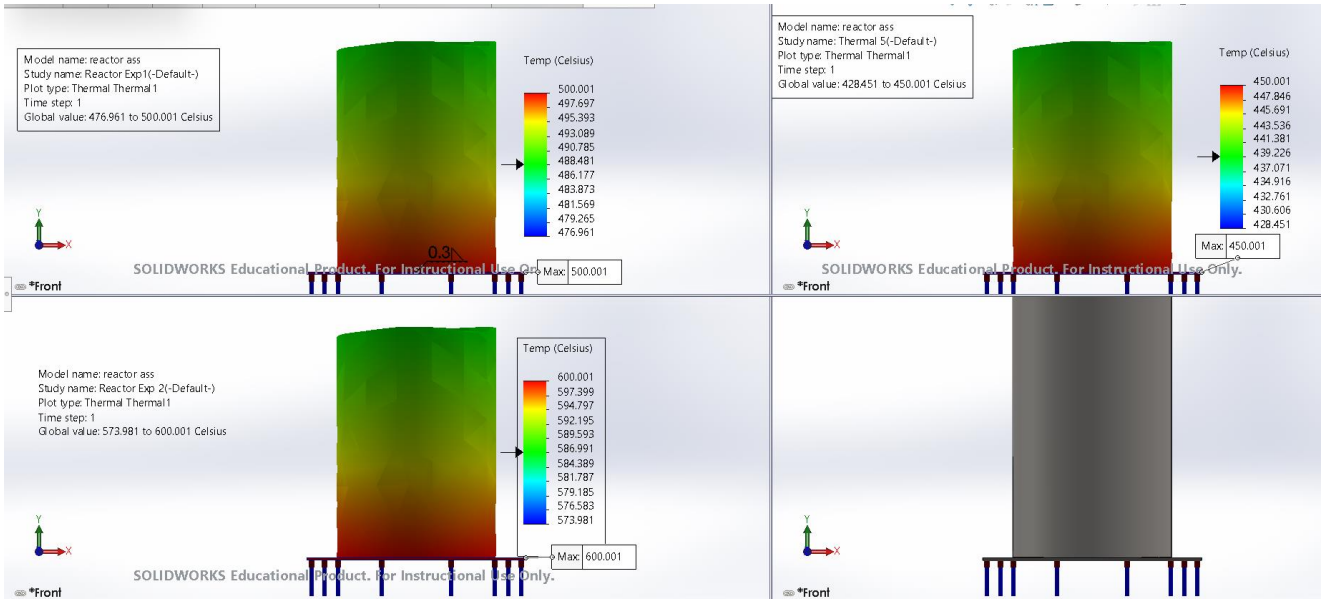

Fig. 16 The working temperature of the Reactor at different Temperature distributions

4. Conclusion

To conclude, the different types of reactors are used for different purposes. It may vary depending upon the places and the requirements for the pyrolysis process, also it needs to take into account the source of energy and types of sources used for heating up the reactor. This research work consists of the study of design as well as the prototype also, the fixed bed reactor has been used for experimental purposes. The rotary kilns are used for mass production as well as for the non-stop continuous working of the pyrolysis reactors. The Condenser system was also designed for the best possible efficient output. It is also possible to create and modify for future purposes like for increasing efficiency and the yield output from the plastics, The same setup along with some additional accessories can be used for the fabrication of the processes. But as per the efficiency, we consider that we can get a yield of up to 60-70% of pyro-oil from the raw shredded plastics without any impurities like metals or other organic components mainly without wax formation.

References

1. Anuar Sharuddin, S. D., Abnisa, F., Wan Daud, W. M. A., & Aroua, M. K. (**2016**). A review on pyrolysis of plastic wastes. Energy Conversion and Management, 115, 308–326. https://doi.org/10.1016/j.enconman.2016.02.037.
2. Chang, S. H. (**2023**). Plastic waste as pyrolysis feedstock for plastic oil production: A review. Science of The Total Environment, 877, 162719. https://doi.org/10.1016/j.scitotenv.2023.162719.
3. Choi, Y., Wang, S., Yoon, Y. M., Jang, J. J., Kim, D., Ryu, H.-J., Lee, D., Won, Y., Nam, H., & Hwang, B. (**2024**). Sustainable strategy for converting plastic waste into energy over pyrolysis: A comparative study of fluidized-bed and fixed-bed reactors. Energy, 286, 129564. https://doi.org/10.1016/j.energy.2023.129564.
4. Lasek, J., Głód, K., Słowik, K., Cygan, A., & Li, Y.-H. (**2022**). Static and dynamic characteristics of rotary kiln reactor during processing of biomass and municipal solid waste. Powder Technology, 404, 117476. https://doi.org/10.1016/j.powtec.2022.117476.
5. Laskowski, R., Smyk, A., Rusowicz, A., & Grzebielec, A. (**2020**). A useful formulas to describe the performance of a steam condenser in off-design conditions. Energy, 204, 117910. https://doi.org/10.1016/j.energy.2020.117910.
6. LDPE vs HDPE. (n.d.). Retrieved 10 May 2024, from http://chembook.org/page.php?chnum=8&sect=7
7. Liang, D., Xie, Q., Wei, Z., Wan, C., Li, G., & Cao, J. (**2019**). Transformation of alkali and alkaline earth metals in Zhundong coal during pyrolysis in an entrained flow bed reactor. Journal of Analytical and Applied Pyrolysis, 142, 104661. https://doi.org/10.1016/j.jaap.2019.104661.
8. Luo, S., Xiao, B., Hu, Z., & Liu, S. (**2010**). Effect of particle size on pyrolysis of single-component municipal solid waste in fixed bed reactor. International Journal of Hydrogen Energy, 35(1), 93–97. https://doi.org/10.1016/j.ijhydene.2009.10.048.
9. Pandey, U., Stormyr, J. A., Hassani, A., Jaiswal, R., Haugen, H. H., & Moldestad, B. M. E. (**2020**). PYROLYSIS OF PLASTIC WASTE TO ENVIRONMENTALLY FRIENDLY PRODUCTS. 61–74. https://doi.org/10.2495/EPM200071.
10. Valizadeh, S., Valizadeh, B., Seo, M. W., Choi, Y. J., Lee, J., Chen, W.-H., Lin, K.-Y. A., & Park, Y.-K. (**2024**). Recent advances in liquid fuel production from plastic waste via pyrolysis: Emphasis on polyolefins and polystyrene. Environmental Research, 246, 118154. https://doi.org/10.1016/j.envres.2024.118154.

11. Vijayakumar, A., & Sebastian, J. (**2018**). Pyrolysis process to produce fuel from different types of plastic – a review. IOP Conference Series: Materials Science and Engineering, 396(1), 012062. https://doi.org/10.1088/1757-899X/396/1/012062.
12. Xu, S., Chen, X., Tang, Q., Li, A., Lu, X., Liu, X., & Yu, F. (**2023**). Pyrolysis of dealkaline lignin to phenols by loading grinding beads in a rotary kiln reactor. Journal of Analytical and Applied Pyrolysis, 169, 105824. https://doi.org/10.1016/j.jaap.2022.105824.
13. Zhang, Y., Kang, S., Allen, S., Allen, D., Gao, T., & Sillanpää, M. (**2020**). Atmospheric microplastics: A review on current status and perspectives. Earth-Science Reviews, 203, 103118. https://doi.org/10.1016/j.earscirev.2020.103118.
14. Wang, Ya-Nan, Jong-Pyo Lee, Min-Ho Park, Byeong-Ju Jin, Tae-Jong Yun, Young-Ho Song, and Ill-Soo Kim. **2017**. 'A Study on 3D Numerical Model for Plate Heat Exchanger'. Procedia Engineering 174:188–94. https://doi:10.1016/j.proeng.2017.01.203.
15. 'Single, Double or Triple Pass Cooling - What's the Difference?' EJ Bowman. Retrieved 25 March **2024** (https://ej-bowman.com/knowledge-centre/single-double-or-triple-pass-cooling-whats-the-difference/.)
16. Bahri, Syaiful, Yosi Ambarwati, Yul Martin, Lina Marlina, and Sri Waluyo. 2021. 'STUDY ON GC-MS PROFILE OF FUELS PRODUCED FROM PLASTIC WASTE CONVERSION VIA THREE-CONDENSER PYROLYSIS REACTOR'. Jurnal Teknik Pertanian Lampung (Journal of Agricultural Engineering) 10:33. doi: 10.23960/jtep-l.v10i1.33-40.
17. Ganzevles, F. L. A., and C. W. M. van der Geld. **2002**. 'On the Prediction of Condenser Plate Temperatures in a Cross-Flow Condenser'. Experimental Thermal and Fluid Science 26(2):139–45. https://doi:10.1016/S0894-1777(02)00120-6.
18. Hazrat, M. A., Mohammad Rasul, M. Masud Khan, Kalam Azad, and Mu Bhuiya. **2014a**. 'Utilization of Polymer Wastes as Transport Fuel Resources- a Recent Development'. Energy Procedia 61:1681–85. https://doi:10.1016/j.egypro.2014.12.191.
19. Hazrat, M. A., Mohammad Rasul, M. Masud Khan, Kalam Azad, and Mu Bhuiya. **2014b**. 'Utilization of Polymer Wastes as Transport Fuel Resources- a Recent Development'. Energy Procedia 61:1681–85. https://doi:10.1016/j.egypro.2014.12.191.
20. Hu, H., H. Chen, Y. Wang, J. Xie, J. Deng, and A. Zhou. **2012**. 'Simulation model and experimental study on parallel flow condenser based on two-phase flow regime'. Huagong Xuebao/CIESC Journal 63(3):806–11. https://doi:10.3969/j.issn.0438-1157.2012.03.019.
21. ISCAP – P Porto, and Enora Guignard. **2023**. 'Lamborghini: An Approach to the Organization Study'. INTERNATIONAL JOURNAL OF MULTIDISCIPLINARY RESEARCH AND ANALYSIS 06(05). https://doi:10.47191/ijmra/v6-i5-35.
22. Kapooria, Raj, S. Kumar, and Sanjay Kasana. **2008**. 'Technological Investigations and Efficiency Analysis of a Steam Heat Exchange Condenser: Conceptual Design of a Hybrid Steam Condenser'. Journal of Energy in Southern Africa 19. https://doi:10.17159/2413-3051/2008/v19i3a3327.
23. Kofi Tulashie, Dr.-Ing Samuel, Enoch Boadu, and Samuel Dapaah. **2019**. 'Plastic Waste to Fuel via Pyrolysis: A Key Way to Solving the Severe Plastic Waste Problem in Ghana'. Thermal Science and Engineering Progress 11. https://doi:10.1016/j.tsep.2019.05.002.
24. Laskowski, Rafał, Adam Smyk, Artur Rusowicz, and Andrzej Grzebielec. **2020**. 'A Useful Formulas to Describe the Performance of a Steam Condenser in Off-Design Conditions'. Energy 204:117910. https://doi:10.1016/j.energy.2020.117910.
25. Li, Yi, James Klausner, Renwei Mei, and Jessica Knight. **2006**. 'Direct Condensation in Packed Beds'. International Journal of Heat and Mass Transfer - INT J HEAT MASS TRANSFER 49:4751–61. https://doi:10.1016/j.ijheatmasstransfer.2006.06.013.
26. Novarini, Sigit Kurniawan, Rusdianasari Rusdianasari, Yohandri Bow, and Ahmad Rifa'i. **2020**. 'Condenser Design on Plastic Oil Distillation Equipment'.
27. Pannucharoenwong, Nattadon, Keyoon Duanguppama, Snunkhaem Echaroj, Chinnapat Turakarn, Kumpanat Chaiphet, and Phadungsak Rattanadecho. **2023**. 'Improving Fuel Quality from Plastic Bag Waste Pyrolysis by Controlling Condensation Temperature'. Energy Reports 9:125–38. https://doi:10.1016/j.egyr.2023.05.231.
28. Parisher, Roy A., and Robert A. Rhea. **2012a**. 'Chapter 6 - Mechanical Equipment'. Pp. 112–33 in Pipe Drafting and Design (Third Edition), edited by R. A. Parisher and R. A. Rhea. Boston: Gulf Professional Publishing.
29. Parisher, Roy A., and Robert A. Rhea. **2012b**. 'Chapter 6 - Mechanical Equipment'. Pp. 112–33 in Pipe Drafting and Design (Third Edition), edited by R. A. Parisher and R. A. Rhea. Boston: Gulf Professional Publishing.
30. Prasad, Arjun, and Kaushik Anand. **2020**. 'Design Analysis of Shell Tube Type Heat Exchanger'. International Journal of Engineering Research And V9. https://doi:10.17577/IJERTV9IS010215.
31. Sanaye, Sepehr, and Masoud Dehghandokht. **2011**. 'Modeling and Multi-Objective Optimization of Parallel Flow Condenser Using Evolutionary Algorithm'. Applied Energy 88(5):1568–77. https://doi:10.1016/j.apenergy.2010.11.032.
32. Shah, Ramesh K., and Dusan P. Sekulic. 2003. Fundamentals of Heat Exchanger Design. John Wiley & Sons.
33. Sookramoon, Krissadang. **2019**. 'THE ANALYSIS OF A CROSS FLOW HEAT EXCHANGER USED IN A SOLAR TUNNEL DRYER'.

34. Spitz, Luis, and Roberto Ferrari. **2016**. '7 - Soap Drying Systems'. Pp. 133–66 in Soap Manufacturing Technology (Second Edition), edited by L. Spitz. AOCS Press.
35. Vodeniktov, Artem, Natalia Chichirova, and Valeriia Melnikova. **2021**. 'Experimental Assessment of the Condenser at Off-Design Modes'. Case Studies in Thermal Engineering 28:101457. https://doi:10.1016/j.csite.2021.101457.
36. Wang, Dingbiao, Qitao Wu, Guanghui Wang, Haoran Zhang, and Honglin Yuan. **2024**. 'Experimental and Numerical Study of Plate Heat Exchanger Based on Topology Optimization'. International Journal of Thermal Sciences 195:108659. https://doi:10.1016/j.ijthermalsci.2023.108659.
37. Wang, Ting, Bo Gu, Bing Wu, Hongtao Ma, and Cheng Qian. **2015**. 'Modeling for Multi-Pass Parallel Flow Condenser with the Effect of Refrigerant Mal-Distribution'. International Journal of Refrigeration 60:234–46. https://doi:10.1016/j.ijrefrig.2015.08.015.
38. Ye, Liang, Ming Wei Tong, and Xin Zeng. **2009**. 'Design and Analysis of Multiple Parallel-Pass Condensers'. International Journal of Refrigeration 32(6):1153–61. https://doi:10.1016/j.ijrefrig.2009.01.012.

Enhancing 3D Printed (Fused Deposition Modelling) Structure with Embedded Strain Gauge Sensor

Justinas BALODIS[1]*, Marius RIMAŠAUSKAS[1], Sigita URBAITĖ[1]

1 Kaunas University of Technology, Kaunas, Lithuania
** jbalodis@gmail.com*

Abstract

This review presents a comprehensive methodology for manufacturing structures with embedded sensors and provides insights from testing and analysis. The methodology involves the development and implementation of manufacturing processes, starting with the construction of sample structures to fine-tune parameters, such as material selection and manufacturing settings. Through iterative adjustments, optimal conditions were established for embedding sensors into structures, ensuring effective integration and minimal impact on structural integrity. Impact tests revealed that structures with embedded sensors experienced minimal structural impact, demonstrating the feasibility of using compact strain gauges for such applications. Subsequent mechanical testing under dynamic and static loads was used to evaluate the behavior of these structures, with strain measurements serving as the primary mechanical property quantified. The results show consistent performance between the embedded strain gauge data and the optical extensometer results, indicating the viability of the integrated sensor system. Cost considerations were also addressed, with a range of options for the data acquisition systems presented. Although higher precision equipment incurs higher costs, the research suggests that economically beneficial outcomes can be achieved with careful selection and testing of data-acquisition systems. Overall, this article of study contributes to the advancement of sensor integration techniques for structural applications and provides practical insights and recommendations for future implementation.

Keywords: Strain measurement. Strain gauge. Embedded Sensor. 3D printing. Fused Deposition Modeling.

1. Introduction

Additive manufacturing technology has revolutionized the way products are designed and manufactured [1]. Integration of strain sensors in 3D printing adds a new dimension of capabilities to the technology. Significance of 3D printing with integrated strain sensors provides several benefits for the industry, e.g. quality control with the use of integrated strain sensors, it is possible to monitor the quality and consistency of the 3D printing process. Moreover the structural health monitoring, when the 3D printed objects with integrated strain sensors can be used for structural condition monitoring, where the sensors can detect any changes in the structural integrity of the object. This can be particularly useful in fields like aerospace and civil engineering, where the safety and durability of structures are critical. In the recent year the increase of research of the smart devices in healthcare segment is significant [2]. The 3D printing with integrated strain sensors can be used to create smart devices that can detect and respond to changes in their environment and send the data to data acquisition device for real time data processing and management. Besides that the use of integrated strain sensors in 3D printing can also improve the efficiency of the manufacturing process. By monitoring the strain on the printed object during the printing process, it is possible to optimize the printing parameters and reduce material waste. Overall, the integration of strain sensors in 3D printing has significant potential to enhance the quality, safety and efficiency of manufactured products, as well as enable the creation of innovative new devices and applications. Variance of 3D printing technologies refers to the diversity and range of different 3D printing methods [3], materials and applications that exist. Additive manufacturing is useful tool in various industries, in various product development stages, e.g. prototyping and testing: 3D printing can be used to quickly create prototypes and test them partially. This allows researchers and manufacturers to test different configurations and materials without the need for expensive and time consuming traditional manufacturing methods.

2. Strain Gauge Definition and Selection

A strain gauge, is a transducer that measures mechanical strain or deformation in an object. Comprising a metallic foil pattern affixed to a flexible substrate, typically made of a polymer, ceramic, or metal, it exhibits electrical resistance changes proportional to the mechanical strain experienced by the object under study. This alteration in resistance, usually gauged by a Wheatstone bridge circuit, enables precise quantification and analysis of the strain, facilitating critical insights into material behavior, structural integrity, and performance characteristics in diverse applications across industries such as aerospace, civil engineering, and biomechanics [4]. After the overview of different strain measurement methods was conducted and based on observations, decision was made to proceed with integration of strain gauge with ability to withstand elevated temperatures. The temperature resistance is needed, because during Fused Deposition Modeling 3D printing process, temperature reaches more than 200° C, when the Prusa PLA material used [5,6]. After evaluation, the 1-LM-6/350GE strain gauge produced by HBM was selected. Strain gauges were prepared Fig.1. and embedded in the specimen during the pause of production process. The Prusa PLA defined as main structure material for sample. After the production and validation of resistance level on each of strain gauge, the data acquisition system was incorporated on the base of Arduino Uno R3 board minicomputer to represent and to log the test results and data.

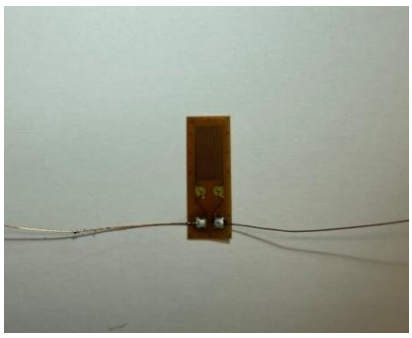

Fig. 1 Strain gauge 1-LM-6/350GE by HBM after preparation [6]

3. Samples Design & Production

The shape and other geometrical properties for the specimens were taken from standard paper ISO 527-2:2012. Nominal length of the specimen is 150mm, the width in the widest area is 20mm and in the narrowest part is 10mm. The thickness of the sample is 4mm. In the Fig. 2 the strain gauge mounting process is demonstrated, the 3D printing on the Prusa MK3 is paused and the Z70 glue by HBM [4] applied on the structure and the strain gauge is secured in place, after the quality check and conformation that sensor is intact the printing process is un-paused and the production process proceeded till the end.

Fig. 2 Strain gauge mounted on the PLA structure [6]

Following sensor fabrication, parameters were systematically measured and verified to ascertain the sensor's operational status and functionality including the electrical resistance to reach the nominal value of 350 Ω. This quality assurance process ensured the sensor's viability and proper functioning. The sensor is connected to the data acquisition system through a Wheatstone bridge. This system comprises an Arduino microcontroller, an HX711 load cell amplifier breakout board, and data logging capabilities utilizing Microsoft Excel Data Streamer on a Surface 6 tablet, which is connected via a USB interface Fig. 3. Principal control for bench and data acquisition scheme is shown in the Fig. 4.

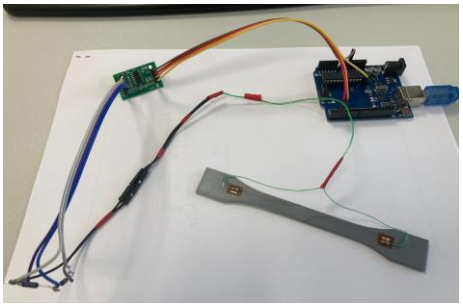

Fig. 3 Assembled system with the sample with embedded gauge [6]

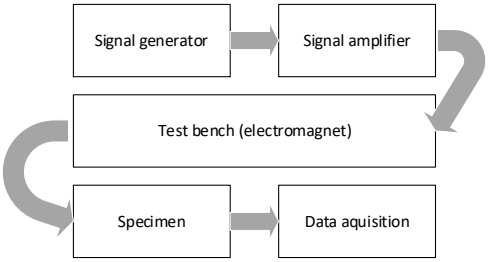

Fig. 4 Control scheme of the test bench control and data acquisition [6]

3. Data Sampling & Data Analysis

To enhance the understanding of structural behavior under excitation, multiple impact tests, including a bump test, were devised. Bump test involves a controlled impact that generates a wide frequency range of structural responses, aiming to analyze the strain sensor's response and gather insights into the structure's characteristics and behavior under dynamic loading conditions. During the test Fig. 5, the specimen is mounted on a test bench designed to replicate specific types of impacts or bumps the product is likely to encounter. The test results are used to evaluate the structure's ability to withstand such shocks and impacts, as well as to identify any potential design issues. The impact tests conducted using the dedicated test bench for the research. In the Fig. 6 the changes in the system responses is seen due the application of bending force on the end of the beam and fixing it for some time where the load is fixed 50 gram loaded on the end of the beam and left for

some time, after that the load is removed. The structure was also tested on a testing bench using different excitation frequencies Fig. 7, with two tests performed at frequencies of 1Hz and 3Hz.

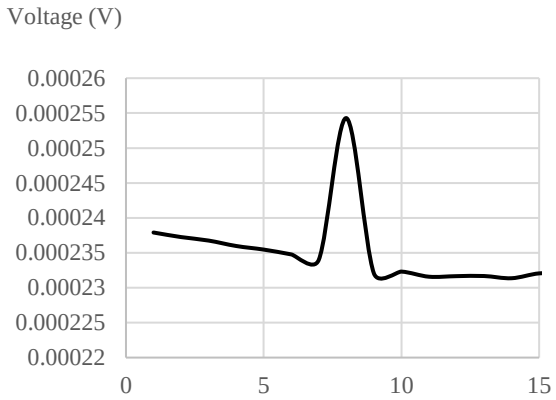

Fig. 5 Voltage change due the non-controlled bump [6]

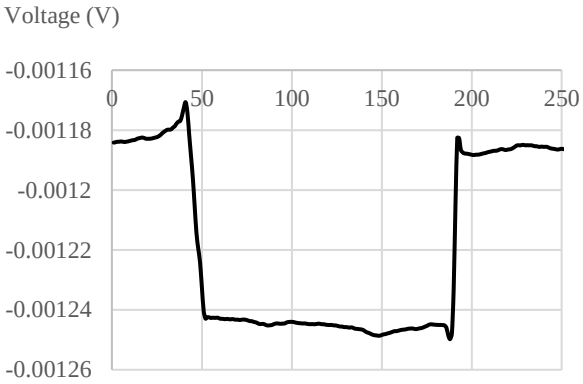

Fig. 6 Voltage change due 50 gram load [6]

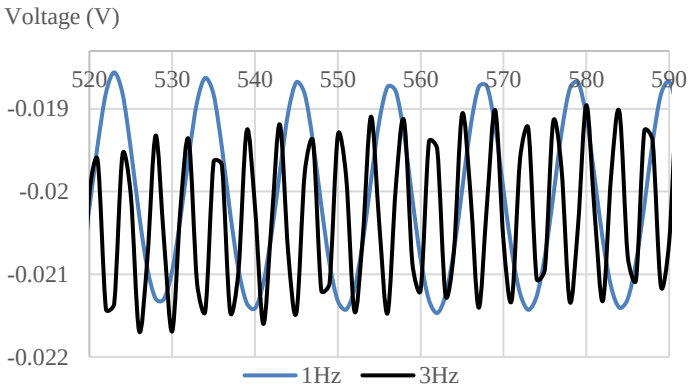

Fig. 7 Comparison between different excitation frequencies [6]

In order to gain more data and know how about the specimens with integrated strain gauges the tests in the testing machine were conducted. The testing machine Tinius Olsen H25KT with VEM 300 series tensiometer was used. The test conducted, was tension of the specimen up to 0,3% of length, with the speed of 2mm per minute. Data obtained shown in Fig. 8, the data from the extensometer is delivered in Fig. 9.

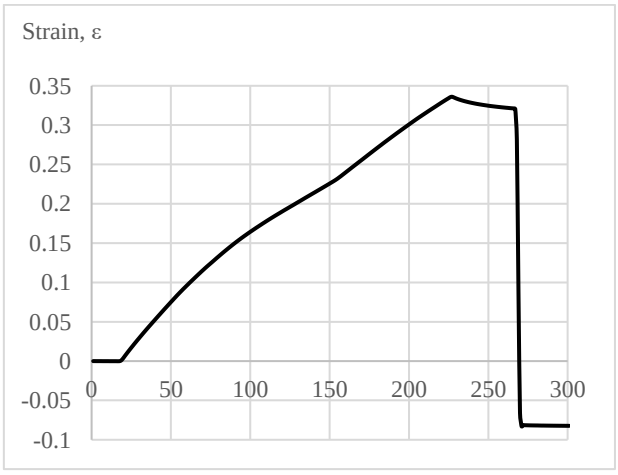

Fig. 8 Strain measured on sample [6]

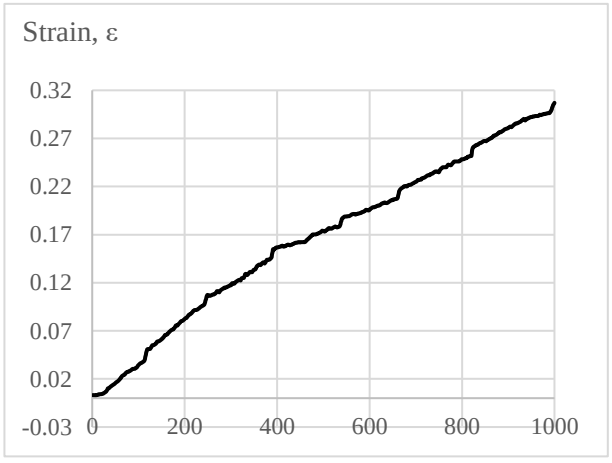

Fig. 9 Strain measured via extensometer [6]

4. Summary of Tests

In summary it can be stated the that result of samples production and testing was implemented successfully, in order to gain more knowledge about the structure, several visual inspection loops were made. Important part was to produce the samples with integrated sensor. Based on data gained it can be sated that the result is positive and strain gauges can be embedded in

various 3D printed structures. Also it is important to mention that the data acquisition part takes significant part in the overall test phase and it must be prepared in best way. In overall it can be stated that the testing phase is successful [6].

5. Conclusions

A methodology for manufacturing structures with embedded sensors was successfully developed and applied to test samples. Initially, samples were created using PLA and a Prusa MK3S 3D printer, optimized with 100% infill and 0.2mm layer thickness. Subsequently, samples with HBM strain gauges capable of withstanding temperatures up to 250°C were produced. Impact tests indicated minimal structural impact, demonstrating the feasibility of using compact strain gauges. Mechanical behavior under dynamic and static loads was evaluated, with tests showing a small deviation (0.016 to 0.043 strain units) between strain gauge and optical extensometer measurements for embedded sensors, confirming the system functional viability.

References

1. Zhou, L.; Miller, J.; Vezza, J.; Mayster, M.; Raffay, M.; Justice, Q.; Al Tamimi, Z.; Hansotte, G.; Sunkara, L.D.; Bernat, J. Additive Manufacturing: A Comprehensive Review. *Sensors* **2024**, 24, 2668. https://doi.org/10.3390/s24092668
2. NAGHDI, Tina and ARDALAN, Sina and ADIB, Zeinab Asghari and SHARIFI, Amir Reza and GOLMOHAMMADI, Hamed. *Biosensors and Bioelectronics*, p. 223. **2023**.
3. Anketa Jandyal, Ikshita Chaturvedi, Ishika Wazir, Ankush Raina, Mir Irfan Ul Haq, 3D printing – A review of processes, materials and applications in industry 4.0, *Sustainable Operations and Computers*, Volume 3, **2022**, Pages 33-42, ISSN 2666-4127, https://doi.org/10.1016/j.susoc.2021.09.004
4. https://www.hbm.com/en/0014/strain-gauges/?product_type_no=HBM%20Strain%20Gauges:%20First%20Choice%20for%20Strain%20Measurements
5. https://help.prusa3d.com/article/pla_2062
6. https://epubl.ktu.edu/object/elaba:167800967/

The Use of Computational Fluid Dynamics (CFD) Method in the Analysis of the Operation of an Engine Turbocharger

Dominik ZERKA[1]*, Dariusz SZPICA[1]

1 Bialystok University of Technology, Faculty of Mechanical Engineering, 45C Wiejska str., 15-351 Bialystok, Poland
**78081@student.pb.edu.pl*

Abstract

The continuous tightening of exhaust emission standards for combustion engines results in a tendency among manufacturers to reduce the displacement volume of engines. This state of affairs results in the frequent use of turbocharging, which allows for greater power with a smaller displacement compared to naturally aspirated engines. The properties of the charge air such as pressure and flow rate are influenced by the parameters of the compressor rotor – its geometry and rotational speed. The article analyses the influence of the pump rotor rotational speed on the turbocharger flow rate using the computational fluid dynamics (CFD) method. The study consisted of assessing the flow parameters within the virtual turbocharger that affect its functional properties. The result will be applicable to the turbocharger configuration for the selected engine type.

Keywords: mechanical engineering, turbocharger, flow simulation, calculation.

1. Introduction

The downsizing trend caused by increasingly stringent emission standards is resulting in the very frequent use of supercharging in internal combustion engines [1]. In Europe, turbocharging is the most popular way of increasing improvements in energy ratings while reducing environmental and economic indicators. Turbocharging increases the unit power output of an engine by increasing the density of the supply air, lowering exhaust emissions and reducing fuel consumption [2]. It is commonly used in engines of trucks as well as cars, trains, aircraft and construction equipment [3]. A turbocharger is a device in which the kinetic energy of the exhaust gas drives a turbine, which drives a pump through a shaft so that the air supplied to the cylinder is concentrated, resulting in increased engine efficiency [4].

The basic parameters describing a turbocharger are boost pressure and discharge. The values of the discharge and boost pressure largely depend on the pump rotor speed and may vary even several times depending on the engine speed [5].

The aim of the study presented in this paper was to analyse the influence of the turbocharger pump rotor speed on its operating parameters, such as discharge and boost pressure. The study was carried out on a virtual model using SolidWorks Flow Simulation software.

2. Materials and methods

The object of the analysis was a virtual model of an IHI VB10 17201-27050 turbocharger from a 1CD-FYV Toyota engine (displacement 2000 cm3, power 90 PS). The engine was found in Toyota Corolla and Toyota Verso cars. A view of the actual object of analysis is shown in Fig. 1a, while a simplified virtual model is shown in Fig. 1b.

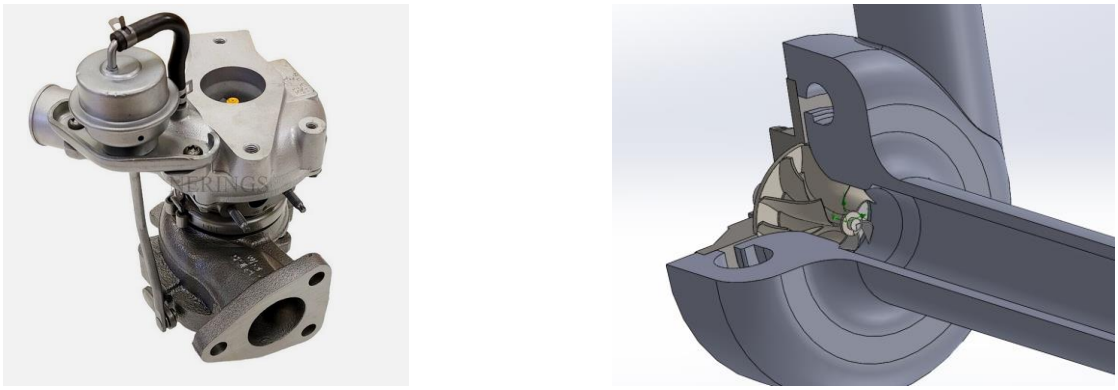

(a) (b)

Fig. 1 IHI VB10 turbocharger: (a) photo, (b) CAD model

The intake and exhaust ducts from the turbocharger have been extended to simulate the volume of the engine's intake system ducting. The outlet diameter was reduced to simulate the restricted flow caused by the opening and closing of the intake valves. Fig. 2a shows the turbocharger pump impeller, while Fig. 2b shows the CAD model.

(a) (b)

Fig. 2 Pump impeller: (a) view of the actual object with main dimensions marked, (b) CAD model

The analysis of the turbocharger pump parameters was carried out in SolidWorks Flow Simulation software. The solution was obtained using the conservation of momentum principle for a moving fluid according to the Navier-Stokes equations and the conservation of mass principle. The solution of these equations allowed the velocity and pressure to be determined at any section or point of the model for each geometry. As flows could occur in the laminar and turbulent range, Favre's mass averaging was added to the Navier-Stokes equations. The turbulence model was assumed to be *k*-*ε*. Due to the voluminous nature of the mathematical descriptions of the calculation methodology in SolidWorks Flow Simulation, they are omitted from this paper. Boundary conditions at the inlet and outlet were defined as atmospheric pressure (Fig. 3).

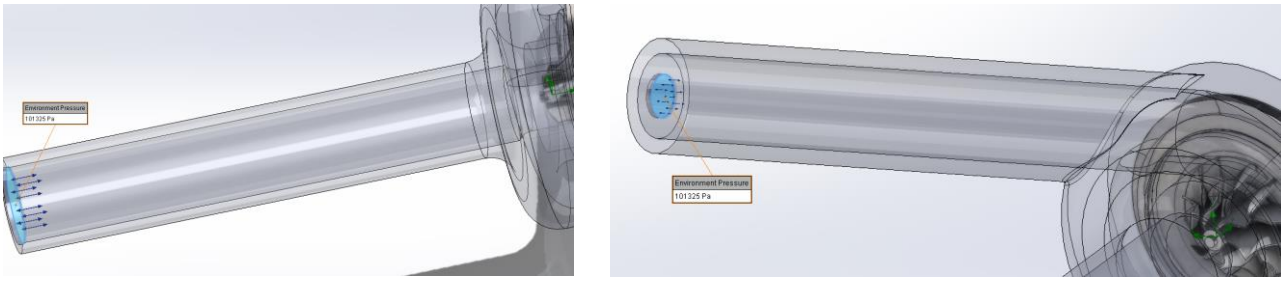

(a) (b)

Fig. 3 Boundary conditions: (a) inlet, (b) outlet

In the pump rotor area, a rotational area with definable speed was set (Fig. 4a). Pressure and density results were determined at point A at the turbocharger exit (Fig. 4b), while mass flow was determined at the wall of the exit boundary condition.

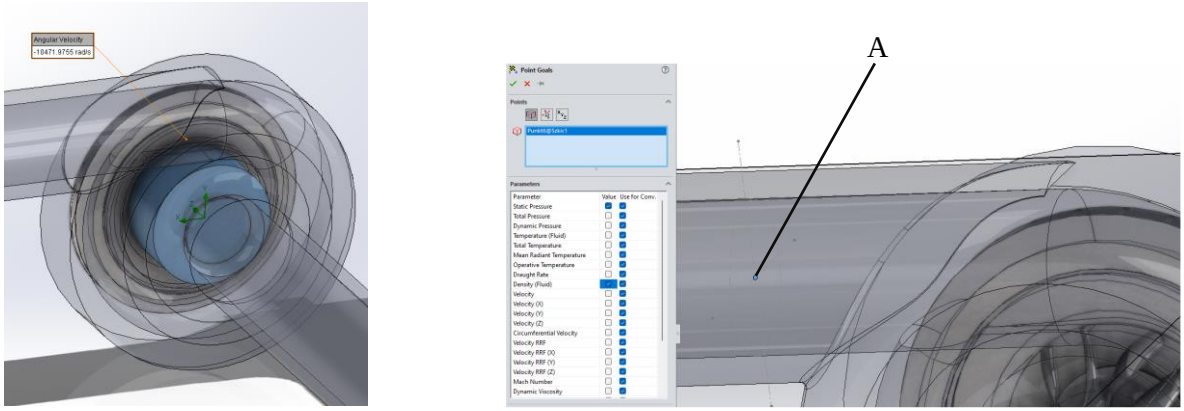

(a) (b)

Fig. 4 Inlet and outlet parameters: (a) rotation on the pump impeller, (b) result parameters

An important step before starting the analysis was to test the convergence of the mesh. The test consisted of globally compacting the grid in the area under consideration and observing the changes in the result values. The parameters calculated were the mass flow at the outlet (G) and the pressure value before the turbocharger (p). The results thus obtained are shown in Fig. 5a and b.

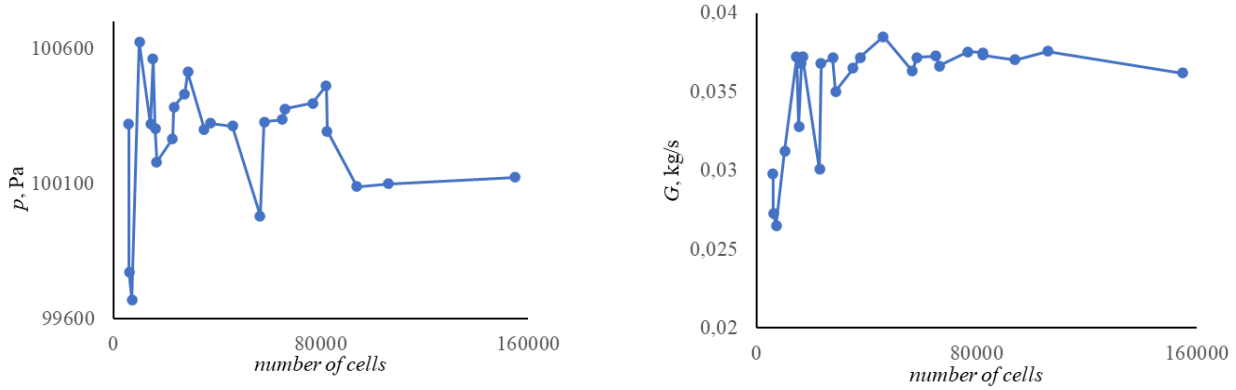

(a) (b)

Fig. 5 Mesh convergence test results: (a) inlet pressure, (b) outlet mass flow rate

Based on the mesh convergence study, a mesh of 105899 cells was adopted, i.e. with a main setting of 5 and a minimum gap size of 2 mm. The view of the adopted mesh includes (Fig. 6).

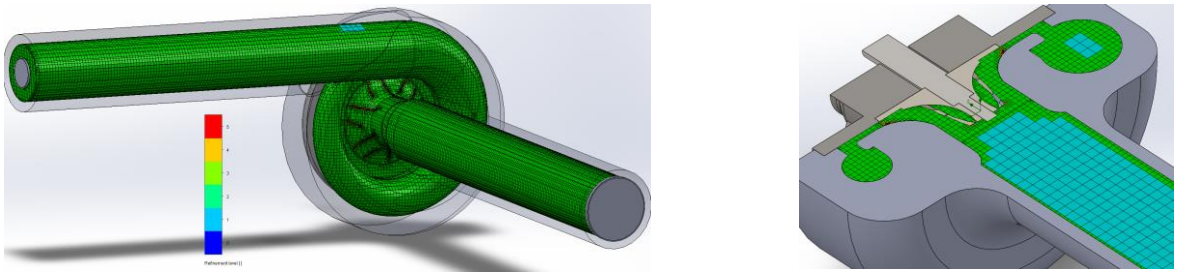

(a) (b)

Fig. 6 Mesh of the model: (a) general view, (b) cross-section through the impeller axis

3. Results and discussion

As part of the analyses, the following turbocharger pump parameters were calculated: mass flow (G), density (□) and pressure (p) at the outlet as described earlier. The calculations were carried out for different pump rotor speeds of: 40,000, 60,000, 80,000, 100,000, 120,000 and 140,000 min-1. The airflow trajectories through the turbocharger pump are shown in (Fig. 7). Their nature showed no significant differences.

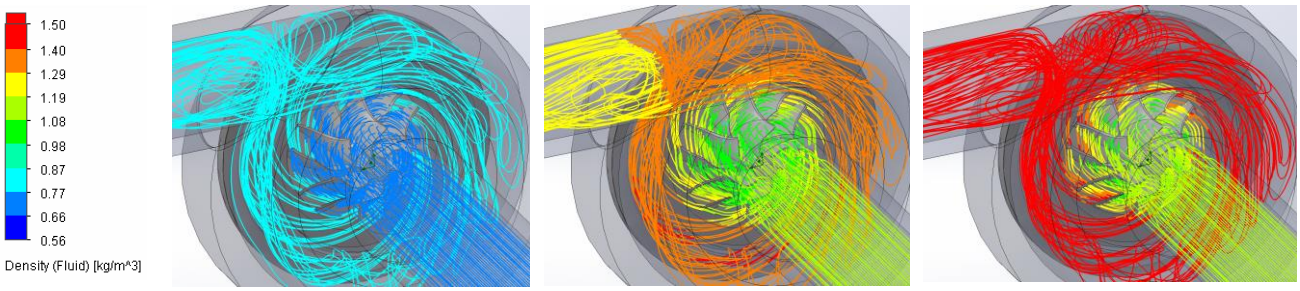

(a) (b) (c)

Fig. 7 Air flow trajectories through the compressor at: (a) 40.000, (b) 100.000, (c) 140.000 min^{-1}

The characteristic parameter values obtained during the calculations are shown in Fig. 8. Each time the results were approximated by a trend line in the form of a 2nd-degree polynomial, obtaining high values of the determination coefficient. Increasing the turbocharger rotor speed resulted in higher values of its characteristic parameters, such as boost pressure, density and mass flow rate. The air mass flow rate increases almost linearly, while density and pressure increase in a way that can be described by a quadratic function. This indicates that the rotational speed of the turbocharger rotor has a significant effect on the turbocharger parameters. Thus, the aim of the study was achieved.

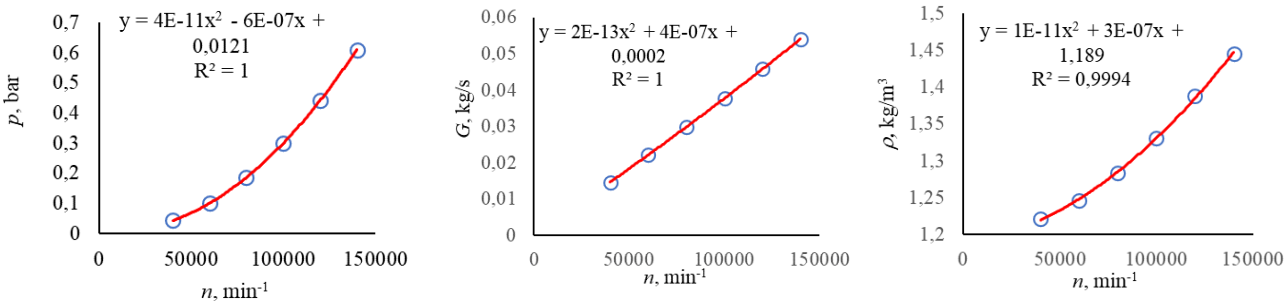

(a) (b) (c)

Fig. 8 Calculation results: (a) boost pressure, (b) mass flow rate, (c) density

The approximation of the results by means of a trend line in the form of a 2nd-degree polynomial with a high coefficient of determination shows that the turbocharger parameters can be accurately described by means of a quadratic function. In this way, it is possible to predict the required pump speed to achieve the desired turbocharger parameters and thus the turbocharger configuration for use in the selected engine type. Drawing up a series of characteristics in this area can result in the determination of the stratified characteristics of the turbocharger.

4. Conclusions

Based on the calculations and analyses carried out in the study, the following conclusions were drawn:

1. Numerical fluid mechanics (CFD) was successfully used to determine the characteristic parameters of a turbocharger as a function of pump rotor speed.
2. SolidWorks Flow Simulation software was used for the simulation, where a simplified model of an IHI VB10 turbocharger was used as a base.
3. The analyses determined the effect of rotational speed on boost pressure, mass flow rate and density, and the results were approximated by a trend line in the form of a 2nd-degree polynomial obtaining high values for the coefficient of determination.
4. The mass output increased almost linearly with increasing speed, and the pressure and density increased in a way that could be described by a quadratic function.
5. The result will be applicable to the turbocharger configuration for the selected engine type.

5. Further research

The calculation and inference proposed in this paper are applicable to the determination of turbocharger characteristics. Ultimately, the effect of the number and shape of the turbocharger's pump blades on its functional parameters will be determined in further analyses. The results obtained in this way will be helpful in assessing the feasibility of modifying the turbocharger for applications in various internal combustion engines, while leaving its external dimensions and mountings unchanged.

References

1. Leduc, P.; Dubar, B.; Ranini, A.; Monnier, G. Downsizing of Gasoline Engine an Efficient Way to Reduce CO2 Emissions. *Oil & Gas Science and Technology* **2003**, 115-127.
2. Uchida, H. Trend of Turbocharging Technologies. *Technical Journal* **2006**.
3. Muqeem, M.; Ahmad, D. M.; Sherwani, D. A. Turbocharging of Diesel Engine for Improving Performance and Exhaust Emissions: A Review. *IOSR Journal of Mechanical and Civil Engineering* **2015**, 22-29.
4. Tetsui, T. Development of a TiAl Turbocharger for passenger vehicles. *Materials Science and Engineering* **2002**, A(329-331), 582-588.
5. Marelli, S. Copobianco, M. Zamboni, G. Pulsating flow performance of a turbocharger compressor for automotive application. *International Journal of Heat and Fluid Flow* **2013**.

Rapid Prototyping Technologies for Hydrogen Storage Materials

Stefan SIJUMBILA[1] and Surendra Kumar SAINI[1]*

1 Department of Mechanical and Metallurgical Engineering, School of Engineering and the Built Environment, University of Namibia, Namibia
** surendra1feb@gmail.com*

Abstract

The increasing demand for clean energy sources has created interest in hydrogen as a possible source of clean energy. This research investigates key aspects of hydrogen energy storage, concentrating on the selection of adequate materials and the use of advanced rapid prototyping technologies. To make cylinders, vessels and tanks for hydrogen storage, various materials such as aluminum and its alloys, composites, polymers, steels are studied closely in relation to their viability in being used as hydrogen storage materials. The rapid prototyping technologies are growing exponentially to certainly meets the demand of different material fabrication. Amongst rapid prototyping techniques direct energy deposition, powder bed fusion, material extrusion and fused deposition modeling are most widely used part printing techniques. The present study highlighted the important properties of hydrogen storage materials and significant role of rapid prototype technologies. Despite the exciting potential of hydrogen as an energy source, safe and effective storage remains a significant challenge. This is creating a need for further research to be done to fully appreciate the potential of hydrogen as a clean energy source.

Keywords: hydrogen energy, rapid prototype, materials.

1. Introduction

There are five variants of hydrogen energy namely grey, brown, blue, turquoise and green. Green hydrogen is produced from water electrolysis process which is a clean energy source that grips massive potential for addressing global energy needs. Hydrogen used for renewable energy can provide a source of clean energy and it has a high energy content per unit weight. It is considered a clean fuel because when consumed in a fuel cell, it creates only water which is not toxic to people [1]. Abe et al. [2] addressed the economy and storage of hydrogen energy. They comprehensively described the different states of hydrogen storage system which are gaseous, liquid and solid. However, efficient storage and transportation methods of green hydrogen energy are major challenges that may retard its potential growth. High pressure tanks are used for the storage of hydrogen. Therefore, these storage tanks materials must be possessing superior mechanical, chemical and thermal properties. Compressed gas and cryogenic liquid hydrogen are the most used in industry. Compact design of hydrogen storage structures is challenges because hydrogen is a low energy density gas. Its storage requires at least three times more spaces than natural gas storage. Therefore, store facilities of green hydrogen are required more space likewise solar cell plate. Osman et al. [3] studied the hydrogen energy economy through its production, storage, utilization and environmental effect. They reported different manufacturing processes of hydrogen energy from distinct resources. Further, challenges in hydrogen production methods have mentioned. Life cycle assessment of hydrogen production and consumption has also studied. Dewangan et al. [4] reported that declining the cost of hydrogen storage is crucial challenges in comparison to conventional energy storage systems. They mentioned that hydrogen storage capacity requires more investigation to set hydrogen economy. Thermal management is another important issue for hydrogen storage tanks and pipelines. Energy content possess by hydrogen is higher than other alternative fuels. However, storage of high-pressure gas or liquid hydrogen energy is a major challenge for the hydrogen economy. Hydrogen storage in metal hydrides may be one of the best storage systems. Metal hydrides possess excellent gravimetric and volumetric storage capacities over other storage systems. Moreover, it has safe operating pressures [5-7]. Study on storage systems of compressed hydrogen has been done by Alves et al. [8]. They reported different storage applications namely light and heavy-duty vehicles, fuel station, maritime, railways, tube trailers etc. Ardarian et al. [9] mentioned that structured porous stainless steel is a suitable material for storage of green hydrogen. Different state of underground storage of hydrogen energy has been studied [10]. The aim of the present study is to explores different green hydrogen energy storage methods and significance of rapid prototyping technologies that support to make the storage structure. The importance of rapid prototyping technologies in developing and testing of hydrogen storage materials is studied. Technologies such as fused deposition modeling, electron beam melting, binding jetting, and another effective means to produce prototypes for optimizing and testing of hydrogen storage systems. By using these technologies, researchers can make the development process go faster, reduce costs, and improve efficiency of hydrogen storage solutions. The present study reveals an insight into the current state and potential improvements in storage methods, and the significant role of rapid prototype technologies in hydrogen storage methods. These methods are key to realizing a sustainable supply of energy in the future.

2. Properties of Hydrogen Storage Materials

The state of hydrogen is mainly relied on temperature and pressure. Solid and gaseous hydrogen are generally found at low and high temperatures, respectively. However, hydrogen is notoriously difficult to storage. One phenomenon which makes it difficult to store is hydrogen embrittlement. High strength steels are more susceptible to hydrogen embrittlement.

Embrittlement is a process which leads to the brittle failure in metal cylinders in which hydrogen gas is stored. Hydrogen storage capacity of different carbon-based materials have been studied [4]. Techniques which involve storing hydrogen in compressed form are being used, however, compressing hydrogen reduces its energy density which makes not viable for large scale energy storage applications. An alternative to compressed gaseous form is liquid hydrogen, this yields a better higher density than compressed gas, but the low boiling point of liquid hydrogen makes it hard to store and manage. This requires specialized and costly equipment. It needs chemical reactions and expensive equipment [7]. Hydrogen storage material should possess mandatory properties; high hydrogen capacity per unit mass and unit volume, dissociation temperature and pressure, low heat of formation, minimum energy loss during charge and discharge of hydrogen, high stability, fast kinetics, high safety, and low cost of recycling and charging infrastructures [11]. Compressed hydrogen and liquid hydrogen should store at a different temperature and pressure [12-13]. Hydrogen storage vessels are categories into four types which includes Type I, Type II, Type III and Type IV [14]. Type I hydrogen storage vessels are made from metals (generally steel), and they are primarily used in industry for fixed use. These vessels store around 1% of hydrogen energy globally at 200-300 bar. Type II vessels are made from mixed composite metal liner. These vessels are lighter than Type I hydrogen storage vessels. Type III vessels are made from composite with an aluminum liner that functions as a hydrogen permeation barrier. Aluminum liners abolish embrittlement and offer more than 5% mechanical resistance. Type IV vessels are made from composite and high-density polyethylene plastic liner. Porous materials are used for hydrogen storage materials. Magnesium and its hydride compounds provide the most safe and efficient means to store hydrogen with high density. Metal hydrides offer great potential for hydrogen storage material because they are of reversible reaction with hydrogen with facilitates compact storage at relatively modest pressures [11-12].

3. Significance of Rapid Prototyping Technology

Rapid prototyping is quick and cost-effective technology which can create prototypes of stringent designed structures. This is important for the design testing and correct manufacturing of parts. Rapid prototyping technologies have revolutionized the development of hydrogen storage materials. This technology makes it possible for us to test how effect a given material will have in storing hydrogen. This allows the designer to verify if the material is adequate or if the design needs further modifications. Rapid prototyping technologies is an effect way to save money by allowing us to test on a model as opposed to using the actual device which is being proposed to be used. Rapid prototyping technologies can contribute to reducing greenhouse gas emissions and pollution while also shortening the time to market for hydrogen.

Free et al. [15] reviewed a study on advanced manufacturing techniques namely binder jetting, material jetting, material extrusion, vat photopolymerization, powder bed fusion, direct energy deposition, sheet lamination for hydrogen storage materials. Description of these rapid prototyping processes are following:

Binder jetting: This method involves deposition of a thin layer of hydrogen storage material usually two layers across the print area. A binding agent like adhesive or solvent acting as the binder is added over the particles which allowed cohesion. After this, binder is either evaporated or removed during the post processing. This process solidifies the hydrogen storage material into the desired shape. Thermal post processing is essential for optimizing the material's hydrogen storage capacity and performance. Binder jetting process is good for the fabrication of hydrogen storage structure like porous metal hydrides, carbon-based materials and ceramics.

Material jetting: This method involves jetting of printing material onto the printing surface. This material is hardened using ultraviolet light. Ease of use and compatibility with various materials make this method more popular for the hydrogen storage applications.

Material extrusion. This is a common method used in rapid prototyping which involves feeding a plastic filament through a heated nozzle, where solid wire filament melts into a liquid state and is deposited layer by layer to form a designed structure. However, material extrusion method is difficult for printing metal parts due to the high melting point possessed by metals which if used, run the risk of damaging the nozzle and print bed. It is possible to extrude ceramics usually in a soft form like unfired clay. This is expensive and the final dimensions of the part may be hard to control. Fused deposition modeling (FDM) is a variant of material extrusion technique which is usually used to make prototype. FDM is relevant because it allows the fabrication of devices used for thermal management and stress build-up prevention in hydride-based hydrogen containers

Vat photopolymerization: In this method liquid resin is exposed with ultraviolet light to make the designed 3D structure. This method is exploring the use of ceramic and ceramic-plastics composites material to make high pressure container and vessels. Stereolithography and light projection printing are two common methods of vat photopolymerization.

Powder bed fusion: In this process, fine metal powder is used as input material and a layer of powder on printing table is exposed with a high-power laser. The laser fuses the powder together and to the bed floor, slowly building a solid metal part. Porous stainless steel (17-PH) fabricated using laser powder bed fusion process for the application of energy storage applications [9].

Direct energy deposition: This method is used to make components from metals and alloys. Unlike powder bed fusion methods which consists of powder bed being selectively melted, direct energy deposition works while feeding wire and using focused energy source like a laser. In direct energy deposition printing, a melt pool is formed on the surface or coated layer using a laser and powder is propelled through the laser and into the melt pool. Each layer is built up track by track using a pre-defined path.

Sheet lamination. This is solid state bonding process in which desired material foils are laid down on printing table and bonded together using adhesive or mechanical energy to make designed structure. This process can occur with a wide range of materials.

4. Conclusions

Green hydrogen is a clean energy source which may accomplish global energy demand and could help to reduce drastically carbon footprint. Rapid prototyping techniques may be more supportive to manufacturing of hydrogen storage and transport materials due to zero wastage of materials as well as energy efficient thereof. In this study, insight of green hydrogen energy, storage properties, and different rapid prototyping techniques namely binder jetting, material extrusion, vat photopolymerization, powder bed fusion, direct energy deposition and sheet lamination have been studied for the manufacturing of hydrogen storage structures.

References

1. Sun C, Wang Y, McMurtrey MD, Jerred ND, Liou F, Li J. Additive manufacturing for energy: A review. Applied Energy. 2021 Jan 15; 282:116041.
2. Abe J.O., Popoola A.P., Ajenifuja E., Popoola O.M. Hydrogen energy, economy and storage: Review and recommendation. International journal of hydrogen energy. 2019 Jun 7;44(29):15072-86.
3. Osman A.I., Mehta N., Elgarahy A.M., Hefny M., Al-Hinai A., Al-Muhtaseb AA., Rooney D.W. Hydrogen production, storage, utilization and environmental impacts: a review. Environmental Chemistry Letters. 2022 Feb 1:1-36.
4. Dewangan S.K., Mohan M, Kumar V, Sharma A, Ahn B. A comprehensive review of the prospects for future hydrogen storage in materials-application and outstanding issues. International Journal of Energy Research. 2022 Oct 10;46(12):16150-77.
5. Züttel A, Rentsch S, Fischer P, Wenger PM, Sudan PH, Mauron P, Emmenegger C. Hydrogen storage properties of LiBH4. Journal of Alloys and Compounds. 2003 Aug 11; 356:515-20.
6. Berube V, Radtke G, Dresselhaus M, Chen G. Size effects on the hydrogen storage properties of nanostructured metal hydrides: A review. International Journal of Energy Research. 2007 May;31(6-7):637-63.
7. Billur Sakintuna, Farida Lamari-Darkrim, Michael Hirscher, Metal hydride materials for solid hydrogen storage: A review, International Journal of Hydrogen Energy, Volume 32, Issue 9, 2007, Pages 1121-1140, ISSN 0360-3199, https://doi.org/10.1016/j.ijhydene.2006.11.022.
8. Alves, M. P., Gul, W., Cimini Junior, C. A., & Ha, S. K. (2022). A review on industrial perspectives and challenges on material, manufacturing, design, and development of compressed hydrogen storage tanks for the transportation sector. *Energies*, *15*(14), 5152.
9. Sardarian, S. & dehgahi, Shirin & Wei, Fei & Secanell, Marc & Qureshi, A.J. (2024). Structured porous 17-PH stainless steel layer fabrication through laser powder bed fusion. International Journal of Sustainable Engineering. 17. 1-16. 10.1080/19397038.2024.2334040.
10. Tarkowski, R. Underground hydrogen storage: Characteristics and prospects. Renew. Sustain. Energy Rev. 2019, 105, 86–94.
11. Zhang, M.; Lv, H.; Kang, H.; Zhou, W.; Zhang, C. A literature review of failure prediction and analysis methods for composite high-pressure hydrogen storage tanks. Int. J. Hydrogen Energy 2019, 44, 25777–25799.
12. Wang, Z.; Wang, Y.; Afshan, S.; Hjalmarsson, J. A review of metallic tanks for H2 storage with a view to application in future green shipping. Int. J. Hydrogen Energy 2021, 46, 6151–6179.
13. Reddi, K.; Elgowainy, A.; Rustagi, N.; Gupta, E. Techno-economic analysis of conventional and advanced high-pressure tube trailer configurations for compressed hydrogen gas transportation and refueling. Int. J. Hydrogen Energy 2018, 43, 4428–4438.
14. Tarasov, B. P., Fursikov, P. V., Volodin, A. A., Bocharnikov, M. S., Shimkus, Y. Y., Kashin, A. M., & Lototskyy, M. V. (2021). Metal hydride hydrogen storage and compression systems for energy storage technologies. International Journal of Hydrogen Energy, 46 (25), 13647-13657.
15. Free Z, Hernandez M, Mashal M, Mondal K. A review on advanced manufacturing for hydrogen storage applications. Energies. 2021 Dec 17;14(24):8513.

MECHANIKA 2024
Proceedings of the 28th International Scientific Conference

ISSN 2783-5677 (online)

SL344. 2024-09-16. 23.5 Printer‘s Sheets. Order No. 168.
Publishing House “Technologija”, Studentų st. 54, LT-51424 Kaunas